Molecular dissection of BV6 induced sensitization of rhabdomyosarcoma spheroids towards NK cell attack

Dissertation
zur Erlangung des Doktorgrades
der Naturwissenschaften

vorgelegt beim Fachbereich Biochemie, Chemie und Pharmazie
der Johann Wolfgang Goethe-Universität
in Frankfurt am Main

von
Vinzenz Särchen
aus Berlin

Frankfurt am Main, 2022
(D 30)

Vom Fachbereich Biochemie, Chemie und Pharmazie (FB14)
der Johann Wolfgang Goethe-Universität als Dissertation angenommen.

Dekan: Prof. Dr. Clemens Glaubitz
Gutachter 1: Prof. Dr. Robert Fürst
Gutachter 2: PD Dr. Meike Vogler

Datum der Disputation: 16.11.2022

Contents

List of Abbreviations

ABD	Antibody dilution buffer
AG	*Arbeitsgruppe*, working group
AML	acute myeloid lymphoma
APAF1	apoptotic protease-activating factor 1
APS	Ammonium persulfate
aRMS	alveolar rhabdomyosarcoma (fusion-positive RMS)
ATCC	American type culture collection
BCA	Bicinchoninic acid
BID	BH3 interacting-domain death agonist
BIR	Baculovirus IAP Repeat
BIRC2	Baculovirus IAP Repeat-containing protein 2 (see cIAP1)
BIRC3	Baculovirus IAP Repeat-containing protein 3 (see cIAP2)
bp	Base pair
BSA	Bovine Serum Albumin
CAR	chimeric antigen receptor
CARD	caspase recruitment domain
CD	cluster of differentiation
cDNA	complementary DNA
CFSE	Carboxyfluorescein succinimidyl ester
cIAP1	cellular inhibitor of apoptosis 1 (see BIRC2)
cIAP2	cellular inhibitor of apoptosis 2 (see BIRC3)
CIK cells	cytokine-induced killer cells
Cq	Cycle of quantification
CRISPR	Clustered regularly interspaced short palindromic repeats
CT	CellTrace™
DAPI	Diamidino-2-phenylindole
DD	Death domain
DEG	differentially expressed gene
ddH_2O	destilled deionised water
DISC	death-inducing signaling complex
DMEM	Dulbecco's Modified Eagle Medium
DMSO	Dimethyl sulfoxid
DNA	Deoxyribonucleic acid
DR	Death receptor
DSMZ	Deutsche Sammlung von Mikroorganismen und Zellkulturen

DTT	Dithiothreitol
ECL	Enhanced chemiluminescence
EDTA	Ethylenediaminetetraacetic acid
ELISA	Enzyme-linked immunosorbend assay
ENDOG	Endonuclease G
eRMS	embryonal rhabdomyosarcoma (fusion-negative RMS)
E:T ratio	effector cell to target cell ratio
FACS	Fluorescence-activated cells sorting
FADD	Fas-associated death domain protein
FC	Flow cytometry
FCS	Fetal calf serum
FITC	Fluorescein isothiocyanate
FNRMS	fusion-negative RMS (eRMS)
FOXO1/FKHR	Forkhead box protein O1
FPRMS	fusion-positive RMS (aRMS)
FSC	Forward scatter
fwd	Forward
G6PD	Glucose-6-phosphate-1-dehydrogenase
GAPDH	Glyceraldehyde-3-phosphate dehydrogenase
GFP	Green fluorescent protein
GO	Gene ontology
GOI	Gene of interest
GRC	German Red Cross
gRNA	guide RNA
GSEA	Gene set enrichment assay
h	hour
HEPES	4-(2-hydroxyethyl)-1-piperazineethanesulfonic acid
HRP	Horse-radish peroxidase
IAP	Inhibitor of apoptosis
IBM	IAP binding motif
IgG	Immunoglobulin G
IXM XLS	ImageXpress Micro XLS
KD	knock-down
KO	knock-out
LAK cells	Lymphokine-activated killer cells
LOH	loss of heterozygosity
LOMMP	Loss of mitochondrial membrane potential

MAP3K14	Mitogen-activated protein kinase kinase kinase 14 (NIK)
MCTS	multicellular tumor spheroid
MFI	median fluorescence intensity
min	minutes
MOMP	mitochondrial outer membrane permeabilization
mRNA	Messenger RNA
MTT	3-(4,5-dimethylthiazol-2-yl)-2,5-diphenyltetrazolium bromide
NET	neuroendocrine tumor
NF-κB	Nuclear Factor kappa light polypeptide gene enhancer of activated B cells
NFKB2	NF-κB p100 subunit (p100)
NFKBIA	NF-κB inhibitor alpha (IκBα)
NIK	NF-κB-inducing kinase (MAP3K14)
NK cells	Natural killer cells
ns	non significant (non sig.)
OMM	outer mitochondrial membrane
p	p-value
PAGE	Polyacrylamid gelelectrophoresis
PAM	protospacer adjacent motif
PARP	Poly(ADP-ribose)-Polymerase
PAX3	Paired-box protein 3
PAX7	Paired-box protein 7
PBMC	peripheral blood mononuclear cells
PBS	Phosphate buffered saline
PBS-T	Phosphate buffered saline-tween
PCA	Principle component analysis
PCR	Polymerase chain reaction
PE	Phycoerythrin
PerCP	Peridinin-Chlorophyll-Protein
pH	Power of hydrogen
PI	Propidium Iodine
PIC	Protease inhibitor cocktail
PMSF	Phenylmethansulfonyl fluoride
P/S	Penicillin/Streptomycin
qRT-PCR	quantitative real-time PCR
RANTES	regulated on activation, normally T cell expressed secreted
RELA	Transcription facrtor p65

rev	Reverse
RING	really interesting new gene
RIPK1	Receptor-interacting serine/threonine-protein kinase 1
RMS	Rhabdomyosarcoma
RNA	Ribonucleic acid
ROS	reactive oxygen species
RPII	RNA polymerase II
rpm	revolutions per minute
RPMI	Roswell Park Memorial Institute
rRNA	ribosomal ribonucleic acid
RT	room temperature
sec	seconds
SD	Standard deviation
SDS	Sodium dodecyl sulfate
SEM	Standard error of mean
siRNA	small-interfering siRNA
SM	Smac mimetic
Smac	second mitochondria-derived activator of caspases
SMP	Skimmed milk powder
SSC	Side scatter
STR	Short tandem repeat
STS	soft tissue sarcoma
tBID	truncated BID
TF	transcription factor
TME	tumor microenvironment
TNF	Tumor necrosis factor
TNFR1	TNF receptor type 1
TNFRSF	TNF receptor super family
TNFRSF10B	TNFRSF member 10B, TRAIL-receptor 2, DR5
TNFSF	TNF super family
TP53	Tumor protein 53
TRADD	TNFR1-associated death domain protein
TRAF	TNF receptor-associated factor
TRAIL	TNF-related apoptosis-inducing ligand
Tris	Tris(hydroxylmethyl)aminomethane
TRITC	5(6)-Tetramethylrhodaminisothiocyanate
TWEAK	TNF-related weak inducer of apoptosis (TNFSF12)

UBA	ubiquitin binding associated domain
untr	untreated
unst	unstained
VAC	Vinchristine-Actinomycin D-Cyclophosphamide
WB	western blot
WHO	world health organization
zAAD-cmk	Benzyloxycarbonyl-Ala-Ala-Asp-chloromethylketone
zVAD.fmk	N-benzyloxy-cabonyl-Val-Asp-fluoromethylketon

List of Tables

List of Figures

1 Abstract

Rhabdomyosarcoma (RMS) is the most common soft tissue sarcoma in early childhood. Despite recent advances in the treatment regimes of rhabdomyosarcoma, the 5-year survival is still alarmingly low for the more aggressive metastasizing alveolar rhabdomyosarcoma subtype. Novel treatment strategies are needed in order to increase the overall survival rate.
One hallmark of tumor cells is to evade cell death induction and evade immune system surveillance. This is mediated in part by the up-regulation of so called inhibitor of apoptosis (IAP) proteins. With the development of Smac mimetic compounds mimicking the endogenous IAP antagonist Smac, this tumor evasion mechanism became exploitable.

In this PhD thesis, a combinatory approach for a putative treatment option of RMS will be presented. Here, the Smac mimetic compound BV6, will be used as a pre-treatment of RMS cells. This pre-treatment leads to a sensitizing effect within the tumor cells, increasing the killing efficacy of natural killer (NK) cells.

Subtoxic concentrations of BV6 were chosen to sensitize RMS cells. At the same time, these concentrations were non-toxic for IL-15 activated primary expanded NK cells. To represent two different RMS subtypes, RD (embryonal) and RH30 (alveolar) cell lines were chosen. To remodel the solid tumor characteristics of RMS, a cultivation method to mimic the three-dimensional shape was utilized. Thus multicellular RMS tumor spheroids were generated.
In both tumor spheroids and conventional monolayer cell culture BV6 induced the degradation of IAP proteins (cIAP1, cIAP2, in spheroids XIAP). Further, BV6 led to the activation of both, the canonical and non-canonical NF-κB signaling pathways. This was demonstrated by an increased IκBα and p65 phosphorylation, and nuclear translocation of p-p65, indicative for an active canonical NF-κB signaling. On the other side, cIAP degradation led to the stabilization and accumulation of NIK and downstream partial degradation of p100 to p52 and its nuclear translocation, indicating non-canonical NF-κB signaling pathway activity. A bulk RNA sequencing approach of BV6 treated RH30 cells validated the NF-κB signaling involvement and identified 182 differentially expressed genes. Among the interesting target genes are *NFKBIA* (IκBα), *BIRC3* (cIAP2), *NFKB2* (p100), *CCL5* and *SSTR2*. *SSTR2* was thoroughly validated as being up-regulated on a transcriptional and on protein level. Here, *SSTR2A*, one of the two alternative splicing variants, is up-regulated and opens a hypothetical tar-

geted treatment strategy, as SSTR2 expression is not associated with RMS, but rather described with neuroendocrine tumor entities. In addition, CCL5 was thoroughly validated as a BV6 induced target. Again, the up-regulated mRNA transcription was validated by an increased translation and by increased secretion of CCL5. As CCL5 being associated as pro-migratory and activating of NK cells, CRISPR/Cas9 mediated *CCL5* knock-out studies were performed to evaluate the influence of CCL5 within a BV6 pre-treatment and NK cell co-cultivation setting. It was shown that *CCL5* knock-out does not rescue BV6 pre-treated RMS spheroids from NK cell attack and killing.
The previous mentioned transcriptional activity by BV6 stimulation was NIK mediated as knock-down of *NIK* reduced the mRNA transcription of several interesting genes. However, NIK mediated down-stream signaling had no influence on the BV6 induced sensitizing effect towards NK cell mediated attack. A *NIK* knock-down had no rescue effect upon BV6 pre-treatment and NK cell co-treatment.

As cIAP proteins are present in receptor bound complexes, e.g. complex I at the TNF receptor 1 (TNFR1), a putative involvement of death receptors in general was evaluated. Indeed, BV6 treatment of RMS cells could increase the surface presentation of DR5, a death receptor ligating TRAIL. Functionally, co-treatment of BV6 with TRAIL led to an additive cell death inducting effect. However, within the NK cell co-cultivation setting, addition of a neutralizing TRAIL anitbody could not rescue BV6 pre-treated RMS spheroids from NK cell killing. A similar effect was observed when neutralizing TNFα by adding Enbrel during the NK cell co-cultivation. BV6 sensitization of RMS spheroids seems to be independent of death receptors.

In addition to activating NF-κB, BV6 as a Smac mimetic is supposed to be able to release caspases bound by IAP proteins. Indeed, BV6 pre-treatment of RMS spheroids and co-cultivation with NK cells could cleave and thereby activate the executioner caspase-3. Further, treatment with a pan-caspase inhibitor, zVAD.fmk, could reduce the BV6 mediated sensitizing effect towards NK cell attack in RD spheroids.

Taken together, BV6 does induce a thoroughly validated NF-κB signaling pathway, leading to a NIK mediated transcriptional signature change. However, the NF-κB activation might not be responsible for the observed sensitization. Further, BV6 in combination with NK cells led to a seemingly death receptor independent, caspase dependent cell death induction of RMS spheroids. Although the mechanism remains partially concealed, a therapeutic benefit by combining a cell death sensitizing compound, i.e. BV6, with cytotoxic lymphocytes is evident.

2 Introduction

2.1 Rhabdomyosarcoma

In 1854, as one of the earlier reports, Weber and Virchow described a neoplasm of the tongue, made out of various stages of embryonal skeletal muscle fibers [1]. In 1946, this case was post-hoc identified as a putative embryonal rhabdomyosarcoma (eRMS) by Stout, who further characterized a case of alveolar rhabdomyosarcoma (aRMS) [2].
Although relatively rare, rhabdomyosarcoma is the most common soft tissue sarcoma (STS) with 4.5-5 % of all pediatric tumors [3, 4]. RMS cells show a rhabdomyoblastic phenotype and resemble skeletal muscle progenitor cells, expressing MyoD1 and myogenin [4]. Additionally, the tumor entity can also originate in non-skeletal muscle cells, like endothelial-progenitor cells [5]. Horn and Enterline classified rhabdomyosarcoma into four subtypes, the pleomorphic, embryonal, alveolar and botyroid [6]. Within 60 years, the classification of RMS, based on their histopathological appearance changed only slightly. The most recent proposed classification system in 2015 removed the differentiation of an own botyroid subtype, instead added a spindle cell/sclerosing, but kept the embryonal, alveolar and pleomorphic subtypes [7].
Within this quartet, the embryonal ($\approx$60-70 %, eRMS) and alveolar ($\approx$20 % aRMS) subtypes arose to be the majority of clinical cases [7, 8]. As classical histopathological criteria might not be sufficient for a detailed classification, molecular, cytogenetic descriptions of RMS subtypes needed to be found. Figure 2.1 depicts the molecular differentiation for the aRMS and eRMS subtypes. Alveolar RMS, alternatively termed fusion-positive RMS (FPRMS), are characterized based on genetic translocations (t(2;13)(q35;q14) and t(1;13)(p36;q14)) of the transcription factors *PAX3* (2q35) or *PAX7* (1p36) to the transcription factor *FOXO1* (13q14) [9]. These translocations are present within $\approx$85 % of all aRMS cases [8]. As presented in fig. 2.1, a minority of aRMS do not show a characteristic translocation, rather a loss of heterzygosity (LOH) at the chromosomal region 11p15.5, leading to a loss of tumor suppressor functions (*H19*, *CDKN1C*) and increased expression of oncogenes (*IGF2*, *HRAS*) [8, 10, 11]. Such LOH at 11p15.5 and other chromosomal losses or chromosomal gains are mainly associated with eRMS, alternatively termed fusion-negative RMS (FNRMS) [10, 11]. FNRMS subtype mutations are predominantly associated to the tumorigenic RAS pathway [12]. Worth to mention is that mutated *p53* emerged in a higher frequency in stable RMS cell lines, rather than within primary RMS samples [13].

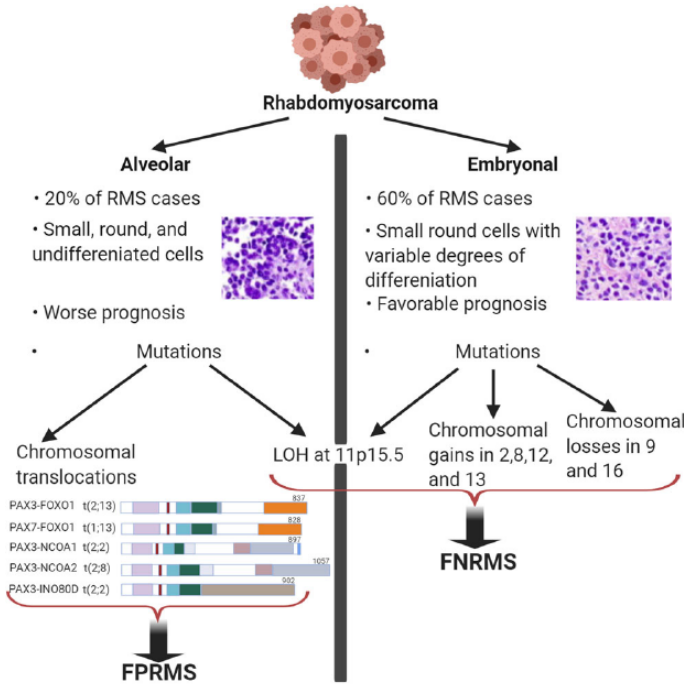

Fig. 2.1: Depiction of the characteristics of aRMS (fusion-positive) and eRMS (fusion-negative) subtypes. Figure adapted from Ramadan et al. [10].

Recent treatment advances and multimodal strategies have increased the overall survival rate of RMS patients up to around 70 % [14, 15]. However, the 5-year survival rate declines to ≈ 46 % for fusion-positive RMS. Whereas, the rate for fusion-negative RMS stays at ≈ 75 % [16]. Alarmingly, the 5-year survival rate drops even further to ≈ 21 %, if the primary RMS has shown metastases at the time of diagnosis [17].
Until today, the classical treatment strategies consists of chemotherapy (vincristine, dactinomycin in combination with cyclophosphamide or ifosfamide), radiotherapy and surgical resection. Hence, novel treatment strategies are needed, particularly for the hard to target and more aggressive alveolar/fusion-positive RMS subtype [3, 18]. In contrast to the ever optimizing chemotherapeutic regiments [19], novel therapies and targeted approaches, like immune-checkpoint inhibitors [20], cellular-immunotherapies (CAR T/NK cells) [21], blockade of PAX-FOXO1 co-regulators by epigenetic targeting [22], sensitizing pro-cell death pathways (autophagy, apoptosis) [23, 24] or combination of mentioned strategies [25, 26] are being investigated.
Focusing on a cellular based immunotherapeutic approach might be challenging, due to an immunosuppressive tumor microenvironment (TME) within the solid RMS tissue [27]. Based on this characteristic, RMS are termed immunological cold tumors, evident by a low tumor infiltrating lymphocyte number, compared to other solid tumor entities (e.g. bladder cancer, melanoma, ovarian cancer) [28].

2.2 Relevant cellular signaling pathways

Hanahan and Weinberg initially described six hallmarks of cancer, among them is the evasion of apoptosis. More generalized, the resistance to cell death pathways [29]. Later added was evasion of immune destruction as another hallmark referring to cell death [30]. Other identified hallmarks of cancer development, e.g. sustained angiogenesis, tumor promoting inflammation, non-mutational epigenetic regulation, are closely associated with the transcriptional master regulatory pathway, termed nuclear factor of κ light polypeptide gene enhancer in B cells (NF-κB) signaling pathways [31, 32]. The following section will give an introduction to apoptosis regulation and the activation patterns of the NF-κB signaling pathways.

2.2.1 Apoptosis

In contrast to spontaneous/accidental cell death, by means of physical, chemical or mechanical stress, apoptosis belongs to the regulated/programmed forms of cell death induction [33].
In 1972, Kerr et al. proposed the term apoptosis (greek; apo ($\dot{\alpha}\pi\acute{o}$): away from, ptosis ($\pi\tau\tilde{\omega}\sigma\iota\varsigma$): falling) for an observed form of cell death, where the cells are falling apart, forming apoptotic bodies, preceded by nuclear and cytoplasmic condensation and fragmentation [34].
In the case of apoptosis, two cellular signaling pathways are generally accepted to be of relevance. Firstly, the intrinsic form of apoptosis, regulated from within the cell with a mitochondrial involvement. Secondly, the extrinsic form of apoptosis, where signals from outside the cell are relayed by cell surface receptors to activate cell death [33, 35, 36].

2.2.1.1 Intrinsic apoptosis

Upon internal disruption of cellular homeostasis, e.g. DNA damage, ROS induced cell stress or suppressed growth factor stimulation, leading to the perforation of the mitochondria, subsequent formation of the apoptosome and activation of the caspase cascade [33, 38]. Involvement of the mitochondria and mitochondrial outer membrane permeabilization (MOMP) is strictly controlled by pro- and anti-apoptotic BCL-2 protein family members [39]. Upon activation, the pro-apoptotic members BAX, BAK and BOK cluster at the mitochondria and oligomerize within the outer mitochondrial membrane (OMM) to form pores [39, 40]. Upon permeabilized OMM, proteins (e.g. cytochrome c and second mitochondria-derived activator of caspases (Smac)) within the intermembrane space are released into the cytoplasm [40, 41].

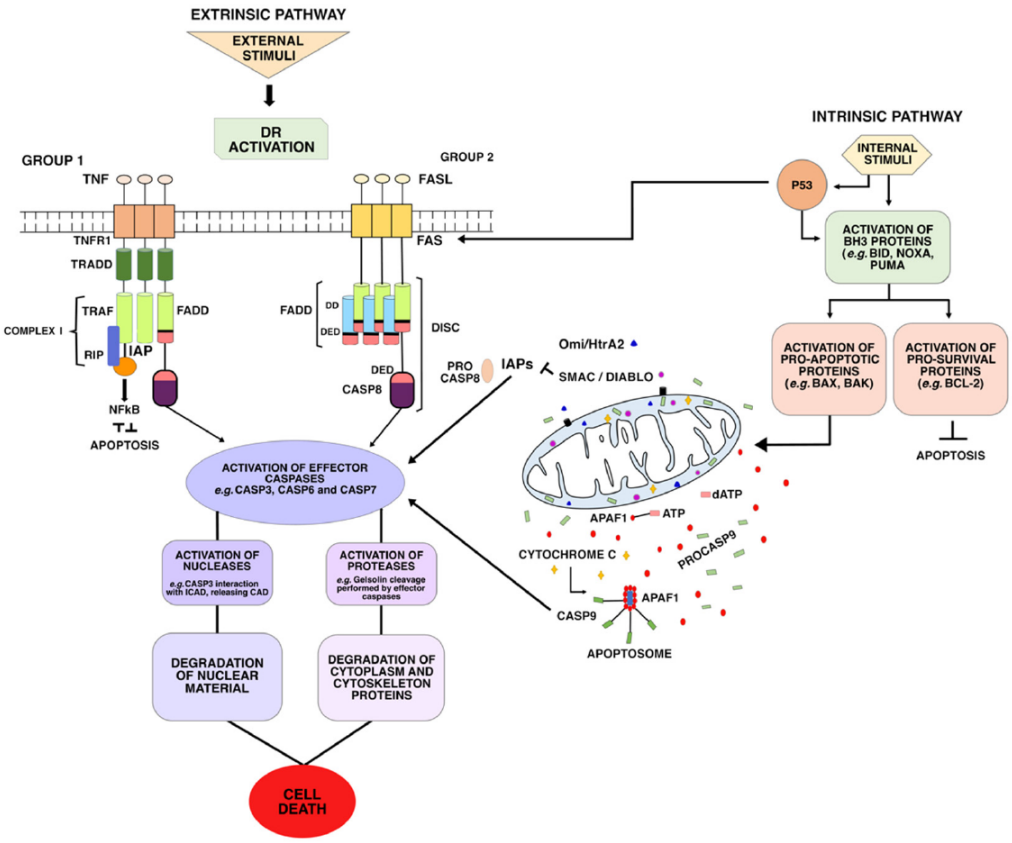

Fig. 2.2: Depiction of both, intrinsic (see sec. 2.2.1.1) and extrinsic (see sec. 2.2.1.2) apoptotic cell death inducing signaling pathways. On the left, binding of death ligands (TNFα, TRAIL, FasL) to their respective death receptors (TNFR1, TRAIL-R, Fas) trigger receptor complex (DISC) formation. DISC leading to the activation of initiator caspase-8, caspase cascade activation and execution of cell death. On the right, internal stimuli, e.g. genotoxic stress, activate pro-apoptotic BCL-2 proteins, leading to BAX/BAK dependent pore formation of the outer mitochondria membrane. Among other, releasing cytochrom c and Smac. Formation of the apoptosome, activation of initiator caspase-9. Again, caspase cascade activation and execution of cell death. Smac, further suppressing inhibitor of apoptosis proteins, subsequent increased caspase activation. Figure adapted from Cavalcante et al. [37].

Pore formation, induced by the pro-apoptotic BCL-2 proteins BAX, BAK and BOK, and MOMP are blocked by anti-apoptotic BCL-2 family members (BCL-2, BCL-x$_L$, BCL-w, MCL-1, BFL and DIVA). Those anti-apoptotic BCL-2 proteins, within the hydrophobic environment of the mitochondrial membrane, can bind to the BH3 domain of BAK and BAX, by that preventing the pore formation activity and inhibiting MOMP [39, 40]. The third party of this activation mechanism are BH3-only proteins (BID, BAD, BIM, BMF, BIK, HRK, BLK, BNIP3, NIX, PUMA, NOXA). As the name

implies, they contain at least one BH3 domain, which can bind to the complex of previously described anti-apoptotic BCL-2 family members and displace BAX and BAK by binding to the anti-apoptotic proteins [39]. This releases BAX and BAK, leading to their oligomerization and eventually MOMP [39, 40].
Apoptotic protease-activating factor 1 (APAF1), dATP and sequestered cytochrome c form a heptameric complex termed apoptosome. This complex formation, leads to a conformational change and exposure of the caspase recruiting domain (CARD) of APAF1. This exposure enables a CARD-CARD interactions of APAF1 and the CARD of pro-caspase-9 [42]. The CARD-CARD binding initiate a putative proximity induced activation and cleavage of pro-caspase-9 to its active state [42, 43]. This in turn cleaves and activates pro-caspase-3 and pro-caspase-7. As executioner caspases, they cleave their target proteins, i.e. ICAD, nuclear lamins, gelsolin, actin, and resulting in the characteristic nuclear fragmentation, presentation of phosphatidylserine and blebbing into apoptotic bodies, leading to apoptotic cell death [33, 44, 45].

2.2.1.2 Extrinsic apoptosis

In contrast to the intrinsic apoptosis activation, the extrinsic activation pathway involves surface residing receptors to relay a death inducing signal to the inside of the cell [33]. Those surface residing receptors can either be functioning as dependence receptors, where the ligation and receptor activation is needed to survive and upon signal deprivation a caspase dependent form of cell death is activated [46, 47]. Other surface receptors binding to death ligands and inducing cell death signaling pathways, are named death receptors (DR) [48]. Death receptors belong to the tumor necrosis factor receptor superfamily (TNFRSF) with their corresponding ligands within the TNF superfamily (TNFSF) [49, 50]. A common characteristic of DR is their intracellular death domain (DD). Upon binding to their respective ligands (FasL, TRAIL: TNF-related apoptosis inducing ligand) the DRs, CD95 (Fas), TRAIL-R1 (DR4) or TRAIL-R2 (DR5), recruit an adapter protein FADD (Fas-associated death domain protein) and further two pro-caspase-8 molecules [50, 51]. Together with pro-caspase-10 and FLICE-inhibitory protein ($FLIP_{L/S}$) this complex is termed death-inducing signaling complex (DISC) [52, 53]. In contrast to the depicted DISC assembly on CD95, TRAIL-R1 and TRAIL-R2, the DR TNFR1 initially recruits a different adapter protein, TRADD (TNFR1-associated death domain protein), which in turn recruits FADD, leading to complete DISC assembly. Further, recruitment of TRAF2, cIAP1/2 and receptor-interacting protein kinase 1 (RIPK1) to the receptors can mediate NF-κB signaling pathways [37, 54–56].
Full DISC assembly, results in the cleavage and activation of caspase-10 and caspase-8,

which in turn can cleave and activate the executioner caspases-3 and -7 [57]. The final state is the proteolytic processing of target proteins leading to cell death, i.e. ICAD, nuclear lamins, gelsolin, actin, and resulting in the characteristic nuclear fragmentation, presentation of phosphatidylserine and blebbing into apoptotic bodies [33, 44, 45, 55]. Active caspase-8 can also connect the extrinsic to the intrinsic apoptotic pathway by cleaving and activating the BH3-only protein BID, forming a truncated form [57]. tBID leads to BAK/BAX dependent MOMP and full activation of the intrinsic apoptotic pathway [58].
Further, ligated death receptors are able to be internalized and signal within intracellular CD95 or TNFR1 receptosomes [59]. This results in active acid sphingomyelinase, ceramide production, activation of cathepsin D, generation of tBID and among others the activation of the caspase cascade [60–62].

2.2.2 Nuclear factor-κB signaling pathways

One of the main signaling pathway coordinating proliferation, survival, cellular differentiation and inflammation is the NF-κB signaling pathway [63, 64]. In humans, the NF-κB family comprises of five monomeric transcription factors sharing a N-terminal Rel homology domain (p50, p52, p65/RelA, RelB, cRel), encoded by *NFKB1*, *NFKB2*, *RELA*, *RELB*, *REL*, respectively [63, 65].
Dimers of some of these transcription factors residing in an inactive state in the cytoplasma, bound by one of three classical inhibitor of κB proteins, IκBα (*NFKBIA*), IκBβ (*NFKBIB*) or IκBϵ (*NFKBIE*). The heterodimer p65/p50 is mainly bound by IκBα. IκBβ and IκBϵ are structurally similar to IκBα and can adopt the binding and inactivation of p65/p50. However, they seemingly differ in their proteolytic processing kinetic and re-expression rate [63]. Further, the functional p50 and p52 transcription factors are inhibited differently, as they are bound in precursor protein forms, p105 and p100, respectively. Upon activation they are partially degraded to generate the active p50 and p52 transcription factors [66].
The release and activation of NF-κB transcription factors from IκB proteins is in turn regulated by phosphorylation by further upstream IκB kinases (IKK), i.e. IKKα (*CHUK*), IKKβ (*IKBKB*) and IKKγ (NEMO, *IKBKG*) [63, 65]. These up-stream initiator kinases are activated by three pathways, the canonical, non-canonical and atypical pathway [63, 65, 67]. Here, the focus will be on the canonical and non-canonical NF-κB signaling pathways.

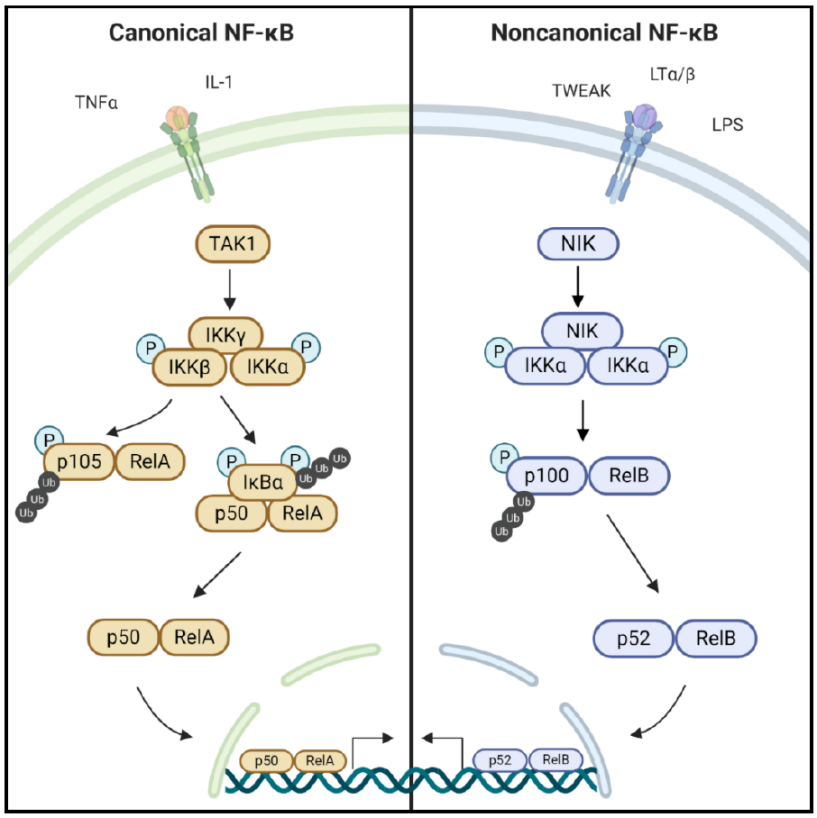

Fig. 2.3: Depiction of keystones for both, the canonical (left) and non-canonical (right) NF-κB signaling pathways. Both pathways, use cell surface receptors to relay signals outside-in. On the left, the canonical pathway uses TAK1 as an apical initiator kinase, activating the IKK complex. In turn, phosphorylating and partially degrading p105 to p50, completely degrading IκBα, further phosphorylating p65, dimerization and nuclear translocation. On the right side, NIK is used as an apical initiator kinase, activating IKK complex. Phosphorylation of p100 and its partial degradation leading to dimerization, nuclear translocation and transcription of target genes. Figure adapted from Pflug and Sitcheran [68].

2.2.2.1 Canonical NF-κB signaling

The canonical NF-κB signaling pathway is characterized by phosphorylation and degradation of IκBα and a further down-stream activation and phosphorylation of p65/RelA (left side of fig. 2.3) [63].

Exemplary for activating the canonical NF-κB pathway is the binding of TNFα to TNFR1. In contrast to the cell death inducing complex, described in section 2.2.1.2, complex I is recruited (complex I can be seen in fig. 2.2). This complex I consists of TRADD, TRAF2, cIAP1, cIAP2 and RIPK1 [69]. K63 poly-ubiquitylation of RIPK1 on K377 by cIAP1 and cIAP2 is responsible for the recruitment of the linear ubiquitin chain assembly complex (LUBAC) to complex I of the TNFR1 [70]. LUBAC adds M1

linear polyubiquitin chains to RIPK1 [71]. Subsequent, leading to the recruitment of a complex containing TAK1, TAB1, 2 and 3 [72]. Additionally, another IKK complex including NF-κB essential modulator (NEMO, IKKγ), IKKα and IKKβ is being assembled at the TNFR1 signalosome [50, 73]. Kinase activity of TAK1 is needed to further phosphorylate IKKβ within the previous assembled IKK complex and induce down-stream NF-κB signaling [74–77]. Upon activation, the IKK complex further phosphorylates IκBα at S32/36, leading to its ubiquitylation and proteasomal degradation, releasing p65/RelA from its bound form [78–80]. Free, cytoplasmic p65/RelA is further phosphorylated by IKK complex proteins at various phosphorylation sites, probably depending on the physiological setting. Thus, leading to its full activation, that is homo- and/or heterodimerization, nuclear translocation and binding to DNA target motifs for transcriptional activation [81–85]. One heterodimerization partner is p50, which is kept inactivated in its unprocessed p105 form. Upon phosphorylation, possibly by IKKβ, at various serine residues, acting as binding sites for a E3 ubiquitin ligase and partial proteasomal degradation [84].

2.2.2.2 Non-canonical NF-κB signaling

In contrast to the canonical TAK1 mediated activation of the IKK complex and subsequent IκBα degradation, the non-canonical NF-κB pathway uses the NF-κB-inducing kinase (NIK) as an apical kinase of IKKα phosphorylation (right side of fig. 2.3) [64]. Under basal conditions, NIK is constitutively ubiquitylated, thus tagged for proteasomal degradation. Ubiquitylation is mediated by cIAP1/2, within a needed complex with TRAF2/3 [86, 87]. By that, under basal, unstimulated conditions the non-canonical NF-κB pathway is not being activated.
Upon external stimulus, that is activation of surface residing receptors, e.g. TNFRSF12A (TWEAK-R), lymphotoxin β receptor (LTβR), receptor activator of NF-κB (RANK), the adapter proteins TRAF2/3 are degraded. Thus, cIAP1/2 are not able to bind and ubiquitylate NIK, leading to its stabilization and accumulation [86, 88, 89]. Followed by a NIK dependent phosphorylation of IKKα at S176 [90]. Further, p100 is phosphorylated at various sites by IKKα and other unidentified kinases. Phosphorylated p100 at specific N- and C-terminal sites (S99, S108, S115, S126 and S872) leads to its ubiquitylation and partial degradation, generating the active transcription factor p52 [91, 92]. p52, similar to p65/RelA, can act as homo- and/or heterodimers, shuttle into the nucleus and bind to and activate target gene transcription [68, 85]. One main binding partner of p52 is the transcription factor RelB, which might act as an inhibitor of p100 processing, as binding to p100 increases RelB stability. Phosphorylation of RelB at S472 by IKKα/β could demonstrate a transcriptional induction [84].

2.3 Inhibitor of apoptosis proteins

Smac, released from the intermembrane space during MOMP (see section 2.2.1.1), acts as an antagonist of inhibitor of apoptosis (IAP) proteins [93]. As the name implies, IAP proteins can suppress the apoptotic execution by binding to and inhibiting caspases. Especially x-linked inhibitor of apoptosis (XIAP), binds to caspase-3 and -7 [94]. As stated in section 2.2.2, cellular IAP proteins (cIAP1 and cIAP2) are involved in NF-κB signaling modulation, residing in complex I they ubiquitylate RIPK1, and drive activation of the canonical NF-κB pathway. At the same time blocking the non-canonical NF-κB pathway, by ubiquitylation of NIK, leading to its degradation [95].
IAP proteins share at least one common baculovirus IAP Repeat (BIR) domain [95]. The baculovirus, where the domain name originates, expresses two proteins containing BIR domains and function by binding to caspases [96]. Until now, there have been eight human IAP proteins identified, NAIP (*NAIP*), cIAP1 (*BIRC2*), cIAP2 (*BIRC3*), XIAP (*XIAP*), Survivin (*BIRC5*), Apollon (*BIRC6*), Livin (*BIRC7*) and ILP-2 (*BIRC8*) [95, 97]. Except for ILP-2, the other IAP family members can bind directly to and block caspase activation. This binding is facilitated by type II BIR domains (BIR2 and BIR3) harboring a tetrapeptide IAP binding motif (IBM), type I BIR domains (BIR1) lack the IBM [94, 98]. In addition to BIR domains, cIAP1 and cIAP2 further contain a CARD, a ubiquitin binding associated (UBA) and a RING (really interesting new gene) domain. With this RING domain cIAP1 and cIAP2 are able to add poly-ubiquitin chains to their targets (e.g. NIK, caspase-3, -7, -9, TRAF2, and others), tagging the targets for proteasomal degradation [86, 87, 99–101]. By that, IAP proteins have a direct negative impact on apoptotic signal processing.

For the cell to be able to induce pro-apoptotic signaling, those IAP proteins need to be suppressed upon cell death induction. The endogenous protein Smac, released during MOMP, adopts this function. In the case for XIAP, it could be shown, that Smac uses its N-terminal tetrapeptide (Alanine-Valine-Proline-Isoleucin) to bind to the BIR3 domain of XIAP [102]. This binding, putatively leads to conformational changes, autoubiquitylation and subsequent degradation of IAP proteins [103]. Thereby, previously bound caspases are released and exert their effector functions and onset of apoptotic signaling [104].

2.4 Smac mimetic

This IAP binding function of Smac and triggered release of caspase activity, sparked the research on using this mechanism as a therapeutic strategy.
Using peptide mimicry and remodelling of the AVPI binding motif, potent nonpeptidic Smac mimetics were developed [105]. Further, a successful structural-based design of IAP antagonistic compounds could increase their binding affinity and cell-permeability [106]. Natural occurring Smac proteins form homodimers, thereby being able to bind to the BIR2 and BIR3 domain of XIAP, releasing not only caspase-9, bound by XIAP's BIR3 domain, but releasing caspase-3/-7 bound by XIAP's BIR2 domain [107]. This dimeric binding mechanism translated into the synthesis of bivalent compounds harbouring two mimetic motifs [107]. A variety of Smac mimetic compounds are under preclinical development, or even in clinical trials. Up to the date of the thesis submission, a total of 15 active ("recruiting", "active, not recruiting" and "not yet recruiting") clinical trials could be identified using IAP antagonist either alone or in combination, ranging from phase 1-3 clinical trials. The active clinical trials are either using ASTX660 (six trials), Debio 1143 (three trials), Birinapant (two trials) or APG-1387 (four trial) (inquiry on clinicaltrials.gov, see table 2.1).

Still under pre-clinical development is the bivalent Smac mimetic BV6. Using B-cell precursor acute lymphoblastic leukemia (BCP-ALL) and pediatric primografts, BV6 could increase the survival in an synergistic manner together with conventional vincristine, dexamethasone and asparaginase treatment [108]. In another pediatric ALL xenograft model, BV6 together with dexamethasone reduced tumor growth and prolonged survival [109]. Additional studies, could show synergy between BV6 and death inducing ligands (TRAIL, FasL) inducing extrinsic cell death, in apoptotic and necroptotic manners [110–114]. Here, it could also be shown that BV6 in lower concentrations is more potent in activating cell death pathways, compared to LCL161 and Birinapant [114].
As can be seen in section 2.2.2, IAP proteins are not only involved in cell death regulation, but additionally in the regulation of NF-κB pathways. Indeed, it could be described that BV6 and other Smac mimetics induce NF-κB pathways [115, 116]
Although not in clinical trials today, BV6 is being used to identify fundamental molecular mechanisms induced by Smac mimetics/IAP antagonists.

Tab. 2.1: Clinical trials, "recruiting", "active, not recruiting" and "not yet recruiting", using Smac mimetics/IAP antagonists for solid cancer and hematological malignancies either as single or in combination treatment (clinicaltrials.gov accessed on 23.08.2022)

NTC-#	Smac mimetics	phase	first posted
02503423	ASTX660	1/2	2015
03386526	APG-1387	1	2017
03803774	Birinapant	1	2019
03871959	Debio 1143	1	2019
04155580	ASTX660	1	2019
04284488	APG-1387	1	2020
04362007	ASTX660	1/2	2020
04459715	Debio 1143	3	2020
04553692	Birinapant	1	2020
04568265	APG-1387	2	2020
04643405	APG-1387	1	2020
05082259	ASTX660	1	2021
05245682	ASTX660	1	2022
05386550	Debio 1143	3	2022
05403450	ASTX660	1	2022

2.5 Natural Killer cells as cellular immunotherapy

Additionally, to the increased cell death by single Smac mimetic (IAP antagonist) treatment, they can also induce an immunomodulation within cancer cells, leading to an enhanced susceptibility to a cytotoxic lymphocyte attack. Overexpression of a pro-Smac fusion protein containing either a cleavage site for granzyme B or caspase-8 could sensitize melanoma cells to a lymphokine-activated killer (LAK) cell attack. The complete mechanism remains elusive. However, it was demonstrated that LAK cells kill their target by activating the granzyme B pathway, rather than the caspase-8 dependent death receptor pathway [117]. In a variety of Hogkin lymphoma cancer cell lines, treatment with a Smac mimetic (obtained from TetraLogic Pharmaceuticals) could restore killing susceptibility to freshly enriched natural killer (NK) cells, with a proposed caspase dependent mechanism and putative involvement of the death receptor and granzyme B mediated cell death pathways [118]. A novel Smac mimetic, APG-1387, could increase the susceptibility of hepatocellular carcinoma to NK cell mediated killing with elevated levels of cleaved caspase-3 [119]. However, a detailed mechanism on how caspase-3 is activated by NK cells and co-treatment with APG-1387 is missing. In addition to NK

cells, Her2 targeting chimeric antigen receptor (CAR) expressing T-cells could attack $Her2^+$ patient-derived colorectal tumoroids and further increase their killing effect in a TNFα dependent manner upon Birinapant, Smac mimetic, co-treatment [120]. Further, the Smac mimetic BV6 could induce a sensitizing effect in rhabdomyosarcoma cell lines, leading to an enhanced killing by cytokine-induced killer (CIK) [121] and NK [25] cells. Within RMS cells, the proposed sensitizing mechanism involves caspases and putatively TRAIL:TRAIL-R activation [25, 121].

NK cells belong to the cellular innate immune system and as cytotoxic lymphocytes, they are characterized by the expression of CD59 and lack the expression of CD3 [122]. As their name implies, they can kill other cells. For that, they need to be able to induce cell death in their target cells by either activating the extrinsic apoptotic pathway, or by secreting cytotoxic granula, inducing an alternative cell death pathway [122]. NK cells present death ligands, i.e. FasL and TRAIL, on their surface and are able to bind to death receptors on their target cell's surface. The second killing mechanism, is the secretion of cytotoxic proteins, e.g. perforins, granzymes and granulysin. Here, perforin forms prepore oligomers on the cell membrane of the target cells. Upon Ca^{2+} binding and induced conformational changes, these oligomers form β-barrel pores within the cell membrane [123]. Granzyme B and other secreted cytotoxic proteins can pass through the formed perforin pore into the target cell to cleave caspases and other target proteins, eventually leading to cell death [124]. It could be shown that secretion of two to four cytotoxic granula of NK cells could lead to the induction of target cell death [125]. Both mechanisms, are taking place at the immunological synapse [126, 127]. Further, NK cells are known to be serial killer. That is, they can attack and kill multiple target cells by using different cell death inducing mechanisms, e.g. switch from cytotoxic granula to death receptor induced killing, and from apoptosis, necrosis or mixed forms of induced cell death [124, 128].
Before the killing can happen, NK cells need to migrate, recognize their target cells and subsequently be activated for cytotoxic attack. The target cell recognition and activation is performed by an intricate interplay of activating and inhibitory receptors on NK cells and is independent from MHC class I antigen recognition (figure 2.4) [129]. Upon binding to their respective ligands, activating receptors, e.g. NKp44, NKp46, CD16, DNAM1, lead to cytoskeleton remodelling, formation of the immunological synapse and induction of the so called "kiss of death" [130]. On the other side, binding of inhibitory receptors, including the killer immunoglobulin-like receptor (KIR) family and NKG2A, blocks the cytotoxic function of NK cells by clustering to and suppressing activating receptor signaling [131].

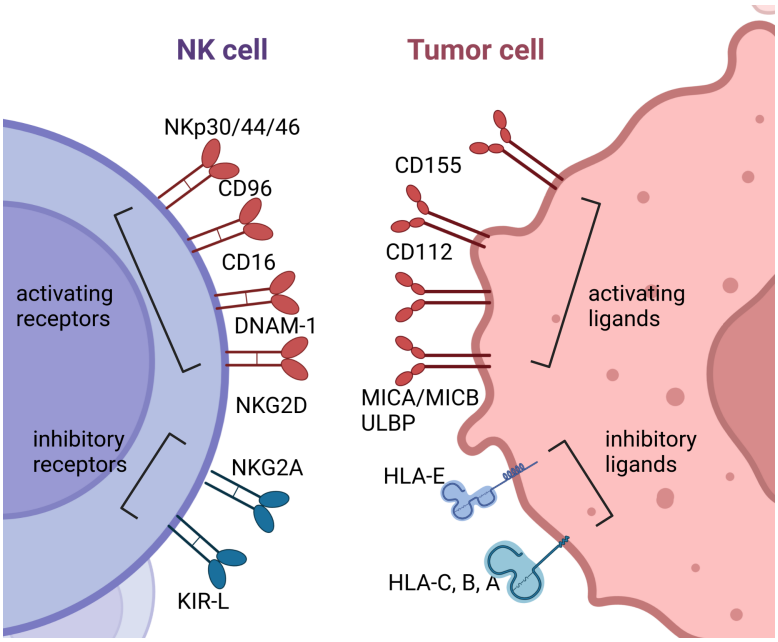

Fig. 2.4: Depiction of selected activating and inhibitory receptors on NK cells and ligands on tumor/target cells. Figure modified from [132] and generated with BioRender.com.

Tumor cells generated mechanisms to evade the recognition by immune cells, i.e. NK cells. Such evasion strategies were included as an additional hallmark of cancer in 2011 [30]. As depicted in figure 2.4, cancer cells present on their cell surface either NK cell activating or inhibitory ligands. KIR-L receptors on NK cells recognize classical HLA-A,B,C molecules on the target cell surface and inhibit NK cell cytolytic functions. Non-classical HLA molecules, e.g. HLA-E, can be recognized by NKG2A and inhibit NK cell cytotoxicity. Activating ligands on tumor cells include MICA/B and ULBP1-6, which are recognized by the NKG2D receptor and activating cytolytic functions in NK cells [133].

Evasion mechanisms of tumor cells include, down-regulation or shedding of activating ligands,e.g. of MICA/B, ULBPs [134, 135], up-regulation of an endogenous granzyme B inhibitor [136], evading extrinsic apoptosis by decoy receptors or increased expression of caspase inhibitory (IAP) proteins [137].

One way to counteract such immune evasion mechanisms was previously described using Smac mimetics. As described above, Smac mimetics lower the apoptotic threshold for a second immunological hit to fully induce cell death in target cells [25, 121]. In addition to Smac mimetics, several other co-treatment strategies were investigated to re-sensitize cell death resisting tumor cells towards an NK cell attack. For example, treatment of melanoma cells with panobinostat, an HDAC inhibitor, in combination with a MICA/B

antibody could synergistically increase the surface expression of MICA/B on tumor cells, leading to an increased NK cell activation and killing of target cells [138]. Further, proteasome inhibition by bortezomib, could increase death receptor (Fas and DR5) presentation, down-regulation of inhibitory HLA-E, subsequently leading to an enhanced NK cell killing [139]. Increased Fas presentation on breast cancer cells, induced by doxorubicin treatment, further enhanced killing by the stable NK-92 cell line, derived from peripheral blood of a non-Hodgkin lymphoma patient [140]. In the field of classical immunotherapy, that is therapeutic approaches with immune checkpoint inhibitors, attack and killing by NK cells could also be influenced. Here, blockade of PD-L1 and a novel immune checkpoint PVRIG on NK cells could enhance killing sensitivity towards colon cancer xenografts [141]. The other way around, expression of granzyme B could be increased upon inhibition of CDK8 and CDK19 in NK cells, leading to an enhanced growth control of breast and melanoma cancer xenografts. In addition, co-treatment with anti-PD-1 antibody and a Smac mimetic further enhanced the survival of breast cancer bearing mice [142].

NK cells are powerful cytotoxic cells of the innate immune system, although tumor cells developed strategies to evade destruction by immune cells, novel treatment strategies exist and are in pre-clinical development to counteract those evasion mechanisms.

3 Research rationale

Previous publications described a favorable therapeutic strategy, not only for RMS, by using Smac mimetics in combination with cytotoxic lymphocytes, i.e. with CAR T-cells [120], CIK cells [121], NK cells [25, 118, 119].
Based on these studies, the aim of the presented project was to elucidate the molecular mechanisms driving the sensitizing effect of BV6 in combination with NK cells.
To remodel the solid RMS tumor phenotype more closely, a three dimensional multicellular RMS spheroid system was chosen. Here, GFP expressing RMS cells were used to follow the spheroid growth and size by quantifying the GFP fluorescence intensity as a read-out of spheroidic change. As introduced, RMS can be classified into several subtypes. To understand, if the BV6 sensitizing mechanism is RMS subtype specific, or a pan-RMS mechanism, the alveolar RH30 cell line and the embryonal RD cell line were utilized.

Earlier investigations could identify an involvement of TRAIL upon XIAP blockade in pancreatic carcinoma [143], described an up-regulation of DR5 upon BV6 stimulation [110] or re-sensitization to a TRAIL induced cell death by the Smac mimetic Birinapant [144] or BV6 [112] in a variety of tumor cell lines. Within this background, the aim of the first part is to analyze the death receptor signaling upon BV6 treatment and will focus on the TRAIL:TRAIL-R system. As death receptor induced apoptosis involves activation of caspases, a hypothesis was formulated that the observed BV6 induced sensitization might depend on a death receptor mediated extrinsic form of cell death and putatively depends on caspase activation. Thus, analysis of caspase activation pattern and targeted knock-down studies will be carried out to resolve this hypothesis.

As BV6 is able to activate transcriptional pathways we hypothesized if this transcriptional effect might be responsible for the sensitization towards an NK cell attack. NIK, as part of the non-canonical NF-κB pathway, is directly tagged for proteasomal degradation by cIAP1/2 mediated ubiquitylation [145]. Thereby, the role of NIK as a putative central facilitator within a BV6 induced transcriptional regulation will be analyzed in more detail.

This transcriptional regulation will comprehensively be analyzed by RNA sequencing, to identify novel BV6 regulated target genes. Thereby, we aimed to unravel a BV6 induced transcriptional signature and help to understand the molecular mechanisms driving BV6 sensitization in RMS cells towards an NK cell mediated killing.

4 Materials and Methods

4.1 Materials

4.1.1 Cell lines

Table 4.1 depicts used human cell lines. RD and RH30 cell lines constitutively expressing green fluorescent protein (GFP) and luciferase (Luc) were produced at the institute of cellular immunology (AG Ullrich, University Hospital, Frankfurt a. M., Germany) by Dr. Juliane Wagner [146].

Tab. 4.1: Used human cell lines with appropriate culture medium

Cell line	Supplier	Culture Medium
RD (embryonal RMS)	ATCC	DMEM
RD-GFP/Luc	AG Ullrich, Frankfurt a. M., Germany	DMEM
RH30 (alveolar RMS)	DSMZ	RPMI-1640
RH30-GFP/Luc	AG Ullrich Frankfurt a. M., Germany	RPMI-1640
HEK293T (embryonal kidney cells)	ATCC	DMEM
primary NK cells (isolated from PBMCs)	GRC-Blood donor service Frankfurt a. M., Germany	NK MACS®

4.1.2 Cell culture reagents

Tab. 4.2: Used reagents for cell culture maintenance

Reagent	Supplier
StemPro™ Accutase™	Life Technologies, Darmstadt, Germany
Enzyme free dissociation buffer	Life Technologies, Darmstadt, Germany
Trypsin/EDTA (0.05 %, phenol red)	Life Technologies, Darmstadt, Germany

Tab. 4.2: Used reagents for cell culture maintenance – continued

Reagent	Supplier
Dulbecco's Modified Eagle Medium (DMEM) GlutaMAX™-I	Life Technologies, Darmstadt, Germany
Dimethyl sulfoxid (DMSO)	Sigma-Aldrich, Deisenhofen, Germany
Dulbecco's phosphate buffered saline (PBS)	Life Technologies, Darmstadt, Germany
Fetal calf serum (FCS)	Life Technologies, Darmstadt, Germany
human AB blood plasma	GRC-Blood donor service, Frankfurt a. M., Germany
NK MACS®	Miltenyi Biotec, Bergisch Gladbach, Germany
Opti-MEM®	Life Technologies, Darmstadt, Germany
Penicillin/Streptomycin (10 000 U/ml)	Life Technologies, Darmstadt, Germany
Roswell Park Memorial Institute (RPMI)-1640 GlutaMAX™-I medium	Life Technologies, Darmstadt, Germany
Roswell Park Memorial Institute (RPMI)-1640 GlutaMAX™-I medium without phenol red	Life Technologies, Darmstadt, Germany
Sodium pyruvate (100 mM)	Life Technologies, Darmstadt, Germany
Trypan blue solution (0.4 %)	Life Technologies, Darmstadt, Germany

4.1.3 Inhibitors

Tab. 4.3: Used inhibitors and neutralizing antibodies

Inhibitors	Target and function	Supplier
BV6	IAP antagonist / Smac mimetic	Genentech, San Francisco, CA, USA
zVAD.fmk	pan-caspase inhibitor	Bachem, Heidelberg, Germany
zAAD-cmk	Granzyme B inhibitor	Sigma Merck, Darmstadt, Germany
Enbrel	anti-TNFα antibody	Sigma Merck, Darmstadt, Germany
antiTRAIL	anti-TRAIL antibody	Enzo LIfe Sciences, Lörrach, Germany

4.1.4 Antibodies

Primary antibodies used for western blot are listed in table 4.4. All western blot antibodies were diluted in 2 % BSA:PBS-T. Secondary antibodies for western blot were diluted 1:10 000 in 5 % skimmed milk:PBS-T and are listed in table 4.5. Table 4.6 depicts fluorochrome conjugated primary antibodies for flow cytometric and immunofluorescence analysis.

Tab. 4.4: Used primary antibodies for western blot detection

Target	Catalog-#	Dilution	Species	Supplier
α-Tubulin	CP06	1:5 000	mouse	Calbiochem, San Diego, CA, USA
Caspase-3	9662S	1:1 000	rabbit	Cell Signaling, Beverly, MA, USA
Caspase-8	ADI-AAM-118-E	1:1 000	mouse	Enzo, Lörrach, Germany
Caspase-9	9502S	1:1 000	rabbit	Cell Signaling, Beverly, MA, USA
cIAP1	271319	1:1 000	mouse	Santa Cruz Biotechnology Santa Cruz, CA, USA

Tab. 4.4: Used primary antibodies for western blot detection – continued

Target	Catalog-#	Dilution	Species	Supplier
cIAP2	3130	1:1 000	rabbit	Cell Signaling, Beverly, MA, USA
DR5	AB16942	1:1 000	rabbit	Sigma-Aldrich, Darmstadt, Germany
GAPDH	NB-29-00852	1:5 000	mouse	BioTrend, Cologne, Germany
Histone H3	ab1791	1:1 000	rabbit	Abcam, Cambridge, UK
IκBα	9242	1:1 000	rabbit	Cell Signaling, Beverly, MA, USA
LaminB1	ab16048	1:10 000	rabbit	Abcam, Cambridge, UK
NIK	4994	1:1 000	rabbit	Cell Signaling, Beverly, MA, USA
p50	7178	1:1 000	rabbit	Santa Cruz Biotechnology Santa Cruz, CA, USA
p52	05-361	1:1 000	mouse	Sigma-Aldrich, Darmstadt, Germany
p65	372x	1:1 000	rabbit	Santa Cruz Biotechnology Santa Cruz, CA, USA
p-p65	3033S	1:1 000	rabbit	Cell Signaling, Beverly, MA, USA
p-IκBα	9246L	1:1 000	mouse	Cell Signaling, Beverly, MA, USA
p-RIP1	65746S	1:1 000	rabbit	Cell Signaling, Beverly, MA, USA
RIP1	133102	1:500	mouse	Santa Cruz Biotechnology Santa Cruz, CA, USA
SSTR2	365502	1:1 000	mouse	Santa Cruz Biotechnology Santa Cruz, CA, USA
Survivin	AF886	1:1 000	rabbit	R&D Systems Minneapolis, MN, USA

Tab. 4.4: Used primary antibodies for western blot detection – continued

Target	Catalog-#	Dilution	Species	Supplier
XIAP	610716	1:1 000	mouse	BD Bioscience, Heidelberg, Germany

Tab. 4.5: Used secondary antibodies for western blot detection and immunofluorescence

Target species	Conjugation	Host species	Catalog-#	Supplier
anti-mouse	HRP	goat	ab6789	Abcam, Cambridge, UK
anti-mouse	FITC	goat	115-097-003	Jackson ImmunoResearch Cambridgeshire, UK
anti-rabbit	HRP	goat	ab6721	Abcam, Cambridge, UK

Tab. 4.6: Fluorochrome conjugated antibodies for flow cytometric and immunofluorescence analysis

Target & fluorochrome	Catalog-#	c(final) $\mu g/ml$	Species	Supplier
CCL5	MAB278-100	3.3	mouse IgG_1	R&D Systems
CD3 BV510	564713	2.5	mouse IgG_{2A}	BD Bioscience
CD16 PE	302008	2.5	mouse IgG_{1k}	Biolegend
CD45 APC	17-0459-42	0.6	mouse IgG_{1k}	Invitrogen
CD56 BV421	562751	2.5	mouse IgG_{2B}	BD Bioscience
Fas PE	556641	5	mouse IgG_1	BD Bioscience
DR4 PE	FAB347P	5	mouse IgG_1	R&D Systems
DR5 PE	FAB6311P	5	mouse IgG_{2B}	R&D Systems
Isoypte PE	IC002P	5	mouse IgG_1	R&D Systems
Isotype PE	IC0041P	5	mouse IgG_{2B}	R&D Systems
Isotype PE	IC003P	5	mouse IgG_{2A}	R&D Systems
Isotype PE	130-113-462	4	REA human	Miltenyi Biotec
SSTR2 PE	FAB4224P	5	mouse IgG_{2A}	R&D Systems
TNFR1 PE	130-106-286	4	REA human	Miltenyi Biotec

4.1.5 Small-interfering RNA constructs (siRNA)

All small-interfering RNA construct where purchased from ThermoFisher Scientifc (*Silencer*® Select siRNA, Roskilde, Denmark)

Tab. 4.7: Used small-interfering RNA construct for specific knock-down

Target	Construct	Assay-#
	#1	s2427
Caspase-8	#2	s2425
	#3	s2426
	#1	s2428
Caspase-9	#2	s2429
	#3	s2430
	#1	s12575
CCL5	#2	s12576
	#3	s12577
	#1	s17187
MAP3K14	#2	s17186
	#3	s17188
non specific	ns	s4390843

4.1.6 Primer sequences for qRT-PCR

All oligonucleotide primers were acquired from Eurofins Genomics (Ebersberg, Germany).

Tab. 4.8: Used oligonucleotide primers for in-house performed qRT-PCR

Target gene	Sequences (5'→3')	
human	Forward	Reverse
28S-rRNA	TTGAAAATCCGGGGGAGAG	ACATTGTTCCAACATGCCAG

Tab. 4.8: Used oligonucleotide primers for in-house performed qRT-PCR – continued

Target gene	Sequences (5'→3')	
human	Forward	Reverse
BIRC2	GATATTGTGTCACGACTTCTTAATGC	TCTGTTCTTCCGAATTAATGACAA
BIRC3	GATGAAAATGCAGAGTCATCAATTA	CATGATTGCATCTTCTGAATGG
CCL5	CGCTGTCATCCTCATTGCTA	GAGCACTTGCCACTGGTGTA
cREL	TGAACATGGTAATTTGACGACTG	ACACGACAAATCCTTAATTCTGC
G6PD	ATCGACCACTACCTGGGCAA	TTCTGCATCACGTCCCGGA
GAPDH	CAAGGTCATCCATGACAACTTTG	GGGTCCAAGTTGTCCAGAATGC
IL-8	CTCTTGGCAGCCTTCCTGATT	TATGCACTGACATCTAAGTTCTTTAGCA
IRF1	ACAGCACCAGTGATCTGTACAAC	TTCCCTTCCTCATCCTCATCT
MAP3K14	CCAGCTGCCATCTCTATCATC	AAAAAGTGGGGCTGAACTCT
MMP9	CTTTGAGTCCGGTGGACGAT	TCGCCAGTACTTCCCATCCT
NFKB2	CTCGACTACGGCGTCACC	GATGATGGCTAGGTGCAGTG
NFKBIA	GTCAAGGAGCTGCAGGAGAT	ATGGCCAAGTGCAGGAAC
RELA	TCATGAAGAAGAGTCCTTTCA	GGATGACGTAAAGGGATAGGG
RELB	GCTCTACTTGCTCTGCAGACA	GGCCTGGGAGAAGTCAGC
RPII	GCACCACGTCCAATGACAT	GTGCGGCTGCTTCCATAA
SSTR2	GCAGCGGAAAAGCAAAGATGTC	TCCATTGAGTGGCTCATCCG
SSTR2A-1	GGAGCGGAGTGACAGTAAGC	GGTCTCCATTGAGGAGGGTC
SSTR2A-2	CCAGAATGTCCTCTGCTTGGT	ATTCAGCCGGGATTTGTCCT
SSTR2B-1	CAGCAAAAGCGGCGAAGAAGG	TTTTGCGGTTTTTGTTGTTGCGA
SSTR2B-2	CCAGAATGTCCTCTGCTTGGT	TGCGGTTTTTGTTGTTGCGAA
TNFRSF10A	GGGTCCACAAGACCTTCAAGT	TGCAGCTGAGCTAGGTACGA
TNFRSF10B	AGACCCTTGTGCTCGTTGTC	TTGTTGGGTGATCAGAGCAG

Tab. 4.9: Used oligonucleotide primers for qRT-PCR Fluidigm® validation

Gene of interest	Sequences (5'→3')	
human	Forward	Reverse
BIRC2	GTGAGTTCTTGATACGAATGAAAGG	GGTCCAAAATGAATAATTGGTGGGT
CAMK1G	ATGACATCTCCGACTCTGCAAAAG	GACTCGTGGATGTTTTTGTTGAGG
CCL5	GCATCTGCCTCCCCATATTCC	CCACTGGTGTAGAAATACTCCTTGA
CTSS	TTTCTTCCTCTACAGAAGTGGTGTC	CATTAAGATCACCATAGCCAACCAC
ESYT3	GAAGACACATACAAGTAAGACCTG	CTGGTCATCATCAAGCACCTTC
HPRT1	TGACACTGGCAAAACAATGCA	GGTCCTTTTCACCAGCAAGCT
IFIT3	GGAAACAGCCATCATGAGTGAGG	TAAGTTCCAGGTGAAATGGCATTTC
IL7R	AAGTGGCTATGCTCAAAATGGAGAC	GCCCCACATATTTCAAATTCCAGAT
ITGAM	CCTGAAACTACAGTTGCCGAATTG	ATGTTGTCATTGCCACAATTCTTCT
MMP9	ATTTGTTCAAGGATGGGAAGTACTG	GAAGAAAAGCTTCTTGGAGAGCC
MSTN	CATTACCATGCCTACAGAGTCTGAT	CTCGACGGGTCTCAAATATATCCAT
NFKB2	AAAGACCTATCCCACTGTCAAGATC	AGGTTGTTAAATTGGGCAGTCATG
NFKBIA	TTCACAGAGGACGAGCTGCC	AGTGTGCAGTGTGGATATAAGTACA
NUPR1	CTGAGACAGAGCTGGAGATGAG	CTCAGTCAGCGGGAATAAGTCCTAG
PLA2G4C	AAGCTAAGGATTGAGGCTGATGAGG	TAGAGAGAAGATATTGCCCAAGTGG
PLCH2	TATGCCTTCATCAAGAATGAGTACC	CATTTTCTTCTGCTGGATGACACTG
SSTR2	GCAGCGGAAAAGCAAAGATGTC	GCCCAGAGATCTTATTCTCACCTTA
TBP	GAGCCAAGAGTGAAGAACAGTC	GCTCCCCACCATATTCTGAATCT
TLR5	TTCTGCTAGGACAACGAGGATCA	CAGAAACGATAAAAGGCTATTCGG
TNFRSF9	ATATGCAGGCAGTGTAAAGGTGTT	TTCTGATCGTTAAATGTCCCAAAGC
TRAF1	GGCTGTACCTGAATGGAGATG	GTTCTGGTCCAGCAGCATGAA
TRIB3	CGCTGACCGTGAGAGGAAGA	TGAGTATCTCAGGTCCCACGTAG
TRIM29	CAATCTCTATGGCACCAAAGGTAAC	AGAGTTCTGAATGCTGGAGGAGTA
UNC13A	AAACATGGCAAGGGATTAGAAAAGG	CTTCTTCTCGTACCATGTGATCCTT
VEGFC	CCTCGGATGCTGGAGATGAC	CACATTGGCTGGGGAAGAGT

4.1.7 Guide RNAs used for knock-out generation of *CCL5*

All oligonucleotides for the generation of gRNAs were manufactured by Eurofins Genomics (Ebersberg, Germany). Sequences for the generation of gRNAs were taken from the Brunello library [147].

Tab. 4.10: Used oligonucleotides for gRNA generation targeting *CCL5*, stock concentration of 100 μM

Construct	Comment	Sequence (5'→3')
	target	AAGGAGTATTTCTACACCAG
gRNA #1	forward	CACCGAAGGAGTATTTCTACACCAG
	reverse	AAACCTGGTGTAGAAATACTCCTTC
	target	GCAATGTAGGCAAAGCAGCA
gRNA #2	forward	CACCGGCAATGTAGGCAAAGCAGCA
	reverse	AAACTGCTGCTTTGCCTACATTGCC
	target	GTAGAAATACTCCTTGATGT
gRNA #3	forward	CACCGGTAGAAATACTCCTTGATGT
	reverse	AAACACATCAAGGAGTATTTCTACC
	target	TCAAGACCAGGACTTACATG
gRNA #4	forward	CACCGTCAAGACCAGGACTTACATG
	reverse	AAACCATGTAAGTCCTGGTCTTGAC

4.1.8 Chemicals

Tab. 4.11: Used chemicals, compounds and ready-to-use solutions

Chemical	Company
2-propanol	Carl Roth, Karlsruhe, Germany
Acetic acid	Carl Roth, Karlsruhe, Germany
Acrylamide mix, 30 %	Carl Roth, Karlsruhe, Germany
Agar	Carl Roth, Karlsruhe, Germany

Tab. 4.11: Used chemicals, compounds and ready-to-use solutions – continued

Chemical	Company
Albumin fraction V (BSA)	Carl Roth, Karlsruhe, Germany
Ammonium persulfate (APS)	Carl Roth, Karlsruhe, Germany
β-Glycerophosphate	Sigma-Aldrich, Deisenhofen, Germany
Blasticidine	Carl Roth, Karlsruhe, Germany
Brilliant stain buffer	BD Bioscience, Franklin Lakes, NJ, USA
Bromphenol blue	Carl Roth, Karlsruhe, Germany
Calcium chloride ($CaCl_2$)	Carl Roth, Karlsruhe, Germany
Carboxyfluorescein succinimidyl ester (CFSE)	ThermoFisher Scientific, Roskilde, Denmark
CasyTon	OMNI Life Science, Bremen, Germany
CellTrace™ far red	Life Technologies, Darmstadt, Germany
CellTrace™ Violet	Life Technologies, Darmstadt, Germany
DAPI	Carl Roth, Karlsruhe, Germany
Dimethyl sulfoxide (DMSO)	Sigma-Aldrich, Darmstadt, Germany
Dihydrothreitol (DTT)	Merck Millipore, Darmstadt, Germany
Disodium phosphate (Na_2HPO_4)	Carl Roth, Karlsruhe, Germany
Ethanol	Carl Roth, Karlsruhe, Germany
Ethylene diamine tetraacetic acid (EDTA)	Carl Roth, Karlsruhe, Germany
FACS Clean solution	BD Bioscience, Heidelberg, Germany
FACS Rinse solution	BD Bioscience, Heidelberg, Germany
FACS Flow sheath fluid	BD Bioscience, Heidelberg, Germany
FACS Shutdown solution	BD Bioscience, Heidelberg, Germany
Formaldehyde	Carl Roth, Karlsruhe, Germany
FuGENE®HD transfection reagent	Promega, Madison, WI, USA
Glycerol	Carl Roth, Karlsruhe, Germany

Tab. 4.11: Used chemicals, compounds and ready-to-use solutions – continued

Chemical	Company
Glycine	Carl Roth, Karlsruhe, Germany
Histopaque-1077	Sigma-Aldrich, Darmstadt, Germany
Hoechst33342	Sigma-Aldrich, Deisenhofen, Germany
Hydrochloric acid (HCl)	Carl Roth, Karlsruhe, Germany
Hydrogen peroxide (H_2O_2, 30 %)	Carl Roth, Karlsruhe, Germany
LB medium	Carl Roth, Karlsruhe, Germany
Magnesium Chloride ($MgCl_2$)	Carl Roth, Karlsruhe, Germany
Methanol	Carl Roth, Karlsruhe, Germany
NP-40 (IGEPAL CA-630)	Carl Roth, Karlsruhe, Germany
Nuclease-free water	ThermoFisher Scientifc, Roskilde, Denmark
Octreotide acetate	Selleckchem, Planegg, Germany
Skimmed milk powder	Carl Roth, Karlsruhe, Germany
S.O.C medium	Life Technologies, Darmstadt, Germany
PageRuler™ Plus Prestained Protein ladder	ThermoFisher Scientific, Roskilde, Denmark
Phenylmethylsulfonyl fluoride (PMSF)	Carl Roth, Karlsruhe, Germany
Potassium chloride (KCl)	Carl Roth, Karlsruhe, Germany
Potassium dihydrogen phosphate (KH_2PO_4)	Carl Roth, Karlsruhe, Germany
Protease Inhibitor Cocktail (PIC)	Roche Diagnostics, Mannheim, Germany
Propidium iodide (PI)	Sigma-Aldrich, Deisenhofen, Germany
RNAlater	Sigma-Aldrich, Darmstadt, Germany
RNAiMAX tranfection reagent	Life Technologies, Darmstadt, Germany
ROENTOROLL HC X-Ray Developer	TETENAL, Norderstedt, Germany
Sodium chloride (NaCl)	Carl Roth, Karlsruhe, Germany

Tab. 4.11: Used chemicals, compounds and ready-to-use solutions – continued

Chemical	Company
Sodium dodecyl sulfate (SDS)	Carl Roth, Karlsruhe, Germany
Sodium fluoride	Sigma-Aldrich, Deisenhofen, Germany
Sodium hydroxide (NaOH)	Carl Roth, Karlsruhe, Germany
Sodium orthovanadate	Sigma-Aldrich, Deisenhofen, Germany
SUPERFIX MRP X-Ray Fixer	TETENAL, Norderstedt, Germany
Tetramethylethylenediamine (TEMED)	Carl Roth, Karlsruhe, Germany
Thiazolyl Blue Tetrazolium Bromide (MTT)	Sigma-Aldrich, Darmstadt, Germany
TrisBase	Carl Roth, Karlsruhe, Germany
TrisHCl	Carl Roth, Karlsruhe, Germany
Triton X-100	Carl Roth, Karlsruhe, Germany
Tween 20	Carl Roth, Karlsruhe, Germany
Vision X®X-ray developer and fixer	röntgen bender, Baden-Baden, Germany

4.1.9 Consumables

Tab. 4.12: Used consumables

Material	Supplier
Aluminium foil	Car Roth, Karlsruhe, Germany
CasyCups	OMNI Life Science, Bremen, Germany
Cell culture dishes (6, 10 or 15 cm diameter)	Greiner Bio-One, Frickenhausen, Germany
Cell culture flasks (25, 75 or 175 cm^2)	Greiner Bio-One, Frickenhausen, Germany
Cell culture plates (6, 12, 24, 48 or 96 well, transparent)	Greiner Bio-One, Frickenhausen, Germany
Cell scraper	BD Bioscience, Heidelberg, Germany

Tab. 4.12: Used consumables – continued

Material	Supplier
Combitips (bulk, different sizes)	Eppendorf, Hamburg, Germany
Centrifuge tubes (Falcon tubes, 15 or 50 ml)	Greiner Bio-One, Frickenhausen, Germany
CELLSTAR® microclear black plate (96 well)	Greiner Bio-One, Frickenhausen, Germany
Corning®Costart® 96 well ultra-low attachment plates	Sigma-Aldrich, Darmstadt, Germany
Cryogenic vials (1.8 ml)	Starlab, Hamburg, Germany
Disposible bags	Carl Roth, Karlsruhe, Germany
Filter tips (sterile, all sizes)	Starlab, Hamburg, Germany
Filter paper	Carl Roth, Karlsruhe, Germany
Hybond ECL nitrocellulose membrane	GE Healthcare, Buckinghamshire, UK
X-ray Hyperfilm ECL	GE Healthcare, Buckinghamshire, UK
Leukosilk® tape	BSN Medical, Hamburg, Germany
MicroAMP™ optical reaction plate (96 well)	ThermoFisher Scientific, Roskilde, Denmark
MicroAMP™ optical reaction plate (348 well)	ThermoFisher Scientific, Roskilde, Denmark
Microcentrifuge tubes (unsterile, all sizes)	Starlab, Hamburg, Germany
Nitrile gloves, powder-free	Starlab, Hamburg, Germany
Parafilm	VWR, Deisenhofen, Germany
Pasteur pipettes	Carl Roth, Karlsruhe, Germany
PCR tubes	Starlab, Hamburg, Germany
Round-bottom FACS tubes	BD Bioscience, Heidelberg Germany
Scalpel	B. Braun, Melsungen, Germany
Sterile filters (0.22, 0.45 μm)	Merck Millipore, Darmstadt, Germany
Sterile stripettes	Greiner Bio-One, Frickenhausen, Germany

Tab. 4.12: Used consumables – continued

Material	Supplier
Syringes (5, 20, 50 ml)	BD Bioscience, Heidelberg, Germany
Whatman filter paper	ThermoFisher Scientific, Roskilde, Denmark

4.1.10 Assay kits

Tab. 4.13: Ready-to-use kits used throughout the project

Kit	Catalog-#	Supplier
ELISA targeting hCCL5	DRN00B	R&D Systems, Minneapolis, MN, USA
GeneJet Plasmid-Miniprep Kit	K0482	ThermoFisher Scientic, Roskile, Denmark
peqGold DNAse I digestion kit	13-1091-01	PeqLab, Erlangen, Germany
peqGOLD MicroSpin Total RNA kit	13-6831-02	PeqLab, Erlangen, Germany
peqGOLD Total RNA kit	13-6834-02P	PeqLab, Erlangen, Germany
Pierce™ BCA protein assay	23225	Thermo Scientific, Roskilde, Denmark
Pierce™ ECL western Blot detection substrate	32106	ThermoFisher Scientific, Roskilde, Denmark
PureLink™ Genomic DNA Mini Kit	K182000	Invitrogen, ThermoFisher Scientific, Roskilde, Denmark
PureLink™ HiPure Plasmid Maxiprep Kit	K210006	ThermoFisher Scientific, Roskilde, Denmark
Qiagen RNeasy Micro Kit	74004	Qiagen, Hilden, Germany
QIAquick Gel Extraction Kit	28704	Qiagen, Hilden, Germany
RevertAid First Strand cDNA synthesis kit	K1612	ThermoFisher Scientific, Roskilde, Denmark

Tab. 4.13: Ready-to-use kits used throughout the project – continued

Kit	Catalog-#	Supplier
SYBR™ Green PCR master mix	4309155	Applied Biosystems, Darmstadt, Germany
Venor® GeM Mycoplasma PCR detection kit	MP0025	Minerva-Biolabs, Berlin, Germany

4.1.11 List of Buffers

Tab. 4.14: Used buffers

Buffer	Components	Final concentration
Antibody dilution buffer (ABD, pH 7.5)	Tris-HCl	10 mM
	NaCl	0.9 %
	EDTA	5 mM
	BSA	1 g/l
Blotting buffer (1x)	TrisBase	5.8 g/l
	Glycine	2.9 g/l
	SDS	0.04 %
	Methanol	20 %
CFSE-staining buffer	PBS	1x
	FCS	5 %
EasySep buffer	PBS	1x
	FCS	2 %
	EDTA	1 mM
FACS-staining buffer	PBS	1x
	FCS	2 %

Tab. 4.14: Used buffers – continued

Buffer	Components	Final concentration
Isotonic buffer (pH 7.4)	Tris-HCl	10 mM
	NaCl	150 mM
Lysis buffer (pH 7.4)	Tris-Base	30 mM
	NaCl	150 mM
	Triton-X100	1 %
	Glycerol	10 %
	PIC	1×
	PMSF	0.5 mM
	DTT	2 mM
	Sodium-orthovanadate	1 mM
	β-glycerophosphate	1 mM
	Sodium-fluoride	5 mM
Nuclear extraction buffer A (pH 7.9)	HEPES-OH	10 mM
	$MgCl_2$	1.5 mM
	KCl	10 mM
	DTT	0.5 mM
	Sodium-orthovanadate	1 mM
	PIC	1x
Nuclear extractio buffer B (pH 7.9)	HEPES-OH	20 mM
	NaCl	420 mM
	$MgCl_2$	1.5 mM
	EDTA	0.5 mM
	Glycerol	25 %
	DTT	0.5 mM
	Sodium-orthovanadate	1 mM
	PIC	1x

Tab. 4.14: Used buffers – continued

Buffer	Components	Final concentration
Phosphate buffered saline (PBS, 10x, pH 7.4)	NaCl	80 g/l
	KCl	2 g/l
	KH_2PO_4	2 g/l
	Na_2HPO_4	14.4 g/l
PBS-T	PBS	1x
	Tween 20	0.01 %
Running buffer (5x)	TrisBase	15.1 g/l
	Glycine	94 g/l
	SDS	0.5 %
SDS-PAGE Loading dye (6x, pH 6.8)	TrisBase	360 mM
	Glycerol	30 %
	SDS	10 %
	DTT	93 g/l
	Bromophenol blue	12 g/l

4.1.12 Equipment

Tab. 4.15: Used equipment and instruments

Instrument	Company
ARE heating magnetic stirrer	VELP Scientifica, Usmate, Italy
Autoclave VX-150	SysTec, Bergheim-Glessen, Germany
Avanti J-26 XP ultracentrifuge	Beckman Coulter, Krefeld, Germany
Biowizard biosafety cabinet	Kojair, Vilpuppla, Finland
Blotting chamber	Bio-Rad, Munich, Germany

Tab. 4.15: Used equipment and instruments – continued

Instrument	Company
CASY cell counter	OMNI Life Science, Bremen, Germany
Centrifuge MIKRO 200 R	Hettich, Baden-Baden, Germany
Centrifuge ROTIXA 50 RS	Hettich, Baden-Baden, Germany
Centrifuge ROTANTA 460 R	Hettich, Baden-Baden, Germany
CO_2 incubator MCO-19-AIC	SANYO, New Brunswick Scientific, Edison, NJ, USA
CO_2 incubator MIR-262	SANYO, New Brunswick Scientific, Edison, NJ, USA
Cryoextra 40, liquid nitrogen tank	ThermoFisher Scientific, Roskilde, Denmark
Easypet® 3	Eppendorf, Hamburg, Germany
Electronic analytical laboratory scale EW	Kern, Balingen, Germany
Electronic precision scale 770	Kern, Balingen, Germany
FACS Canto II	BD Bioscience, Franklin Lakes, NJ, USA
Freezer (-20°C)	EWALD Innovationstechnik, Bad Nenndort
Freezer (-80°C)	SANYO, New Brunswick Scientific, Edison, NJ, USA
Fridge (4°C)	EWALD Innovationstechnik, Bad Nenndort
Glass plates for SDS-PAGE	Bio-Rad, Munich, Germany
ImageXpress Micro XLS widefield, transmitted light option	Molecular Devices, San Jose, CA, USA
Infinite M100 microplate reader	Tecan, Crailsheim, Germany
Innova 4230 bacteria shaker	New Brunswick Scientific, Edison, NJ, USA
Mastercycler® pro	Eppendorf, Hamburg, Germany
Microcentrifuge	Benning, Bocholt, Germany

Tab. 4.15: Used equipment and instruments – continued

Instrument	Company
Microscope CKX41, cell culture	Olympus, Hamburg, Germany
Microscope IX71, fluorescence	Olympus, Hamburg, Germany
Mini-PROTEAN Tetra Cell electrophoresis system	Bio-Rad, Munich, Germany
Multichannel pipette eppendorf Research® 10 μl	Eppendorf, Hamburg, Germany
Multichannel pipette eppendorf Research® Plus 200 μl	Eppendorf, Hamburg, Germany
Multichannel pipette eppendorf Research® 300 μl	Eppendorf, Hamburg, Germany
Multipette® M4	Eppendorf, Hamburg, Germany
Nalgene® Mr. Frosty™ freezing container	Sigma-Aldrich, Darmstadt, Germany
NanoDrop 1000 spectrophotometer	PeqLab, Erlangen, Germany
Neubauer improved counting chamber	Carl Roth, Karlsruhe, Germany
PerfectBlue Dual Gel Twin L electrophoresis system	PeqLab, Erlangen, Germany
pH meter inoLab pH7310	WTW, Weilheim, Germany
Pipette eppendorf Research® Plus 2.5 μl	Eppendorf, Hamburg, Germany
Pipette eppendorf Research® 10 μl	Eppendorf, Hamburg, Germany
Pipette eppendorf Research® 20 μl	Eppendorf, Hamburg, Germany
Pipette eppendorf Research® 100 μl	Eppendorf, Hamburg, Germany
Pipette eppendorf Research® 200 μl	Eppendorf, Hamburg, Germany
Pipette eppendorf Research® 1000 μl	Eppendorf, Hamburg, Germany
Power Pac HC high-current power supply	Bio-Rad, Munich, Germany
QuantStudio™ 7 Flex qRT-PCR System	Applied Biosystems™, Darmstadt, Germany
Rocking shaker	MS-L, Wiesloch, Germany
Roller mixer	Ratek, Victoria, Australia

Tab. 4.15: Used equipment and instruments – continued

Instrument	Company
Spinning whel	MS-L, Wiesloch, Germany
Sunrise microplate reader	Tecan, Crailsheim, Germany
Thermomixer comfort	Eppendorf, Hamburg, Germany
Trans-Blot SD semi-dry transfer chamber	Bio-Rad, Munich, Germany
Vacuum pump HLC	Ditabis, Pforzheim, Germany
Vortex mixer ZX classic	VELP Scientifica, Usmate, Italy
Water bath SWB20	Medingen, Arnsdorf, Germany
X-ray cassette type G	Rego, Augsburg, Germany

4.1.13 Software

Tab. 4.16: Software used throughout the project

Software	Version	Company
EndNote	X7.8	Thomson Reuters, Toronto, Canada
FACS-DIVA	6.1.3	BD Bioscience, Heidelberg, Germany
FIJI-ImageJ	1.53c	National Institute of Health, USA [148]
FlowJo	10.6.2	BD Bioscience, Heidelberg, Germany
GraphPad Prism	9.3.1(471)	GraphPad Software, San Diego, CA, USA
Magellan data analysis	7.2	Tecan, Crailsheim, Germany
MetaXpress	6.7.1.157	Molecular Devices, San Jose, CA, USA
Metascape	3.5	[149]
Microsoft-Office	2019	Microsoft, Redmond, WA, USA

Tab. 4.16: Software used throughout the project – continued

Software	Version	Company
NanoDrop Software	3.8.1	ThermoFisher Scientific, Roskilde, Denmark
QuantStudio™ Real-Time PCR Software	v1.3	Applied Biosystems, Darmstadt, Germany
Tecan i-control	1.10	Tecan, Crailsheim, Germany

4.2 Methods

4.2.1 Cell culture

The following section describes the methods for routine maintenance of stable cancer cell cultures, i.e. cultivation, freezing and treatment. Further, it will contain methods for 3-dimensional multicellular spheroid formation, treatment protocols, generation of knock-down and knock-out cell lines and enrichment and maintenance of primary NK cells. All mentioned cell lines, kits, instruments, chemical and cell culture reagents are listed in the material section 4.1.
All stable cancer cell lines were regular tested negative for mycoplasma contamination using the Venor®GeM Mycoplasma PCR detection kit (Minerva-Biolabs). Further, stable cell lines were authenticated by STR (short tandem repeat) analysis and DNA profiling at the German Collection of Microorganisms and Cell Cultures GmbH (DSMZ).

4.2.1.1 Maintenance of stable cell lines

All stable cell lines and primary cells were cultivated in a humidified atmosphere containing 5 % CO_2 at 37°C. The embryonal RMS cell line RD and RD-GFP/Luc were cultured in DMEM GlutaMAX™-I complete growth culture medium. The alveolar RMS cell line RH30 and RH30-GFP/Luc were cultured in RPMI1640 GlutaMAX™-I complete growth culture medium. For complete growth medium, both basal media were supplemented with 10 % FCS, 1 % penicillin/streptomycin (P/S) and 1 mM sodium pyruvate. The embryonal human kidney cell line HEK293T, used for lentiviral particle production, was cultured in DMEM GlutaMAX™-I, supplemented with 10 % FCS, 1 % P/S and 1 mM sodium pyruvate.
Cells grew until confluent and passaged twice a week. For cell detachment, either

Trypsin/EDTA dissociation reagent, or an enzyme free detachment reagent was added at a sufficient volume to cover the growth surface and incubated at 37°C for 5 min. After incubation, the dissociation reagent was neutralized with the same volume of complete growth medium and used for further experiments or routine cell culture.
Cells were cultivated until reaching a passage number of 30-35. Higher cell passages were autoclaved and discarded.

4.2.1.2 Freezing cells as cryo-stocks

For generating cryo-stocks, cells were detached as described above, centrifuged for 5 min at 1800 rpm by room temperature and supernatant discarded. Depending on the size, cell pellets were re-suspended in 10 % DMSO in FCS to fill 1 ml per cryo-vial, transferred into a Mr.Frosty™to ensure a constant freezing rate and stored at -80°C. For long time storage, cryo-vials were transferred into the vapor phase of a liquid nitrogen tank.

4.2.1.3 Treatment of tumor cell lines for *in vitro* experiments

Treating adherent growing RMS cell lines cultured on a 2D growth surface, was either performed in 96 well plates for cytotoxicity measurements (cell death determination: PI/Hoechst staining), or in culture dishes (6 cm, 10 cm) for isolation of proteins and RNA. The standard seeding cell density was 0.2×10^5 cells/cm^2 and cells were seeded 24 h pre-treatment in complete growth culture medium, for complete cell attachment. On the day of treatment, medium was aspirated and either fresh culture medium as control or medium containing the final concentration of treatment was carefully added into the wells/dishes (for treatment see respective figure legends). After addition of treatment, cells continued to grow in an incubator at 37°C, with 5 % CO_2 for desired time of treatment (see respective figure legends).

4.2.1.4 siRNA transfection of cell lines

Knock-down of interesting targets by small interfering RNA followed the reverse siRNA transfection protocol of the manufacturer of the Lipofectamine™RNAiMAX reagent (Invitrogen, Thermo Fischer Scientific). In brief, Lipofectamine RNAiMAX was diluted in OptiMEM in a ratio of 3:50 μl. Subsequently, target siRNA was diluted in OptiMEM to reach a concentration 20× higher than the final concentration. This siRNA:OptiMEM mixture was further diluted 1:2 with the previously prepared Lipofectamine RNAiMAX:OptiMEM mixture and incubated for 5 min at room temperature. During the incubation time, target cells were detached and counted.
Following incubation, the transfection mixture was distributed into needed well/dish

numbers. For a 96 well plate 10 μl per well, for a 6 cm dish 400 μl and for a 10 cm dish 800 μl of transfection mixture was needed. The final concentration of all used siRNA constructs was 10 nmol/l. After distribution of transfection mixture, cell suspension was seeded into the needed wells/dishes at desired cell density. By adding the cell suspension, the previously added transfection mixture was diluted 1:10 reaching final concentration (10 nmol/l). Plates and dishes were cultivated at 37°C with 5 % CO_2 humidified atmosphere. 24 h after transfection, either medium was changed to complete growth medium and cultivation continued, or medium was changed with added treatment for the desired treatment time. Knock-down efficiency was validated by either western blot and/or mRNA isolation and qRT-PCR.

4.2.1.5 Formation of multicellular tumor spheroids

Multicellular tumor spheroids, as an *in vivo*-like 3D model, were formed by seeding the initial cell numbers in ultra-low attachment plates. By that, RMS cells could not adhere to the surface and self-assemble into spheroidic clusters. For assessing spheroidic growth, GFP expressing RMS cell lines were used and fluorescence intensity acquired on an ImageXpress Micro XLS. After seeding the appropriate cell number per 100 μl per well (see table 4.17), the plate was centrifuged at 1 000×g for 10 min at room temperature with lowest active break setting (Setting R = 1). Initial accumulated cells were cultivated in the same conditions as described above in section 4.2.1.1. After centrifugation, spheroids grew for 3 days before adding the treatment. Treatment was added, by adding 100 μl of fresh medium, or medium containing treatment, double the desired concentration. The solution was slowly added into the spheroid containing wells, as not to agitate the settled spheroid. If co-cultivation with NK cells was desired, NK cell were added at day 4 post spheroid seeding and continued to co-cultivate for additional 5 days (120 h) (see figure 4.1). For that, 150 μl medium was carefully removed and fresh medium containing the needed amount of NK cells, reaching wanted E:T ratios, added. On day 7 post spheroid formation (day 3 post NK cell addition), the medium was again changed by removing 100 mul and carefully adding the same amount of fresh medium. Followed by continued incubation.

Tab. 4.17: Empirical determined initial cell numbers for the formation of multicellular tumor spheroids

Cell line	initial cell number per well
RH30-GFP/Luc	2500
RD-GFP/Luc	5000

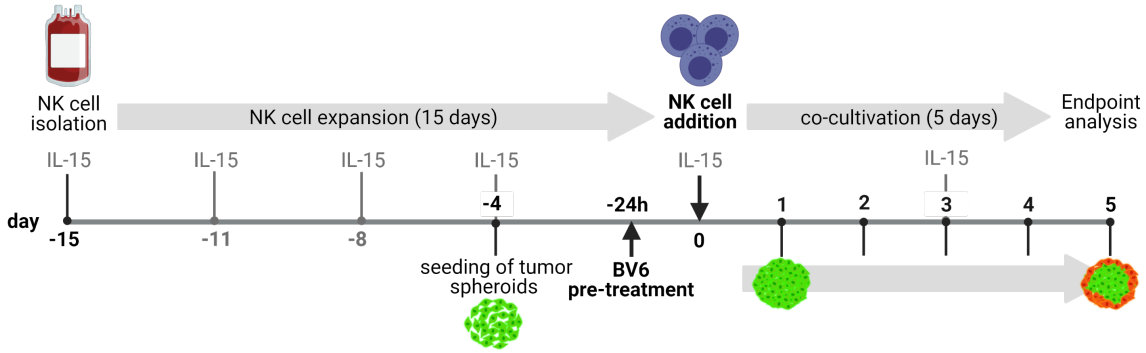

Fig. 4.1: Experimental setting of the 3D co-culture experiments. Figure was created with BioRender.com.

4.2.1.6 Enrichment of human NK cells from PBMCs

NK cells were enriched from peripheral blood monocytic cells (PBMC). For that, buffy coats were acquired from the german red cross blood donation service (GRC-blood donation service Frankfurt). Blood of the buffy coat bag was transferred into a 50 ml falcon tube and diluted with the same volume of PBS. 35 ml of this blood:PBS mixture was layered onto 15 ml Histopaque-1077 (Sigma Aldrich, Merck) for density centrifugation and centrifuged at 800×g for 20 min at room temperature without a brake. After density centrifugation, the upper layer containing blood serum was halved. Using a transfer pipette the cloud fraction on top of the Histopaque layer, containing blood leukocytes, was carefully removed and transferred into a fresh 50 ml falcon tube. Initial leukocytes were washed trice with PBS and centrifuged at 400×g for 7 min at room temperature with full brakes. The final pellet was again respuspended in 50 ml PBS and cells counted.

Enrichment of NK cells of PBMCs was carried out following the instructions for the negative EasySep human NK cell enrichment kit (StemCell). Routinely, 50×10^6 PBMCs were used to isolate NK cells from. The volume to reach said cell number was transferred from the initial PBMC preparation into a fresh tube and centrifuged at 400×g for 7 min at room temperature. The pellet was resuspended with 1 ml of EasySep buffer (1×PBS, 2 % FCS, 1 mM EDTA) to reach a cell concentration of

50×10^6 cells/ml and transferred into a 5 ml round bottom tube (with cap). 50 μl of antibody enrichment cocktail was added into the cell suspension, gently vortexed and incubated for 10 min at room temperature. After incubation, 100 μl magnetic particles were added, again gently vortexed and incubated for 5 min at room temperature. 1.35 ml EasySep buffer was added to the cell suspension, to reach a final volume of 2.5 ml, before placing the tube into a pink EasySep magnet (StemCell) for 2.5 min without the cap on the tube. Following magnetic separation, the cell suspension was transferred into a new 15 ml falcon tube by leaving the tube:magnet assembled and decanting the cell suspension in one smooth movement into a new tube. Enriched NK cells were again washed with PBS, centrifuged (400×g, 7 min, room temperature) and resuspended in complete NK MACS®growth medium (Miltenyi, basal medium supplemented with 5 % human AB plasma, 1 % Pen/Strep, 1 % non-generic manufactures supplements) at a cell concentration of 2×10^6 cells/ml and seeded in a 48 well plate with the addition of IL-15 (Peprotech) at a final concentration of 10 ng/μl. Cultivation took place at 37°C, enriched with 5 % CO_2.
Purity of the initial enriched NK cell population and PBMCs were determined using an antibody staining panel and flow cytometric analysis (see section 4.2.3.3). IL-15 activated NK cells expanded for 15 days in NK MACS®are referred herein as NK cells. On day 11 and 15 post enrichment, purity of expanded NK cells were again analyzed.

4.2.1.7 Maintenance of NK cells

As described above (section 4.2.1.6), primary enriched NK cells were cultivated in complete NK MACS®growth medium supplemented with IL-15 (final concentration 10 ng/μl), at 37°C, humidified air enriched with 5 % CO_2. Every 3-4 days half of the medium per well was carefully removed and fresh complete NK MACS®growth medium supplemented with fresh IL-15 carefully added into the well. Additionally, NK cells were counted and if necessary split into new wells, reaching a cell concentration of 2×10^6 cells/ml. On day 7 and 11, a complete medium exchange was performed. For that, all NK cells lying on the bottom of the wells were resuspended and transferred into a 15 ml falcon tube, centrifuged (400×g, 7 min, room temperature), supernatant discarded and pellet resuspended in fresh complete NK MACS®growth medium supplemented with IL-15, reaching a cell concentration of 2×10^6 cells/ml. Cell suspension was then reseeded into a 48 well plate. If NK cells were used on day 15 of expansion, day 11 was the last time were cultivated NK cells received fresh IL-15.

4.2.2 CRISPR/Cas9 mediated knock-out generation

The following section comprises methods to perform a CRISPR/Cas9 mediated knock-out of a target gene in RMS cells. First, cloning of the needed gRNAs into the respective plasmid will be illustrated, including transformation of *E.coli* bacteria. Followed by the production of lentiviral particles for the transduction of mammalian target cells and the final validation of the induced knock-out.
A two step protocol was used for the knock-out generation. The first step, generating doxycycline inducible Cas9 expressing target cells, by transducing pCW-Cas9-Blast plasmid via lentiviral particles. The second step includes the lentiviral transduction of the Cas9 expressing target cells with the gRNA containing plasmid pLentiguide-Puro. After the second transduction step, the bulk culture is screened for a successful knock-out and cultivation of single clone cultures. Finally, the validation process of single clone cultures with a putative knock-out will be described.

4.2.2.1 Cloning of gRNA into pLentiguide-Puro

First step was the digestion of the circular plasmid pLentiguide-Puro. For that, 5 μg of the plasmid was incubated with: 5 μl FastDigest *BsmBI* (Fermentas), 5 μl restriction buffer NEB 3.1, 0.6 μl and filled with nuclease-free water reaching 50 μl in total. The digestion mixture was incubated for 2 h at 55°C. After which, the enzyme was heat-inactivated by incubation for 20 min at 80°C. The digested plasmid was gel purified on an agarose gel using QIAquick® Gel Extraction Kit (Qiagen).
The forward and reverse gRNA oligonucleotides needed to be annealed, to form the double stranded gRNA. For that, 10 μl of each was mixed with 80 μl nuclease-free water, incubated for 5 min at 95°C, before left to cool down to room temperature.
For the ligation of gRNA oligo-duplexes into digested pLentiguide-Puro plasmid, 1 μl of digested plasmid was mixed with: 0.5 μl annealed gRNAs, 1 μl T4 NDA ligase buffer, 1 μl T4 DNA ligase and 6.5 μl nuclease-free water. Ligation took place over night at 16°C.
E. coli Stbl3 bacteria were used for the multiplication of the final plasmid containing gRNA. The Stbl3 bacteria were thawn on ice for 10 min. Using 100 μl of bacteria suspension 10 μl of ligation mixture was added, mixed by gentle tipping and incubated for 30 min on ice. The heat shock transformation was performed for 42 seconds at 42°C and cooled down on ice for 2 min. 250 μl of 37°C pre-warmed SOC medium was added to the bacteria suspension and incubated for 1 h at 37°C on a shaker with 225 rpm. The bacterial suspension was then spread onto a pre-warmed LB-Agar plate supplemented with the respective antibiotic, respective to the plasmid requirements. Agar-plates were incubated upside-down at 37°C over night. On the next day, single colonies were picked

and resuspended in 5 ml LB-antibiotic medium and cultured over night at 37°C. The plasmid was isolated out of the bacterial cell suspension according the manufacturer, using a GeneJet Plasmid-Miniprep kit (ThermoFisher Scientifc).
As a quality control step, isolated plasmids (12 μl) including either fwd or rev primers (3 μl) were send to Microsynth for sequencing (Microsynth Seqlab GmbH, Göttingen, Germany). Following primers were used for the sequencing, U6 forward 5'→3' GAGGGCCTATTTCCCATGATT and hGATA4 reverse 5'→3' ATTGTGGATGAATACTGCC.

4.2.2.2 Lentiviral particle production

Successfully generated plasmids, with error-free sequence, were further used to generate lentiviral particles for target cell transduction. The general protocol for lentiviral particle generation is as follow, 1.1 μg of pLentiguide-Puro gRNA containing plasmid, mixed with 1.0 μg of pMD2.g, 2.7 μg psPAX2 as plasmid mixture. To this mixture trice the volume of FuGENE® HD transfection reagent (Promega) was added, using the volume of the plasmid mixture as reference. To the complete transfection mixture OptiMEM was added to reach a total volume of 200 μl and incubated for 15 min at room temperature. This solution was dropwise added to one well of 24 h pre-seeded HEK293-T cells (4×10^5 cells per well, in 6 well plate).
From now on, every waste needs to be inactived by UV irradiation for 1 h prior to autoclaving. One day after transfection, medium was changed to complete DMEM growth medium and cultivation continued. On day 2 and 3 after transfection started, the viral particle containing culture supernatant was collected and filtered through a 0.45 μm filter, stored at 4°C and fresh culture medium added onto the cells. On the last day of harvesting viral particles, the combined viral particle containing solution is shock frozen by submerging in liquid nitrogen and stored at -80°C until further use.

4.2.2.3 Target cell transduction

Target cells are seeded in 6 well plates at a density of 30 %, one day before the addition of viral particles. After 24 h, 500 μl of the viral particle containing supernatant was added dropwise into one well. As an transduction enhancer protamine sulfate in a concentration of 4 μg/ml was added into the same well. The plate was then centrifuged for 2 h, at 37°C, with 1200×g, acceleration setting '1' and no brake. After centrifugation, the plate was cultivated at 37°C and 5 % CO_2. After 24 h, the transduction medium was aspirated and inactivated by UV irradiation for 1 h and fresh complete growth medium supplemented with puromycin added, to select for positive transduced cells. The final concentration of puromycin ranged from 1 μg/ml to 20 μg/ml.

4.2.2.4 Knock-out validation

First, the *CCL5* knock-out generation was validated on an mRNA level by qRT-PCR and agarose gel electrophoresis. Second, exon 2 was PCR amplified on isolated genomic DNA and send for DNA sequencing to detect a possible deletion.
For the first part, the RNA isolation and qRT-PCR analysis was performed according to the manufacturers manuals and as described in section 4.2.6.
For the second part, genomic DNA was isolated using the PureLink™ Genomic DNA Mini Kit (Invitrogen, ThermoFisher Scientific). Using the isolated genomic DNA, exon 2 was amplified by PCR with following primers, forward: GAATCCCCACTCTGCCACTG and reverse: GTGGAAGTGGGTAGGGCATC. For the PCR reaction 100 ng of genomic DNA as template was used. Adding 2.5 μl of each primer (stock concentration 10 μM), 1 μl of 10 mM dNTP mix, 1 unit (0.5 μl) of Phusion polymerase, 10 μl of 5× HF buffer (Phusion high-fidelity DNA polymerase buffer) and filled up to a total volume of 50 μl with nuclease-free water. The thermocycler protocol can be found in table 4.18. PCR was followed by agarose gel electrophoresis, excision and purification of interesting bands by QIAquick gel extraction kit (Qiagen). Excised and purified bands were send for sequencing using *CCL5* exon 2 primers (Microsynth Seqlab GmbH, Göttingen, Germany). Sequencing results were aligned to *CCL5* of the human reference genome and deletion sites identified.

Tab. 4.18: Thermocycler protocol for *CCL5* exon 2 amplification from genomic DNA

Step	Time	Temperature	Number of cycles
Initial denaturation	30 sec	98°C	1
Denaturation	10 sec	98°C	
Annealing	20 sec	65°C	×35
Extension	45 sec	72°C	
final extension	10 min	72°C	1
hold	indefinetly	4°C	∞

4.2.3 Flow cytometric methods

The following section will describe methods for flow cytometric analysis using a BD FACS Canto II. It was used to assess the NK cell cytotoxicity in 2D co-cultivations, to determine the state of receptor surface presentation and to assess the purity of the NK cell population within PBMCs or enriched and expanded NK cell cultures. Post-acquisition analysis was performed using FlowJo (v10.6.2).

4.2.3.1 NK cell cytotoxicity assay in 2D co-cultivations

Target cells, i.e. wild type RMS cells, were seeded before the start of the co-cultivation, the time for possible pre-treatments was taken into account. NK cells were used on day 15 of IL-15 activation and expansion as described in section 4.2.1.7.
On the day of co-cultivation, target cells were stained with CFSE. For that, target cells were detached as previously described and 1.5×10^6 target cells washed with PBS, transferred into a 15 ml falcon tube and centrifuged for 5 min, at 300×g. The pellet was resuspended in 1 ml CFSE staining buffer. Subsequently, 20 μl of a 1:100 in PBS diluted CFSE stock solution (CFSE stock concentration = 5 mM) was added to the target cell suspension, to reach a final CFSE concentration of 1 μM and incubated for 5 min, at room temperature in the dark. Stained target cell suspension was washed with CFSE-staining buffer and centrifuged for 5 min, at 300×g. Supernatant was discarded and the stained target cell pellet resuspended in 6 ml complete growth medium, to reach a cell concentration of 0.25×10^6 cells per ml. 100 μl of this cell suspension was pipetted into a 96 well U-bottom plate, thereby seeding 25 000 cells per well.
Effector NK cells were washed with PBS, centrifuged for 5 min, at 300×g, left unstained and resuspended in complete NK cell growth medium. The effector NK cell concentration depend on the desired effector to target (E:T) cell ratio, with the restriction of adding only 100 μl of effector cell suspension to the target cells. By that, reaching a total volume of 200 μl within the 96 well U-bottom plate. After addition of the effector cells to their targets, the plate was incubated for 4 h at 37°C with a 5 % CO_2 enriched humidified air.
After 4 h of co-cultivation, the supernatant was transferred into a labeled FACS tube and remaining cells detached by adding 50 μl Accutase and incubated for 5 min at 37°C. Subsequently, 100 μl PBS was added into the wells and gently resuspending the remaining cells and transferring them into the same labeled FACS tube. FACS tubes were then centrifuged for 5 min, 1800 rpm, at 4°C. Supernatant discarded and cell pellet resuspended in 100 μl PBS. Directly before acquisition 5 μl of a 1:300 in PBS diluted DAPI solution was added into the tubes, incubated for approximately 3 min, to reach a final dilution of DAPI of 1:6 000 within the FACS tube. Using the flow cytometer,

fluorescence intensities of the FITC and Pacific blue channels were acquired. By that, the FITC channel could be used to distinguish between CFSE positive target and CFSE negative effector cells. By using the Pacific blue channel, dead, DAPI positive target cells could be identified by their CFSE and DAPI double positivity. Figure 4.2 shows an exemplary gating strategy to identify dead target cells. Equation 4.1 displays how the specific NK cell lysis was calculated [150]. Using the % CFSE:DAPI double positive target cells of the untreated control as the basal cell death, and % CFSE:DAPI double positive target cells of each treatment as the sample cell death.

$$\text{specific lysis} : \%\ \text{specific lysis} \ = \ 100 * \frac{((\%\ \text{sample} - \%\ \text{basal}))}{(100 - \%\ \text{basal})} \tag{4.1}$$

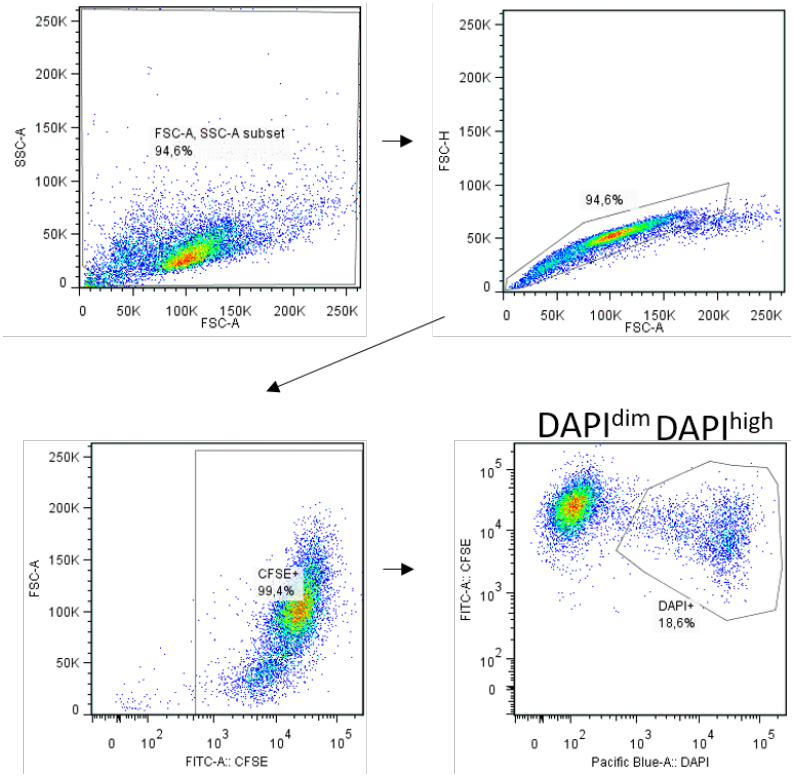

Fig. 4.2: Gating strategy for flow cytometry based NK-RMS cell killing assay. Exemplary identification of dead DAPI$^+$ CFSE$^+$ target cells.

4.2.3.2 Detection of surface proteins

Surface proteins were detected by antibody mediated staining and fluorescent signal acquisition by flow cytometry (see table 4.15). Adherent cells were washed with PBS and detached using an enzyme free dissociation buffer (see table 4.2), volumes were chosen to sufficiently cover the growth surface. Single cell suspension was counted and 1×10^5 cells per sample transferred into a round bottom FACS tube, for each sample

an additional tube was prepared for isotype staining.
500 µl PBS was added and cell suspension centrifuged for 5 min at 4°C at 1800 rpm. Supernatant was discarded and the cell pellet resuspended in 50 µl FACS-staining buffer (table 4.14) in which the primary antibodies were diluted to reach the desired final concentration. Used primary antibodies and respective concentrations are listed in table 4.6.
The cell suspension:antibody dilution was incubated at 4°C in the dark for 30 min, after which 500 µl FACS-staining buffer was added and centrifuged for 5 min, at 4°C at 1800 rpm. Washing was repeated in total for three times. All primary antibodies were directly conjugated to the fluorochrome PE, no secondary staining was required. The final cell pellet was resuspended with 100 µl PBS and covered in tinfoil until measurement. Before a tube was acquired, 5 µl DAPI (1:300 pre-diluted in PBS, final dilution 1:6 000) was added into the 50 µl stained cell suspension and incubated 3 min on ice, after which the tube was measured and 10 000 alive cells acquired.

4.2.3.3 Determination of NK cell purity

Following the enrichment of primary NK cells from PBMCs, see section 4.2.1.6, the purity of the NK cell population was determined compared to the initial PBMC population. To observe changes within the NK cell population, purity was checked on day 11 and day 15 post enrichment. Measurement on day 15 was specially important, confirming the NK population purity for co-cultivation cytotoxicity assays.
The staining of a minimum of 200 000 cells was performed in 5 ml FACS tubes. After washing with 1 ml PBS and centrifugation for 5 min at 500×g, the supernatant was discarded and the pellet resuspended in 82.5 µl brilliant stain buffer (BD Bioscience). Into which the fluorochrome conjugated primary antibodies were added, see table 4.19. Antibody containing cell suspension was incubated for 20 min at 4°C in the dark. Again, the cell suspension was washed with 1 ml PBS, centrifuged for 5 min, at 500×g and supernatant discarded. Cell pellet resuspended in 100 µl PBS and 2.5 µl 7-AAD added, followed by an incubation for 5-10 min, at 4°C in the dark. At the flow cytometer, the respective fluorescence channels, as indicated in table 4.19, were chosen. Figure 4.3 depicts an example on the gating strategy to determine NK cell population purity. For further down-stream assays a purity of at least 95 % was desired.

Tab. 4.19: Application of fluorochrome conjugated antibodies for NK cell population purity assessment

Surface target	Volume (μl)	conjugated fluorochrome	Channel
CD3	5	BV510	FITC
CD16	2.5	PE	PE
CD45	5	APC	APC
CD56	5	BV421	Pacific blue

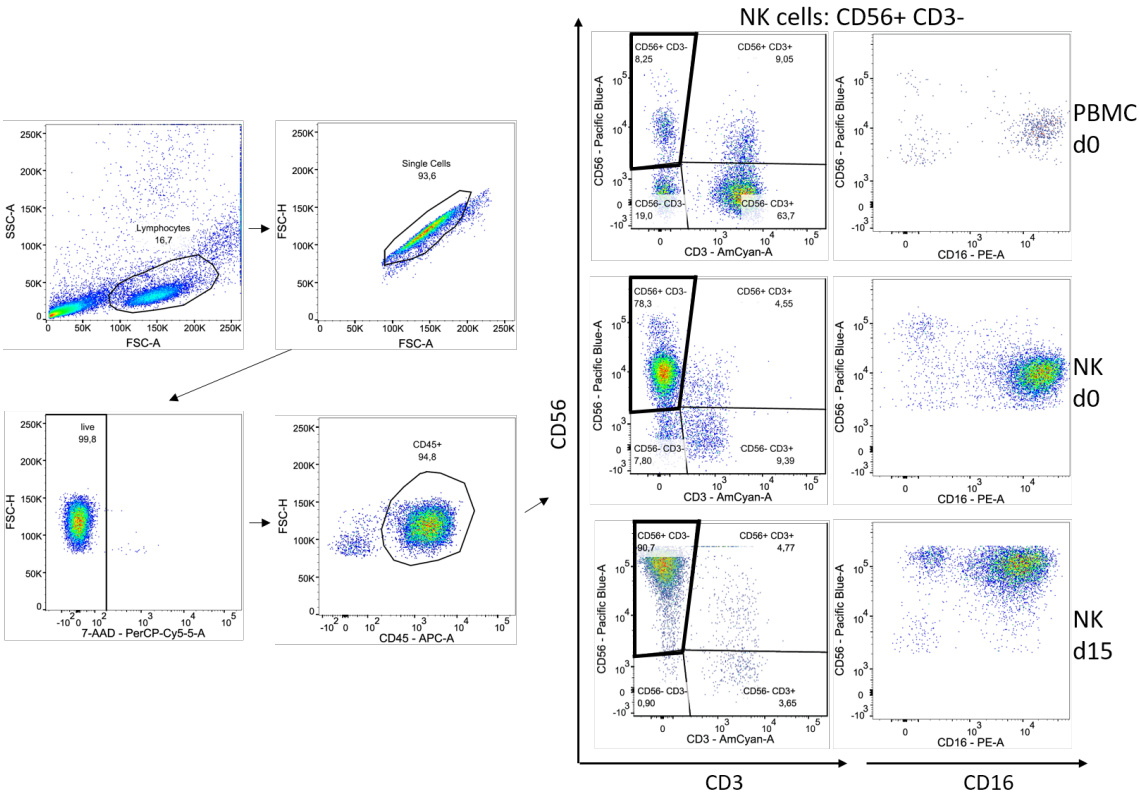

Fig. 4.3: Gating strategy to define the purity of the NK cell population defines as $CD45^+$ $CD56^+$ double positive. Shown are exemplary scatter plots for one healthy donor pre- and post-enrichment and on the last day of expansion.

4.2.4 Microscopy based methods

The following section will describe methods based on using microscopical techniques, i.e. cell death evaluation by PI and Hoechst staining, acquisition of multicellular tumor spheroids using z-stacks and staining of NK cells for migration analyses. The ImageXpress Micro XLS Widefield Analysis System (IXM XLS, Molecular Devices) with environmental control and transmitted light option was used throughout the project. Down-stream semi-automated analysis was performed using MetaXpress analysis soft-

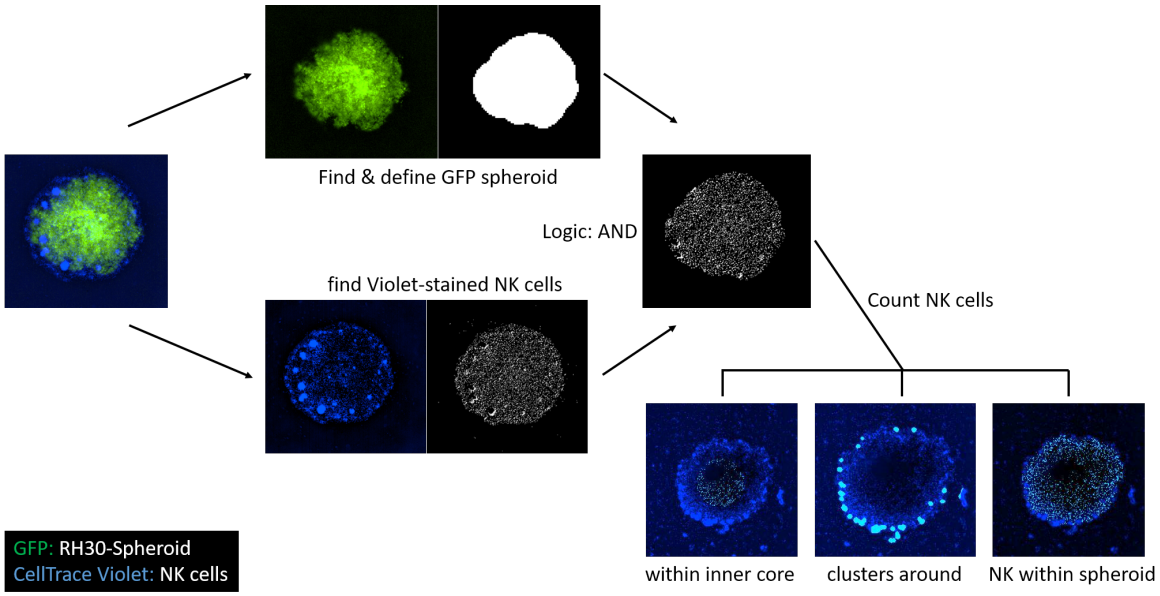

Fig. 4.4: Depiction of the MetaXpress algorithm to identify GFP expressing spheroids and CellTrace™ violet stained NK cells. Upper path: signals within the FITC channel were used to generate a binary mask for the spheroid by applying an intensity and size threshold. Lower path: signals within DAPI channel were used to generate binary mask for NK cells by applying an intensity threshold and size threshold.

ware (Molecular Devices) and FIJI as an image manipulation software for color adjustments, crop and scale bar integration.

4.2.4.1 Measurement of tumor spheroids

Multicellular tumor spheroids generated using GFP expressing RD or RH30 cells were imaged by an IXM XLS fluorescence microscopy. Based on the GFP expressing cells, morphological changes could be detected and visualized by acquiring the fluorescence signal taking the FITC filter cube.
For finding the best focus plane, a z-stack of 12-25 layers was acquired per well and one best focus image was saved into data storage. Using this image and applying a custom made algorithm to detect only the GFP positive spheroid, a binary mask was generated based on the FITC channel. Using this mask, the GFP fluorescence intensity could be measured and exported. Intensity was measured in arbitrary fluorescence intensity units. Further analysis used the untreated spheroids on day 0 as a reference point.

4.2.4.2 Cell death evaluation in 2D and 3D

Cell death in 2D and 3D cultures was assessed by the uptake of propidium iodide (PI). This dye does not pass through an intact plasma membrane of healthy cells. On the

other hand, the plasma membrane of dead and dying cells becomes leaky, PI passes through and stain dead and dying cells.
The PI stock solution (stock concentration 1 mg/ml) was pre-diluted 1:100 in PBS. This working solution was used to achieve a final concentration of 1 μg/ml, followed by an incubation for 5 min at 37°C in the dark.
As an overall cell co-staining, Hoechst33342 was used. This dye can pass through both, intact and leaky plasma membranes and specifically stains DNA.
Hoechst33342 was used in a final concentration of 10 μg/ml, using a 1:100 pre-diluted working solution in PBS (stock concentration 10 mg/ml). Before image acquisition, stained cells were incubated for 5 min at 37°C in the dark.
On the IXM XLS microscope, PI fluorescence was acquired using the TRITC filter cube. Hoechst33342 fluorescence signal was acquired using the DAPI filter cube. Within the MetaXpress analysis software a pre-made cell scoring algorithm was used to calculate the percentage of PI stained cells, taking all Hoechst33342 stained cells as a reference value.

PI staining as an end-point measurement was performed to detect cell death in GFP expressing multicellular tumor spheroids (3D cultures). For that, a final concentration of 2 μg/ml was adjusted in a total volume of 200 μl per well. Before image acquisition on the IXM XLS microscope, PI counter-stained spheroids were incubated for 30 min at 37°C in the dark. PI fluorescence was acquired by using the TRITC filter cube. To detect the remaining spheroid, the GFP signal was acquired using the FITC filter cube. Image analysis was performed using customized algorithm within the custom module editor of MetaXpress analysis software (see fig. 4.4). Integrated fluorescence intensity measured in arbitrary fluorescence intensity units of both channels were exported to calculate PI/GFP ratios, normalized to untreated samples as a reference value.

4.2.4.3 Measurement of NK cell migration into tumor spheroids

To evaluate the migratory behaviour of NK cells into GFP expressing RMS multicellular spheroids, NK cells were labeled with CellTrace™ violet. By that, labeled NK cells could be tracked and migration pattern detected.
On the day of NK cell addition to the GFP expression RMS spheroids, NK cells were stained. For that, 1×10^6 NK cells were used (day 15 post enrichment), washed with PBS and centrifuged for 5 min at 1800 rpm. After discarding the supernatant, the remaining cell pellet was resuspended in 1 ml CFSE staining buffer. To which 60 μl of a 1:100 in PBS pre-diluted CellTrace™ violet (stock concentration 5 mM) solution was added. The final staining concentration was set to 3 μM. After incubation for

20 min at room temperature in the dark, 5 ml of CFSE staining buffer was added to the NK cell suspension. Centrifuged for 5 min at 1 800 rpm and the remaining cell pellet resuspended in complete growth medium reaching a cell concentration needed for the E:T ratio of respective experiment.
The final volume of the co-culture was 200 μl per well. As the generation and treatment of spheroids took place in 100 μl, NK cells in the appropriate cell concentration reaching the desired E:T ratio was added in 100 μl culture medium supplemented with IL-15. Fluorescence signal of CellTrace™ violet stained NK cells was acquired using the DAPI filter cube on the IXM XLS microscope.
Migration of labeled NK cells was observed within a time period of 8 h. Every hour images were acquired. By that, being able to follow the labeled NK cells into the respective spheroids. To identify the GFP labeled spheroids, fluorescence signals in the FITC channel were acquired.
Using a custom module algorithm, a mask of the GFP fluorescent tumor spheroid was made. Using this mask, i.e. identified spheroid, CellTrace™ violet labeled migrated NK cells were counted within the spheroid. Values were exported for further statistical analysis. Figure 4.4 depicts the used algorithm to illustrate mentioned masks, to identify either GFP positive spheroids, or CellTrace™ violet labeled NK cells.

4.2.4.4 Immunofluorescence staining of RMS cells

Intracellular proteins were stained within adherent RMS cells in 2D culture systems. For that, cells were seeded in a cell density of 0.5×10^5 cells per cm^2, higher than indicated in section 4.2.1.3, to account for cell losses due to excessive washing steps. Cells were seeded in 96-well black clear bottom plates in a volume of 100 μl growth medium.
After respective treatment was added for the desired time, cells were fixed by adding 100 μl 7.4 % formaldehyde into the well, reaching a final concentration of 3.7 % formaldehyde. Fixation took place at room temperature for 20 min, after which the solution was removed and discarded. For staining intracellular proteins the cells needed to be permeabilized. For that, 100 μl of a 0.1 % Triton-X100 in PBS solution were added into the well. Incubated for 10 min at room temperature and solution discarded afterwards. Subsequently, wells were washed trice by adding 100 μl PBS into the wells and washing solution discarded. After washing, cells were blocked by adding 100 μl antibody dilution (ABD) buffer into the wells and incubated for 30 min at room temperature. The blocking solution was again discarded and primary antibody added in a volume of 50 μl and incubated over night at 4°C. On the next day, primary antibody was collected to be reused. Wells were washed with 100 μl PBS per well for five times. Followed

by addition of the secondary antibody, diluted in the desired concentration in ABD buffer and incubated for 90 min at room temperature in the dark. Together with the secondary antibody, a nuclear stain, i.e. DAPI, in a final dilution of 1:6 000 was added. The wells were subsequently washed trice with 100 μl PBS. Finally, 100 μl PBS were added into the wells and stored at 4°C until microscopic image acquisition. Appropriate filter cubes at the IXM XLS microscope were chosen, depending on the used secondary antibody. Chosen objective is indicated in the respective figures legend.

4.2.5 Analysis of protein expression

Apart from the protein analysis on the cell surface by flow cytometry (section 4.2.3.2) or intracellular by microscopy (section 4.2.4.4), endogenous protein expression was detected by western blot. For that, whole cell lysates were generated (section 4.2.5.1), protein lysates electrophoretically separated (section 4.2.5.4), blotted and detected using chemiluminescence (sections 4.2.5.5 & 4.2.5.6). All methods belonging to this experimental setup will be described in the following section. Additionally, the generation of nuclear fragments as input material for protein detection by western blot is explained in section 4.2.5.2.

4.2.5.1 Whole cell lysate generation

All Steps to generate whole cell lysates were performed on ice. Adherent cells were mechanical detached using a cell scraper. Cell suspension was transferred into a falcon tube and centrifuged at 1 800 rpm for 5 min at 4°C. Pellets were washed with 1 ml PBS, transferred into a new labeled 1.5 ml reaction tube and centrifuged at 1 800 rpm for 5 min at 4°C. Washed cell pellets were resuspended in lysis buffer (see table 4.14) using an equal volume of the pellet. Incubation of the lysates were performed on ice for 45 min. To increase the protein yield, lysates were frozen at -20°C over night. On the next day, lysates were thawed on ice and centrifuged at 14 000 rpm for 20 min at 4°C. Soluble proteins were contained within the supernatant, which was transferred into a new labeled 1.5 ml reaction tube. Undissolved cell components were discarded and the protein concentration of the supernatant, i.e. whole cell lysate, determined (section 4.2.5.3).

4.2.5.2 Nuclear fragmentation

For a subcellular fragmentation to enrich the cell nucleus, cells were harvested as described above (section 4.2.5.1). The 1.5 ml reaction tube containing the washed cell pellets were resuspended in 150-300 μl nuclear fragmentation buffer A (see table 4.14),

without vortexing, only by careful pipetting. Resuspended cells were incubated on ice for 15 min, before a 10 % NP-40 (IGEPAL CA-630) solution was added into the tube and vortexed for 30 sec. The added volume of the NP-40 buffer was 10 % of the total resuspended cell volume. This suspension was centrifuged at 2 500 rpm for 5 min at 4°C. Supernatant aspirated and transferred into a new tube labeled with "cytosolic fraction". The remaining pellet, containing the cell nuclei, was washed by resuspending the pellet in 500 μl isotonic buffer and centrifugation at 2 500 rpm for 5 min at 4°C. Supernatant discarded and pellet resuspended in 40-80 μl nuclear fragmentation buffer B and incubate for 20 min on ice. After incubation the suspension was centrifuged by 14 000 rpm for 10 min at 4°C. Again, the supernatant, containing nuclear proteins, was transferred into a new tube labeled with "nuclear fraction". Protein concentration of both fractions were determined (section 4.2.5.3). For long time storage, fractions were snap frozen in liquid nitrogen and stored at -80°C.

4.2.5.3 Protein determination and samples generation

Protein concentration in either whole cell lysates or subcellular fractions were determined using the Pierce™ BCA protein assay. It was carried out according to the manufacturer's manual regarding the determination on 96-well plates. In brief, the first nine wells contained 10 μl of a BSA protein calibration standard in a serial dilution of 2 mg/ml to 15.6 μ/ml. Additionally, a 0 μg/ml water sample at position A2 was placed. Unknown samples were measured in triplicates in a 1:10 dilution, i.e. 1 μl of sample per well. To the wells containing the calibration standard or samples, 200 μl per well of the assay master mix was added. Assay master mix consists of a 1:50 diluted assay solution B in assay solution A. After addition into the wells, the 96-well plate was incubated for 30-45 min at 37°C, during which the colorimetric change happened. The change in color is detected by measuring the absorbance at 560 nm on a TECAN sunrise microplate reader. Absorbance values were exported, blank corrected and further analysed. Using the protein standard, a calibration curve was plotted and the unknown protein concentration of the samples calculated using linear regression analysis.
For SDS-PAGE sample generation a protein amount of 70 μg per gel lane was used. Those SDS-PAGE samples were generated using the SDS-PAGE loading buffer (see table 4.14), which was diluted to 1× with the sample volume and distilled water. Prepared samples were incubated for 5 min at 96°C, shaking at 550 rpm. Final samples were either used directly, or frozen at -20°C until further used.

4.2.5.4 SDS-PAGE

For separation of the complex protein mixture, a polyacrylamide gel electrophoresis (PAGE) was carried out. For that, a discontinuous polyacrylamide gel was home-made with a 12 % separation gel and a 5 % stacking gel on top (see table 4.20). Additional to the samples containing 70 μg total protein per gel lane, 4-5 μl of a protein ladder (PageRuler™ ThermoFisher) was pipetted into a pocket adjacent to the sample lane of the gel. Electrophoresis was performed in 1× running buffer (table 4.14) at constant voltage. The run started with 100 V, so that the samples can slowly migrate into the stacking gel. After 30 min, voltage was increased to 140 V continued until the bromophenol blue migration front reached the bottom of the gel.

Tab. 4.20: Recipe for home-made polyacrylamide gels

Gel	Solution	Final concentration
12 % separation gel	30 % Acrylamide	12 %
	1.5 M Tris (pH 8.8)	375 mM
	10 % SDS	0.1 %
	10 % APS	0.1 %
	TEMED	0.04 %
5 % stacking gel	30 % Acrylamide	5 %
	1 M Tris (pH 6.8)	125 mM
	10 % SDS	0.1 %
	10 % APS	0.1 %
	TEMED	0.01 %

4.2.5.5 Western blotting

Successful separated proteins, as indicated by the protein ladder, were transferred onto the surface of a nitrocellulose membrane using a semi-dry blotting procedure. For that, a sandwich of Whatman filter paper, nitrocellulose membrane and protein-containing gel was constructed. As a first layer, two Whatman filter papers soaked with 1× blotting buffer were placed on the bottom electrode (anode). The second layer was a nitrocellulose membrane, wetted with 1× blotting buffer. On top of the nitrocellulose membrane, the polyacrylamide gel was carefully placed. Using a small drum, air bubbles trapped between the membrane and the gel were rolled out, as not to block the migration pathway. The top layer consisted of two Whatman filter papers soaked in 1× blotting buffer. The sandwich was closed with the top electrode (cathode).

Electroblotting was performed using a constant current of 1 mA/cm^2 for 1:40 h. After which the membrane was blocked by incubation for 1 h in 5 % skimmed milk powder dissolved in PBS-T (milk:PBS-T).

4.2.5.6 Protein detection

After blocking, the membrane was washed trice with PBS-T. Subsequently, the first primary antibody was added (see table 4.4) and incubated over night at 4°C under constant agitation. The next day, primary antibody was collected and stored at -20°C to be reused. Again, the membrane was washed trice with PBS-T, each 20 min under constant shaking. Followed by the addition of the horseradish (HRP) conjugated secondary antibody (1:10 000 dilution in 5 % milk:PBS-T, see table 4.5) targeting the respective host species of the primary antibody. The secondary antibody was incubated for 1 h at room temperature under constant shaking. Followed by, trice washing the membrane for 20 min each. Subsequently, the membrane was placed on a transparent foil, covered with ECL substrate master mix according to manufacturer (Pierce™ ECL western blot detection substrate, ThermoFisher), incubated for 1 min. Afterwards, the solution was removed, membrane placed into an X-ray cartridge and chemiluminescence signal acquired using X-ray hyperfilms. Exposed X-ray films were developed using Vision X®X-ray developer and fixer solution within a dark room and scanned for digital post-hoc analysis.
In order to reuse the membrane for an additional incubation with a different primary antibody, the HRP of the first round was inactivated. Inactivation was performed by placing the membrane into a 30 % H_2O_2 solution for 15 min at room temperature under constant shaking. Subsequently, the membrane was washed with ddH_2O and PBS-T, before re-blocking with 5 % milk:PBS-T for 1 h at room temperature under constant shaking. Blocking solution was removed and membrane washed trice with PBS-T. Afterwards, the second primary antibody was added and procedure followed as described above. In total, the membrane could be reused to apply 3-4 different primary antibodies, as previously described [151].

4.2.6 Relative RNA quantification

To determine the gene expression status in cells, the total RNA content was isolated and analyzed by quantitative real time-polymerase chain reaction (qRT-PCR). Relative quantification was performed using an untreated sample as reference and calculation of fold change expression values by $2^{-\Delta\Delta Cq}$ procedure [152]. The following section will describe the overall procedure beginning with total RNA isolation, cDNA synthesis and

qRT-PCR. Additionally, the steps for the exploratory RNA sequencing (RNAseq) and high throughput qRT-PCR using a Fluidigm® platform are described. Both, RNAseq and analysis by Fluidigm® were performed by a cooperation partner, the Medical Genomics department of TRON gGmbH in Mainz.

4.2.6.1 RNA isolation

Total RNA was isolated by following the manufacturer's protocol. Two kits were used depending on the initial cell number and prospective RNA content of the cell. For 2D cultures of RMS and RMS-GFP cells, the peqGOLD total RNA kit was used. For 3D multicellular RMS-GFP spheroids and NK cells, the peqGOLD MicroSpin total RNA kit was used.
In brief, samples were lysed with 350 μl of the respective lysis buffer. Depending on the kit, the lysate was directly applied on a homogenization column, or was further centrifuged. Cleared lysates were diluted with an equal volume of 70 % ethanol and applied onto a RNA binding column. Using both kits, the optional peqGOLD DNAse I digestion was included following the manufacturer's manual. After washing twice with washing buffer, the bound RNA was eluted with nuclease-free water. RNA concentration was analysed with a Nanodrop 1000 spectrophotometer (PeqLab). RNA purity was determined by calculating a ratio of the optical density at 260/280 nm. RNA samples with a value higher than 1.9 were further used.

4.2.6.2 cDNA synthesis

Highly pure RNA samples were further used to synthesized cDNA (complementary DNA). For that, the Revert Aid First Strand cDNA synthesis kit (ThermoFisher) was utilized, according to manufacturer's manual. A constant amount of 1 μg RNA was added into a PCR reaction tube and topped up to 11 μl with nuclease-free water, to which 9 μl of the cDNA master mix was added. This master mix consisted of 5× reaction buffer, 20 U Riboblock RNAse inhibitor, 20 nmol dNTP mix, 0.1 nmol random hexamer primer, 200 U RevertAid reverse transcriptase. The PCR reaction tube including cDNA and master mix was briefly centrifuged and placed in a Thermocycler, settings are listed in table 4.21. The final synthesized cDNA samples were further diluted 1:10 with nuclease-free water. Samples were either stored at -80°C or used directly for qRT-PCR reaction.

Tab. 4.21: Thermocycler protocol for cDNA synthesis from isolated total RNA

Step	Time	Temperature	Number of cycles
Primer extension	5 min	25°C	1
Polymerisation	60 min	42°C	1
Termination	5 min	70°C	1
hold	indefinitely	4°C	∞

4.2.6.3 qRT-PCR

For all qRT-PCR experiments SYBR™ green, a double-strand DNA intercalating dye, was used to quantify the amplicon amount. Being able to maximize the analyzed genes of interest (GOI), qRT-PCR experiments were performed on a 384-well plate. Within each well 10 μl of assay master mix was added. This assay-master mix consisted of 0.25 μl forward and 0.25 μl reverse primer specific for the GOI, each of a working concentration of 10 pmol/μl (stock concentration 100 pmol/μl), 4.5 μl nuclease-free water and 5 μl of 2× SYBR™ green PCR master mix (including AmpliTaq Gold® DNA-polymerase, dNTPs, SYBR™ green, passive reference ROX). Together with these 10 μl of assay-master mix, 1 μl previously 1:10 diluted cDNA sample (section 4.2.6.2) was added into the well. All measurements for the GOI and water non-template controls were performed in technical triplicates. Primers for the GOI are listed in table 4.8, each was designed to reach a primer melting temperature of approximately 60°C.
After complete pipetting of the plate, qRT-PCR and fluorescence signal acquisition was carried out using a QuantStudio™ 7 Flex System (Applied Biosystems™). Table 4.22 shows the PCR protocol for the qRT-PCR system.
Threshold and Cq determination was software aided and Cq values exported for further statistical analysis. Data was normalized using three reference genes, 28S-rRNA, RPII, G6PD [153]. Further analysis was performed using the $2^{-\Delta\Delta Cq}$ calculation [152, 154]. Each GOI and respective water non-template control was validated by analyzing the melting curve for possible inconsistencies. If needed, final amplified samples were further analyzed on a 2.5 % agarose gel, validating the predicted amplicon size and identifying possible additional unwanted bands.

4.2.6.4 RNA sequencing

For an exploratory global RNA transcriptome approach, BV6 treated RH30 cells and untreated control cells were send to TRON gGmbH Mainz for bulk RNA sequencing. RH30 cells were treated for 24 h with 5 μM BV6 within a 10 cm cell culture dish, further see section 4.2.1.3. On the next day, cells were detached and $1 * 10^6$ RH30 cells washed

Tab. 4.22: Protocol for the qRT-PCR assay, except for melting curve acquisition, a constant 1.6 °C/sec was used.

Step	Time	Temperature	Number of cycles
Initial denaturation	2 min	50°C	×1
	10 min	95°C	
Amplification	15 sec	95°C	×40
	1 min	60 celsius	
melting curve	15 sec	95°C	one cycle with constant signal acquisition by 0.05 °C/sec
	1 min	60°C	
	15 sec	95°C	

with PBS, centrifuged (5 min, 500×g, RT), supernatant discarded and cell pellet snap frozen in liquid nitrogen. Frozen samples were stored at -80°C until transferred on dry ice to Mainz. At TRON gGmbH, RNA was isolated, mRNAseq library prepared, sequencing carried out and inital data analysis performed.
A threshold of a p value < 0.05 and a $\log_2$ fold change $> |1|$ was used to define differential expressed genes (DEG) within the comparison of BV6 treated RH30 cells using untreated RH30 cells as a reference.
Additionally to the analysis performed by TRON gGmbH, data was further analysed using web-based analysis platforms by myself (https://metascape.org, [149], https://www.grnpedia.org/trrust/ [155]). For *CCL5*, a survival analysis was performed using OncoInc.org and data exported for further analysis [156].

4.2.6.5 Fluidigm® platform

As an RNA sequencing validation, TRON gGmbH also performed a high-throughput qRT-PCR Fluidigm® analysis. Again, BV6 treated and untreated RH30 cells were used (section 4.2.6.4). As targets, previously identified GOIs by RNAseq were chosen. Those target genes, with the respective primers, can be found in table 4.9. The ΔΔCq and fold change data analysis was performed by TRON gGmbH, using HPRT1 and TBP as reference genes. Further down-stream comparisons and interpretation was done in-house by myself.

4.2.7 Quantification of secreted proteins

Secreted proteins were quantified using an enzyme-linked immunosorbend assay (ELISA) specific for CCL5/RANTES, following the manufacture's protocol. In brief, samples were collected by removing the supernatant, where the secreted protein of interest is present, and adding 25× protease inhibitor cocktail reaching a final 1× concentration. These samples were either frozen at -20°C or used directly for ELISA analysis.
First, 100 μl of assay diluent RD1W was pipetted into each ELISA well, into which 100 μl sample, or protein standard was added. The plate was then incubated for 2 h at RT. Afterwards, the solution was aspirated and wells washed trice with 400 μl wash buffer. Second, 200 μl RANTES conjugate was added into the well and incubated for 1 h at RT. Again, the wells were washed trice with 400 μl wash buffer. To measure the colorimetric signal, 200 μl substrate solution was added into the well, incubated for 20 min at room temperature in the dark, after which 50 μl stop solution was added and the plate gently tapped to ensure thorough mixing. Using a TECAN infinite M100 microplate reader the optical density was measured at a wavelength of 450 nm, together with a corrective wavelength set to 540 nm. Values exported and a calibration curve calculated by the help of the protein standard using a four parameter logistic (4-PL) curve-fit. Using the equation of the 4-PL fit the unknown sample concentration was calculated.

4.2.8 Statistical analysis

Descriptive statistical analysis was performed using Microsoft Excel and GraphPad Prism (table 4.16). For inferential statistical data analysis the software GraphPad Prim was used. Depending on the respective performed experiment, the appropriate statistical test was chosen. Where two groups needed to be analysed a two-side Student's t-test was used. For more than two groups either a one-way or two-way ANOVA was chosen, including a post-hoc analysis for multiple comparison. Where appropriate a two-way ANOVA with repeated measurements were applied.
For all statistical tests a significance level of a p value of 0.05 was applied. Below or equal that threshold, differences were assumed to be significant and not significant (ns) with > 0.05. Further, significance levels are depicted as asterisks: $* \leq 0.05$, $** \leq 0.01$, $*** \leq 0.001$ or $**** < 0.0001$. Data depicted in figures are expressed as mean and either SD, or SEM (further defined in respective figure captions). Data included within the text is exclusive expressed as mean $\pm$ SEM.

5 Results

The following chapter is split into three parts. Part 5.1 illustrates the observed sensitizing effect by BV6 in combination with NK cells. Part 5.2 characterizes a transcriptional effect of BV6 on NF-κB signaling pathways. Part 5.3 shows the results of an exploratory RNA sequencing approach and its validation.

5.1 Sensitization by BV6 towards NK cell attack

5.1.1 BV6 induced cell death in RMS cells

As the overall project deals with the effect of the Smac mimetic BV6 on rhabdomyosarcoma cells, the first step was to assess BV6' cytotoxicity on RH30 (aRMS) and RD (eRMS) cells. Fig. 5.1 depicts the dose response curves for both cell lines. Based on the sigmoidal dose-response curve fit for the RH30 cells (fig. 5.1(a)) a EC50 (24h) value of (5.5 $\pm$ 0.2) μM and an EC50 (48h) of (4.0 $\pm$ 0.2) μM could be calculated. The same can be applied to RD cells (5.1(b)), resulting in an EC50 (24h) value of (6.5 $\pm$ 0.3) μM and an EC50 (48h) value of (6.2 $\pm$ 0.5) μM. To achieve a sensitizing and no killing effect of BV6 on both cell lines, concentrations of 2.5 μM and 5.0 μM were chosen to continue throughout the project.

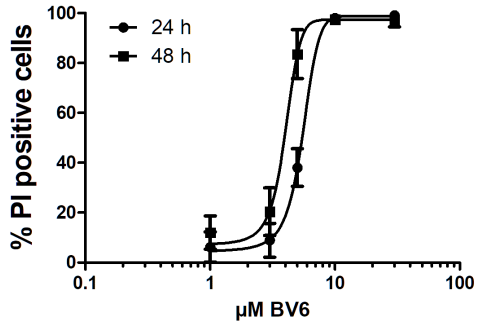

(a) Dose-response curve for RH30 cells, N = 4

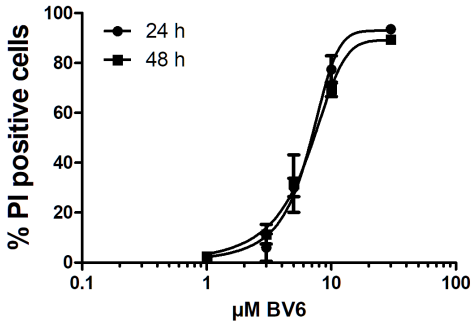

(b) Dose-response curve for RD cells, N = 3

Fig. 5.1: Dose-response curves for RH30 (a) and RD (b) cells upon BV6 treatment. Cell death was measured by PI staining as an end-point measurement at 24 and 48 h post treatment. Data is depicted as mean $\pm$ SEM

5.1.2 Induced IAP degradation

The molecular function of BV6 as a Smac mimetic is a proposed degradation of IAP proteins. 5.2 shows western blots of a kinetic BV6 treatment of RMS cells, grown in 2D monolayers.

In both, RH30 (5.2(a)) and RD (b) cells, BV6 induces a rapid cIAP1 degradation, starting after 30 min (0.5 h) of BV6 addition at 2.5 and 5 μM. After 24 h of BV6 treatment no re-expression of cIAP1 can be observed. Concerning cIAP2, it is rapidly degraded in RH30 cells after 30 min of BV6 treatment at both concentrations. After 24 h, a slight re-expression might be observable. RD cells do not express cIAP2. Survivin and XIAP are not degraded upon BV6 treatment in 2D RMS cell cultures.

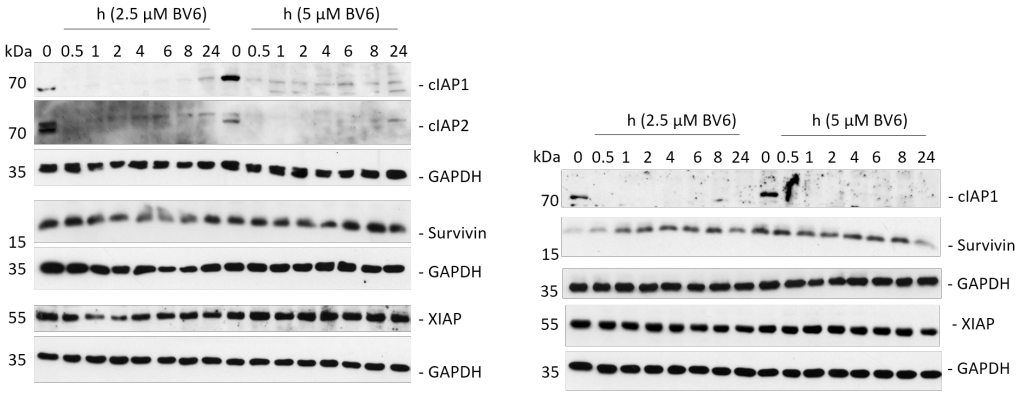

(a) Western blot of RH30 cells **(b)** Western blot of RD cells

Fig. 5.2: Western blot of BV6 treated RMS cells in 2D with 2.5 and 5 μM, identifying IAP degradation. RMS cells, cultured in 2D, were treated with BV6 for the indicated concentrations and incubation times. Images are representative of two independent western blots of different biological replicates. Membranes were re-probed after stripping (section 4.2.5.6).

Multicellular RMS spheroids, treated with BV6 for 24 h behave similar. In both, RH30 (5.3(a)) and RD (b) spheroids, cIAP1 is degraded by BV6 at 24 h treatment. In RH30 spheroids, cIAP2 degradation is not present. Here, the incubation time of 24 h might already induce re-expression, similarly to 2D treated RH30 cells. In contrast to 2D cultures, in both RH30 and RD spheroids, XIAP degradation can be observed.

BV6's ability to degrade IAP proteins is visible in both cell culture methods, with an additional degradation of XIAP in RMS spheroids.

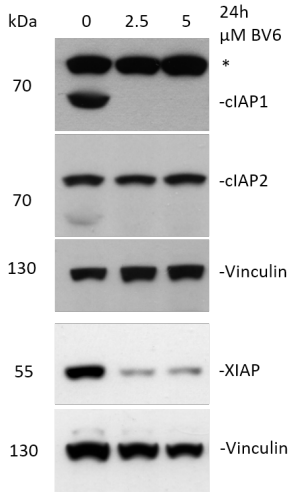

(a) Western blot of RH30 spheroids

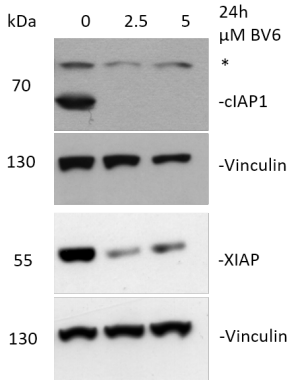

(b) Western blot of RD spheroids

Fig. 5.3: Western blot of BV6 treated RMS spheroids, identifying IAP degradation. RMS spheroids were treated with BV6 for 24 h using the indicated concentrations (2.5 & 5 μM). Images are representative of two independent western blots of different biological replicates. *: unspecific signal. Membranes were re-probed after stripping (section 4.2.5.6).

5.1.3 Sensitization of TRAIL mediated cell death

One aspect of the project is to characterize the sensitizing effect towards an NK cell mediated killing. As described in section 2.5 one killing mechanism relies on the death receptor-death ligand interaction. Following this aspect, the basal expression levels of death receptors DR4, DR5, Fas and TNFR1 were analyzed on RH30 (fig. 5.4) and RD (fig. 5.5) cells by flow cytometry.

It can be seen that RH30 cells do not present DR4 (fig. 5.4(a)) and Fas (fig. 5.4(c)) on their surface. As the fluorescence signal of the specific antibody does not shift to higher intensities compared to the isotype control. However, a minor TNFR1 surface presentation by a shift towards higher fluorescence intensities can be seen (fig. 5.4(d)). DR5 (fig. 5.4(b)) shows a very high fluorescence intensity, translating to a strong surface presentation on RH30 cells.

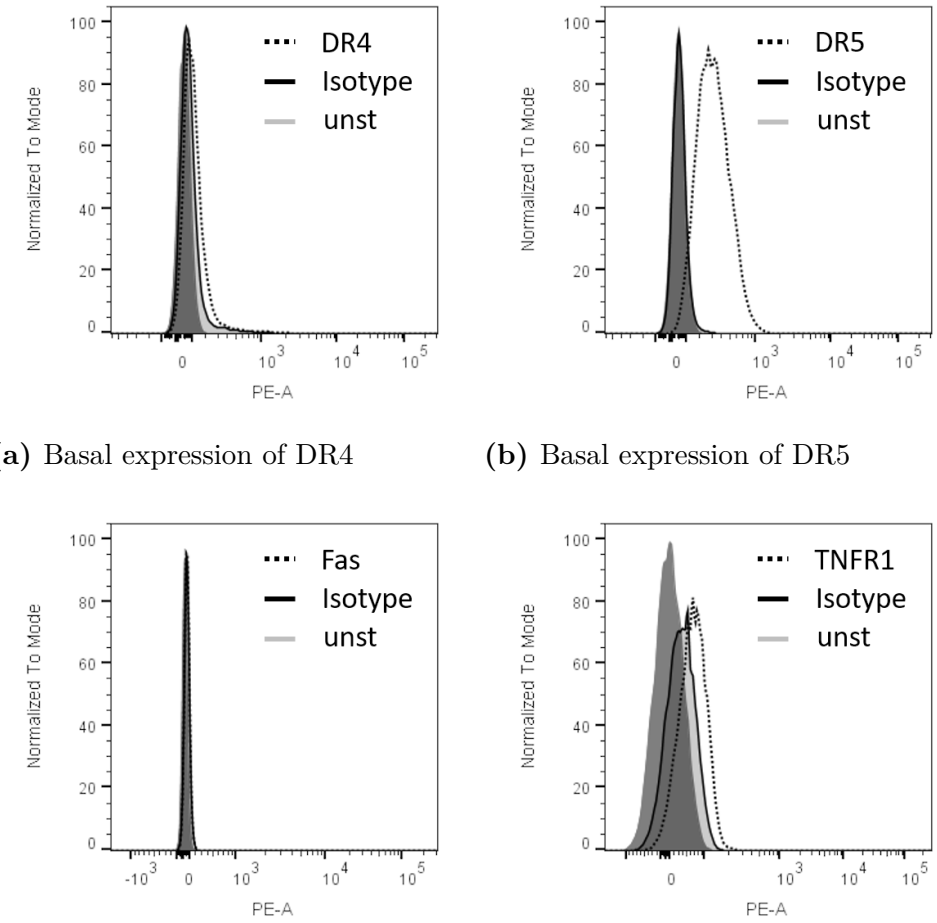

(a) Basal expression of DR4

(b) Basal expression of DR5

(c) Basal expression of Fas

(d) Basal expression of TNFR1

Fig. 5.4: Flow cytometric analysis of basal death receptor expression on RH30 cells. Images are representative of three independent flow cytometric experiments.

On RD cells (fig. 5.5) the basal expression pattern look different. Fas (fig. 5.5(c)) and TNFR1 (fig. 5.5(d)) could note be observed as surface presented by RD cells. For both, the signal of the specific antibody does not show a shift towards higher intensities, compared to the isotype control. A minor shift for DR4 is visible (fig. 5.5(a)) and very high shift for DR5 (fig. 5.5(b)).

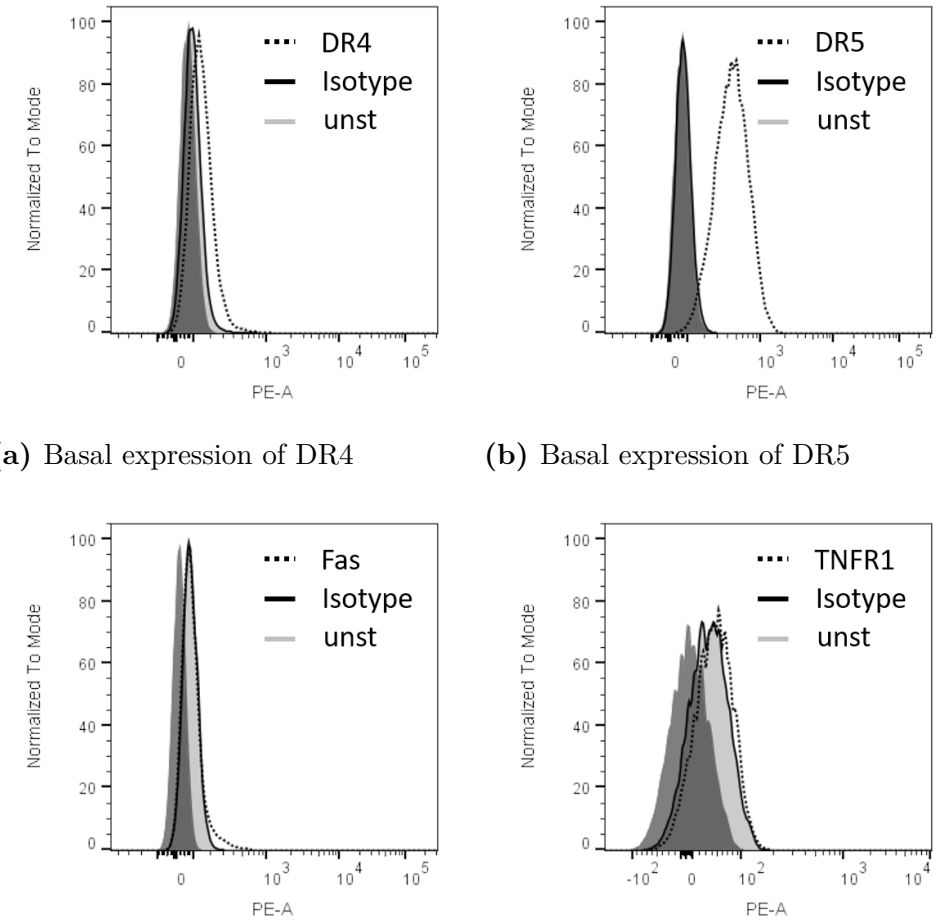

(a) Basal expression of DR4

(b) Basal expression of DR5

(c) Basal expression of Fas

(d) Basal expression of TNFR1

Fig. 5.5: Flow cytometric analysis of basal death receptor expression on RD cells. Images are representative of three independent flow cytometric experiments.

As Fas is not expressed on RH30 and RD cells, Fas is disregarded for further analysis. Fig. 5.6 shows the flow cytometric data, analyzing surface presentation of DR4, DR5 and TNFR1 on RH30 cells upon BV6 treatment. It can be seen that RH30 cells remained DR4 negative (fig. 5.6(a)). Again, the fluorescence intensity using a specific DR4 antibody, did not differ from the isotype control. Surface presentation of TNFR1 on RH30 cells remained on a similar levels upon BV6 treatment (fig. 5.6(c)) compared to untreated conditions. Nevertheless, a slight intensity shift of TNFR1 is visible, compared to isotype control. In regard to DR5, the treatment with BV6 (24 h, 5 μM) increased surface presentation, as indicated by a shift towards higher fluorescence intensities (fig. 5.6(b)).

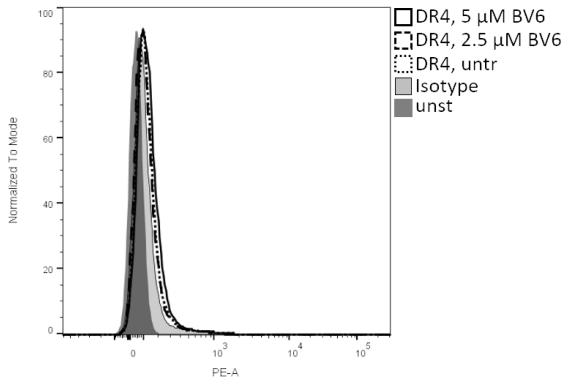

(a) DR4 expression upon BV6 treatment

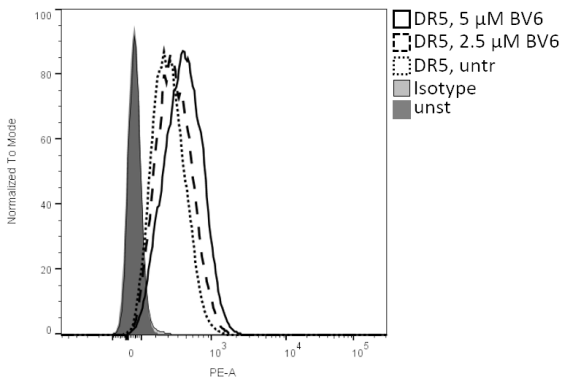

(b) DR5 expression upon BV6 treatment

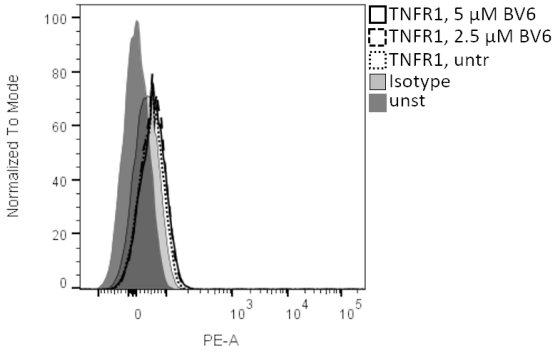

(c) TNFR1 expression upon BV6 treatment

Fig. 5.6: Flow cytometric analysis of death receptor expression on RH30 cells treated for 24 h with BV6. Grey line-saturated filled: unstained (unst) control sample, black line-tinted filling: isotype control, dotted line-not filled: DR specific staining untreated sample, dashed line-not filled: DR specific staining treated with 2.5 μM BV6, solid line-not filled: DR specific staining treated with 5 μM BV6. Images are representative of three independent flow cytometric experiments.

Fig. 5.7(a) depicts the surface presentation of DR4 on RD cells, which is not changed upon BV6 treatment. The fluorescence intensities remained on a similar level upon BV6 treatment, but differ from the isotype control. Similarly to RH30 cells, RD cells increased DR5 surface presentation upon BV6 treatment (5.7(b)). Compared to untreated RD cells, the fluorescence intensity of BV6 treated RD cells (24 h, 5 μM) shifted to higher intensity values. Fig. 5.7(c) shows that RD cells stay TNFR1 negative, even after BV6 treatment. As the staining with a specific antibody targeting TNFR1 does not increase the fluorescence intensity, compared to isotype staining.

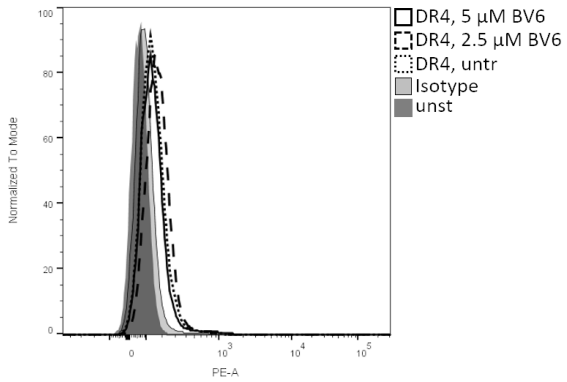

(a) DR4 expression upon BV6 treatment

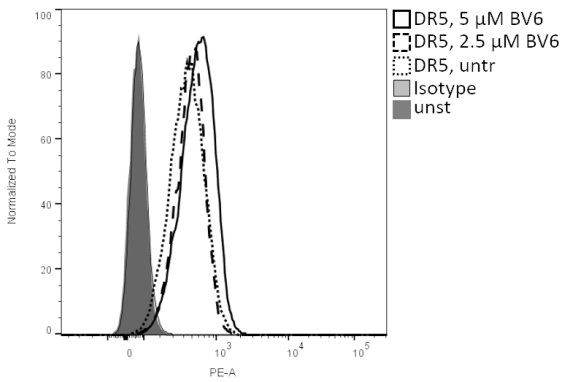

(b) DR5 expression upon BV6 treatment

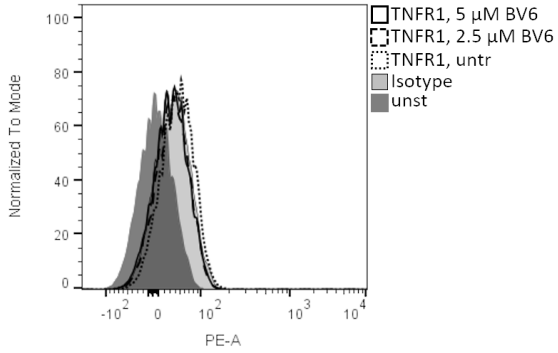

(c) TNFR1 expression upon BV6 treatment

Fig. 5.7: Flow cytometric analysis of death receptor expression in RD cells treated for 24 h with BV6. Grey line-saturated filled: unstained (unst) control sample, black line-tinted filling: isotype control, dotted line-not filled: DR specific staining untreated sample, dashed line-not filled: DR specific staining treated with 2.5 μM BV6, solid line-not filled: DR specific staining treated with 5 μM BV6. Images are representative of three independent flow cytometric experiments.

The increased surface presentation of DR5 on RH30 cells, as shown in fig. 5.6(b), was further validated using qRT-PCR and western blot. Only DR5 was further analyzed in RH30 cells, as DR4 is not being expressed. First, fig. 5.8(a) shows the mRNA fold change of *DR5* upon a time dependent BV6 stimulation, using untreated RH30 cells as a reference. Over time, an increased transcription using both BV6 concentrations can be seen. Between 4 to 8 h, a plateau was reached, seemingly decreasing at 24 h of BV6 stimulation. This increased mRNA fold change, is followed by an increased DR5 protein translation. DR5 protein content in whole cell lysates can be seen in fig. 5.8(b). DR5 shows a double band, as the antibody might detect the short and long isoform of DR5. The western blot depicts an increased protein expression, for 5 μM BV6 treatment beginning at 6 h, indicated by an increased chemiluminescence signal. DR5 signals for

both stimulations using 2.5 and 5 μM concentrations are reaching a maximum at 24 h. By that, the protein expression in fig. 5.8(b) follows the induced mRNA transcription in fig. 5.8(a), which might led to the increased surface presentation on RH30 cells (fig. 5.6(b)).

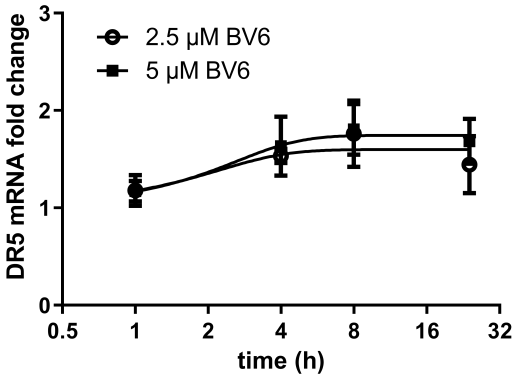

(a) qRT-PCR analysis of BV6 induced *DR5* transcription in RH30 cells

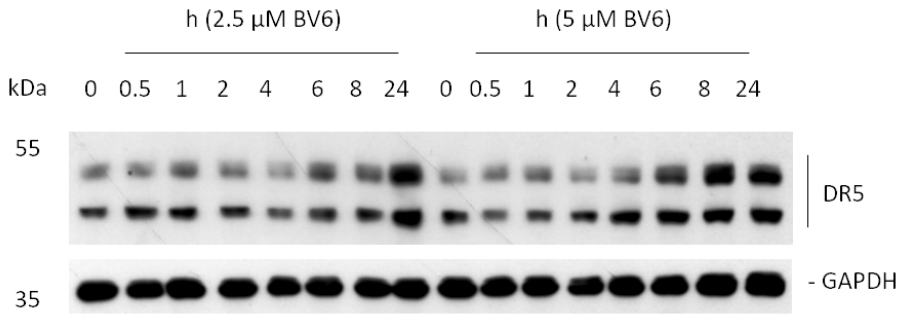

(b) Western blot analysis of DR5 in RH30 cells treated with BV6

Fig. 5.8: qRT-PCR (a) and western blot (b) analysis of DR5 in RH30 cells. Expression was normalized to untreated RH30 cells. Treatment was performed for the indicated time points and concentrations of BV6. Data is depicted as mean $\pm$ SEM, N = 3. Western blot images are representative of two independent experiments of different biological replicates.

The transcriptional regulation of DR4 and DR5 also applies to RD cells. Fig. 5.9(a) shows the mRNA fold change of *DR4* and fig. 5.9(b) the mRNA fold change of *DR5*, using untreated RD cells as reference. Both target genes (*DR4* & *DR5*), only showed an increased transcription using 5 μM BV6. Regarding the kinetic, for *DR4* (fig. 5.9(a)) the highest mRNA fold change is reached at 24 h. For *DR5* (fig. 5.9(b)), the onset started at approximately 8 h of BV6 stimulation and reached a maximum at 24 h.
The transcriptional up-regulation of *DR4* and *DR5* in RD might be translated into the previous described increased surface presentation (fig. 5.7(a) & fig. 5.7(b)).

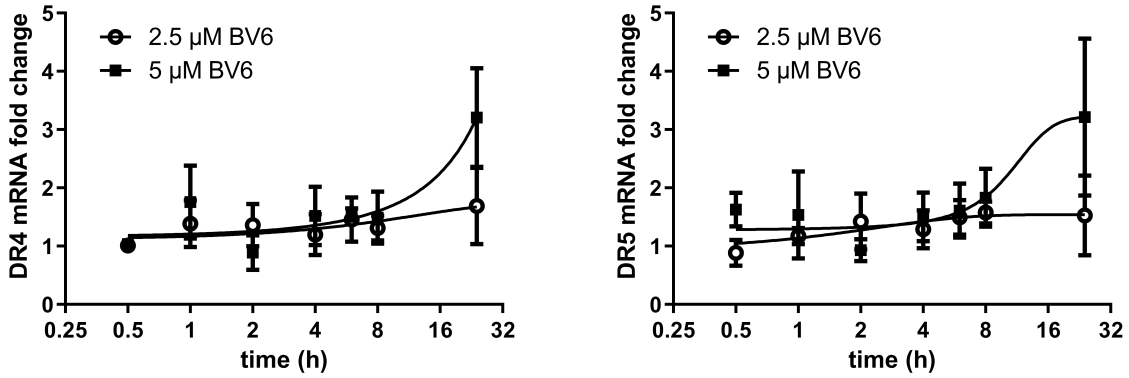

(a) BV6 induced *DR4* transcription in RD cells **(b)** BV6 induced *DR5* transcription in RD cells

Fig. 5.9: Relative mRNA quantification of *DR4* (a) and *DR5* (b) by qRT-PCR in RD cells. Expression was normalized to untreated RD cells. Treatment was performed for the indicated time and concentration of BV6. Data is depicted as mean ± SEM, N = 3.

Functionally, 24 treatment with BV6 induced a sensitization towards a TRAIL induced cell death. Fig. 5.10 depicts the cell death analysis of RH30 (fig. 5.10(a)) and RD (fig. 5.10(b)) cells, measured by PI uptake upon co-treatment with BV6 and TRAIL. In both cell lines, cell death is induced upon single treatment with 5 μM BV6 at 24 h. Treatment with TRAIL (100 ng/ml) alone induces cell death to a lesser extend at 24 h, compared to BV6 alone in both cell lines. Combined TRAIL and BV6 treatment, showed a significant additive effect for 5 μM BV6 in both RH30 and RD cells. For the lower 2.5 μM BV6 concentration, this effect seems to be highly additive only in RH30 cells (not tested for synergy).

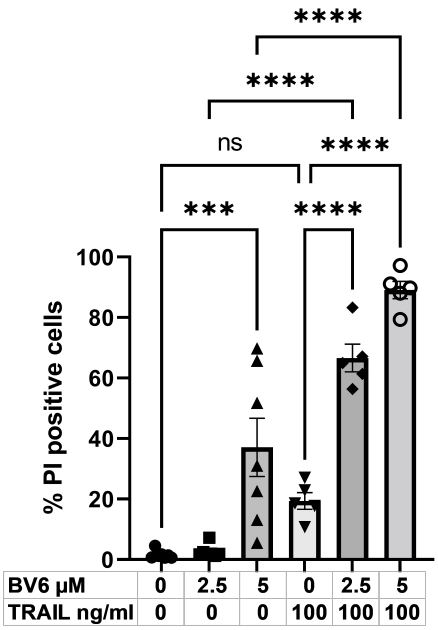

(a) Cell death analysis of RH30 cells co-treated with BV6 and TRAIL, N = 7

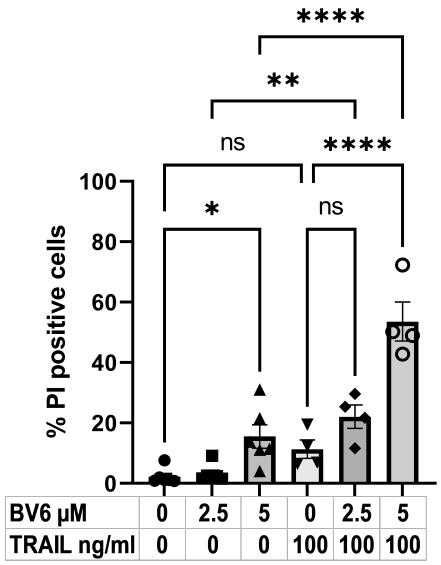

(b) Cell death analysis of RD cells co-treated with BV6 and TRAIL, N = 6

Fig. 5.10: Cell death measurement of RH30 (a) and RD (b) cells co-treated with BV6 and TRAIL for 24 h. Concentrations of BV6 and TRAIL are indicated within the figure. Dead cells were identified by PI positive staining and counterstained with Hoechst33342. Data is depicted as mean ± SEM. ns: $p > 0.05$, *: $p \leq 0.05$, **: $p \leq 0.01$, ***: $p \leq 0.001$, ****: $p < 0.0001$.

5.1.4 Sensitization towards NK cell mediated cytotoxicity

As previous stated, the project's objective is to elucidate the molecular mechanisms of a BV6 sensitization towards NK cell mediated killing. For that, the cytotoxic effect of BV6 on NK cells needed to be tested. Figure 5.11 depicts the dose-response curve of BV6 treated NK cells at different concentrations for 24 h. The uptake of PI was chosen as a cell death indicator. It can be seen that with increasing concentrations, higher percentage of NK cells appear to be dead. At the highest used concentration of 20 μM BV6, up to (31 ± 5.0) % cells died. Throughout the project, BV6 was used at concentrations of 2.5 μM and 5 μM. At those concentrations, NK cells show a cell death induction of (7.3 ± 1.7) % and (12 ± 2.6) %, respectively. With that, the cell death of NK cells was within an acceptable level for further co-cultivation and co-treatment experiments.

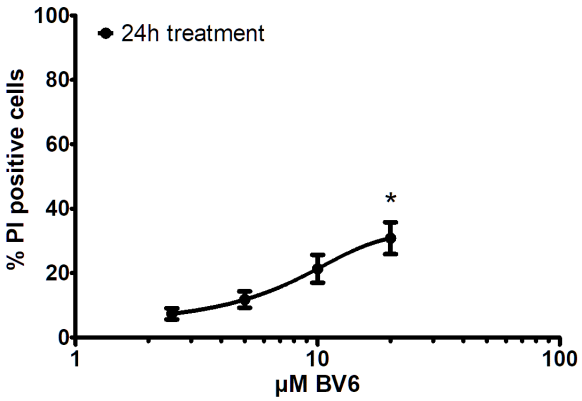

Fig. 5.11: Dose-response curve of BV6 treated primary expanded, IL-15 activated NK cells. Data is depicted as mean ± SEM, N = 9. *: $p \leq 0.05$

After subtoxic concentrations of BV6 (figure 5.1 & 5.11) were established, co-culture experiments of RMS cells and NK cells followed.
RMS cells, grown in 2D monolayers, were pre-treated with 5 μM BV6 for 24 h. After BV6 was removed, pre-treated RMS cells were co-cultured for 4 h together with NK cells at an effector to target (E:T) ratio of 5:1. Figure 5.12 illustrates the specific lysis, i.e. the NK cell derived killing (see equation 4.1) towards RMS cells. It can be seen that in 2D co-culture experiments, untreated RH30 cells are killed with a higher specific lysis (48.0 ± 5.1) %, than are untreated RD cells (12.1 ± 3.9) %. Pre-treatment with BV6 resulted in a sensitization of both RH30 and RD cells towards an NK cell attack. Resulting in a higher killing effect from NK cells. The specific lysis towards BV6 pre-treated RH30 cells increased to (67.3 ± 4.2) %, with a p-value of 0.0057 compared to untreated RH30 cells. The specific lysis towards BV6 pre-treated RD cells increased to (39.4 ± 10.8) %, with a p value of 0.0895 compared to untreated RD cells. Although non-significant, NK cell killing of RD cells ± BV6 resulted in a higher difference with $\Delta = 27.3$ %, than for RH30 cells $\Delta = 19.3$ %.

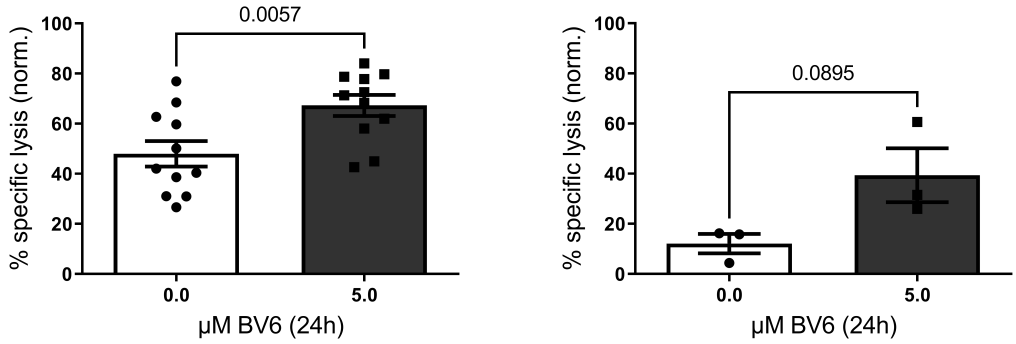

(a) BV6 pre-treated RH30 cells in 2D co-cultured with NK cells, N = 11

(b) BV6 pre-treated RD cells in 2D co-cultured with NK cells, N = 3

Fig. 5.12: NK cell cytotoxicity measurement in co-culture with BV6 pre-treated RMS cells. NK cell cytotoxicity is measured by FACS based method (see section 4.2.3.1) with an E:T ratio of 5:1. RMS cell were pre-treated for 24 h with BV6. Data is depicted as mean ± SEM, and analysed by Student's t-test.

The co-culture experiments in figure 5.12 were performed in a 2D culture setting (according to method 4.2.3.1). However, rhabdomyosarcoma is a solid growing tumour entity. For a better representation of the solid nature, a culture method in 3D was chosen (see method 4.2.1.5). Figure 5.13 shows the co-cultivation of GFP expressing RMS spheroids ± BV6 with or without NK cells. The experimental setting how this 3D co-culture was performed is depicted in figure 4.1 (page 41).

Over the observation period, untreated RH30-GFP spheroids form a heterogenous 3-dimensional structure with a rim high in fluorescence intensity, correlating to a putative high proliferative area (subfigure 5.13(a)). Pre-treatment with BV6 alone does not induce a phenotypic change, rather a slight growth retention, as the highly fluorescent rim developed at later time points. Co-cultivation with NK cells alone does induce a phenotypic change. It seems, as if the spheroid is braking apart, still being able to form smaller microspheres. Overall, no significant loss of GFP intensity could be detected, as shown in subfigure 5.13(b). Phenotypically, combination of BV6 pre-treatment with NK cell co-cultivation led to a perforation of the spheroid, no formation of a proliferative rim is visible and reduction of microspheres. The phenotypic loss of spheroid integrity is also evident in the GFP intensity quantification. It shows a significant reduction (5.13(b)).

In contrast to the heterogenous RH30-GFP spheroid morphology, RD-GFP cells form highly homogenous, compact, ball-like spheres (subfigure 5.13(c)). In contrast to the RH30-GFP spheroids, where NK cells attack more perforative, RD-GFP spheroids are seemingly attacked from outside inwards. Quantification of the GFP intensity confirm, that the BV6 pre-treatment alone did not change alter the spheroidic growth. On the

other hand, NK cell addition alone induces a growth control, as the intensity is not increasing over the observation period. Again, combining BV6 pre-treatment with NK cell co-cultivation led to a significant reduction in spheroid size and GFP intensity, indicating a combinatory effect towards spheroid killing.

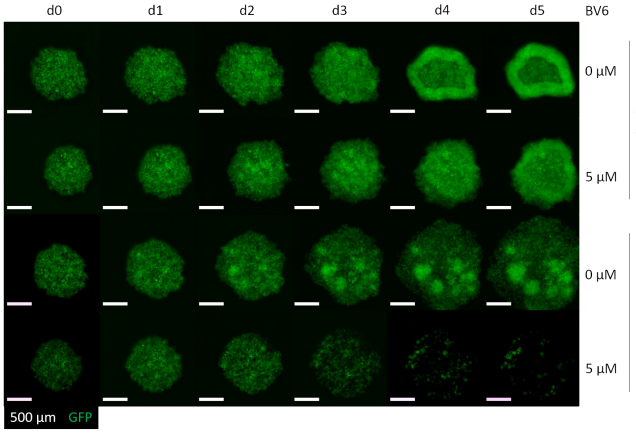

(a) Images of the observation period of 5 days of BV6 pre-treated RH30-GFP spheroids co-cultured with NK cells

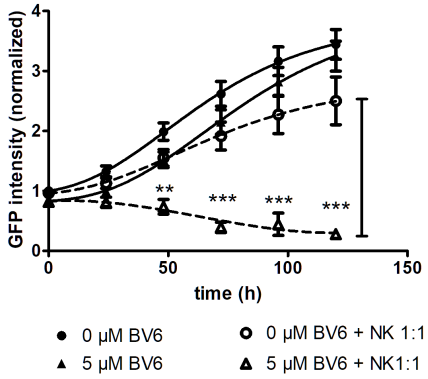

(b) Quantification of GFP fluorescence intensities of RH30-GFP spheroids

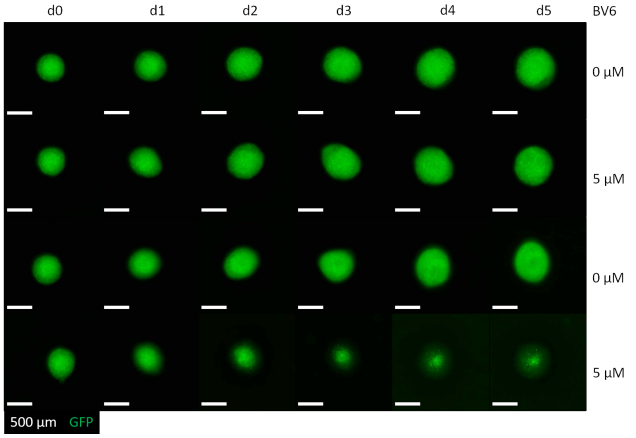

(c) Images of the observation period of 5 days of BV6 pre-treated RD-GFP spheroids co-cultured with NK cells

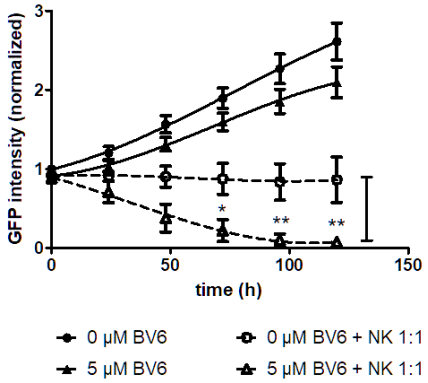

(d) Quantification of GFP fluorescence intensities of RD-GFP spheroids

Fig. 5.13: BV6 pre-treated RMS-GFP spheroids co-cultivated with NK cells. On day 3 of spheroid growth treatment with BV6 for 24 h was performed. NK cells in an E:T ratio of 1:1 were co-cultivated with RMS-GFP spheroids for 5 days. GFP fluorescence intensity was measured every day. Data is depicted as mean ± SEM, N = 5 and analyzed by two-way ANOVA, *: $p \leq 0.05$, **: $p \leq 0.01$, ***: $p \leq 0.001$.

As another measurement of cell death in RMS-GFP spheroids, dead cell were stained with PI at the last day of co-cultivation. Figures 5.14(a) & 5.14(c) depicts the overlay of GFP and PI signal of RMS-GFP spheroids on day 5. Again, combining BV6 pre-

treatment with NK cells increased cell death induction, visible by an increased overall PI signal intensity. All the characteristics described previously can be observed. Using both fluorescence channel intensity quantifications, a PI to GFP fluorescence intensity ratio could be calculated, as indicator for cell death induction.
Figures 5.14(b) & 5.14(d) illustrate the PI/GFP ratios of NK cell co-cultivations at different E:T ratios. For RH30-GFP spheroids the BV6 sensitizing effect is only visible using an E:T ratio of 1:1. As expected, higher NK cell E:T ratios led to a higher RH30-GFP spheroid killing, i.e. higher PI/GFP ratios.
For RD-GFP spheroids, the BV6 sensitizing effect is visible using all three E:T ratios. Again, higher E:T ratios leads to higher RD-GFP spheroid killing and higher PI/GFP ratios. The biggest BV6 sensitizing effect is visible at an E:T ratio of 1:1. For that reason, an E:T ratio of 1:1 was chosen throughout the project.

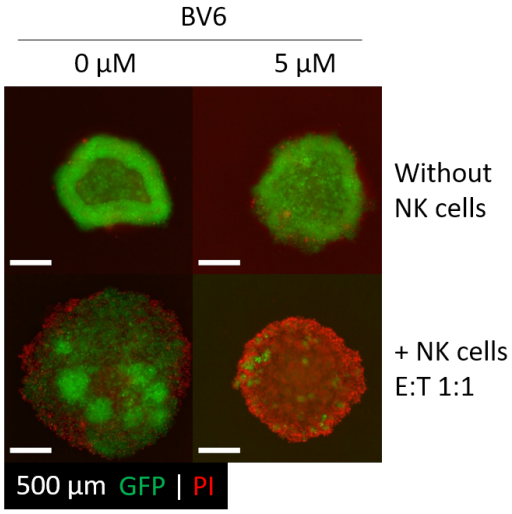

(a) Microscopic illustrations of RH30-GFP (alive) and PI (dead) fluorescent cells/spheroids

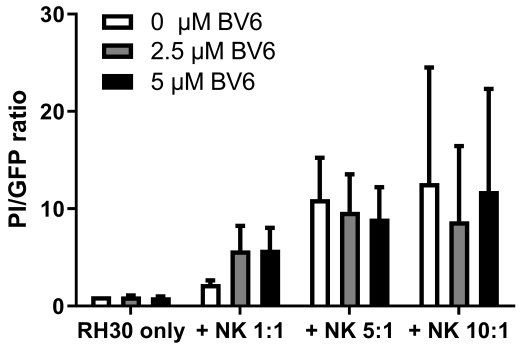

(b) Quantification and calculation of PI to GFP fluorescence ratios in BV6 pre-treated RH30-GFP spheroids co-cultured with NK cells. N = 4

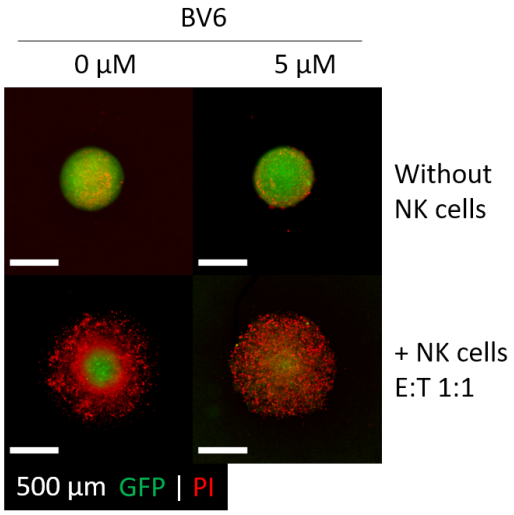

(c) Microscopic illustrations of RD-GFP (alive) and PI (dead) fluorescent cells/spheroids

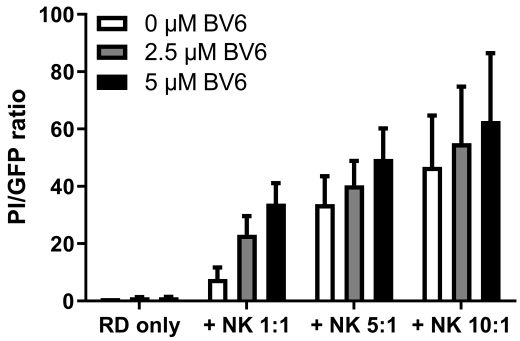

(d) Quantification and calculation of PI to GFP fluorescence ratios in BV6 pre-treated RD-GFP spheroids co-cultured with NK cells. N = 6

Fig. 5.14: Depiction of BV6 pre-treated RMS-GFP spheroid killing by NK cells at different E:T ratios. Figures (a) and (c) depict the GFP fluorescence of alive RMS cells with PI counterstained dead cells at day 5 post NK cell addition. Figures (b) and (d) illustrates the quantification and ratio calculation of PI to GFP fluorescence intensity. Data is depicted as mean + SEM.

5.1.4.1 TRAIL dependency

TRAIL, as a cell death inducing ligand on the surface of NK cells is one mechanism how cytotoxic effector cells induce target cell killing. In section 5.1.3 it was shown that co-treatment of BV6 with TRAIL had an additive effect on cell death induction.
Figure 5.15 depicts the role of TRAIL within RMS-GFP spheroid NK cell co-cultivation. First, in both, RH30-GFP (a) & (b) and RD-GFP (c) & (d) spheroids the BV6 induced sensitization towards an NK cell mediated killing could be reproduced in this experiment again.
However, co-treatment with an antibody targeting TRAIL (αTRAIL) during the co-cultivation of RMS-GFP spheroids and NK cells, did not affect the NK cell mediated killing, as no change at the PI/GFP ratio is visible upon αTRAIL co-treatment. Examination by fluorescence microscopy did not show a changed phenotype compared to the samples without αTRAIL co-treatment.

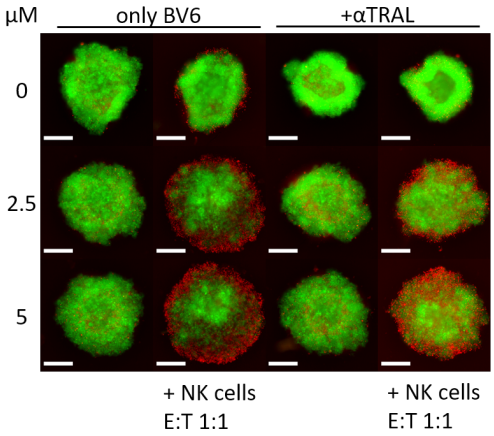

(a) Microscopic illustrations of RH30-GFP (alive) and PI (dead) fluorescent cells/spheroids. Scale bar = 500 μm

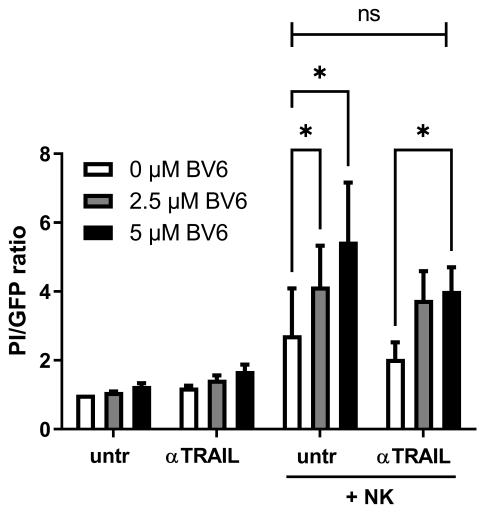

(b) Quantification and calculations of PI to GFP fluorescence ratio in BV6 pre-treated RH30-GFP spheroids co-cultured with NK cells and co-treated with αTRAIL antibody

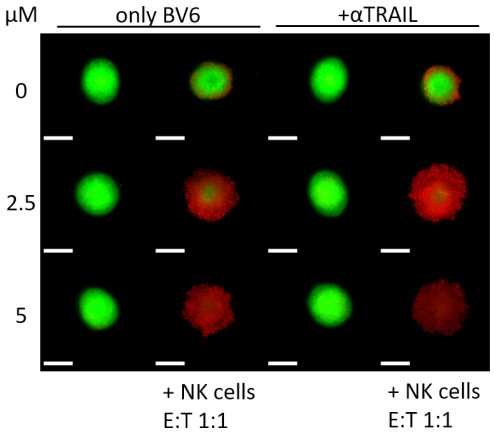

(c) Microscopic illustrations of RD-GFP (alive) and PI (dead) fluorescent cells/spheroids. Scale bar = 500 μm

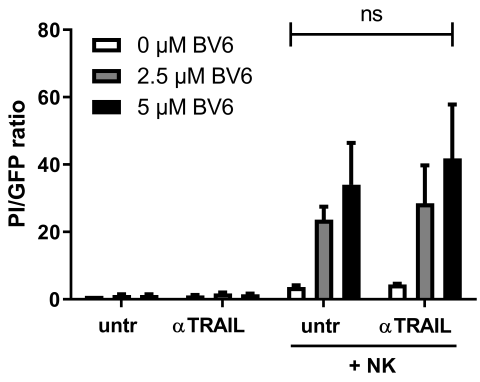

(d) Quantification and calculations of PI to GFP fluorescence ratio in BV6 pre-treated RD-GFP spheroids co-cultured with NK cells and co-treated with αTRAIL antibody

Fig. 5.15: Influence of TRAIL neutralization on BV6 pre-treated RMS-GFP spheroids in co-culture with NK cells (E:T 1:1). Figures (a) and (c) depict the GFP fluorescence of alive RMS cells/spheroids with PI counterstained dead cells. Figures (b) and (d) illustrates the quantification and calculation of PI to GFP fluorescence intensity ratio. Data is depicted as mean + SEM, N = 3 and analyzed by two-way ANOVA, *: $p \leq 0.05$.

The neutralizing effect of the used αTRAIL antibody at the used concentration was validated by co-treatment of RMS-GFP spheroids with exogenous TRAIL (100 ng/ml) and can be seen in fig. 5.16. Treatment with TRAIL induced cell death in RMS-GFP spheroids, indicated by an increased PI/GFP ratio. This TRAIL induced cell death could be blocked by addition of the αTRAIL antibody (1 μg/ml), indicated by the reduction of PI/GFP ratio to the untreated RMS-GFP spheroid level.

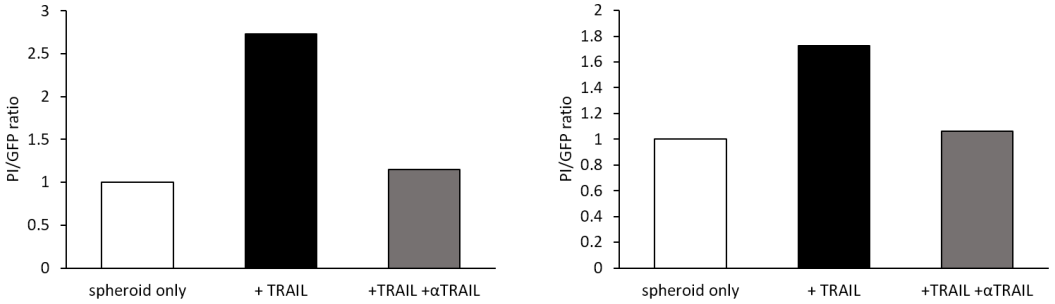

(a) RH30 spheroids treated with TRAIL and together with αTRAIL antibody

(b) RD spheroids treated with TRAIL and together with αTRAIL antibody

Fig. 5.16: Validation of zVAD.fmk within RMS spheroids upon exogenous TRAIL treatment. Treatment was performed for 24 h, with a TRAIL concentration of 100 ng/ml and an αTRAIL antibody concentration of 1 μg/ml. Data of one biological replicate. Control samples of only spheroid and exogenous TRAIL treatment are shared in fig. 5.16 and fig. 5.22.

5.1.4.2 TNFα dependency

Apart from TRAIL, as a cell death inducing ligand, TNFα can activate the extrinsic apoptosis by TNFR1 ligation. Figure 5.17 depicts BV6 pre-treated RMS-GFP spheroids co-cultivated with NK cells for a duration of 5 day with an endpoint PI measurement. Here, Enbrel, as an TNFα neutralizing compound, was added as a co-treatment starting at the BV6 pre-treatment and continued during the NK cell co-cultivation period.
Again, pre-treatment with BV6 could successfully sensitize both RH30-GFP (a) & (b) and RD-GFP (c) & (d) spheroids towards an NK cell mediated killing, indicated by an increased PI positive edge around the spheroids and an increased PI/GFP ratio. In the presence of Enbrel, RMS-GFP spheroids are not rescued from the NK cell attack, evident by a lost spheroidic integrity (RH30-GFP (a) & RD-GFP (c) spheroids) and unchanged PI/GFP ratio compared to the samples without Enbrel.
Although the PI endpoint measurement did not show any change, Enbrel might have an impact on a time dependent level. Figures 5.17(e) & (f) illustrates a kinetic GFP fluorescence intensity measurement of the RMS-GFP spheroids. Again, RH30-GFP (e) spheroids co-treated with Enbrel (dotted lines) did not alter the NK cell mediated attack.

However, a slight rescue effect from the NK cell attack might be present at Enbrel co-treated BV6 pre-treated RD-GFP (f) spheroids. This change is not significant, only a slight upwards trend of the Enbrel treated curves (dotted lines) might be apparent.

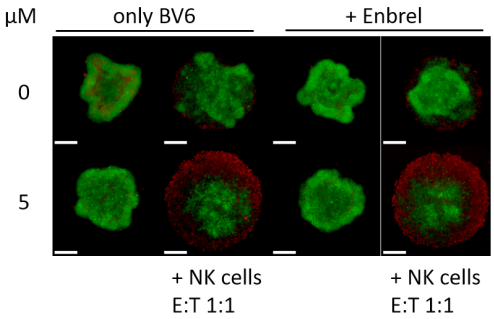

(a) Microscopic illustrations of RH30-GFP (alive) and PI (dead) fluorescent cells/spheroids. Scale bar = 500 μm

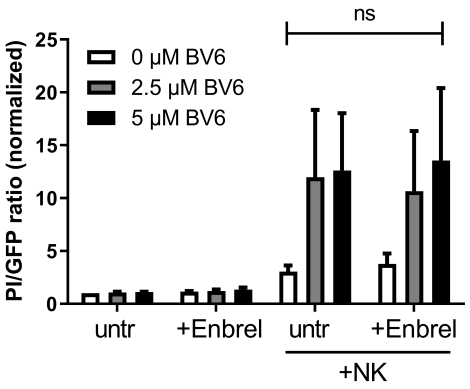

(b) Quantification and calculations of PI to GFP fluorescence ratio in BV6 pre-treated RH30-GFP spheroids co-cultured with NK cells and co-treated with Enbrel, N = 3

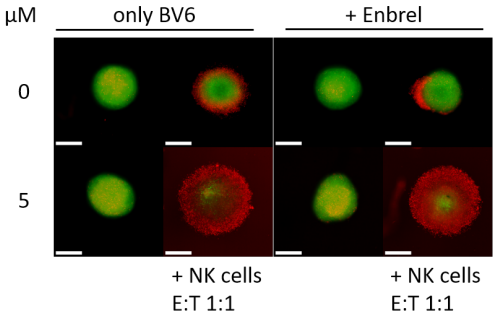

(c) Microscopic illustrations of RD-GFP (alive) and PI (dead) fluorescent cells/spheroids. Scale bar = 500 μm

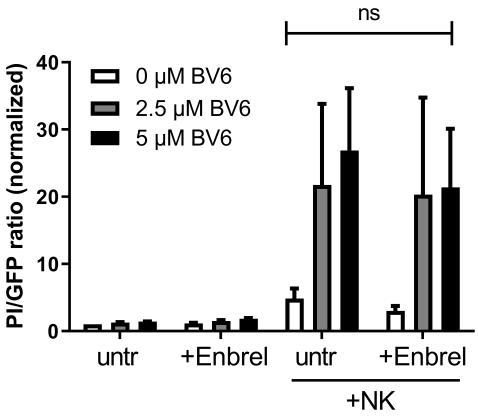

(d) Quantification and calculations of PI to GFP fluorescence ratio in BV6 pre-treated RD-GFP spheroids co-cultured with NK cells and co-treated with Enbrel, N = 3

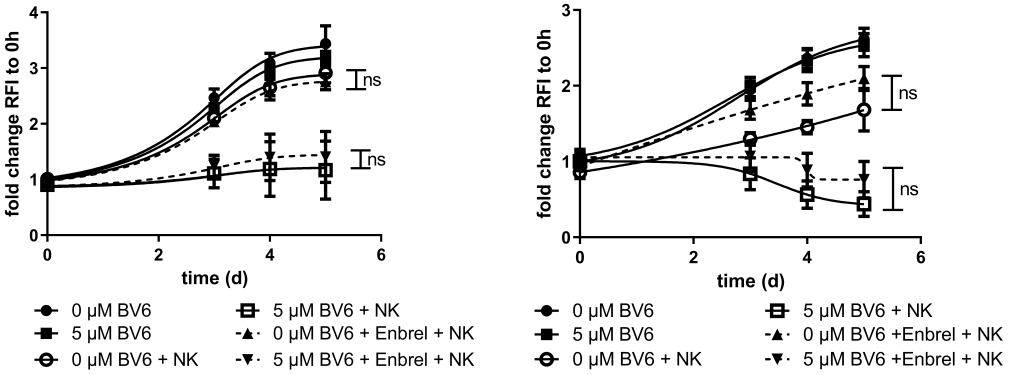

(e) Kinetic depiction of BV6 pre-treated RH30-GFP spheroids co-cultured with NK cells, continuously co-treated with Enbrel, N = 4

(f) Kinetic depiction of BV6 pre-treated RD-GFP spheroids co-cultured with NK cells, continuously co-treated with Enbrel, N = 4

Fig. 5.17: Influence of TNFα neutralization on BV6 pre-treated RMS-GFP spheroids in co-culture with NK cells (E:T 1:1). Figures (a) and (c) depict the GFP fluorescence of alive RMS cells/spheroids with PI counterstained dead cells. Figures (b) and (d) illustrates the quantification and calculation of PI to GFP fluorescence intensity ratio as a read-out for cell death induction within RMS spheroids. A kinetic measurement of GFP fluorescence over time is depicted in fig. (e) and (f). Data is depicted as mean ± SEM and analyzed by two-way ANOVA.

5.1.4.3 Granzyme B dependency

Another killing mechanism deployed by NK cells is the release of cytotoxic granules, containing granzymes (see section 2.5). Blocking granzyme B using zAAD-CMK within the NK cell co-culture of RMS-GFP spheroids should reduce the NK cell mediated killing. Figure 5.18 depicts the results of the granzyme B inhibition within RH30-GFP (a), (b) & (e) and RD-GFP (c), (d) & (f) spheroids co-cultured with NK cells. Again, the BV6 induced sensitization towards an NK cell mediated attack could be reproduced. Evident by the increased PI positive edge around RMS-GFP spheroids (a) & (c) and increased PI/GFP ratios (b) & (d).

Treatment with two concentrations of zAAD-CMK did not significantly change the NK cell killing, indicated by an equal level of PI/GFP ratios compared to untreated RMS-GFP spheroids (b) & (d). In contrast to RD-GFP (c) spheroids, RH30-GFP (a) spheroids co-cultured with NK cells show a slightly different morphology when co-treated with zAAD-CMK. Here, it seems that the spheroidic integrity is marginal retained. Although not significant, this retention is also visible by a time dependent observation of RH30-GFP (e) spheroids co-cultured with NK cells and co-treated with zAAD-CMK (dotted lines). RD-GFP (f) spheroids co-treated with zAAD-CMK show a

slight delay of NK cell killing, compared to only BV6 pre-treated, NK cell co-cultured samples.

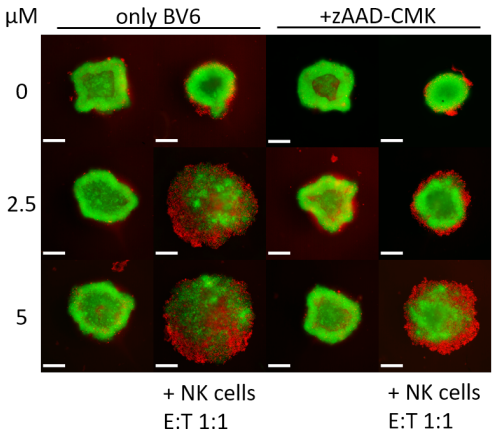

(a) Microscopic illustration of RH30-GFP (alive) and PI (dead) fluorescent cells/spheroids. Scale bar = 500 μm

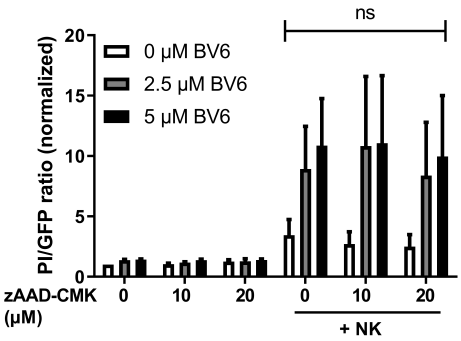

(b) Quantification and ratio calculation of PI to GFP fluorescence in BV6 pre-treated RH30-GFP spheroids co-cultured with NK cells and co-treated with zAAD-CMK, N = 4

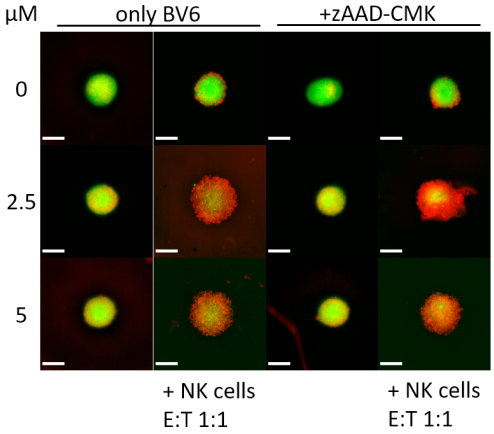

(c) Microscopic illustration of RD-GFP (alive) and PI (dead) fluorescent cells/spheroids. Scale bar = 500 μm

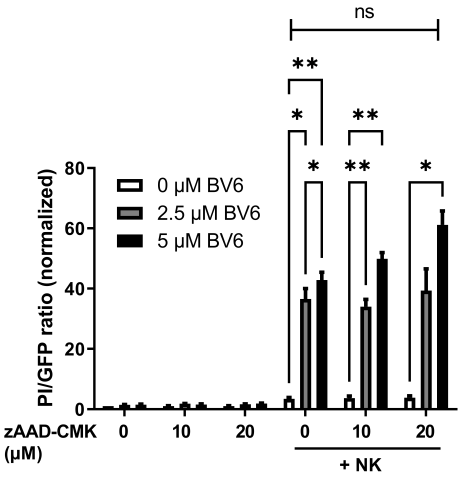

(d) Quantification and ratio calculation of PI to GFP fluorescence in BV6 pre-treated RD-GFP spheroids co-cultured with NK cells and co-treated with zAAD-CMK, N = 3

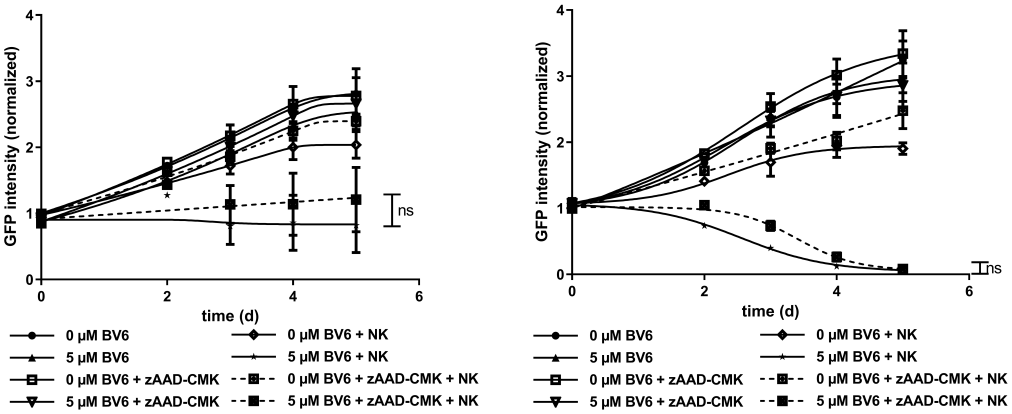

(e) Kinetic depiction of BV6 pre-treated RH30-GFP spheroids co-cultured with NK cells, continuously co-treated with zAAD-CMK, N = 4

(f) Kinetic depiction of BV6 pre-treated RD-GFP spheroids co-cultured with NK cells, continuously co-treated with zAAD-CMK, N = 3

Fig. 5.18: Influence of a granzyme B inhibitor (zAAD-CMK) on BV6 pre-treated RMS-GFP spheroids in co-culture with NK cells (E:T 1:1). Figures (a) and (c) depict the GFP fluorescence of alive RMS cells/spheroids with PI counter-stained dead cells. Figures (b) and (d) illustrates the quantification and ratio calculation of PI to GFP fluorescence intensity. A kinetic measurement of GFP fluorescence over time is depicted in fig. (e) and (f). If not shown otherwise, a concentration of 20 μM of zAAD-CMK was used. Data is depicted as mean ± SEM and analyzed by two-way ANOVA, *: $p \leq 0.05$, **: $p \leq 0.01$, ***: $p \leq 0.001$.

5.1.4.4 Caspase dependency

For a mechanistic understanding of the BV6 pre-treatment and induced sensitizing effect, the caspase activation was evaluated by western blot in RMS cells (2D) (fig. 5.19). Figures 5.19(a) and (c) depicts western blots probed against caspase-8 and 9 at different time points. After 24 h of BV6 treatment RH30 cells (a) show a signal for a cleaved, putative active form for caspase-8, and a less intense signal for the cleaved, active form of caspase-9. Whereas, RD cells (c) show no signal for the cleaved, active form of caspase-8 and a similar cleaved, active signal for caspase-9.

Western blots probed against caspase-3 are depicted in the figures 5.19(b) and (d). For RH30 cells (b), a cleaved, active caspase-3 fragment is visible after 24 h of BV6 treatment. For RD cells (d), a cleaved, active caspase-3 fragment is only visible upon a long exposure of the film. Here, a signal of the cleaved, active form starts to become visible after 6-8 h of BV6 treatment.

Overall, after 24 h of BV6 treatment, active forms of caspase-8, 9 and 3 are visible in both, RH30 and RD cells.

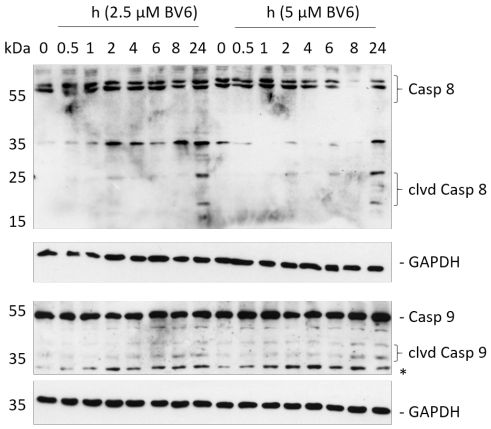

(a) RH30 cells treated with BV6, western blot probed against caspase-8 and caspase-9

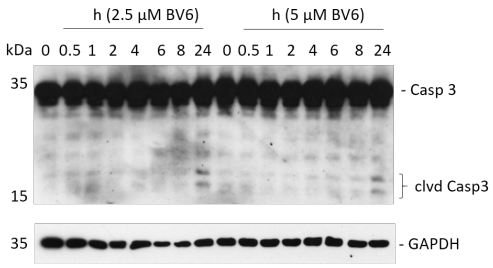

(b) RH30 cells treated with BV6, western blot probed against caspase-3

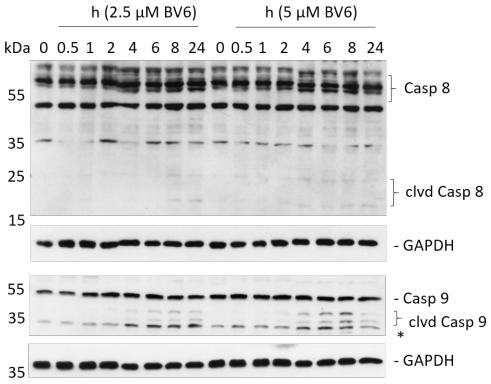

(c) RD cells treated with BV6, western blot probed against caspase-8 and caspase-9

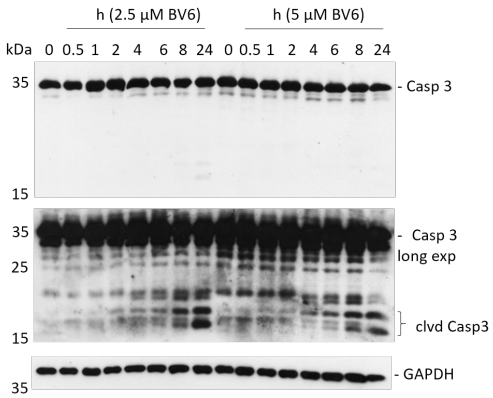

(d) RD cells treated with BV6, western blot probed against caspase-3

Fig. 5.19: Western blot of BV6 treated RMS cells in 2D, identifying caspase activation. RMS cells, cultured in 2D, were treated for the indicated concentrations and time with BV6. Images are representative of two independent western blots of different biological replicates. *: unspecific signal

Following the caspase activation upon single BV6 treatment, figure 5.20 illustrates caspase activation patterns of BV6 pre-treated (24 h) RMS spheroids co-cultivated with NK cells for further 24 h. In both, RH30 (a) and RD (c) spheroids no cleaved, active form (< 25 kDa) of caspase-8 is visible. Upon co-cultivation with NK cells, an intermediate ($\approx$ 40-45 kDa) pro-form of caspase-8 is detectable, with a reduced signal of this intermediate pro-form upon BV6 pre-treatment combined with NK cells.
Figures (b) and (d) depicts western blots of RH30 and RD spheroids probed against caspase-3. Again, no cleaved, activated form is visible within the single BV6 pre-treated samples. Whereas, NK cell co-cultivation resulted in the characteristic cleaved, active

caspase-3 pattern. Combination of BV6 pre-treatment with NK cell co-cultivation resulted in an increased signal of the lower cleavage fragment with a molecular weight of $\approx 15\,\mathrm{kDa}$.

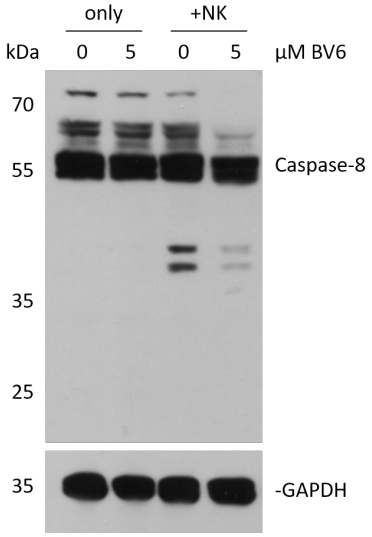

(a) Co-lysates of BV6 treated RH30 spheroids together with NK cells, western blot probed against caspase-8

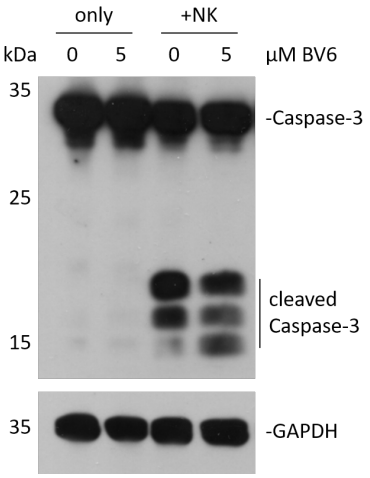

(b) Co-lysates of BV6 treated RH30 spheroids together with NK cells, western blot probed against caspase-3

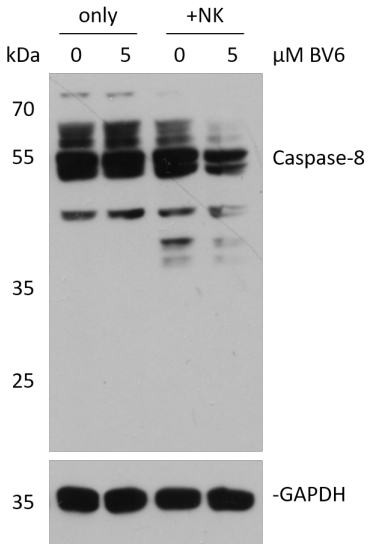

(c) Co-lysates of BV6 treated RD spheroids together with NK cells, western blot probed against caspase-8

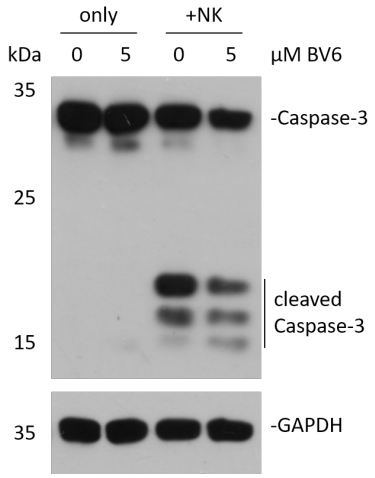

(d) Co-lysates of BV6 treated RD spheroids together with NK cells, western blot probed against caspase-3

Fig. 5.20: Western blot of BV6 treated RMS spheroids, co-cultivated with NK cells for 24 h, before co-lysates were generated. Caspase activation was identified by western blot. Images are representative of two independent western blots of different biological replicates. The western blots in (a) and (b) have the same loading control, and in (c) and (d) have the same loading control, membranes were re-probed after stripping (section 4.2.5.6).

The increased caspase-3 activation (fig. 5.20) and subsequent induction of cell death within the BV6 pre-treated RMS spheroids co-cultured with NK cells, is evident in the microscopic images in fig. 5.21(a) and (c). A higher PI fluorescence is visible around the spheroids indicative for an increased cell death.

The involvement of caspases within the NK cell mediated killing is apparent when adding a pan-caspase inhibitor (zVAD.fmk) to the RMS spheroid-NK cell co-cultivation. In both, RH30-GFP (b) and RD-GFP (d) spheroids, zVAD.fmk significantly reduces the PI/GFP ratio, i.e. spheroid killing by NK cells. This rescue from NK cell attack can also be seen in the microscopic images, where the spheroidic integrity remains intact upon zVAD.fmk co-treatment. Although, the images for the RD-GFP spheroids, co-cultured with NK cells and co-treated with zVAD.fml show a high PI positive edge.

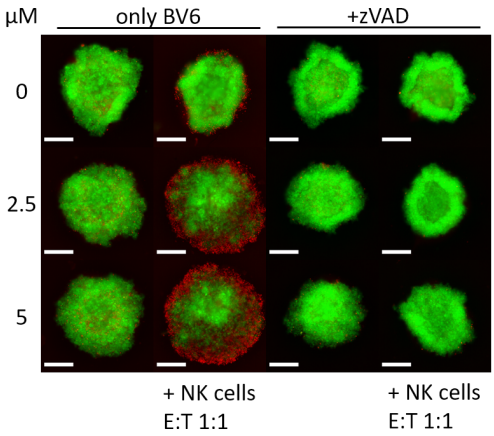

(a) Microscopic illustration of RH30-GFP (alive) and PI (dead) fluorescent cells/spheroids. Scale bar = 500 μm

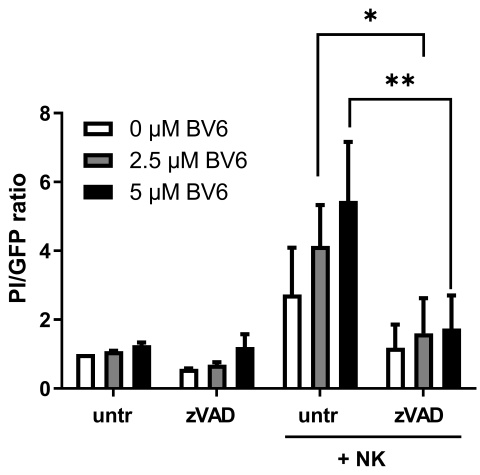

(b) Quantification and calculation of PI to GFP fluorescence ratio in BV6 pre-/ and zVAD.fmk co-treated RH30-GFP spheroids co-cultured with NK cells

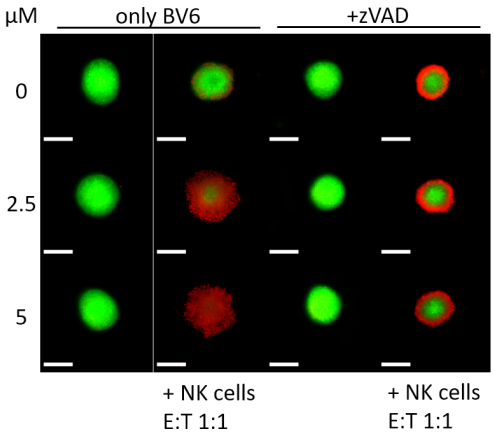

(c) Microscopic illustration of RD-GFP (alive) and PI (dead) fluorescent cells/spheroids. Scale bar = 500 μm

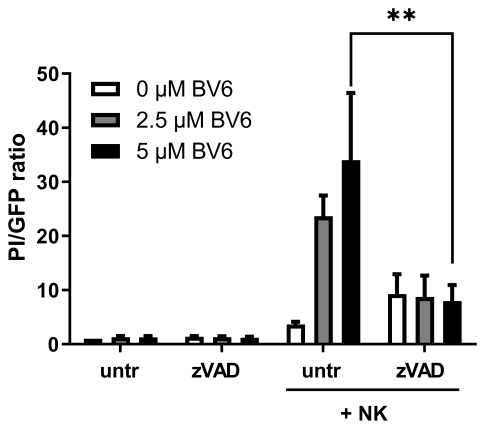

(d) Quantification and calculation of PI to GFP fluorescence ratio in BV6 pre-/ and zVAD.fmk co-treated RD-GFP spheroids co-cultured with NK cells

Fig. 5.21: Influence of caspase inhibition by zVAD.fmk on BV6 pre-treated RMS spheroids in co-culture with NK cells (E:T 1:1). Figures (a) and (c) depict the GFP fluorescence of alive RMS cells with PI counterstained dead cells. Figures (b) and (d) illustrates the quantification and ratio calculation of PI to GFP fluorescence intensity. Data is depicted as mean + SEM, N = 3 and analyzed by two-way ANOVA, *: $p \leq 0.05$, **: $p \leq 0.01$.

To validate the pan-caspase inhibitory effect of zVAD.fmk, RMS-spheroids were treated with TRAIL and co-treated with zVAD.fmk. Figure 5.22 shows that treatment with

TRAIL induces cell death within RMS-spheroids, as illustrated by the increased PI/GFP ratio. Co-treatment of TRAIL with zVAD.fmk successfully reduced the PI/GFP ratio, i.e. cell death induction, to a level comparable to untreated spheroids.

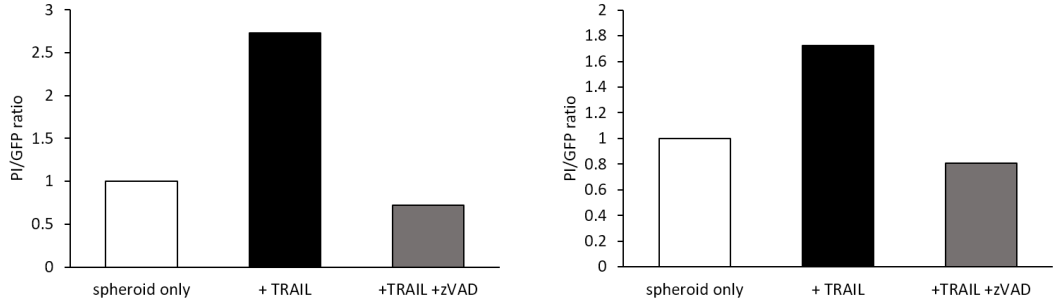

(a) RH30 spheroids treated with TRAIL, co-treated with zVAD.fmk

(b) RD spheroids treated with TRAIL, co-treated with zVAD.fmk

Fig. 5.22: Validation of zVAD.fmk within RMS spheroids upon exogenous TRAIL treatment. Treatment was performed for 24 h, with a TRAIL concentration of 100 ng/ml and zVAD.fmk of 50 μM. Data of one biological replicate. Control samples of only spheroid and exogenous TRAIL treatment are shared in fig. 5.22 and 5.16.

As caspase-9 is slightly activated upon BV6 treatment and is important within the intrinsic apoptotic pathway (fig. 5.19), caspase-9 was knocked-down in RMS-GFP spheroids by siRNA technology.

The previously described BV6 sensitization towards NK cell attack could be reproduced in RH30-GFP and RD-GFP spheroids, shown in fig. 5.23. Knock-down of caspase-9 did not alter NK cell mediated killing, as PI/GFP ratio is not reduced (fig. 5.23(b) and (d)) compared to siRNA control cells. Further, no phenotypical change can be observed upon caspase-9 knock-down. Loss of spheroidic integrity is apparent spheroids in all tested conditions of RMS-GFP spheroids (fig. 5.23(a) and (c)).

Knock-down of caspase-9 in RMS-GFP spheroids was validated by western blot (fig. 5.23(e)). RH30-GFP and RD-GFP spheroids treated with two different caspase-9 targeting siRNAs showed a reduced caspase-9 expression, compared to a non-specific targeting siRNA control (siCtrl).

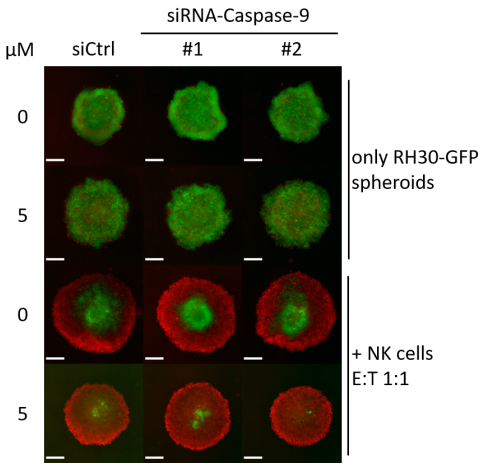

(a) Microscopic illustration of RH30-GFP (alive) and PI (dead) fluorescent cells/spheroids. Scale bar = 500 μm

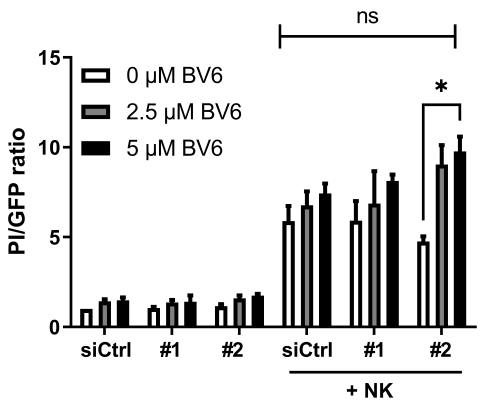

(b) Quantification and calculation of PI to GFP fluorescence ratio in BV6 pre-treated caspase-9 knock-down RH30-GFP spheroids co-cultured with NK cells

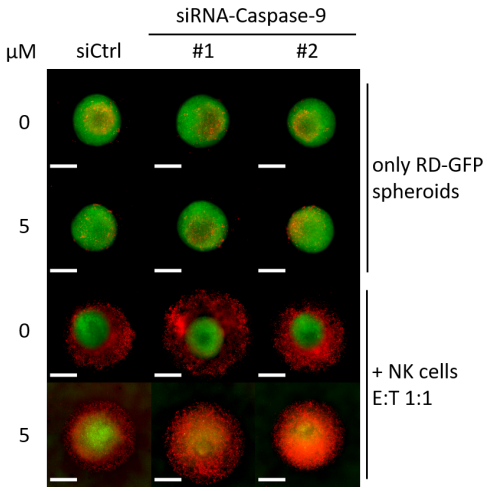

(c) Microscopic illustration of RD-GFP (alive) and PI (dead) fluorescent cells/spheroids. Scale bar = 500 μm

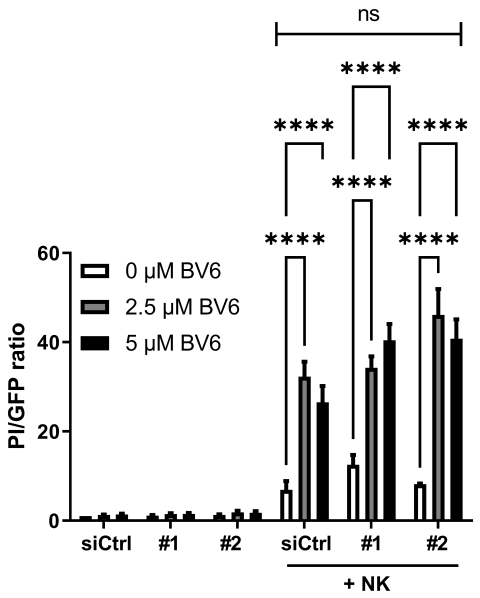

(d) Quantification and calculation of PI to GFP fluorescence ratio in BV6 pre-treated caspase-9 knock-down RD-GFP spheroids co-cultured with NK cells

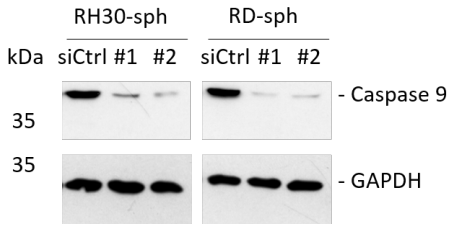

(e) Caspase-9 expression level in siRNA treated RMS-GFP spheroids analyzed by western blot

Fig. 5.23: Influence of siRNA mediated caspase-9 knock-down in BV6 pre-treated RMS spheroids in co-culture with NK cells (E:T 1:1). Figures (a) and (c) depict the GFP fluorescence of alive RMS cells with PI counterstained dead cells. Figures (b) and (d) illustrates the quantification and ratio calculation of PI to GFP fluorescence intensity. (e) shows the expression levels of caspase-9 analyzed by western blot. Data is depicted as mean + SEM, $N = 3$ and analyzed by two-way ANOVA, *: $p \leq 0.05$, ****: $p < 0.0001$.

Caspase-8, as an initiator caspase at the DISC and mainly responsible within the extrinsic apoptotic pathway, was knocked-down in RMS-GFP spheroids.
Here, the BV6 sensitization is clearly visible and could be reproduced (fig. 5.24). In RH30-GFP spheroids, knock-down of caspase-8 had no influence on NK cell mediated killing. That is, no phenotypical change of the microscopic images is visible between caspase-8 knocked-down and control RH30-GFP spheroids (fig. 5.24(a)). Caspase-8 independency is also visible within the fluorescence intensity quantification and PI/GFP ratio calculation (fig. 5.24(b)), as no difference can be seen among the RH30-GFP spheroid NK cell co-cultivated samples.
In contrast to RH30-GFP spheroids, RD-GFP spheroids show a caspase-8 dependency. Here, siRNA construct #3 leads to a rescue and stabilization of spheroidic integrity (fig. 5.24(c)), further leading to a reduction of PI/GFP ratio (d), i.e. rescue from NK cell induced killing.
Caspase-8 knock-down was validated by western blot (fig. 5.24(e)). RH30-GFP and RD-GFP spheroids were treated with three different caspase-8 targeting siRNAs. Construct #1 had no effect on caspase-8 expression and was dismissed from further experiments. Construct #2 and #3 reduced the expression of caspase-8 in both RMS-GFP spheroids. However, in RD-GFP spheroids construct #2 had a lesser knock-down effect than construct #3.

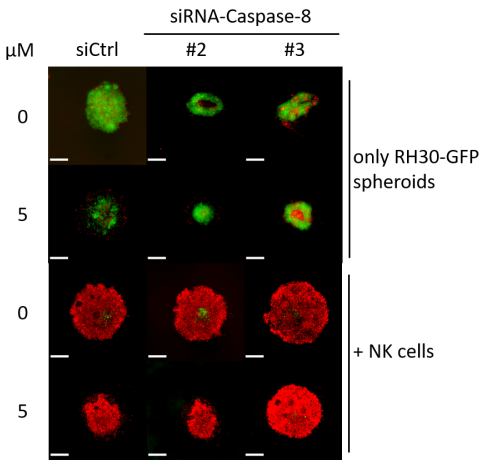

(a) Microscopic illustration of RH30-GFP (alive) and PI (dead) fluorescent cells/spheroids. Scale bar = 500 μm

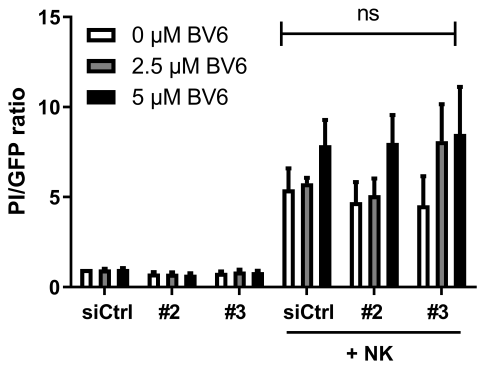

(b) Quantification and calculation of PI to GFP fluorescence ratio in BV6 pre-treated caspase-8 knock-down RH30-GFP spheroids co-cultured with NK cells

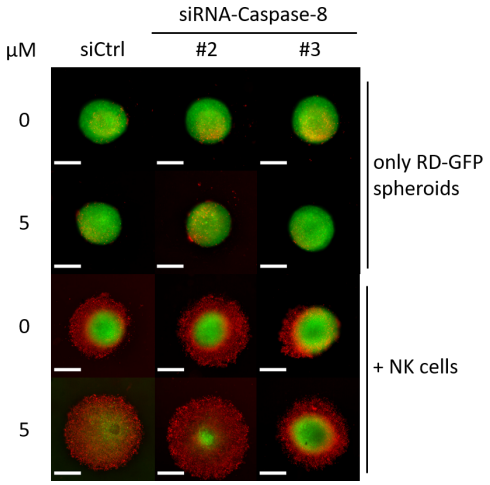

(c) Microscopic illustration of RD-GFP (alive) and PI (dead) fluorescent cells/spheroids. Scale bar = 500 μm

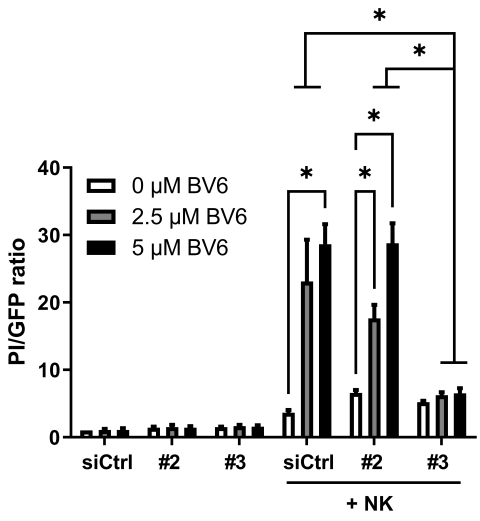

(d) Quantification and calculation of PI to GFP fluorescence ratio in BV6 pre-treated caspase-8 knock-down RD-GFP spheroids co-cultured with NK cells

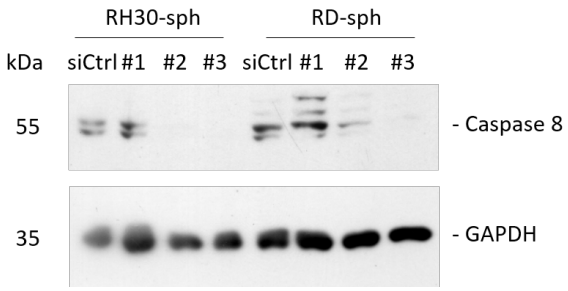

(e) Caspase-8 expression level in siRNA treated RMS-GFP spheroids analyzed by western blot

Fig. 5.24: Influence of siRNA mediated caspase-8 knock-down in BV6 pre-treated RMS spheroids in co-culture with NK cells (E:T 1:1). Figures (a) and (c) depict the GFP fluorescence of alive RMS cells with PI counterstained dead cells. Figures (b) and (d) illustrates the quantification and ratio calculation of PI to GFP fluorescence intensity. (e) shows the expression levels of caspase-8 analyzed by western blot. Data is depicted as mean + SEM, $N = 3$ and analyzed by two-way ANOVA, *: $p \leq 0.05$.

5.1.5 NK cell migratory behaviour

The previous section 5.1.4 described killing effects of NK cells on RMS-GFP spheroids and the BV6 induced sensitization of it. As yet, the migratory property of NK cells into the 3-dimensional sphere was ignored and only assumed. The following section depicts evidence on the NK cell migratory behaviour and how BV6 affects the migratory behaviour.

Figure 5.25 illustrates GFP expressing RH30 and RD spheroids co-cultivated with CellTrace™ violet stained NK cells (CT stained, blue signals). As can be seen in fig. 5.25(a), NK cells are able to penetrate and migrate into both RH30-GFP and RD-GFP spheroids. The CellTrace™ violet signal intensities within the RMS-GFP spheroid was quantified, as described in section 4.2.4.1 and illustrated in fig. 4.4.

By comparing NK cell migration into RH30-GFP and RD-GFP spheroids, it becomes apparent that NK cells more readily migrate into RD-GFP (5.25(a) right panel & (c)), than RH30-GFP spheroids (5.25(a) left panel & (b)). This observation is robust at different E:T ratios. Fig. 5.25(b) illustrates that even at E:T ratios of 5:1 and 10:1, NK cells are not as easily penetrating RH30-GFP spheroids, than into RD-GFP spheroids (c).

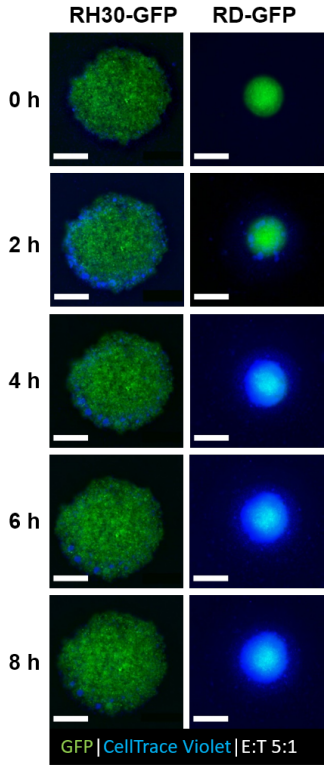

(a) Microscopic illustrations of RMS-GFP spheroid:NK cell co-culture. Scale bar = 500 μm

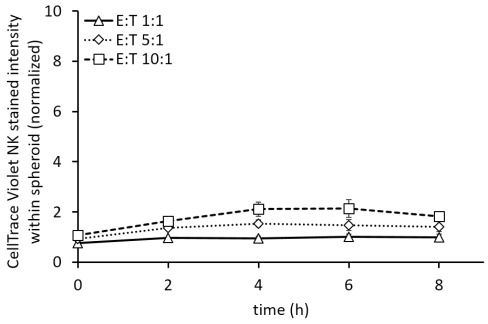

(b) Quantification of CellTrace™ violet fluorescence intensity within RH30-GFP spheroids

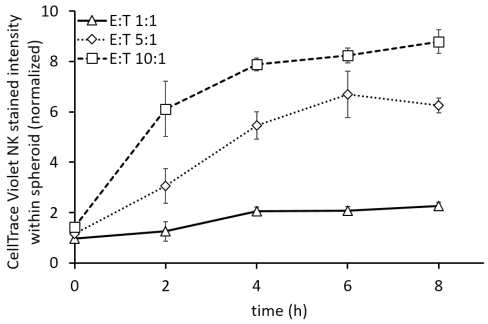

(c) Quantification of CellTrace™ violet fluorescence intensity within RD-GFP spheroids

Fig. 5.25: Migration of NK cells into RMS-GFP spheroids at different E:T ratios. Figure (a) depicts the GFP fluorescence of RMS spheroids co-cultivated with CellTrace™ violet stained NK cells (E:T 5:1). Images were taken at indicated time points. Figures (b) and (c) illustrates the quantification of CellTrace™ violet fluorescence intensity of NK cells within RMS-GFP spheroids at different time points and different E:T ratios. Data is depicted as mean ± SEM, N = 3.

Figure 5.26 illustrates the quantification of CellTrace™ violet stained NK cells inside of RH30-GFP 5.26(a)-(c) and inside of RD-GFP 5.26(d)-(f) spheroids. Here, RMS-GFP spheroids were pre-treated with BV6 and migratory NK cell behaviour measured over a time period of 8 h. As illustrated in fig. 5.26, no significant difference between BV6 pre-treated and untreated RMS-GFP spheroids regarding the NK cell migratory behaviour at different E:T ratios is visible.

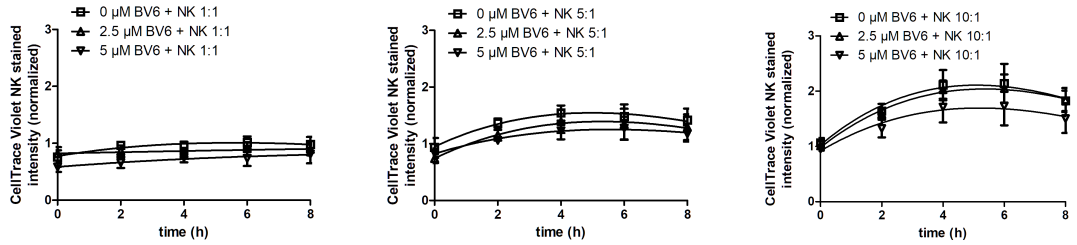

(a) violet NK cells:RH30-GFP spheroids E:T at 1:1

(b) violet NK cells:RH30-GFP spheroids E:T at 5:1

(c) violet NK cells:RH30-GFP spheroids E:T at 10:1

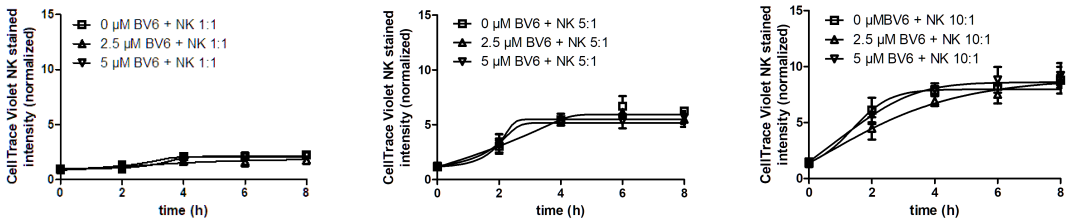

(d) violet NK cells:RD-GFP spheroids E:T at 1:1

(e) violet NK cells:RD-GFP spheroids E:T at 5:1

(f) violet NK cells:RD-GFP spheroids E:T at 10:1

Fig. 5.26: Quantification of CellTrace™ violet stained NK cells within BV6 pre-treated RMS-GFP spheroids at different E:T ratios. RMS-GFP spheroids were pre-treated for 24 h with BV6 before CT stained Nk cells were added and violet fluorescence (Pacific Blue channel) was measured at the indicated time points. CT violet stained NK cells were added at different E:T ratios, 1:1 (fig. (a) and (d)), 5:1 (fig. (b) and (e)) or 10:1 (fig. (c) and (f)). Data is depicted as mean ± SEM, N = 3.

5.2 Induced NF-κB signaling pathways by BV6

5.2.1 Activation of canonical NF-κB signaling pathway

The proteins cIAP1/2 interacting within complex I at surface receptors and are able to activate NF-κB signaling pathways (see section 2.2.2). Based on that, BV6's ability to activate the classical, canonical NF-κB signaling pathway was analyzed. Figure 5.27 depicts a western blot of RMS cells, cultured in 2D and probed for phosphorylation, activation status, of IκBα (at S32/36) and of the transcription factor p65 (at S536). Fig. 5.27(a) shows the results for RH30 cells, cultured in 2D. It can be seen that IκBα is slightly phosphorylated over the time of BV6 treatment. The phosphorylation starts to appear around one to two hours of BV6 treatment. This phosphorylation is not accompanied by a complete degradation of IκBα, although a slight decrease of signal intensity might be observed around two hours of BV6 treatment. RD cells 5.27(b), show a slightly higher phosphorylation of IκBα, compared to RH30 cells. Here, the phosphorylation appears around two hours of BV6 treatment. Again, no degradation of IκBα is visible.
Further, phosphorylation and activation of p65 occurs at a late stage within the canonical NF-κB pathway. In both, RH30 5.27(a) and RD (b) cells, a strong phosphorylation of p65 can be observed. Seemingly, with a first maximum of signal intensity at 4 h and a second maximum at 24 h of BV6 treatment.

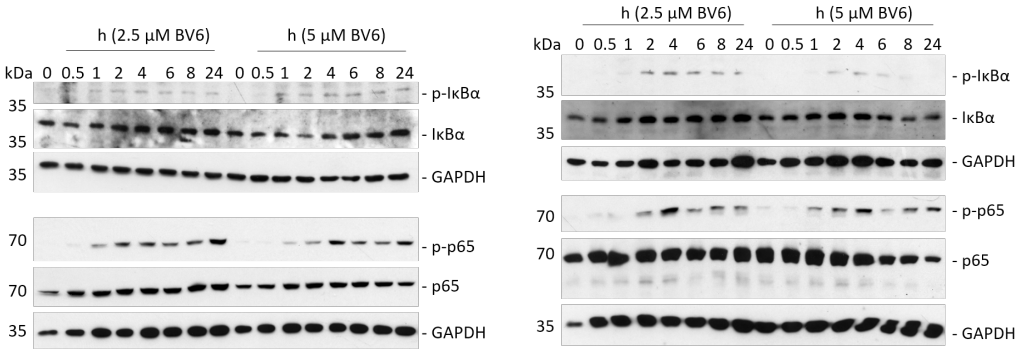

(a) RH30 cells treated with BV6 **(b)** RD cells treated with BV6

Fig. 5.27: Western blot of BV6 treated RMS cells in 2D, identifying canonical NF-κB activation by phosphorylation events of IκBα and p65. RMS cells, cultured in 2D, were treated for the indicated concentrations and time with BV6. Images are representative of two independent western blots of different biological replicates. Membranes were re-probed after stripping (section 4.2.5.6).

The behaviour of 3D cultured RMS spheroids regarding the canonical NF-κB activation (fig. 5.28) follows that of the 2D cultures. In both, RH30 5.28(a) and RD (b) spheroids,

a high signal intensity of the phosphorylated IκBα form can be seen at 24 h BV6 stimulation. A similar intense signal is visible of phosphorylated p65 at 24 h of BV6 stimulation. RD spheroids show a reduced p65 phosphorylation at 24 h stimulated with 5 μM BV6.
In both cell culture methods, the classic, canonical NF-κB signaling pathway is activated by BV6.

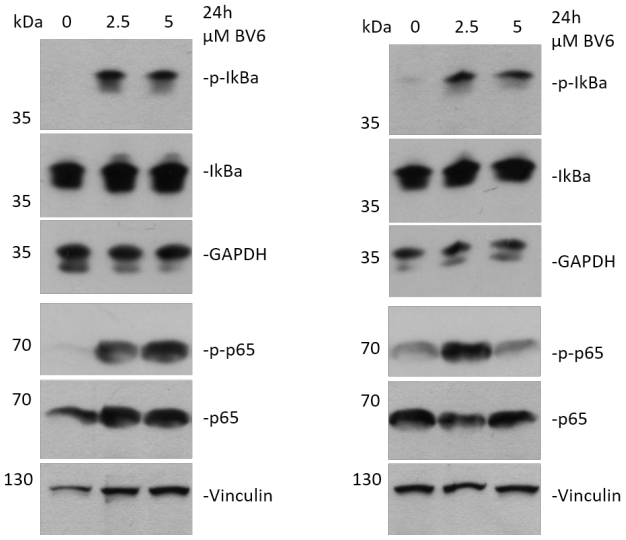

(a) RH30 spheroids treated with BV6 **(b)** RD spheroids treated with BV6

Fig. 5.28: Western blot of BV6 treated RMS spheroids, identifying canonical NF-κB activation by phosphorylation events of IκBα and p65. RMS spheroids were treated for the indicated concentrations and time with BV6. Images are representative of two independent western blots of different biological replicates. Membranes were re-probed after stripping (section 4.2.5.6).

5.2.2 Activation of non-canonical NF-κB signaling pathway

In addition to the canonical NF-κB signaling pathway, the non-canonical NF-κB signaling pathway was analyzed, as cIAP1/2 are directly involved in the proteasomal degradation of NIK. Figure 5.29 depicts the non-canonical NF-κB activation pattern of RMS cells, cultured in 2D. As can be seen, RH30 5.29(a) and RD (b) cells, behave similarly. Upon stimulation with BV6, a time dependent accumulation of NIK is visible, culminating at a time point around 24 h of BV6 stimulation. Following this kinetic, p100 is partially degraded to the transcriptional active p52 form. Which is visible by the time dependent increase of signal intensity of the p52 form.

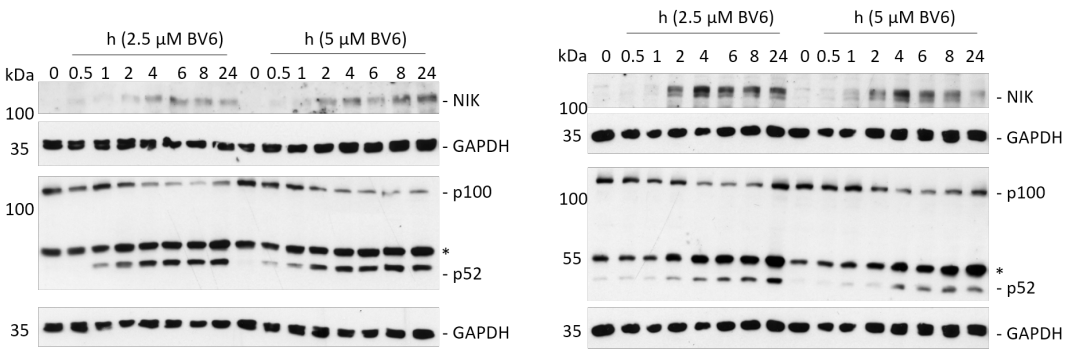

(a) RH30 cells treated with BV6 **(b)** RD cells treated with BV6

Fig. 5.29: Western blot of BV6 treated RMS cells in 2D, identifying non-canonical NF-κB activation by NIK accumulation and p52 generation. RMS cells, cultured in 2D, were treated for the indicated concentrations and time with BV6. Images are representative of two independent western blots of different biological replicates. *: unspecific signal

Stimulation of RH30 5.30(a) and RD (b) spheroids with BV6 lead to a similar activation pattern of the non-canonical NF-κB signaling pathway. Again, NIK accumulation is evident in both RMS spheroids. The partial degradation of p100, with associated loss of signal intensity, is not as pronounced as for the 2D RMS cell culture. However, an increase of signal intensity of the transcriptional active p52 form is visible in both, RH30 and RD spheroids. Here, RH30 spheroids already show a signal for the p52 fragment at untreated conditions.

Both cell culture methods are able to activate the non-canonical NF-κB signaling pathway upon BV6 stimulation.

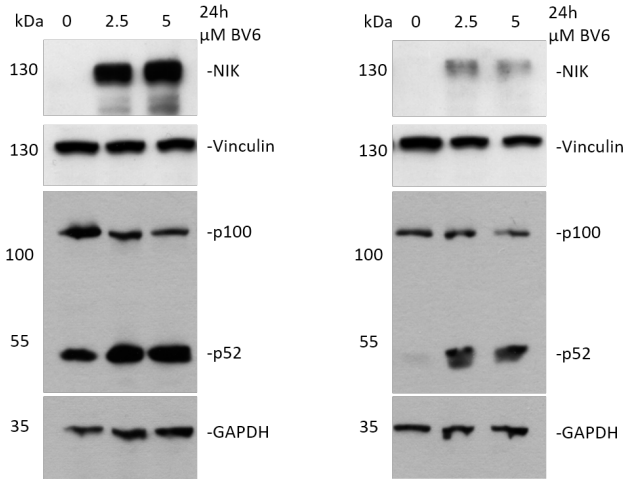

(a) RH30 spheroids treated with BV6 **(b)** RD spheroids treated with BV6

Fig. 5.30: Western blot of BV6 treated RMS spheroids identifying non-canonical NF-κB activation by NIK accumulation and p52 generation. RMS spheroids were treated for the indicated concentrations and time with BV6. Images are representative of two independent western blots of different biological replicates.

5.2.3 Nuclear fragmentation of BV6 treated RH30 cells

Active NF-κB forms, as seen in fig. 5.27(a) and 5.29(a), were further analyzed regarding their nuclear translocation. Fig. 5.31 depicts the results of a subcellular fragmentation of RH30 cells cultured in 2D treated with BV6 for different time points.

The canonical NF-κB pathway, based on the active phosphorylated form of p65 (at S536), arises within the nuclear fraction around 4 h of BV6 treatment, with a second signal at 24 h of BV6 treatment with 2.5 μM.

The non-canonical NF-κB signaling pathway, with its active p52 form shows a signal within the nuclear fraction starting from 4 h of BV6 treatment towards 24 h.

Purity validation of the subcellular fractions was performed by probing for the cytosolic protein GAPDH, which shows no signal within the nuclear fraction. As a positive nuclear marker the nuclear envelop protein LaminB1 was chosen, showing a signal around 70 kDa. Here, this signal is only present at the nuclear fraction.

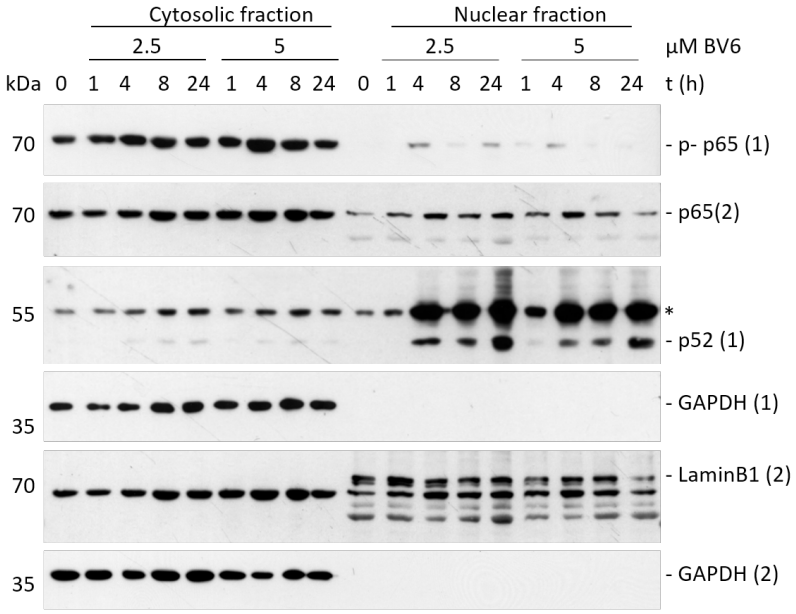

Fig. 5.31: Western blot analysis of nuclear fragmented BV6 treated RH30 cells. RH30 cells were treated for the indicated concentrations and times with BV6, followed by nuclear fragmentation and identification of NF-κB proteins by western blot. Membranes indicated by the same numbers were re-probed after stripping (section 4.2.5.6). *: unspecific signal

5.2.4 Transcriptional regulation of NF-κB target genes

Section 5.2.1 and 5.2.2 shows evidence on a protein level that BV6 activates both NF-κB signaling pathways. Activated transcription factors bind to their target genes and induce the transcription of their targets.

Figures 5.32 (RH30) and 5.33 (RD) shows qRT-PCR results of NF-κB target gene transcription indicated as mRNA fold change upon BV6 stimulation in RMS cells cultured in 2D. mRNA fold changes were calculated by the $2^{-\Delta\Delta Cq}$ method, using multiple reference genes and using untreated samples as references (dotted line) [152–154].

In RH30 cells, BV6 induces a maximum transcription at 24 h of *cIAP1* with ≈ 2.5 fold change (fig. 5.32(a)) and of *cIAP2* with ≈ 15 fold change (fig. 5.32(b)), reaching a plateau around 8 h of BV6 treatment. Transcription of *IκBα* is also induced with a peak of ≈ 4 fold change at 4-8 h of BV6 treatment, followed by a decrease to ≈ 2 fold change until 24 h of observation. BV6 does not induce the transcription of *p65*, as no distinct fold change is visible. BV6 induced transcription of *NIK* culminates at ≈ 2 fold change around 4 h of 5 µM BV6 treatment and reaches a plateau of ≈ 1.5 fold change around 1 h of BV6 treatment with 2.5 µM. mRNA transcription of *p100* starts around 4 h of BV6 treatment at both BV6 concentrations, reaching a plateau of ≈ 2 fold change

with 5 μM BV6 and $\approx$3 fold change with 2.5 μM BV6 stimulation.

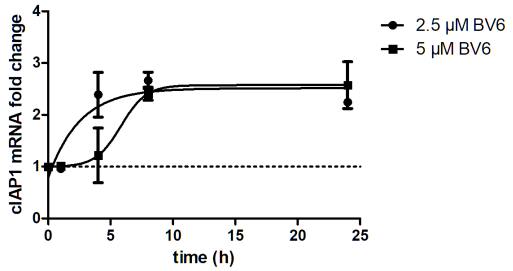

(a) *cIAP1* mRNA fold change

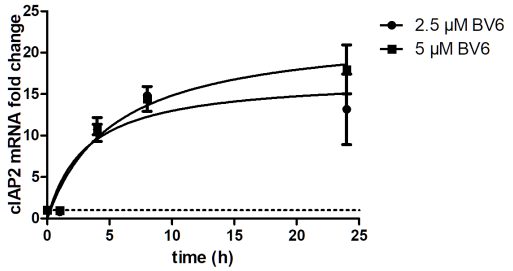

(b) *cIAP2* mRNA fold change

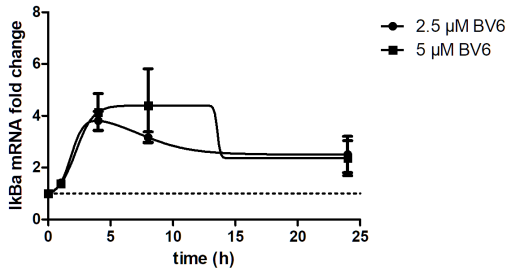

(c) *IκBα* mRNA fold change

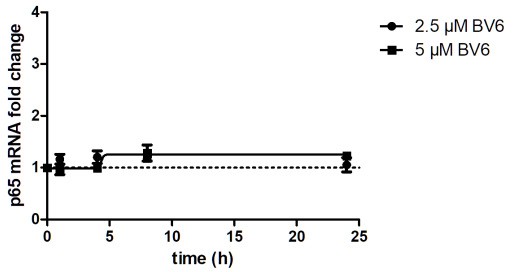

(d) *p65* mRNA fold change

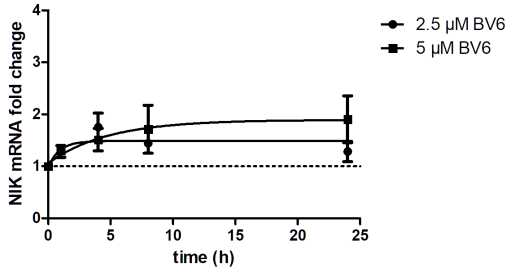

(e) *NIK* mRNA fold change

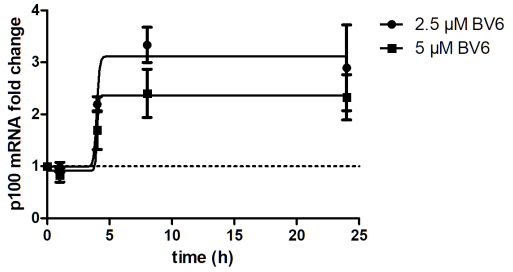

(f) *p100* mRNA fold change

Fig. 5.32: mRNA analysis of BV6 treated RH30 cells by qRT-PCR identifying NF-κB target genes. Dotted line depicts untreated level. Data is depicted as mean $\pm$ SEM, N = 3.

In contrast to the transcriptional induction of *cIAP1* in RH30 cells upon BV6 treatment, BV6 treated RD cells do not induce *cIAP1* mRNA transcription upon BV6 treatment. Transcription of *IκBα* in RD cells treated with 2.5 *mu*M BV6 shows a peak at 4-5 h of BV6 treatment with $\approx$3 fold change, which decreases over time to $\approx$2 fold change at 24 h. Treatment with 5 μM BV6 induces a rapid *IκBα* transcription reaching a plateau around 2 h of BV6 treatment at $\approx$2.5 fold change.

Comparable to RH30 cells, BV6 does not induce a transcription of *p65* in RD cells.

Fig. 5.33(d) shows a rapid transcription of *NIK* mRNA, which peaks at an ≈2 fold change for 2.5 μM, and ≈1.5 fold change for 5 μM BV6 treatment, starting from 0.5 h to ≈10-15 h BV6 treatment. This peak decreases at 24 h of BV6 stimulation to the basal transcriptional level.

BV6 induces *p100* transcription in RD cells comparable to RH30 cells. The mRNA fold change increases at ≈2 h, reaching a plateau of ≈5 fold change for 2.5 μM, and a plateau of ≈8 fold change for a BV6 treatment of 5 μM. This elevated *p100* transcription is stable for the observed time period.

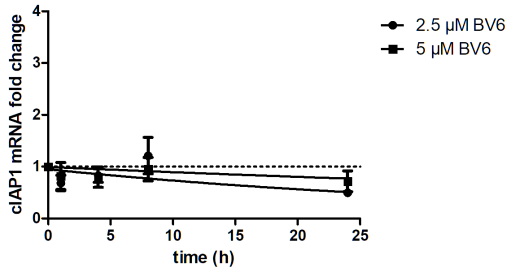

(a) *cIAP1* mRNA fold change

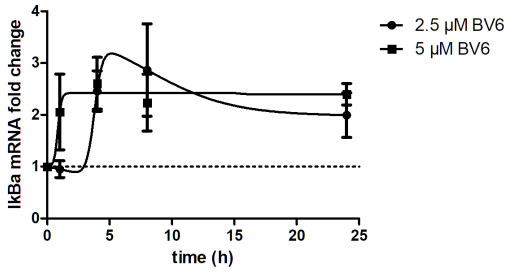

(b) IκBα mRNA fold change

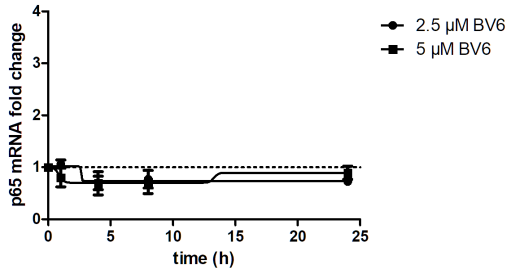

(c) *p65* mRNA fold change

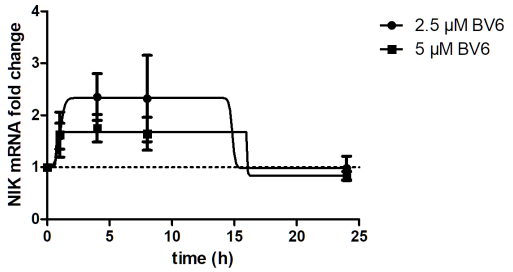

(d) *NIK* mRNA fold change

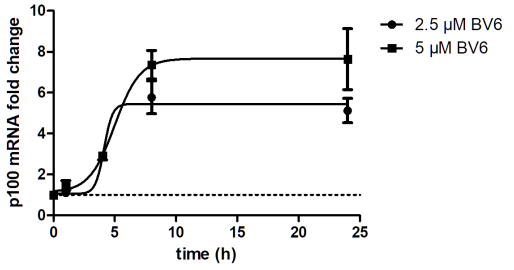

(e) *p100* mRNA fold change

Fig. 5.33: mRNA analysis of BV6 treated RD cells by qRT-PCR identifying NF-κB target genes. Dotted line depicts untreated level. Data is depicted as mean ± SEM, N = 3.

Figure 5.34 shows mRNA fold change values for RMS spheroids treated with BV6 (2.5 & 5 μM) for 24 h. The transcriptional activation in RH30 spheroids 5.34(a) is comparable to the activation pattern seen in 2D RH30 cell cultures. BV6 induced transcription of *cIAP2* is higher than for the transcription of *cIAP1*, comparable to the induction in 2D RH30 cultures. In a similar behavior to 2D RH30 culture, mRNA transcription of *IκBα*, *NIK* and *p100* in RH30 spheroids are induced upon BV6 treatment. *p65* transcription is not induced in 3D, similar was observed in 2D cultures. A significant increased transcription of *DR5* can be observed in RH30 spheroids, comparable to the regulation in 2D (fig. 5.8).
Comparison of the BV6 induced transcriptional activation of RD spheroids (fig. 5.34(b)) to the activation pattern in 2D cultured RD cells (fig. 5.33) can be seen as similar. mRNA transcription of *cIAP1* and *p65* is not up-regulated upon BV6 stimulation. *IκBα*, *NIK* and *p100* are up-regulated in RD spheroids, comparable to the regulation in 2D cultures.
Further, both RMS spheroids show an increased transcription of *RelB*, as an additional NF-κB target gene. In this line, *cRel* is not regulated upon BV6 treatment. In RD spheroids *IL-8* is not regulated on a transcription level. In contrast to RH30 spheroids, where the transcription of *IL-8* can be seen as decreased. Further, comparing RH30 5.34(a) to RD 5.34(b) spheroids, BV6 induced mRNA transcription of *CCL5* and *SSTR2* is only visible in RH30 spheroids, not in RD spheroids.

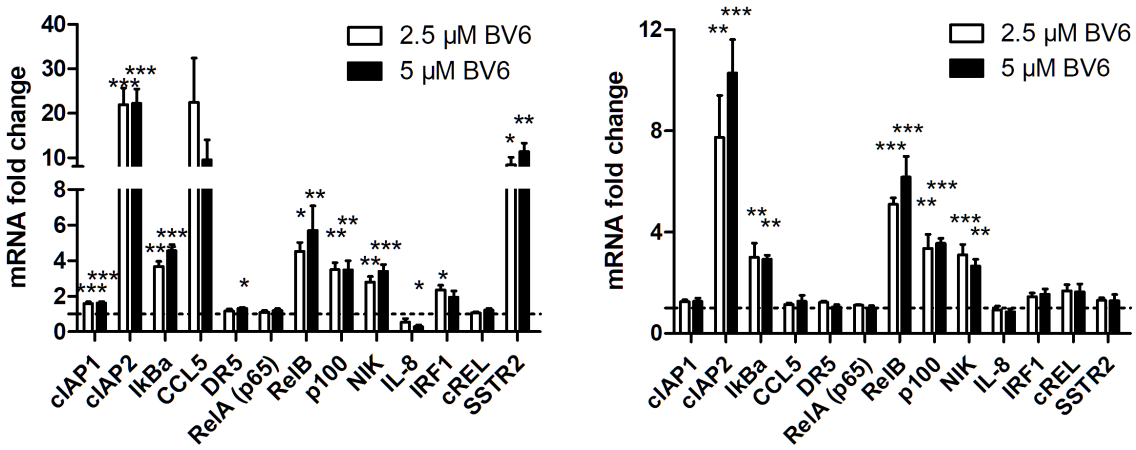

(a) mRNA analysis of RH30 spheroid **(b)** mRNA analysis of RD spheroid

Fig. 5.34: mRNA analysis of BV6 treated RMS spheroids by qRT-PCR targeting NF-κB target genes. Dotted line depicts untreated level. Data is depicted as mean ± SEM, N = 4-5, analysed by two-way ANOVA, *: $p \leq 0.05$, **: $p \leq 0.01$, ***: $p \leq 0.001$.

5.2.5 NIK as central player for BV6 induced transcription

Sections 5.2.2 shows that BV6 induces non-canonical NF-κB signaling pathway. Within this pathway, NIK is directly regulated by ubiquitylation by cIAP1/2 and might play a major role in the BV6 induced transcriptional regulation observed in section 5.2.4. NIK was knocked-down using siRNA technique, to evaluate its function role within BV6 induced sensitization.

Figure 5.35 and 5.36 shows qRT-PCR and western blot data to validate the knock-down effect on NIK expression. As can be seen in fig. 5.35(a), *NIK* mRNA is down-regulated upon siRNA treatment in untreated RH30 cells. Both siRNA constructs reduce the *NIK* mRNA to $\approx 50\,\%$ compared to its basal transcription. Western blot analysis (fig. 5.35(b)) of BV6 treated RH30 cells, pre-treated with *NIK* targeting siRNA, shows a missing signal accumulated NIK upon BV6 treatment, compared to siCtrl samples.

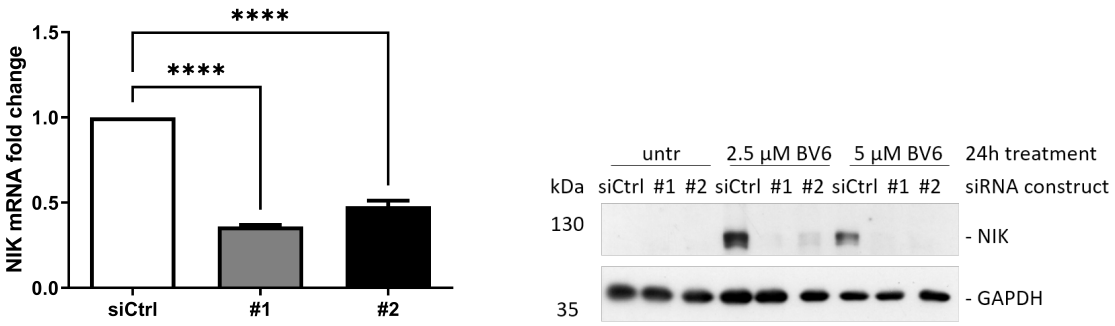

(a) qRT-PCR analysis in RH30 cells

(b) Western blot analysis in RH30 cells, treated with BV6 for 24 h

Fig. 5.35: Validation of NIK knock-down RH30 cells, treated with BV6 for 24 h. Data of qRT-PCR analysis is depicted as mean $\pm$ SEM, N = 3, analyzed by one-way ANOVA, ****: $p < 0.0001$.

Figure 5.36(a) shows the qRT-PCR results of BV6 treated RD cells pre-treated with *NIK* targeting siRNA constructs. In contrast to RH30 cells, in RD cells show no reduced *NIK* mRNA levels under untreated, basal conditions. However, the knock-down effect of *NIK* becomes visible upon BV6 treatment, where siRNA treatment suppress BV6 induced *NIK* mRNA up-regulation. On a protein level, analyzed by western blot (fig. 5.36(b)), knock-down of *NIK* mRNA results in a missing signal for NIK accumulation, comparable to RH30 cells.

In both, RH30 and RD cells, siRNA mediated knock-down of NIK was successfully validated.

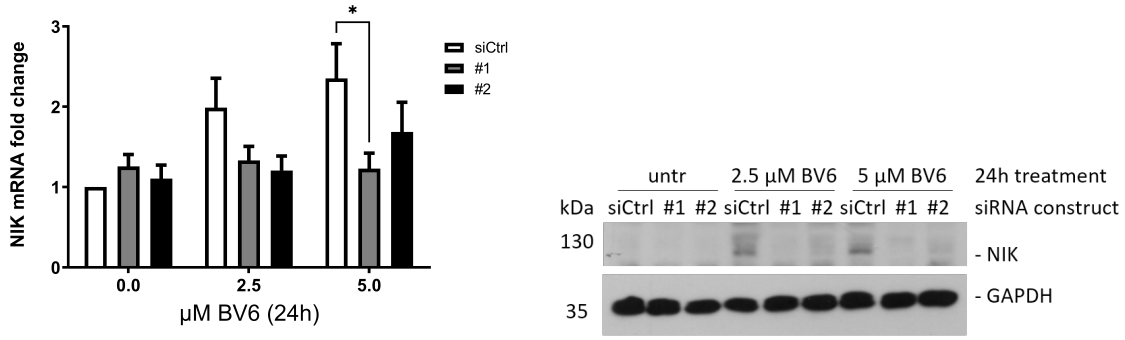

(a) qRT-PCR analysis in RD cells **(b)** Western blot analysis in RD cells

Fig. 5.36: Validation of NIK knock-down in RD cells, treated with BV6 for 24 h. Data of qRT-PCR analysis is depicted as mean ± SEM, N = 3, analysed by two-way ANOVA, *: $p \leq 0.05$.

Figure 5.37 (RH30) and 5.38 (RD) show effects of siRNA mediated *NIK* suppression on NF-κB signaling pathways.

In RH30 cells (fig. 5.37(a)), cIAP1 and cIAP2 is degraded upon BV6 treatment. Here, the re-expression of cIAP2 is visible in the siCtrl samples. This effect seems to be NIK dependent, as in samples with *NIK* knock-down, this re-expression can not be observed. Non-canonical NF-κB activation is characterized by the partial degradation of p100 to p52. Here, the *NIK* knock-down in RH30 cells show a slightly higher signal of p100 upon BV6 treatment, accompanied with a faint or no signal for the transcriptional active p52 form. Figure 5.37(b) shows the signal for p65 and its phosphorylated form (at S536) upon BV6 treatment. siRNA mediated *NIK* knock-down in RH30 cells suppress the phosphorylation of p65 upon BV6 treatment for 24 h using 2.5 and 5 μM.

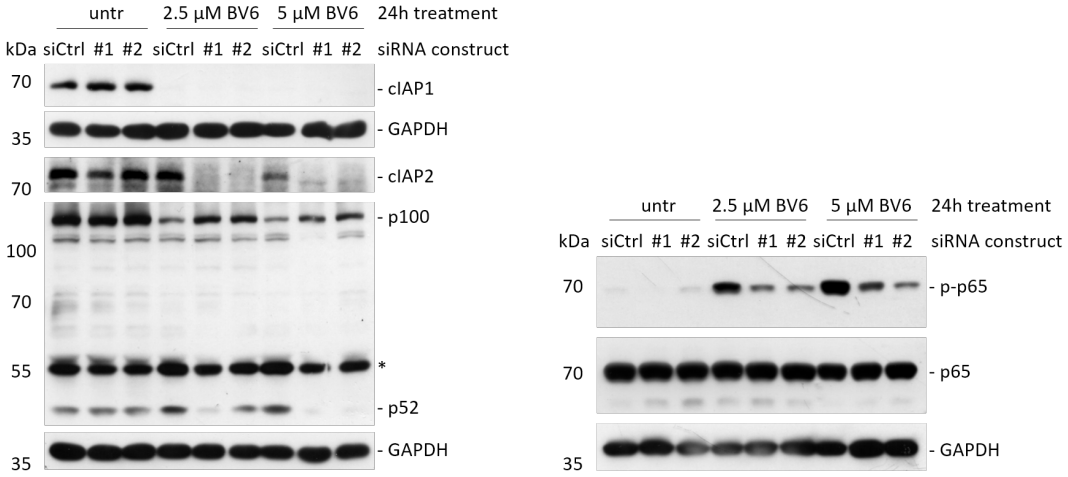

(a) Western blot of non-canonical NF-κB signaling components

(b) Western blot of canonical NF-κB signaling components

Fig. 5.37: Western blot analysis of BV6 induced NF-κB signaling within *NIK* knocked-down RH30 cells. Images are representative of two independent western blots of different biological replicates. *: unspecific signal

RD cells (fig. 5.38) treated with *NIK* targeting siRNA constructs show comparable effects as described for RH30 cells. As expected, cIAP1 is degraded upon BV6. No signal for cIAP2 could be detected, as the protein is not being translated.
NIK knock-down in RD cells show a reduced partial degradation of p100 to p52.
In figure 5.38(b) p65 and its phosphorylated form (at S536) is depicted. It can be seen that p65 is phosphorylated in untreated conditions and a slight increased signal intensity can be observed upon BV6 treatment in siCtrl samples. Knock-down of *NIK* vaguely suppresses p65 phosphorylation, as slightly less intense phospho-p65 signals are visible.

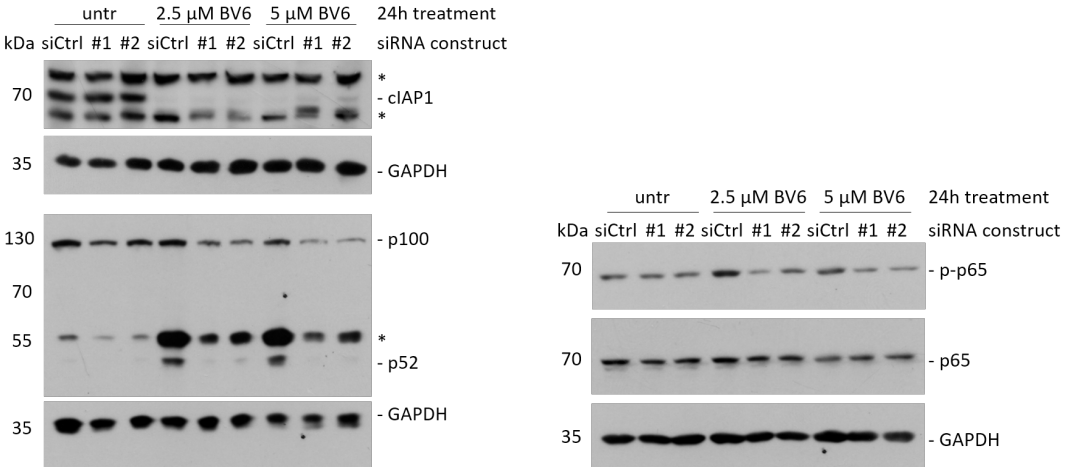

(a) Western blot of canonical NF-κB signaling components

(b) Western blot of non-canonical NF-κB signaling components

Fig. 5.38: Western blot analysis of BV6 induced NF-κB signaling within *NIK* knocked-down RD cells. Images are representative of two independent western blots of different biological replicates. *: unspecific signal

The previously shown effects of siRNA mediated knock-down of *NIK* on NF-κB signaling, can be further traced down to a transcriptional effect.

Figure 5.39 depicts qRT-PCR analysis of NF-κB target genes upon BV6 treatment, of RH30 cells pre-treated with *NIK* targeting siRNA constructs. It can be seen, that the level of mRNA fold change for *cIAP1* (a), *cIAP2* (b), *DR5* (c), *IL-8* (d) and *MMP9* (e) does not increase upon BV6 treatment, if *NIK* is targeted by siRNA construct, in contrast to siCtrl samples, where an increase of mRNA fold change is visible.

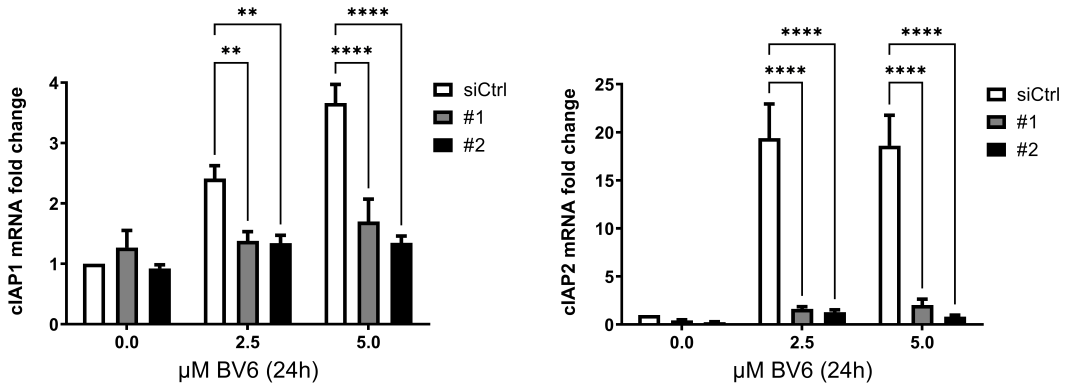

(a) cIAP1 mRNA fold change

(b) cIAP2 mRNA fold change

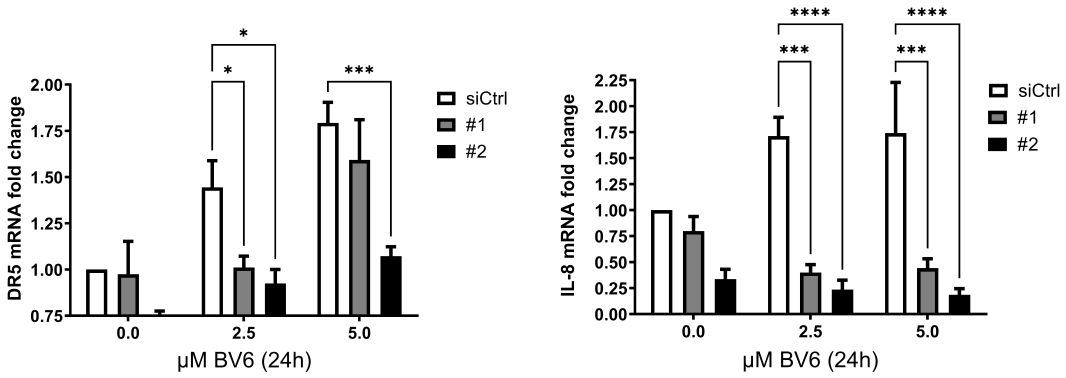

(c) DR5 mRNA fold change

(d) IL-8 mRNA fold change

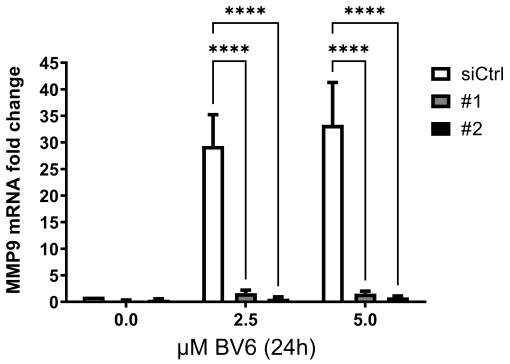

(e) MMP9 mRNA fold change

Fig. 5.39: mRNA analysis of BV6 treated NIK knocked-down RH30 cells by qRT-PCR. Data is depicted as mean ± SEM, N = 3, analysed by two-way ANOVA, *: $p \leq 0.05$, **: $p \leq 0.01$, ***: $p \leq 0.001$, ****: $p < 0.0001$.

The transcriptional suppression of NF-κB target genes in *NIK* targeted siRNA construct pre-treated RD cells is no as pronounced as in RH30 cells. Here, only for *cIAP2* (b) and *MMP9* (e) a suppressed BV6 induced mRNA transcription is visible. It seems, as if the *cIAP2* mRNA is transcriptional regulated in RD cells, although not translated into a protein.

The BV6 induced transcription of *cIAP1* (a), *DR5* (c) and *IL-8* (d) in RD cells is not impaired upon *NIK* knock-down.

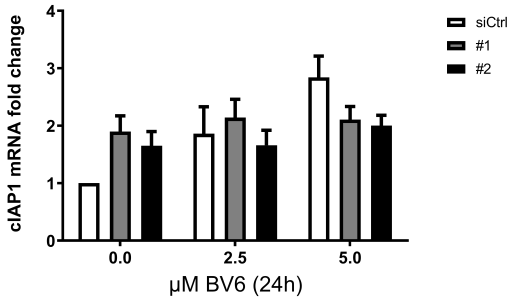

(a) *cIAP1* mRNA fold change

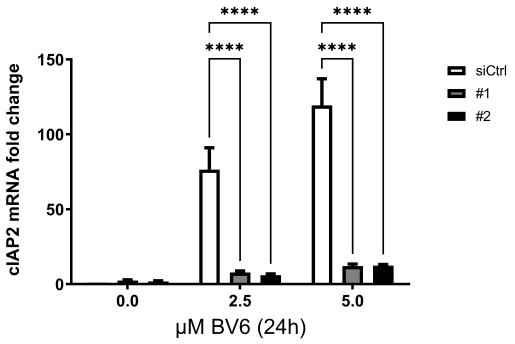

(b) *cIAP2* mRNA fold change

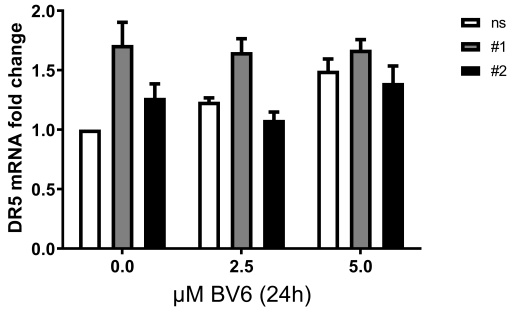

(c) *DR5* mRNA fold change

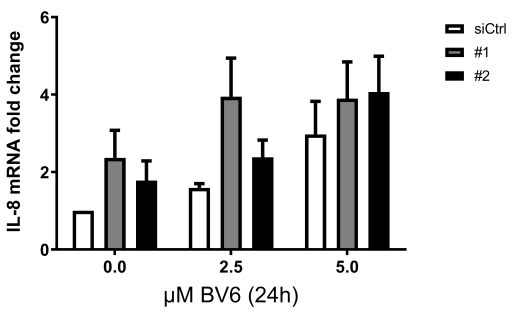

(d) *IL-8* mRNA fold change

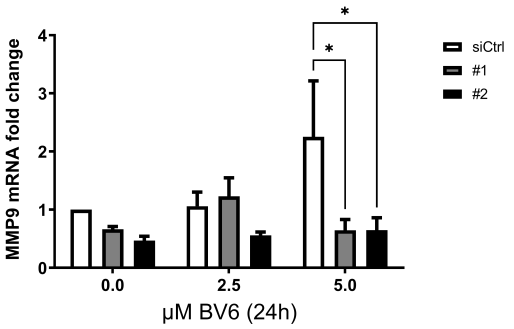

(e) *MMP9* mRNA fold change

Fig. 5.40: mRNA analysis of BV6 treated NIK knocked-down RD cells by qRT-PCR. Data is depicted as mean ± SEM, N = 3, analysed by two-way ANOVA, *: $p \leq 0.05$, ****: $p < 0.0001$.

5.2.6 NIK dependency on NK cell mediated killing

Section 5.2.4 shows evidence of a BV6 induced transcription in RH30 and RD cells. As section 5.2.5 illustrated, this transcriptional regulation is putatively controlled by NIK as a main facilitator.

The following section will show the results (fig. 5.41) of an RMS-GFP spheroid approach combining siRNA mediated knock-down of *NIK*, 24 h BV6 pre-treatment and co-cultivation with NK cells at an E:T ratio of 1:1. The efficiency of siRNA mediated *NIK* knock-down in a spheroid model is shown in 5.41(e). No accumulation of NIK can be observed upon BV6 treatment, validating the successful knock-down of *NIK*.

Within the spheroid killing assay, the BV6 sensitizing effect can be reproduced in all sample conditions, in RH30-GFP (fig. 5.41(b)) and RD-GFP (d) spheroids. However, no significant change is shown comparing the PI/GFP fluorescence ratios of samples showing a *NIK* knock-down compared to siCtrl spheroids. Apart from the PI/GFP ratio, observation of the microscopic images does not show a phenotypic difference neither in RH30-GFP (fig. 5.41(a)), nor in RD-GFP (a) co-cultivated with NK cells upon *NIK* knock-down compared to siCtrl. Concluding, that the loss of GFP signal intensity and diminished spheroid size upon NK cell attack with an additional BV6 induced sensitization is independent of the presence of NIK.

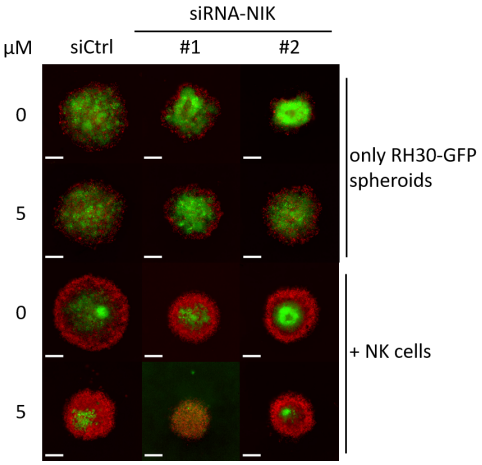

(a) Microscopic illustrations of RH30-GFP (alive) and PI (dead) fluorescent cells/spheroids. Scale bar = 500 μm

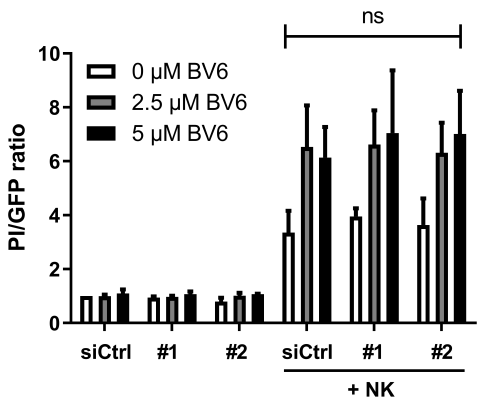

(b) Quantification and ratio calculation of PI to GFP fluorescence in BV6 pre-treated NIK knock-down RH30-GFP spheroids co-cultured with NK cells

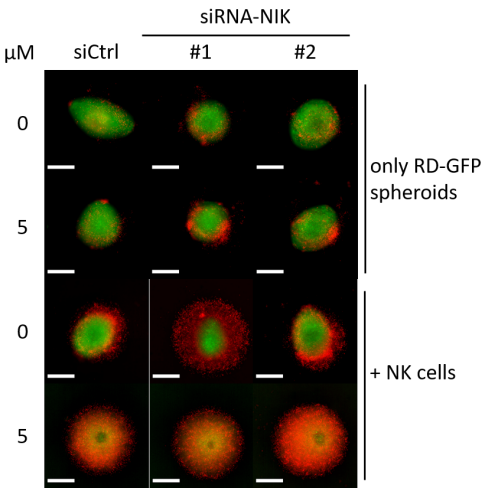

(c) Microscopic illustrations of RD-GFP (alive) and PI (dead) fluorescent cells/spheroids. Scale bar = 500 μm

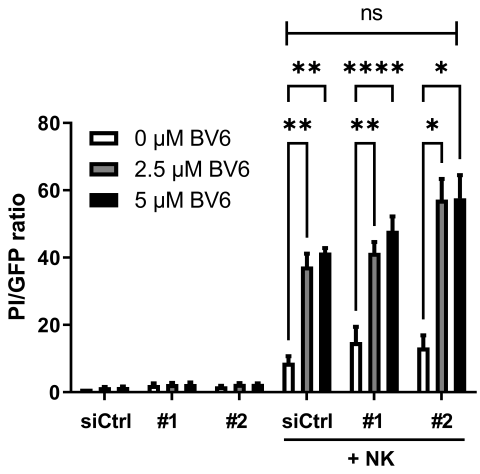

(d) Quantification and ratio calculation of PI to GFP fluorescence in BV6 pre-treated NIK knock-down RD-GFP spheroids co-cultured with NK cells

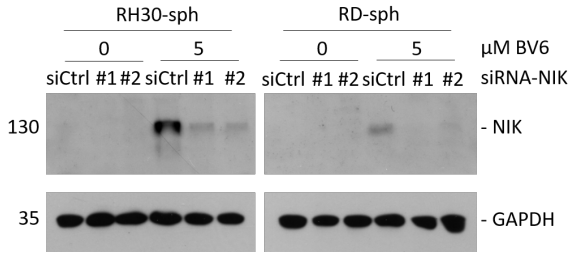

(e) NIK expression level in siRNA treated RMS-GFP spheroids upon BV6 treatment, analyzed by western blot

Fig. 5.41: Influence of siRNA mediated *NIK* knock-down in BV6 pre-treated RMS spheroids in co-culture with NK cells (E:T 1:1). Figures (a) and (c) depict the GFP fluorescence of alive RMS cells with PI counterstained dead cells. Figures (b) and (d) illustrates the quantification and ratio calculation of PI to GFP fluorescence intensity. (e) shows the expression levels of NIK in BV6 treated RMS-GFP spheroids, analyzed by western blot. Data is depicted as mean + SEM, N = 3 and analyzed by two-way ANOVA, *: $p \leq 0.05$, **: $p \leq 0.01$, ****: $p < 0.0001$.

5.3 Transcriptomic analysis of RH30 cell

5.3.1 RNA sequencing of RH30 cells upon BV6 treatment

As described in section 5.2, treatment of RMS cells with BV6 activates transcriptional NF-κB signaling pathways. To deepen the understanding of the BV6 mediated regulation and to identify novel target genes putatively responsible for the BV6 induced sensitization a bulk RNA sequencing was performed on RH30 cells $\pm$ BV6 (5 μM, 24 h). The sequencing was performed in cooperation with TRON gGmbH, Mainz.
Figure 5.42 shows the principle component analysis (PCA) of untreated and BV6 treated RH30 cells. Untreated RH30 cell samples are depicted in black dots and reside in the upper left corner, whereas BV6 treated RH30 cell samples reside in the lower right corner of the PCA (red dots). A variability within each group of the replicates is visible. The samples of the group cluster together, at different corners of the PCA analysis. By that, illustrating differences between the group.

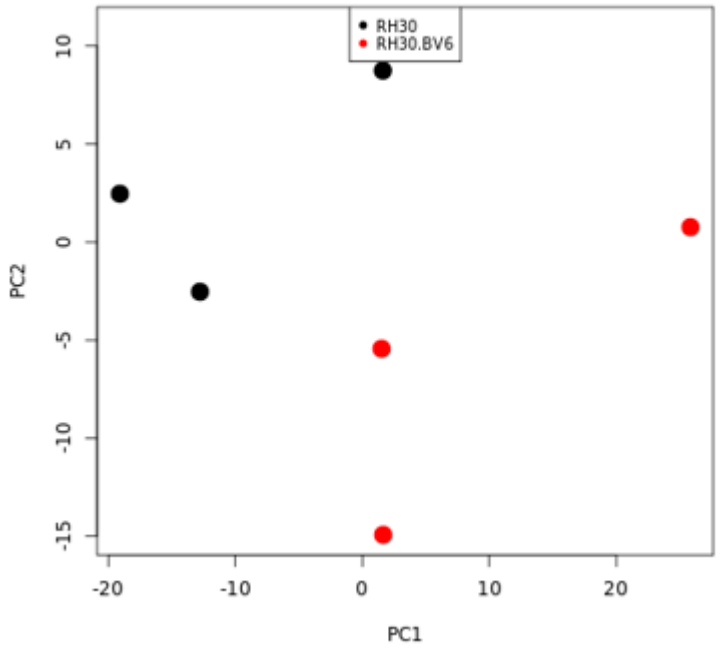

Fig. 5.42: Principle component analysis of RNAseq results for RH30 cells treated with BV6, black dots: untreated RH30 cells, red dots: BV6 treated RH30 cells (5 μM, 24 h)

The PCA analysis shows that the two groups differ from each other. Based on this, a differentially expressed gene (DEG) analysis was performed. By applying a threshold of p_{adj} value < 0.05 and $\log_2$ fold change $> |1|$, 182 genes were identified to be differentially

expressed in BV6 treated RH30 cells compared to untreated RH30 cells.These identified DEGs were plotted to generate a volcano plot (see fig. 5.43(a) and tab. A.1) and the top 50 up- and down-regulated DEGs are shown as a heatmap (fig. 5.43(b)). Among the top 50 candidates are cellular inhibitor of apoptosis protein 2 (*cIAP2*, *BIRC3*), C-C motif chemokine 5 (*CCL5*), matrix metalloproteinase-9 (*MMP9*), somatostatin receptor type 2 (*SSTR2*) and NF-κB inhibitor α (*IκBα*, *NFKBIA*).

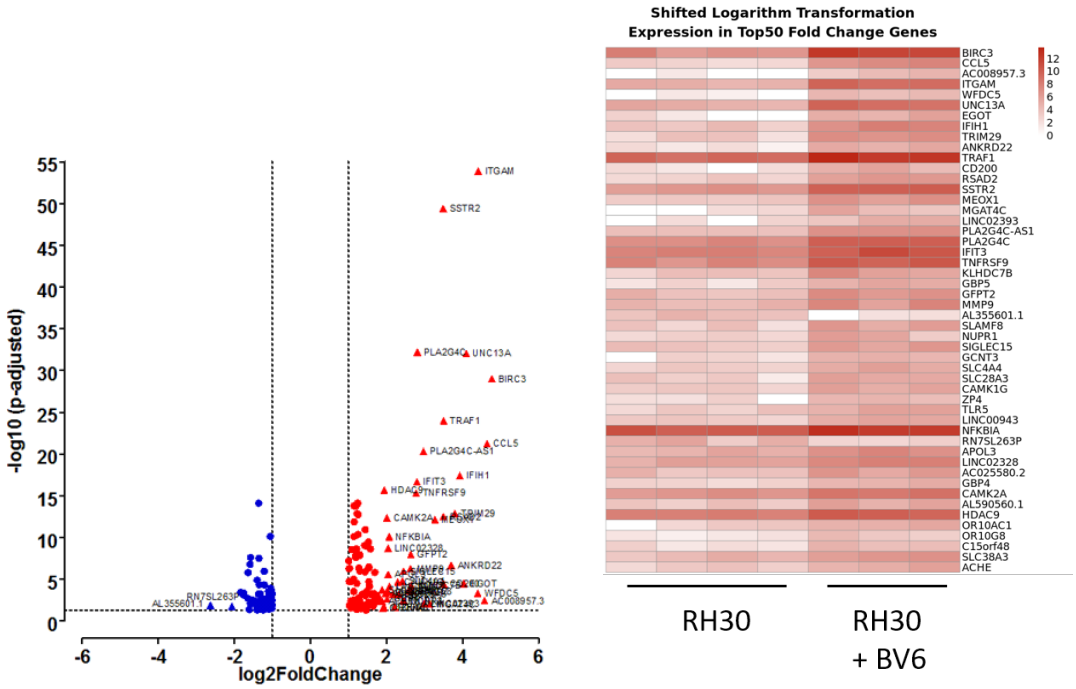

(a) Volcano plot of differentially expressed genes

(b) Heatmap of top 50 differentially expressed genes

Fig. 5.43: RNA sequencing analysis of differentially expressed genes in BV6 treated RH30 cells. (a) depicts 182 DEGs in a volcano plot with applied threshold of p_{adj} value < 0.05 and $\log_2$ fold change $> |1|$. (b) shows top 50 up- and down-regulated DEGs.

Identified DEGs were further used in pathway enrichment analysis (as described in section 4.2.6.4). Figure 5.44(a) depicts the gene ontology (GO) annotations for down-regulated pathways, i.e.phagocytosis, platelet degranulation and cellular carbohydrate metabolic process.

In (b) the GO annotation for up-regulated pathways are listed. Among them are, regulation of innate immune response, NF-kappa B signaling pathway, regulation of immune effector process and macrophage migration.

Further, a transcription factor analysis (TRRUST) was performed on the up-regulated DEGs [155]. This function is implemented within the Metascape algorithm [149]. Figure 5.44(c) shows the putative transcription factors, possibly involved in the regulation of

the identified up-regulated DEGs. Here, the top 3 candidates are transcription factor p65 (RELA), nuclear factor NF-kappa-B p105 subunit (p105, NFKB1) and transcription factor PU.1 (SPI1).

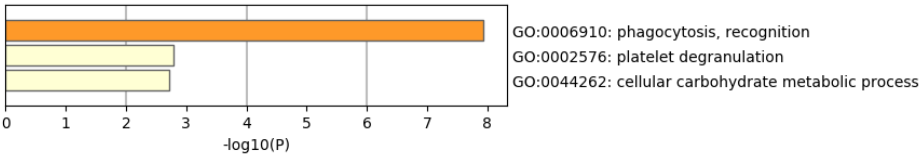

(a) Down-regulated pathways

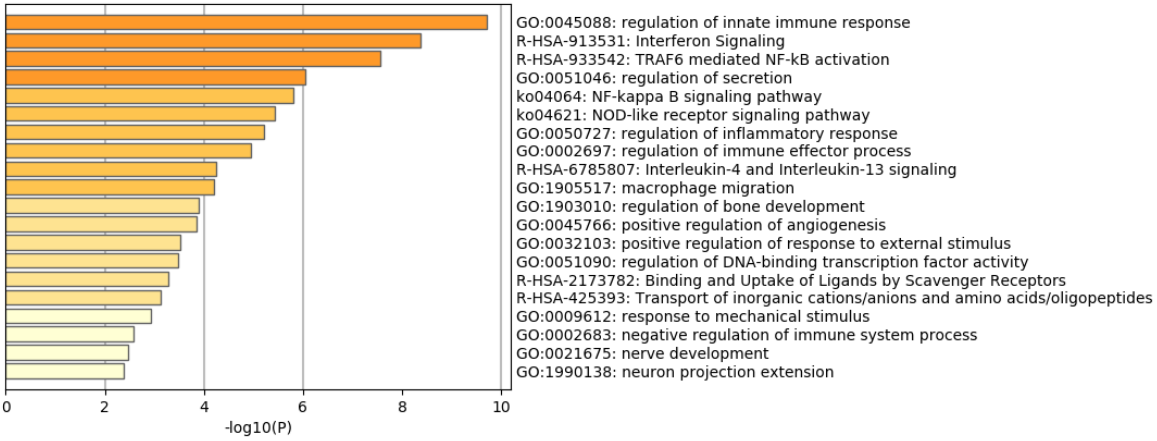

(b) Up-regulated pathways

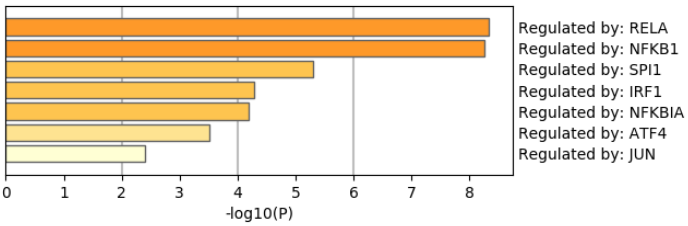

(c) TRRUST analysis of up-regulated DEGs

Fig. 5.44: RNA sequencing analysis - GO annotations by Metascape. Fig. (a) show the GO annotation of down-regulated pathways and fig. 5.44(b) GO annotations of up-regulated pathways. Fig. (c) depicts transcription factor putatively involved in the up-regulated DEGs.

5.3.2 Validation by Fluidigm®

A selection of 23 DEGs previously identified by the RNAseq were chosen and analyzed using a high-throughput qRT-PCR screening platform Fluidigm® to correlate the $\log_2$ fold change values with each other. This assay was performed in cooperation with the TRON gGmbH, Mainz, using the primers listed in table 4.9. The $\log_2$ fold change value correlation of both RNA quantifying methods is shown in fig. 5.45 (values are shown in tab. A.2). As can be seen, a coefficient of determination of $R^2 = 0.8373$ was calculated, indicating a high linear correlation between the $\log_2$ fold change values of the two used methods. Thereby, the Fluidigm® assay validates the RNAseq results, for the selected DEGs, which can be extrapolated and transferred to the complete RNAseq identified DEGs.

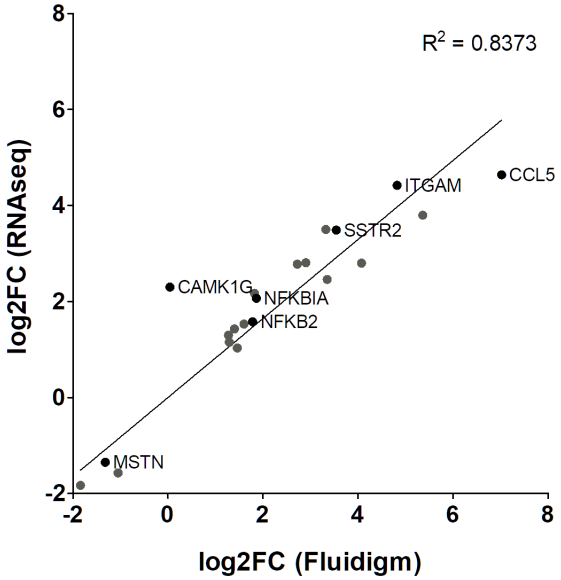

Fig. 5.45: Comparison of Fluidigm® analysis with RNA sequencing. Selected DEGs were analysed by Fluidigm® and $\log_2$ fold change (log2FC) values compared to $\log_2$ fold change values of RNA sequencing of BV6 treated RH30 cells.

5.3.3 Validation of genes of interest

The next section will describe the validation process for two genes of interest (GOI) in more detail. Both GOIs are among the top 50 identified DEGs. The first GOI is the C-C motif chemokine 5 (*CCL5*). The second will be the somatostatin receptor type 2 (*SSTR2*). Table 5.1 lists the respective $\log_2$ fold change values and adjusted p values of BV6 treated RH30 cells compared to untreated RH30 cells, identified by RNAseq.

Tab. 5.1: RNA sequencing data of two chosen genes of interest for further validation experiments.

Gene of interest	log_2fold change	p_{adj} value
CCL5	4.64	5.48^{-22}
SSTR2	3.49	4.10^{-50}

5.3.3.1 C-C motif chemokine 5

CCL5 is on of the top identified GOIs within the previous described bulk RNA sequencing analysis. To illustrate the importance of *CCL5* expression within the sarcoma tumor group, a computational *in situ* analysis of the SARC study group of the TCGA database was performed using OncoInc.org [156]. Figure 5.46(a) depicts the highly significant difference in *CCL5* expression between the lower and upper 20 %. This expression difference correlates with the survival of each group (fig. 5.46(b)). A higher *CCL5* expression (black line) seems to positively influence the survival probability. In contrast to lower *CCL5* expression (red dotted line), which is correlated to a lower survival probability.

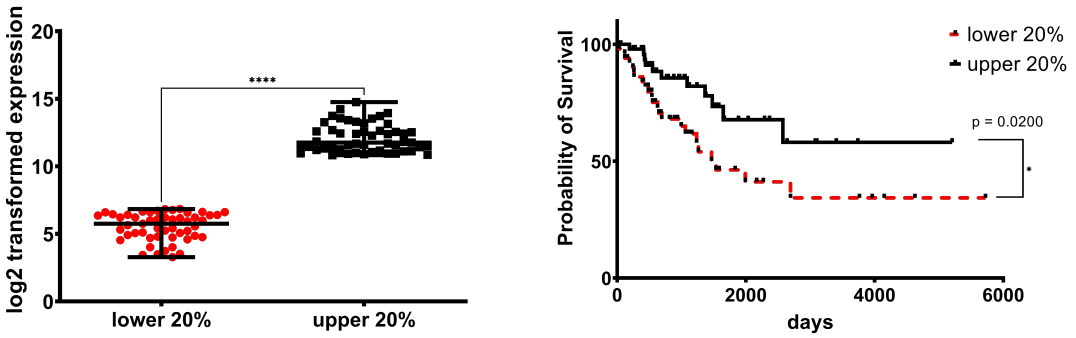

(a) *CCL5* expression analysis within SARC studygroup

(b) Survival curve within SARC studygroup regarding *CCL5* expression

Fig. 5.46: Survival analysis within SARC studygroup in regards to *CCL5* expression. Fig. (b) depicts survival curves of the top 20 % upper and lower *CCL5* expressing samples. Fig. (a) shows the expression levels of upper and lower 20 % *CCL5* expressing cases within SARC studygroup. Significance calculated using Student's t-test, ****: $p < 0.0001$. TCGA SARC raw data exported using OncoInc.org [156]

Figure 5.47 depicts qRT-PCR results measured in-house of BV6 treated RMS cells upon pre-treatment with *NIK* targeting siRNA. Both, RH30 5.47(a) and RD (b) cells show a BV6 mediated up-regulation of CCL5 transcription in the siCtrl samples. Knock-down of *NIK* significantly suppressed BV6 induced transcription of *CCL5* in both, RH30 and

RD cells.

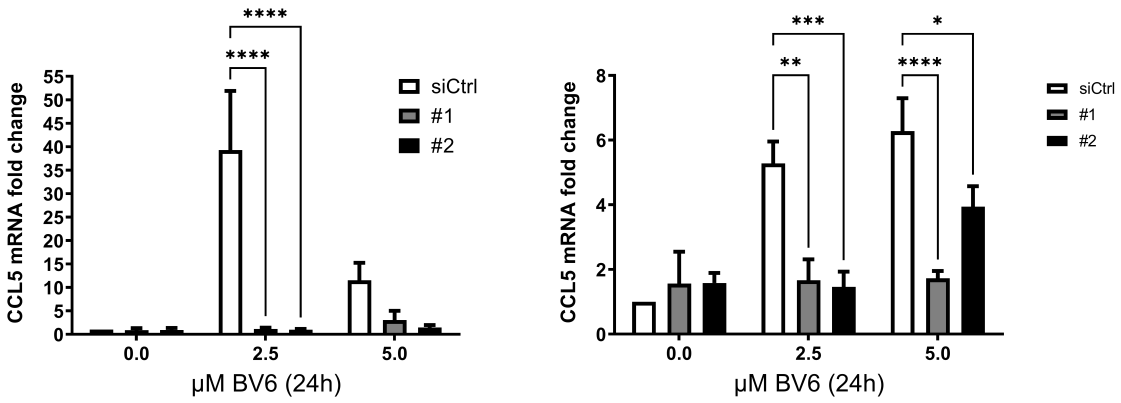

(a) *CCL5* transcription analysis within *NIK* knocked-down RH30 cells

(b) *CCL5* transcription analysis within *NIK* knocked-down RD cells

Fig. 5.47: Expression analysis of *CCL5* upon BV6 treatment in RMS cells with *NIK* knock-down. Data is depicted as mean + SEM, N = 3, analysis by two-way ANOVA, *: $p \leq 0.05$, **: $p \leq 0.01$, ***: $p \leq 0.001$, ****: $p < 0.0001$.

To compare the transcriptional activation of *CCL5* to its protein level, CCL5 secretion was measured using an ELISA. Figure 5.48 depicts the results of the ELISA analysis. Both, RH30 5.48(a) and RD (b) cells, show higher concentrations of CCL5 in the cell culture supernatant upon BV6 treatment. Additionally, it can be seen that the basal CCL5 secretion differs in RH30 to RD cells. Untreated RH30 cells (a) secrete CCL5 at a concentration which is below the limit of detection. Whereas, untreated RD cells (b) secrete CCL5 in much higher concentration compared to RH30 cells.
Further, CCL5 is secreted in a similar pattern as could be seen for the transcriptional regulation of *CCL5*.

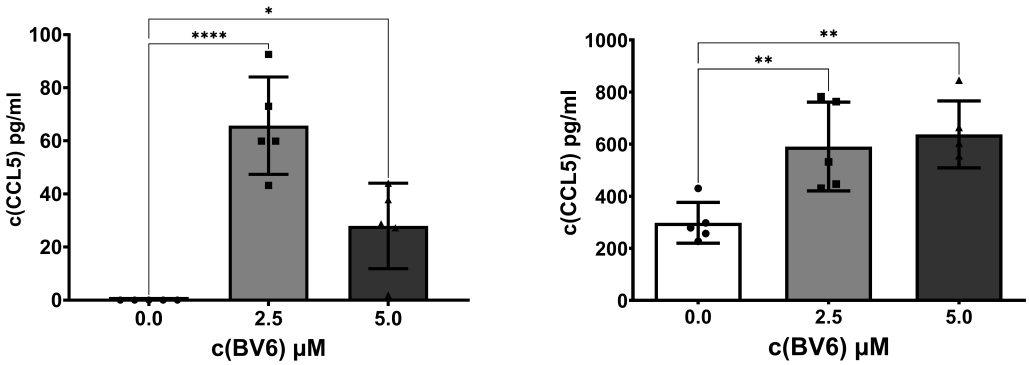

(a) ELISA analysis of secreted CCL5 in RH30 cells

(b) ELISA analysis of secreted CCL5 in RD cells

Fig. 5.48: ELISA analysis of secreted CCL5 in BV6 treated RH30 (a) or RD (b) cells. Data is depicted as mean ± SD, N = 5, analysis by one-way ANOVA, *: $p \leq 0.05$, **: $p \leq 0.01$, ****: $p < 0.0001$.

The observed increased CCL5 secretion and transcription by BV6 was additionally analyzed by a third method of staining intracellular stored CCL5 (fig. 5.49). Figures 5.49(a) and (c) depict microscopic images of RH30 and RD cells upon BV6 stimulation for 24 h and intracellular stained targeting CCL5. In both RMS cell lines BV6 treatment increases the fluorescence intensity of CCL5 stained granula. The number of these CCL5 positive stained granula were quantified and are depicted in fig. 5.49(b) and (d). BV6 at 5 μM leads to a significant increase of the number of CCL5 positive stained granula in both RMS cell lines.

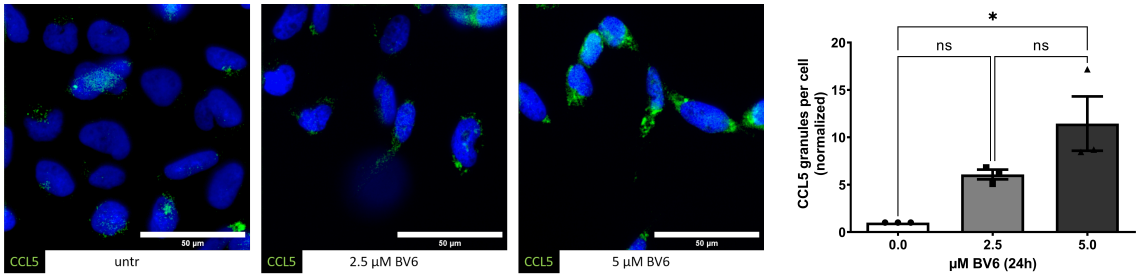

(a) Immunofluorescence staining targeting CCL5 in RH30 cells

(b) Quantification of CCL5 granules within RH30 cells

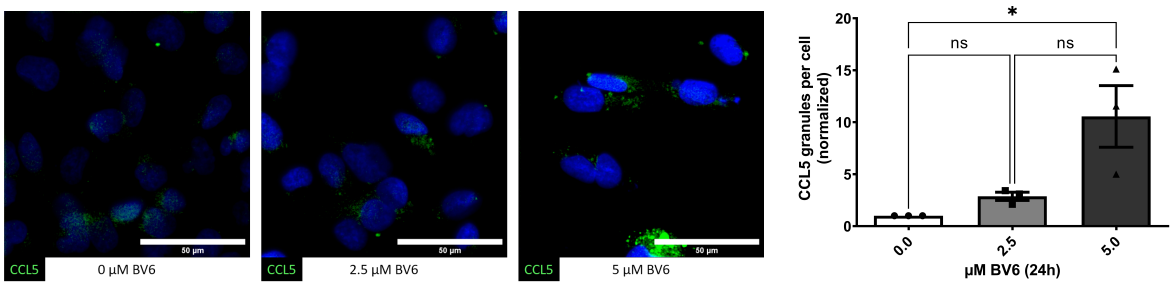

(c) Immunofluorescence staining targeting CCL5 in RD cells **(d)** Quantification of CCL5 granules within RD cells

Fig. 5.49: Immunofluorescence staining of intracellular stored CCL5 in BV6 treated RH30 (a) or RD (c) cells for indicated concentration for 24 h. Quantification of intracellular CCL5 positive granules are shown for RH30 (b) and RD (d) cells. Data is depicted as mean ± SEM, N = 3, analyzed by one-way ANOVA, ns: $p > 0.05$, *: $p \leq 0.05$. Scale bar = 50μm, using a 60× objective

To evaluate the function role of CCL5 within the BV6 induced sensitization, a CRISPR/Cas9 based knock-out of *CCL5* in RH30-GFP cells was performed.
Figure 5.50 shows the binding sites of three chosen guide RNAs. The knock-out was performed with all three gRNAs simultaneously. As an assay control, a non human targeting guide RNA control (gCtrl) was used in parallel.

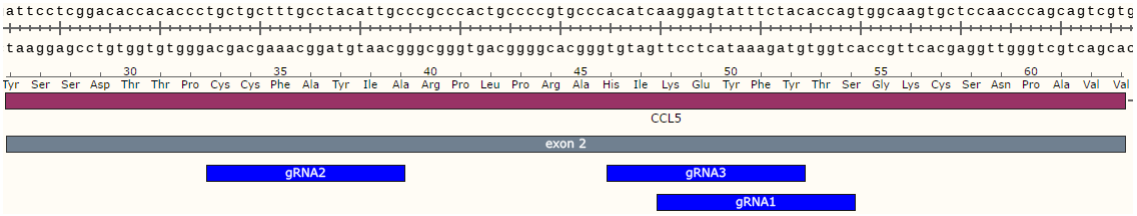

Fig. 5.50: Binding sites of guide RNAs targeting exon 2 within *CCL5*. Depicted is only exon 2.

The knock-out efficiency can be seen in fig. 5.51(a), showing an agarose gel of PCR amplified exon 2 of *CCL5* of parental RH30-GFP, two RH30-GFP gCtrl gRNA clones and two RH30-GFP *CCL5* targeting gRNA clones. It can be seen, that parental RH30-GFP cells and both RH30-GFP-gCtrl clones show an expected signal of *CCL5* exon 2. Both *CCL5* targeting gRNA clones show a different signal pattern. For clone RH30-GFP-CCL5-1, a predominant signal at a lower height, as expected, is visible. Additionally, a faint signal at the expected height and one faint signal above the expected height can be seen. Clone RH30-GFP-CCL5-2 shows three equal intense signals at different heights, one at the expected form and two signals at lower heights.
Going back to the binding sites of the targeting guide RNAs (fig. 5.51(b), a putative cleavage fragment can be deduced situated between gRNA1 and gRNA2 with

an approximate size of ≈60 base pairs (bp). The most intense signal of the clone RH30-GFP-CCL5-1 might be possibly ≈60 bp below the expected height of exon 2. Sequencing of this PCR product of clone RH30-GFP-CCL5-1 (fig. A.1) revealed a missing fragment situated within the approximate gRNA1 & gRNA2 binding sites with an approximate size of 58-59 bp (fig. A.2).

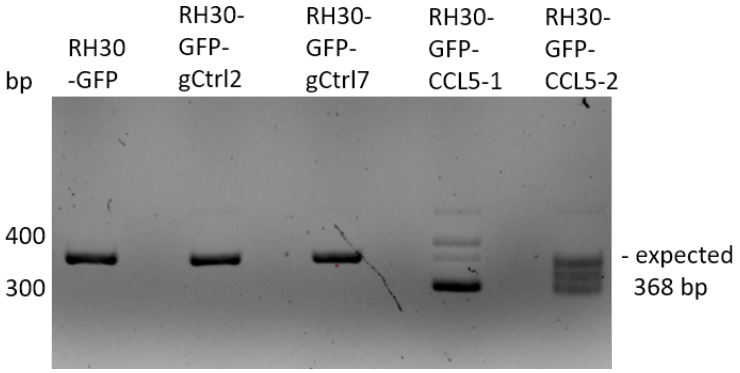

(a) Agarose gel of amplified exon 2 of *CCL5*

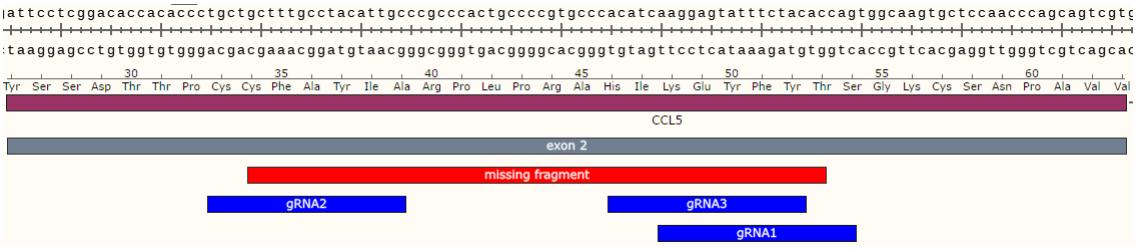

(b) Putative cleavage fragment within exon 2 of *CCL5*

Fig. 5.51: Detection of cleaved *CCL5* in RH30 knock-out cells. (a): agarose gel of parental RH30-GFP cells, guide control and CCL5 knock-out clones of RH30-GFP cells, (fig. (b)) deduced cleaved fragment.

As an additional validation of the putative *CCL5* knock-out, fig. 5.52 shows an agarose gel with PCR amplified *CCL5* mRNA of parental RH30-GFP, guide control clone 2 and the interesting clone 1 of the *CCL5* targeting gRNA. As evident, the parental RH30-GFP and guide control (RH30-GFP-gCtr2) cells show a signal for *CCL5* mRNA upon BV6 treatment. In contrast, clone RH30-GFP-CCL5-1 does not show any signal for *CCL5* mRNA upon BV6 treatment.

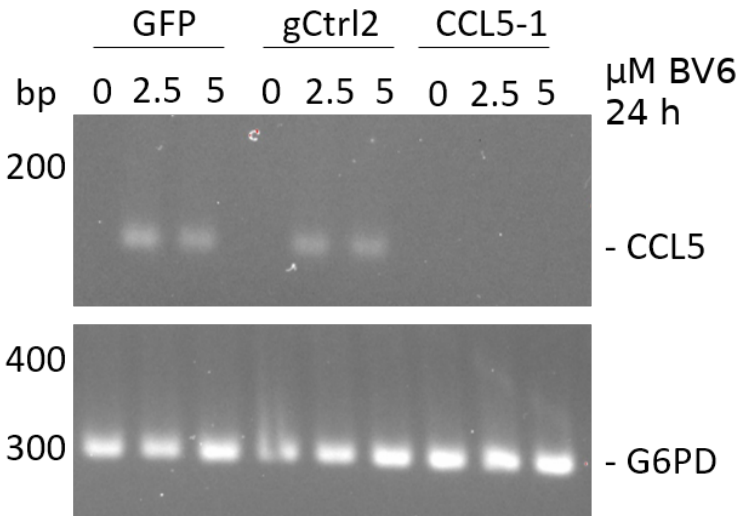

Fig. 5.52: Knock-out validation on mRNA level for *CCL5*. Agarose gel showing amplified *CCL5*, and *G6PD* as reference gene, of RH30-GFP cells upon BV6 treatment at different concentrations for 24 h stimulation.

For further functional assay the guide control clone RH30-GFP-gCtrl2 and *CCL5* targeting gRNA clone RH30-GFP-CCL5-1 were used. Using these clones spheroids were generated, BV6 pre-treated and co-cultivated with NK cell at an E:T ration of 1:1. Figure 5.53 illustrates the results of these spheroid experiments. PI and GFP fluorescence quantification and calculation of the PI/GFP ratio (fig. 5.53(b)) shows no difference between the gCtrl and *CCL5* knock-out spheroids. In both modified cell lines BV6 induces a significant sensitization towards NK cell mediated killing, illustrated by the increased PI/GFP ratio upon NK cell addition.
Examination of the microscopic images of GFP fluorescent spheroids (fig. 5.53(a)) indicate a different growth behaviour of untreated RH30-GFP-gCtrl2 spheroids compared to RH30-GFP-CCL5-1 spheroids. That is, *CCL5* knock-out spheroids seem to generate a highly fluorescent rim, comparable to parental wild type spheroids (fig.5.13(a)). Whereas, gCtrl spheroids seem to grow in a more loose aggregation.
A kinetic killing analysis (fig. 5.53(c)) did not show a significant difference between BV6 pre-treated gCtrl spheroids or *CCL5* knock-out spheroids co-cultured with NK cells. However, a significant difference is evident comparing the influence of BV6 and NK cells within the clones, not between the clones.

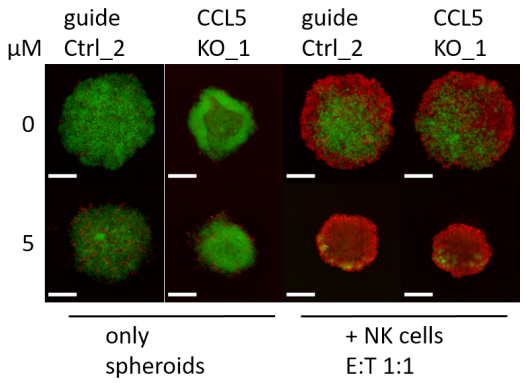

(a) Microscopic illustration of BV6 treated guide control and *CCL5* knock-out RH30 spheroids in co-cultivation with NK cells

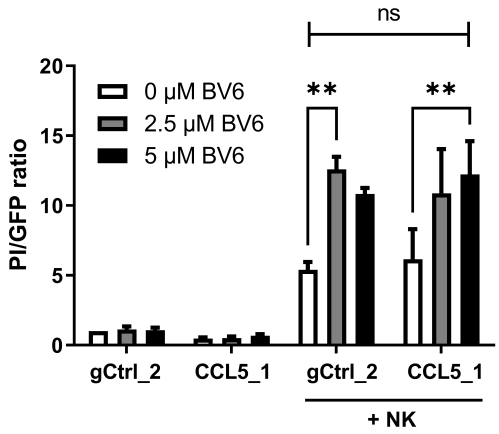

(b) Quantification and ratio calculation of PI to GFP fluorescence in BV6 treated guide control and *CCL5* knock-out RH30 spheroids in co-cultivation with NK cells. N = 3

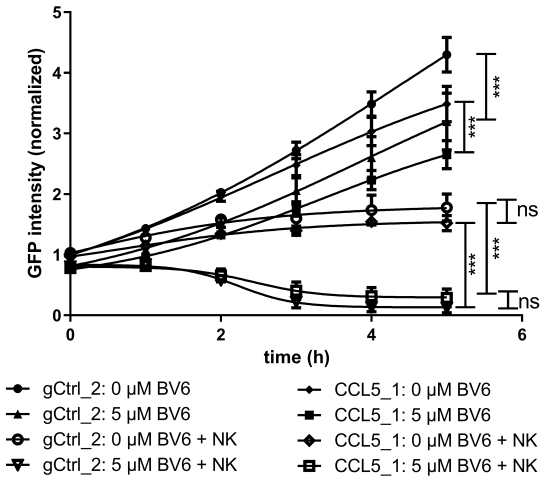

(c) Kinetic analysis of quantified GFP fluorescence in BV6 treated guide control and *CCL5* knock-out RH30 spheroids in co-cultivation with NK cells. N = 5

Fig. 5.53: Influence of *CCL5* knock-out in RH30 spheroids upon BV6 sensitized NK cell mediated killing. Data is depicted as mean ± SEM, analysis by two-way ANOVA, ns: $p > 0.05$, **: $p \leq 0.01$, ***: $p \leq 0.001$.

5.3.3.2 Somatostatin receptor 2

The second gene of interest to perform a more detailed analysis on was the somatostatin receptor 2 (*SSTR2*). As can be seen in table 5.1 *SSTR2* is among one of the identified top candidates in RH30 and up-regulated upon BV6 treatment.
SSTR2 exists in two different transcript variants, *SSTR2A* and *SSTR2B*. The first task was, to design qRT-PCR primers to distinguish both transcript variants from each other. Figure 5.54 shows a schematic representation on how this primer strategy was chosen. The primer indicated with "SSTR2", detects both transcript variants. For each transcript variant two different primer pairs were designed. The first of both binds within the variant tail. The second of both generates an amplicon spanning the position at which the variants begin.

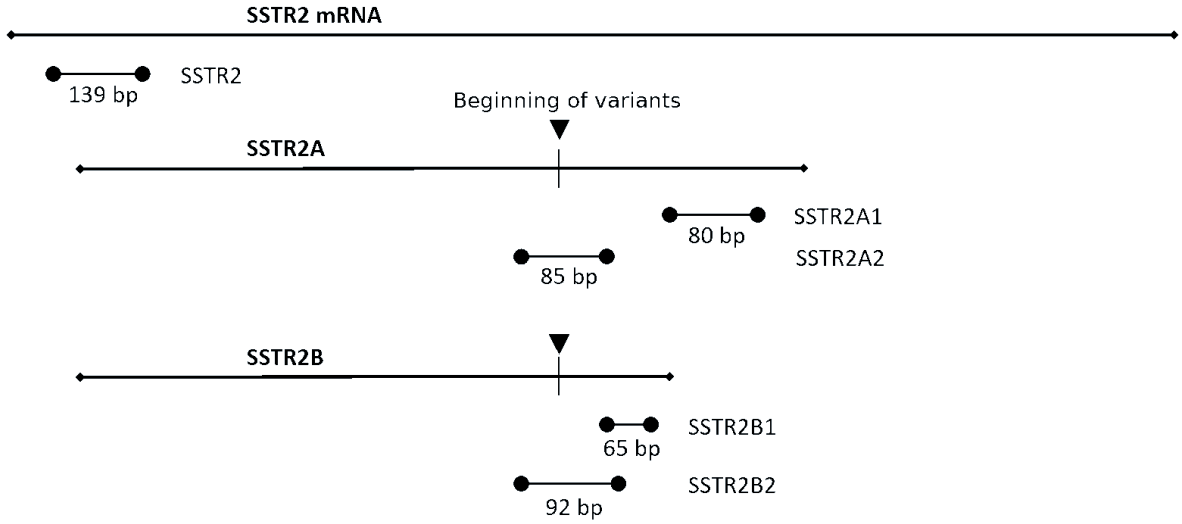

Fig. 5.54: Schematic depiction of primer design to distinguish between *SSTR2* transcription variants. Length o the respective amplicon is depicted as a size in bp.

Figure 5.55 depicts the qRT-PCR analysis for the primer "SSTR2", detecting both transcript variants. Further it shows both primers for detecting *SSTR2A*, i.e. "SSTR2A1" and "SSTR2A2". Figure 5.55(a) illustrated an agarose gel showing the respective amplicons, all used primers show a signal at the expected amplicon size. As an additional quality control the melting curves of the respective synthesized amplicons are generated and depicted in 5.55(b)-(d). All generated melting curves show one discrete peak at their respective melting temperature, no additional peaks are visible. It validates that only one respective PCR amplicon product was generated.
Figure 5.56 shows the agarose gels and melting curves for the primers detecting the *SSTR2B* transcript variant. As can be seen in figure 5.56(a), no signal ca be detected at

the expected height for the amplicon. Further, figure 5.56(b)/(c) illustrates the melting curve, where no discrete peak is visible, instead a variety of small peaks with varying melting temperatures. The melting curves validate the absent signals on the agarose gel, no specific *SSTR2B* amplicon was generated.

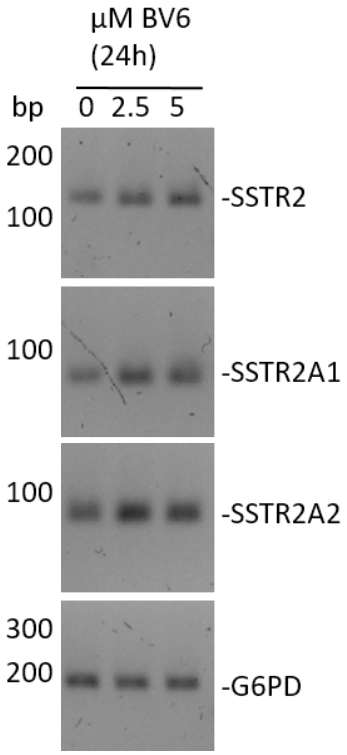

(a) Agarose gel of different primer pairs to detect *SSTR2* and variant "A"

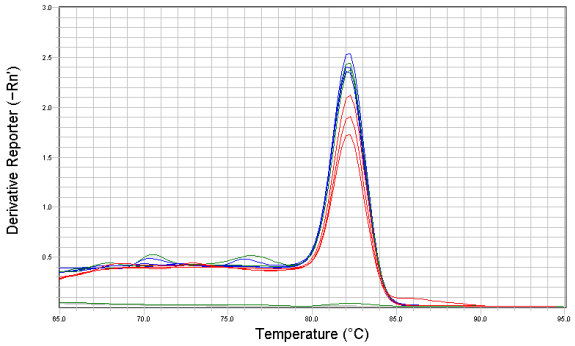

(b) Melting curve for *SSTR2*

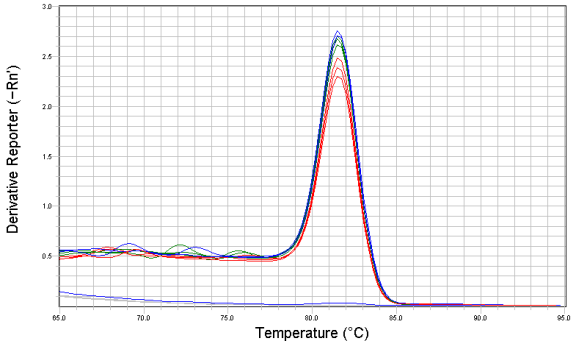

(c) Melting curve for *SSTR2A1*

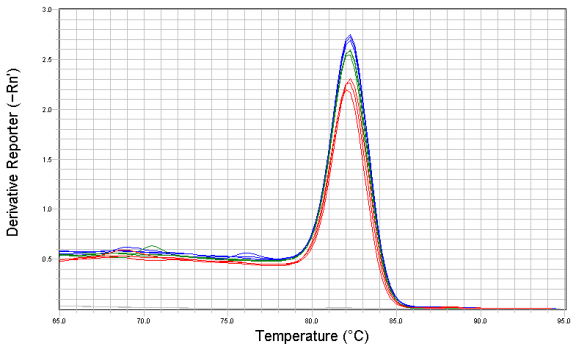

(d) Melting Curve for *SSTR2A2*

Fig. 5.55: Analysis of *SSTR2A* transcript variant on agarose gel and by melting curve. Primer pair "SSTR2" detects both transcript variant A and B. Melting curves are representative for six independent replicates.

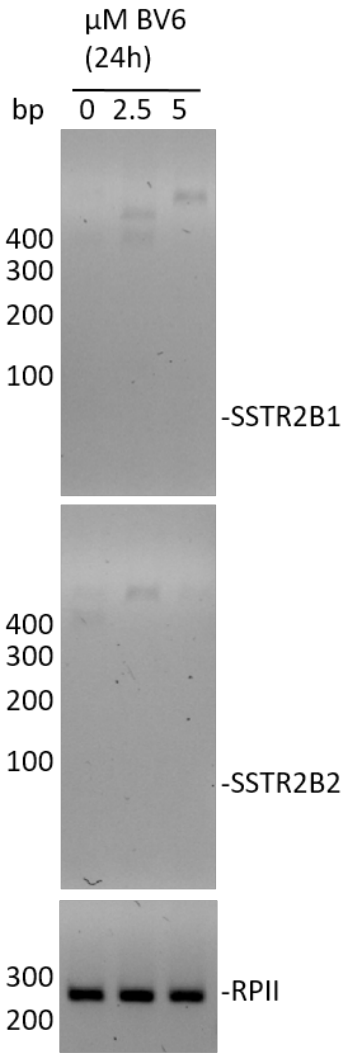

(a) Agarose gel of different primer pairs to detect *SSTR2B* variant

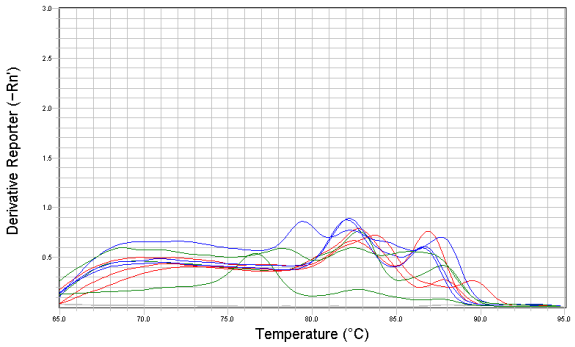

(b) Melting curve for *SSTR2B1*

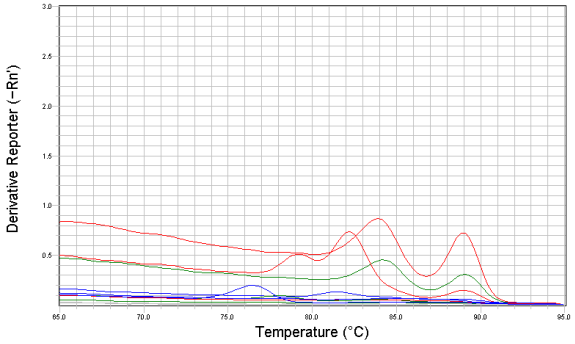

(c) Melting curve for *SSTR2B2*

Fig. 5.56: Analysis of *SSTR2B* transcript variant on agarose gel and by melting curve. Melting curves are representative for six independent replicates.

Figure 5.57 shows *SSTR2* and *SSTR2A* mRNA fold change values fro RH30 cells stimulated with BV6 for 24 h. A significant BV6 induced up-regulation of *SSTR2A* in RH30 cells can be seen using different primer pairs to detect *SSTR2A*. These results validate the RNAseq identified up-regulation of *SSTR2*.

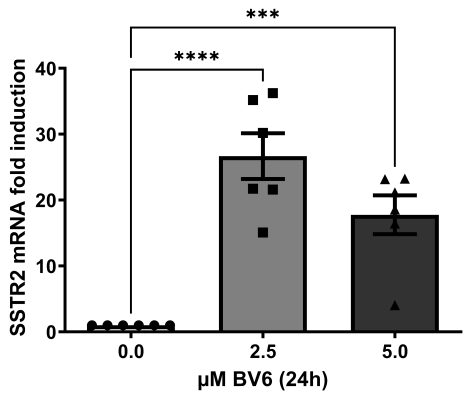

(a) qRT-PCR analysis of *SSTR2*

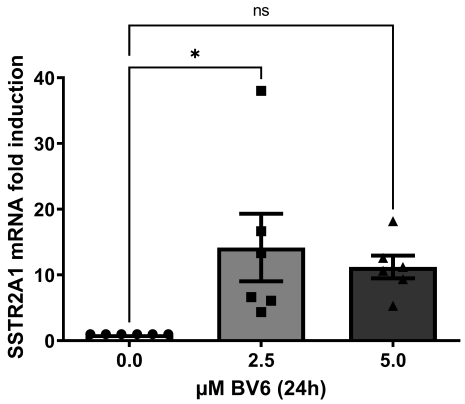

(b) qRT-PCR analysis of *SSTR2A1*

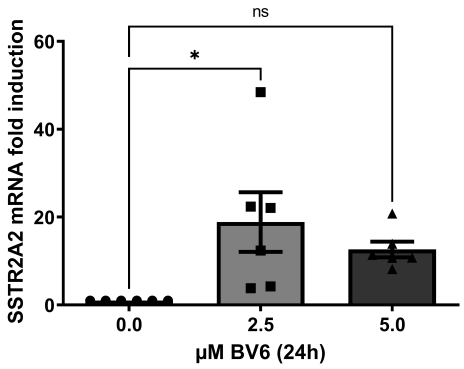

(c) qRT-PCR analysis of *SSTR2A2*

Fig. 5.57: qRT-PCR analysis of *SSTR2* and transcript variant A in BV6 treated RH30 cells for 24 h. Data is depicted as mean ± SEM, N = 6, analysis by one-way ANOVA, ns: non significant, *: $p \leq 0.05$, ***: $p \leq 0.001$, ****: $p < 0.0001$.

As described, NIK might has a central role in mediating the transcriptional regulation of BV6. Figure 5.58 depicts the qRT-PCR results analyzing the *SSTR2A* transcription in BV6 treated *NIK* knocked-down RH30 cells. Knock-down of *NIK* suppresses the BV6 induced up-regulation of *SSTR2A*, leading to the assumption that *SSTR2* is a NIK mediated target gene.

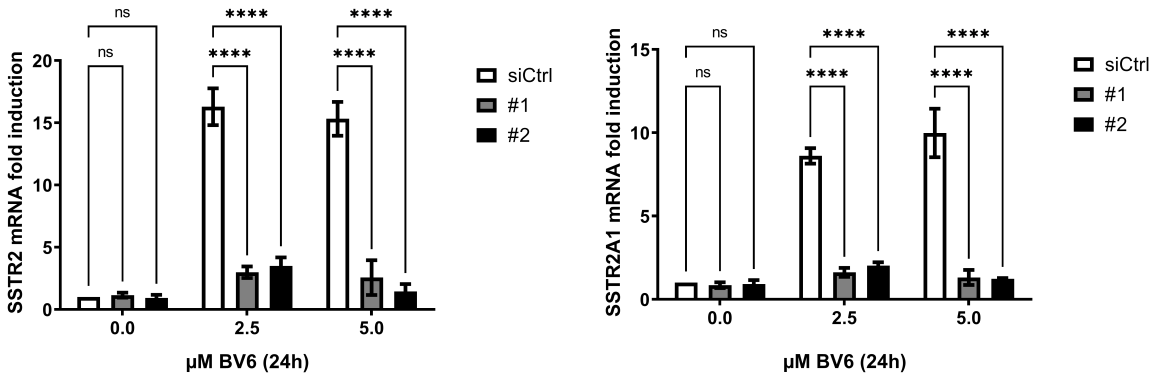

(a) qRT-PCR analysis of *SSTR2* **(b)** qRT-PCR analysis of *SSTR2A1*

Fig. 5.58: qRT-PCR analysis of *SSTR2A* expression within BV6 treated RH30 cells upon *NIK* knock-down. Data is depicted as mean ± SEM, N = 3, analysis by two-way ANOVA, ns: non significant, ****: $p < 0.0001$.

Previous analysis only validated the up-regulated transcription of *SSTR2* by BV6, but missing the analysis on protein level. Figure 5.59 depicts a flow cytometric surface staining targeting SSTR2. The used antibody (tab. 4.6) does not distinguish between the two different transcription variants.

Figure 5.59(a) illustrates a BV6 induced increase of SSTR2 surface presentation on RH30 cells. Deduced by the peak shift towards higher fluorescence intensities upon BV6 treatment. Figure 5.59(b) depicts a significant increase of the median fluorescence intensity (MFI) for SSTR2 staining on RH30 cells upon BV6 treatment.

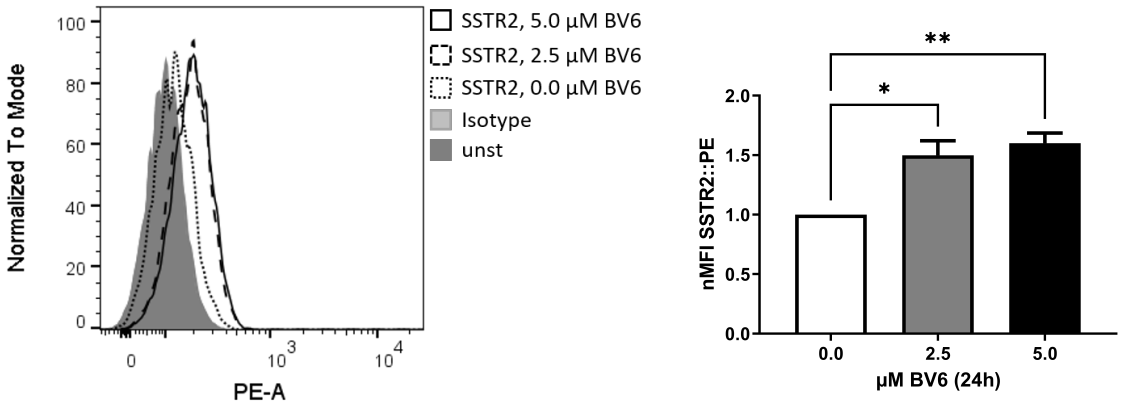

(a) Flow cytometry analysis of SSTR2 **(b)** Analysis of nMFI of SSTR2:PE

Fig. 5.59: Flow cytometric analysis of SSTR2 presentation upon BV6 treatment on RH30 cells (a). Analysis of normalized median fluorescence intensity (MFI) to untreated control (b). Data is depicted as mean + SEM, N = 3, analysis by one-way ANOVA, *: $p \leq 0.05$, **: $p \leq 0.01$.

Octreotide mimics the endogenous protein somatostatin and is able to activate SSTR2. Figure 5.60 depicts cell death measurements, dead cells identified by PI/Hoechst staining of RH30 cells, co-treated with 5 μM BV6 and various concentrations of octreotide. It can be seen, that Octreotide does not induce cell death at any used concentration in RH30 cells. BV6 alone does induce cell death in RH30 cells. Upon co-treatment of BV6 with Octreotide no significant increased cell death is visible. Although not significant, at high Octreotide concentrations of 100 μM the co-treatment with BV6 might show a higher cell death susceptibility than BV6 alone.

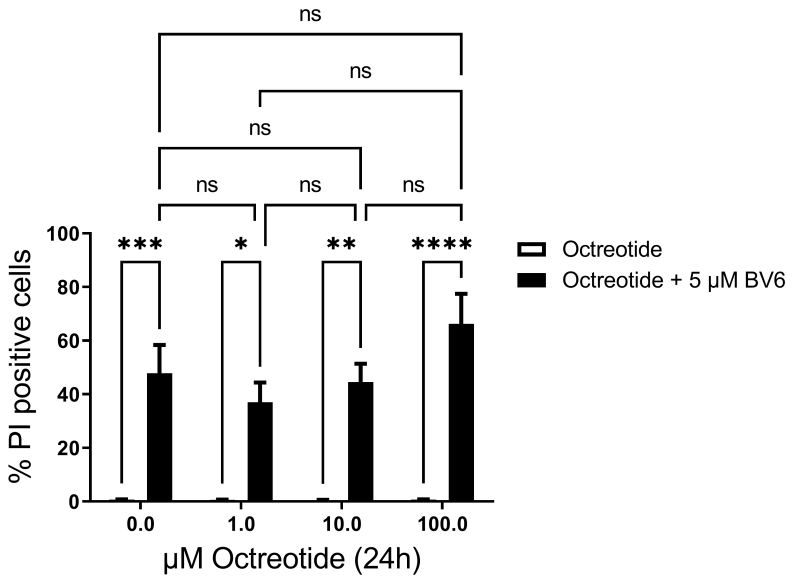

Fig. 5.60: Cell death measurement, by PI/Hoechst staining of RH30 cells upon co-treatment of BV6 (5 μM) with Octreotide for 24 h. Data is depicted as mean + SEM, N = 5, analysis by two-way ANOVA, ns: non significant, *: $p \leq 0.05$, **: $p \leq 0.01$, ***: $p \leq 0.001$, ****: $p < 0.0001$.

6 Discussion

As described above, this dissertation aims at dissecting the observed sensitizing effect by BV6 towards an NK cell mediated attack. This study is based on previous work by Fischer et al., using BV6 in combination with IL-2 activated NK cells, and by Rettinger et al., using BV6 in combination with cytokine induced killer (CIK) cells. Both studies lack a mechanistic description on how BV6 induces this sensitization. Although, they propose an involvement of caspase and TRAIL.
The following chapter will incorporate the results and collected evidence of the study in hand (section 5), to suggest an underlying mechanism of this BV6 sensitization.
Fist, the observed BV6 sensitizing effect will be elaborated and validated in multicellular RMS tumor spheroids. Further, cell death inducing mechanisms within the RMS target cells will be evaluated.
In a second part, the intracellular signaling pathways leading to a transcriptional induction by BV6 will be discussed. NIK, being in a direct interaction with cIAP1/2 will be presented as a central player for this transcriptional regulation.
Further, selected genes of interest (*CCL5* and *SSTR2*) identified by an exploratory RNA sequencing approach will be discussed.
The unique feature of this study is that multicellular tumor spheroids, as a more *in vivo*-like structure, are used to describe the effect and its putative molecular mechanism. Further, it is the first time in RMS cells that a BV6 changed transcriptome was identified, validated and selected genes of interest further analyzed.

6.1 BV6 as a sensitizer towards an NK cell attack

6.1.1 Application of subtoxic concentrations of BV6

In previous studies, BV6 was used to induce cell death in co-treatment with other cytotoxic agents, e.g. TRAIL [112], reactive oxygen species (ROS) [157] or IFNα [158]. In this study, BV6 was again not used as a single treatment, but in combination with cytotoxic NK cells. The first objective was, to validate that subtoxic concentrations of BV6 were used for all cell types, the rhabdomyosarcoma (RH30 and RD) cells and primary IL-15 activated, expanded NK cells. Throughout this study two BV6 concentrations were used, one subtoxic (2.5 μM) and one concentration (5 μM) close to the EC50 value for both RMS cell lines. Within the dose-response curves for the RMS (fig. 5.1) and NK (fig. 5.11) cells the chosen concentrations appear not to be highly toxic. Both chosen concentrations are within the range of previously used concentrations for

BV6 in co-treatment with other compounds. Fischer et al. had to use a higher BV6 concentration of 10 μM to see the sensitizing effect in RMS cells towards NK cells killing [25]. The reason for this difference might be the different expansion protocol for the NK cells, Fischer et al. used IL-2. Whereas the study in hand used IL-15. BV6 concentrations of 2.5 and 10 μM were used to induce a sensitizing effect in hematological and solid tumor entities in combination with CIK cells [121]. Others studies used BV6 in concentrations ranging from 0.5-10 μM, either alone or in combination with ROS [112, 158].
BV6 mimics the molecular function of Smac, i.e. the inhibition of inhibitor of apoptosis proteins (IAPs) [105]. Figures 5.2 & 5.3 depicts western blots of the rapid IAP degrading effect in RH30 and RD cells upon BV6 treatment. cIAP2 is not depicted within western blot panel for RD cells (fig. 5.2(b)). Own observations could validate a previous study showing cIAP2 to be absent in RD cells [159]. In both, RH30 and RD spheroids, cIAP1 is being degraded upon BV6 treatment for 24 h. In contrast to 2D, no cIAP2 degrading effect could be seen in 3D cultures at 24 h of BV6 treatment. This observation might be explained by a putative BV6 induced up-regulation and translation of cIAP2 at 24 h BV6 stimulation. A very strong transcriptional up-regulation of *cIAP2* is present in RH30 cells and spheroids upon BV6 treatment (fig. 5.32 & 5.34). In addition, knock-down of *NIK* could suppress the re-expression of *cIAP2*. It confirms an initial cIAP2 degradation, which might be masked by a NIK dependent re-expression. Concluding that BV6 putatively does induce cIAP2 degradation in spheroids comparable to 2D cultures, but a possible re-expression masks this effect at the investigated time point.

Further comparison of IAP degradation in 3D versus 2D RMS cultures showed an XIAP degradation exclusively in RMS spheroids, but not in 2D monolayer cultures. BV6's inability to degrade XIAP in 2D monolayer cell cultures could previously observed in pediatric ALL [109], colorectal cancer cell lines [160] and lung cancer cells [161]. XIAP is seemingly a more robust target for Smac mimetic induced IAP degradation, as treatment with the Smac mimetic Birinapant was also not able to degrade XIAP in a variety of colon cancer cell lines and melanoma cell lines [144, 162, 163].
Gallardo-Pérez et al. demonstrated in breast cancer, head and neck cancer and cervical cancer spheroids the importance of NF-κB signaling pathways and down-stream XIAP up-regulation as a driver for spheroidic growth and drug resistance. Knock-down of XIAP re-sensitized tumor spheroids to cytotoxic drugs and could reduce the tumor volume [164]. A similar effect might have occurred here in BV6 treated RMS spheroids. This study shows a marked XIAP degradation upon BV6 in RMS spheroids, which might be a driver to re-sensitize RMS spheroids to an NK cell killing mechanism. How-

ever, XIAP degradation by single BV6 treatment in RMS spheroids could not reduce the spheroidic growth. In contrast to Gallardo-Pérez et al., where siRNA mediated XIAP knock-down reduced spheroidic volume [164]
As mentioned above, the chosen BV6 concentrations were in the subtoxic range for primary IL-15 activated, expanded NK cells (see fig. 5.11). Previous studies showed a slight cytotoxicity of BV6 towards other immune cells, 10 μM BV6 could reduce the viability of monocyte derived dendritic cells to 75 % [165], the same BV6 concentration could induce ≈20-30 % cell death in CIK cells [121]. IL-2 activated NK cells demonstrated a high resistance towards BV6 induced cell death, only a very high concentration of 50 μM BV6 reduced the viability of IL-2-activated NK cells to ≈ 60 % [25]. Here, the presented data on BV6 induced cell death in IL-15 activated NK cells shows a cell death induction of ≈ 20 % at a concentration of 10 μM BV6.
Overall it shows a higher resistance towards BV6 induced cell death in immune cells, as the same BV6 concentration induced > 80 % cell death in RMS cells (fig. 5.1). One mechanism why NK cells might be more resistant towards BV6, could be an up-regulation of anti-apoptotic BCL-2 family proteins, e.g. MCL1 [166] and activation of survival signaling pathways during the IL-15 activation and expansion process [167].

6.1.2 Multicellular RMS tumor spheroids as a co-culture model

BV6 induces a molecular mechanism in RMS cells to enhance the susceptibility towards NK cell mediated killing. Figure 5.12 depicts this effect in a 2D flow cytometry based cytotoxicity assay. It resembles previous studies, using a similar 2D flow cytometry methodology. BV6 could sensitize RH30 and RD cells to an immune attack by CIK [121] or IL-2 activated NK [25] cells. Not only the Smac mimetic BV6 enhances the susceptibility, but a variety of other Smac mimetics, e.g. an unspecified Smac mimetic by TetraLogic Pharmaceuticals increased the killing of Hodgkin lymphoma cells by NK cells [118], APG-1387 by Ascentage Pharma Group Corp. Ltd. could lower the resistance of hepatocellular carcinoma cells towards an NK cell attack [119] or Birinapant in combination with CAR T-cells showed an enhanced killing effect, if combined [120]. Further, a pro-Smac fusion protein with caspase-8 or granzyme B cleavage sites demonstrated an increased killing effect upon NK cell co-cultivation, possibly mediated by an increased release and pro-Smac signaling upon NK cell engagement [117]. The effect of Smac mimetic sensitization is not only present in combination with immune cells, but applies to immune stimulation on tumor cell side, as the Smac mimetic LCL-161 by Novartis showed an increased cytotoxicity on tumor cells if combined with oncolytic viruses [168, 169].
Again, these studies either used 2D flow cytometric cytotoxicity assays [25, 117, 118,

121], and/or used artificial models of immunocompromised mice [119, 168].
Following the 3R principles of animal research (Replacement, Reduction, Refinement), we utilized a multicellular RMS spheroid model, as an *in-vivo*-like model resembling the solid rhabdomyosarcoma tumor phenotype more closely [26, 170–172].
Having a more robust 3-dimensional structure, might influence the migratory behaviour of NK cells, by that reduce the killing efficiency towards those tumor spheroids. Figure 5.25 demonstrates that this is not the case, as NK cells are still able to penetrate into RH30 and RD spheroids. This ability was previously published by our group in 2022 [26]. Further studies showed an NK cells infiltration into cervical carcinoma spheroids [173], NK cells migrating into colorectal cancer spheroids [174] and NK and T cells infiltrating colon cancer spheroids [175]. Concluding, that immune cells in general are able to penetrate tumor spheroids and this characteristic is not limited to RMS spheroids.
Further, the study in hand shows no effect of the BV6 pre-treatment of the RMS spheroids on the NK cell migratory behaviour, no pro- or anti-migratory phenotype is observable (see fig. 5.26).
However, this BV6 pre-treatment of RH30 and RD spheroids could induce a higher killing by NK cells (see fig. 5.13). This observation validates the BV6 sensitizing effect previously observed and described in 2D and successfully transfers the effect to the 3D RMS spheroid model. This enhanced killing effect is even more robust and pronounced in RMS spheroids, as compared to 2D RMS cell cultures. A side-by-side comparison of 2D vs. spheroid killing shows that 2D cultured untreated RD cells are more resistant towards an NK cell attack, than 2D cultured RH30 cells, as observed by Ray et al. [176]. 3D RMS spheroid cultures demonstrate a different killing behaviour. Here, RH30 spheroids are more resistant to an NK cell attack. NK cell are able to control the growth of RD spheroids. However, both models show the BV6 sensitizing effect, leading to an increased NK cell mediated killing. The difference of this NK cells attack, of 2D vs. spheroid, might be explained by a changed proteome upon spheroid formation compared to 2D monolayer cultures, as was previously identified for hepatocellular carcinoma spheroids [177] and head and neck cancer spheroid [178]. Schmidt et al. identified a global transcriptional up-regulation of genes associated to cell adhesion and xenobiotics metabolism in head and neck cancer spheroids compared to monolayer cultures [178]. A similar effect was reported in hepatocellular carcinoma spheroids, an increased expression of genes associated to extracellular matrix, cytoskeleton and metabolism was observed [177]. Here, BV6 does induce the degradation of XIAP exclusively in RMS spheroids, but not in 2D cultured cells. Leading to an assumption that XIAP might be a main facilitator of the RMS killing resistance to NK cells.

6.1.3 Role of death ligands within BV6 sensitization

Chemotherapy and cytotoxic agents other than BV6, are also able to sensitize tumor cells towards an immune cell attack. For example, bortezomib increases DR5 on multiple myeloma cell surface and increases NK cell killing [139]. In this line, BV6 and other IAP antagonists show a synergistic effect together with TRAIL in inducing cell death in pancreatic, bladder or breast cancer cells [143, 179, 180]. Another aspect, why the TRAIL and TRAIL-receptor system might be important is that NK cells express the ligand TRAIL on their cell surface [25, 146]. This enables NK cell to activate the extrinsic cell death pathway in their target cells.
The results of a TRAIL and DR5 involvement was presented in sections 5.1.3 and 5.1.4.1. Both, RH30 and RD cells express DR5 on their cell surface and are able to activate TRAIL dependent cell death, comparable as previous studies demonstrated [25, 181]. Further, it could be illustrated that BV6 induces the mRNA up-regulation and increases the cell surface presentation on RH30 and RD cells (fig. 5.6 - 5.9). Co-treatment of BV6 with TRAIL shows an additive cell death induction (fig. 5.10). Similar effects were observed in hepatocellular carcinoma cells, a novel Smac mimetic APG-1387 enhanced the susceptibility towards a TRAIL and caspase dependent form of cell death, putatively involving RIPK1 activity [119]. Other cytotoxic compounds, e.g. a casein kinase II inhibitor, increases the recruitment of pro-caspase-8 to the DISC and increases the sensitivity towards a TRAIL and caspase dependent cell death in rhabdomyosarcoma cell lines [182]. Additionally, Komdeur et al. demonstrated that doxorubicin restores the sensitivity towards a TRAIL dependent cell death mechanism in rhabdomyosarcoma cell lines [183].
However, in our RMS spheroid model where pre-treatment with BV6 induces a sensitization towards an NK cell attack no TRAIL dependency was observed, as TRAIL neutralization did not suppress the NK cell mediated killing of RMS spheroids (fig. 5.15). Our finding opposes a putative TRAIL dependency, which could be observed by Fischer et al. The difference might again be explained by the different NK cell expansion protocols and killing assays applied, IL-2 activated NK cells and a 2D flow cytometry based co-cultivation model [25], compared to IL-15 activated NK cells and a 3D spheroid based cytotoxicity assay used in this study. Although seemingly similar in function IL-2 and IL-15 might differ in their property to activate NK cells, resulting in a different activation pattern and killing preference. Additionally, the RMS spheroids might have a different exhibition property of DR5 on their cell surface compared to 2D cultured RMS cells. The outer cells within the spheroid might have different surface presenting proteome, than cells further inwards of the spheroid, leading to a different NK cell attack response regarding the TRAIL dependency.

Apart from TRAIL and TRAIL-receptor system, RMS cells are equipped with the death receptor TNFR1. However, neutralization of TNFα by continuous addition of Enbrel had no impact on the BV6 induced sensitization towards an NK cells attack (fig. 5.17). This implies a TNFα independent mechanism of BV6 induced sensitization. This finding is in contrast to previous investigations, describing a BV6 induced TNFα autocrine feedback mechanism driving BV6 induced cell death [115, 158]. However, these studies did not utilized a cytotoxic lymphocytes in combination with BV6 but either INFα [158] or used a TNFR1 knock-down to illustrate a TNFα dependency [115].

One major death inducing ligand on NK cells is FasL (CD95L). However, this thesis shows evidence that the receptor Fas is not expressed on RH30 and RD cells (see fig. 5.4 and 5.5). Thereby, this study validates a previous study showing a similar result [181].

A second main mechanism of NK cells to induce cell death in their target cells is the secretion of cytotoxic granula, which contain among others granulysin, granzymes and perforin [184, 185]. During the serial killing activity of NK cells, they can rapidly switch from death ligand mediated to cytotoxic granula mediated killing [124].
A granzyme B inhibitor (zAAD-CMK) was added continuously to the BV6 pre-treated RMS spheroid NK cell co-culture, to evaluate the functional role of granzyme B (see fig. 5.18). Previous investigations could show that zAAD-CMK reduced the cytotoxicity of LAK cells against oral squamous cancer cells [186], suppressed activation induced cell death in T-cell subsets [187] and blocked NK cell cytolytic activity targeting myelogenous leukemia cell line [188] at concentrations similar to the zAAD-CMK concentrations used in this presented study. Here, the addition of zAAD-CMK into the co-culture of BV6 pre-treated RMS spheroids and NK cells did not show any effect on the NK cell mediated cytotoxicity. The calculated PI/GFP ratio, as a cell death read-out, indicates no significant change of induced cell death upon co-treatment with zAAD-CMK (fig. 5.18(b) and 5.18(d)).
However, the kinetic analysis of GFP fluorescence (RMS spheroids) over the whole co-cultivation period depicts a slight upwards trend if BV6 pre-treated RH30 spheroids co-cultivated with NK cells were co-treated with zAAD-CMK (fig. 5.18(e)). This minor rescue effect might indicate a partial involvement of the granzyme B mediated killing mechanism within the BV6 induced sensitization towards NK cell attack. BV6 pre-treated RD spheroids co-cultivated with NK cells do not show this pronounced rescue effect, rather a slight divergence on day 3 of co-cultivation. Putatively different RMS subtypes might be killed differently by NK cells.

6.1.4 Involvement of caspases in NK cell mediated killing

Ligation of death receptors leads to the activation of intracellular extrinsic apoptotic pathways. Caspases are bound to these receptor complexes and are activated upon death ligand binding. As a Smac mimetic, BV6 is able to degrade IAP proteins in both RMS cell lines and spheroids. Further, IAP degradation releases caspases previously bound by IAP proteins. Based on this mechanism, a hypothesis was formulated of a putative caspase involvement within the BV6 mediated sensitization.
Indeed, treatment with BV6 alone leads to an activation of caspases. In 2D cultured RH30 cells BV6 induces a minor cleavage and activation of caspase-8, 9 and 3. Western blot shows that this minor activation is only visible at very late time points (24 h). Similar effects are visible for RD cells, cultured in 2D. Here, caspase-8 seems to be not as strongly activated compared to RH30 cells, caspase-9 is activated at a similar level. Caspase-3 might be higher activated in RD cells compared to RH30 cells. Caspase cleavage upon treatment with Smac mimetics is not a novel discovery, as it is one of the main functions of Smac mimetics and an intended mode of action [105, 110, 189]. The study in hand validates this intended mode of action for BV6 in RMS cells and expands this molecular function to RMS spheroids.

BV6 as a single treatment is not able to induce cell death at the used concentrations. Co-cultivation with NK cells and their cytotoxic function is necessary as a second hit to fully activate cell death execution (fig. 5.12 and 5.13). Western blot analysis show that combination of BV6 pre-treatment with NK cell co-cultivation in RMS-GFP spheroids does not lead to an enhanced generation of the active caspase-8 p18 fragment. Although, BV6 pre-treatment and NK cell co-cultivation leads to a slightly decreased signal of the p43/41 pro-caspase-8 form. On the other hand, BV6 pre-treatment and NK cell co-cultivation resulted in a higher activation of caspase-3 than NK cell co-cultivation alone.
The increased caspase-3, but not caspase-8, activation might be caused by the observed BV6 induced degradation of XIAP. It was shown that XIAP is exclusively degraded in RMS spheroids, not in RMS monolayer cell cultures. This XIAP degradation might lead to the release of pro-caspase-3 in RMS spheroids. Thereby it presumably enhances the susceptibility towards NK cell killing mechanisms and increases pro-caspase-3 cleavage. Previous studies demonstrated that the BIR2 domain in XIAP favours the binding to caspase-3 and possibly to its closest relative caspase-7, but not to caspase-8 [94, 190].

Based on this increased caspase-3 cleavage upon BV6 treatment, a functional evaluation was performed using the pan-caspase inhibitor zVAD.fmk to evaluate if caspase

activation is needed for the NK cell mediated attack. Indeed, zVAD.fmk suppresses the NK cell mediated killing and BV6 induced sensitization in both RMS spheroid models (fig. 5.21). This validates the hypothesis of a putative caspase involvement within the BV6 mediated sensitization of RMS spheroids. In brief, NK cells are able to kill RMS spheroids via a caspase dependent mechanism, which is further increased by BV6, as an increased caspase-3 cleavage could be seen. Caspase-3 is considered as an executioner caspase and can be activated by both the extrinsic and intrinsic apoptotic pathways [33].
As zVAD.fmk could block NK cell mediated killing, the interest arose to identify the responsible initiator caspases. Induction of the intrinsic apoptotic pathway is associated with the activation of pro-caspase-9 within the generated apoptosome complex [43, 191]. Here, the underlying hypothesis is that BV6 putatively primes RMS cells to MOMP. This leads to an induction of intrinsic apoptotic pathways upon NK cell co-cultivation and activation of pro-caspase-9. The NK cell mediated killing might be caspase-9 dependent, if only the intrinsic apoptotic pathway is influenced by BV6. To test this, the caspase-9 expression was successfully suppressed by siRNA in RMS spheroids (fig. 5.23). As no significant killing difference was seen in the caspase-9 knock-down spheroids compared to the siCtrl spheroids, the hypothesis of a caspase-9 involvement has to be rejected. This observation is in contrast to a recent study, describing a mitochondrial involvement and activation of caspase-9 in HeLa and AML cell lines co-cultured with NK cells [192]. The difference might be explainable by different NK cell activation methods, Pan et al. used IL-2 activated NK cells expanded in RPMI culture medium, in contrast to IL-15 activated NK cells expanded in NK MACS® in this project. Another aspect might be the method of co-cultivation and cytotoxicity assessment, Pan et al. used a flow cytometry based NK cell cytotoxicity assay (similar to the one described in section 4.2.3.1). However, the caspase-9 knock-down studies in this project were performed using a RMS-GFP spheroid model. The 3-dimensional shape of the RMS-GFP spheroids might have an impact on the surface presentation of activating ligands, e.g. MICA [134].Differences in recognition of RMS spheroids by either IL-2 or IL-15 activated NK cells might lead to a different killing mechanism, probably towards a more mitochondrial/caspase-9 independent mode.

Apart from caspase-9 as an initiator caspase within the intrinsic mitochondrial apoptotic machinery, caspase-8 is recognized as an initiator caspase for the extrinsic death receptor mediated apoptosis pathway [37, 193]. Upon death receptor ligation the DISC is formed, consisting of either Fas or DR4/DR5, FADD and either pro-caspase-8/-10 and c-FLIP [194, 195].

Although it was demonstrated that TRAIL does not play a major role in the NK cell mediated killing of RMS-GFP spheroids, caspase-8 remains to be an interesting initiator caspase to investigate. Using siRNA caspase-8 was knocked-down in RH30-GFP and RD-GFP spheroids (see fig. 5.24).The successful knock-down of caspase-8 was validated by western blot in RMS spheroids.

The removal of caspase-8 in RH30-GFP spheroids did not influence NK cell mediated killing, nor the BV6 induced sensitization. As no reduction of PI/GFP ratio indicative for a caspase-8 dependency was visible. In contrast to RD cell, it has been described that RH30 cells additionally express caspase-10 [196, 197]. Although caspase-10 differs from caspase-8, an overlapping substrate specificity and initiator caspase function could be demonstrated [57, 198, 199]. However, Horn et al. described an opposing effect of caspase-10, i.e. caspase-10 induces pro-survival signaling rather than compensating the loss of caspase-8 [200]. Horn et al. used HeLa cells and artificial FasL induced cell death, focusing on the Fas induced DISC signaling and not as presented here on a BV6 pre-treatment of RMS spheroids in combination with NK cell co-cultivation. In RH30 spheroids caspase-10 might be able to compensate the siRNA mediated reduction of caspase-8 expression, by that NK cells are still able to induce cell death in RH30 spheroids.

Caspase-8 knock-down in RD-GFP spheroids shows a different behaviour than described for RH30-GFP spheroids. Here, caspase-8 knock-down (by siRNA construct #3) suppressed the induction of an NK cell attack and reduced the BV6 induced sensitization (fig. 5.24(c) & (d)). Assuming, that the NK cell killing mechanism in RD spheroids is caspase-8 dependent. Various studies show contrary information on caspase-10 expression in RD cells, several describe RD cells as caspase-10 negative [196, 197]. However, caspase-10 expression is observed upon enterovirus 71 infection in RD cells [201].

As mentioned above caspase-8 is considered to be the initiator caspase within the extrinsic, death receptor mediated apoptosis pathway [33]. However, the study in hand shows evidence of a death receptor independent NK cell killing mechanism, as neutralization of TRAIL and TNFα could not suppress NK cell killing. One explanation, which was previously observed for Smac mimetic induced loss of cIAP1/2 proteins, might be a formation of the ripoptosome [202]. Tenev et al. and Feoktistova et al. described a spontaneous, death receptor independent generation of a death inducing complex termed ripoptosome upon Smac mimetic treatment which consists of RIPK1, FADD and pro-caspase-8 [202, 203]. A possible follow up project would be to test a putative relationship of a BV6 mediated ripoptosome formation in RMS spheroids and the observed sensitization towards an NK cell mediated attack. A putative link was already described, where treatment of RD or RH30 cells with two different undefined

Smac mimetics led to a RIPK1-dependent sensitization towards DR5 mediated cell death [159]. Additionally, a recent study described a putative pathomechanism of drug induced acute liver failure. The authors could show an up-regulation of TWEAK, a non-canonical NF-κB activator, leading to a RIPK1-dependent apoptotic cell death [204].
In the study at hand, BV6 might be able to bypass receptor ligation and directly induce downstream receptor complex activation putatively involving RIPK1 and ripoptosome complex formation.

6.2 Transcriptional regulation by BV6

6.2.1 Regulation of NF-κB signaling pathways

IAP proteins function not only as inhibitors of apoptosis, but they are involved in the regulation of NF-κB signaling pathways [205]. cIAP1/2 are located at the receptor complex I and act as E3 ubiquitin ligases aiding the canonical NF-κB activation [206].Further, cIAPs constitutively ubiquitylate NIK, leading to the proteasomal degradation of NIK and suppressed activation of the non-canonical NF-κB signaling [86].
Treatment with BV6 leads to the degradation of IAP proteins (see fig. 5.2 & 5.3), putatively block constitutive degradation of NIK and activate the non-canonical NF-κB signaling pathway. At the same time suppressing the activity of the canonical NF-κB pathway. Indeed, treatment with BV6 leads to a time dependent accumulation of NIK, partial degradation of p100 and nuclear translocation of p52 (see fig. 5.29 & 5.31). This mode of action is observable in both culture methods, RMS monolayer and spheroids (see fig. 5.30).
Non-canonical NF-κB pathway activation by Smac mimetics is already known, and not a novel observation [103]. A previously mechanism was proposed of a NIK stabilized processing of p100 within a TRAF2:TRAF3:cIAP1/2:NIK complex upon cIAP1/2 degradation, which shows similar activation pattern to the ones observed in BV6 treated RMS cells [86]. Gray et al. described an additional cIAP1/2 independent NIK degradation, mediated by IKKα as an autoinhibitory feedback mechanism [207]. Such autoinhibitory mechanism could not be seen in RMS cells. The NIK accumulation seems to be stable up to 24 h of BV6 stimulation.
On the other hand, Jin et al. could show that cIAP1 directly ubiquitylates IKKγ (NEMO) at K277 and K309 activating canonical NF-κB activation [206]. These ubiquitylation sites were already described as being responsible for NF-κB activation [208].
Taken together the literature describes a rather activating function of cIAP proteins on the canonical NF-κB signaling. If cIAP proteins are degraded, for example upon

BV6 treatment, the canonical NF-κB pathway should be suppressed. Here, BV6 shows an inducing effect on the canonical NF-κB signaling pathway. In RMS cell monolayer and 3D multicellular spheroids, a phosphorylation of IκBα can be observed, further phosphorylation and nuclear translocation of p65 is visible (see fig. 5.27 - 5.31). BV6 mediated phosphorylation of IκBα and p65 was previously described in glioblastoma cell lines [209]. Interestingly, the phosphorylation of IκBα in RMS cells is not associated with a loss of IκBα, which is usually described as a read-out for canonical NF-κB activation [78, 210]. Among other, BV6 leads to a transcriptional up-regulation of IκBα, as analyzed by qRT-PCR (see fig. 5.32 - 5.34), identified by RNAseq (see fig. 5.43) and validated by Fluidigm® analysis (see fig. 5.45). The up-regulated IκBα mRNA translates to the observed re-expression and steady levels of IκBα. BV6 might induce a putative negative feedback loop of the canonical NF-κB signaling pathway. Downstream of p-IκBα p65 is phosphorylated and translocates into the nucleus. Such a canonical NF-κB activation pattern was thoroughly review in [84]. In contrast to the stable nuclear translocation of p52 upon BV6 stimulation (see fig. 5.31), p-p65 seems to fluctuate with signal maxima at 4 and 24 h of BV6 stimulation. Such an oscillating behaviour of NF-κB signaling was described for TNFα stimulation, which was mediated by a re-expression and nuclear shuttling of IκBα:p65 complexes [211].

The observed canonical and non-canonical NF-κB activation pattern on a protein level culminate in a transcriptional regulation of NF-κB target genes. Using in-house qRT-PCR, several NF-κB target genes could be identified. Both RH30 and RD cells cultivated with both culture methods showed similar mRNA fold change induction. As mentioned before the protein IκBα remains on a relatively constant level, which might be explained by an induced *IκBα* mRNA transcription around 4 h of BV6 treatment. Further, BV6 induces the up-regulation of the NF-κB target genes *p100*, *NIK*, *RelB*, *cIAP1*, *cIAP2* (in 2D and 3D).
The ligand TWEAK (TNF-related weak inducer of apoptosis), has been described as an inducer of the non-canonical NF-κB signaling pathway [145, 212]. Indeed, the activation pattern of TWEAK activated non-canonical NF-κ signaling pathways seem to be similar to the presented activation pattern by BV6. With the difference that BV6 additionally activates the canonical NF-κB signaling pathway. A side-by-side illustration is depicted by Cherry et al. here treatment with TNFα shows mainly a canonical NF-κB activation and TWEAK treatment activates only the non-canonical NF-κB signaling pathway, accompanied by a *NIK* and *MMP9* mRNA up-regulation [213]. *MMP9* was identified by the RNAseq approach as BV6 induced and *NIK* was found using in-house qRT-PCR analysis to be induced upon BV6.

Comparing the small number of target genes tested by in-house qRT-PCR with the RNAseq approach revealed *cIAP1 (BIRC2)*, *cIAP2 (BIRC3)* and *IκBα (NFKBIA)* to be similar induced by BV6. Interestingly, pathway enrichment analysis resulted in the identification of activated NF-κB signaling pathways as a top up-regulated candidate pathway (fig. 5.44(b)). This pathway identification further validates the previous illustrated NF-κB activation pattern on a protein level and transcriptional mRNA up-regulation of NF-κB target genes. Schmidt et al. performed a microarray to analyze BV6 induced transcriptional changes in breast cancer cell lines. Again, BV6 induced a NF-κB mediated transcriptional regulation. A comparison of identified target genes revealed a number of common genes regulated in both Schmidt et al. and in the study in hand, among others *NFKB2 (p100)*, *NFKBIA (IκBα)*, *BIRC3 (cIAP2)*, *CCL5* and *MMP9* are identified as common targets [115]. Further, using a microarray of BV6 treated patient derived chronic lymphocytic leukemia (CLL) cells showed again an NF-κB induced regulation. Compared to the study in hand *BIRC3 (cIAP2)* and *NFKBIA (IκBα)* are among others common target genes [214]. This might imply an underlying pan-cancer cell type BV6 specific transcriptional program.
Further, the presented RNAseq data was analyzed by TRRUST, a literature-curated database of transcriptional regulation networks. This analysis validated the hypothesis of an activated NF-κB signaling pathway by BV6, as the TRRUST analysis revealed an involvement of the transcription factors (TF) p65 (RELA) and p50 (NFKB1). Noticeable, these putative relevant transcription factors, are the major transcription factors of the canonical NF-κB signaling, but not of the non-canonical NF-κB signaling pathway [64]. This could imply a crosstalk between the canonical and non-canonical NF-κB signaling pathways increasing the complexity of the BV6 induced transcriptional network.

6.2.2 NIK as central player within BV6 induced regulation

As already mentioned above, one main target of cIAP1 and cIAP2 for ubiquitylation and subsequent proteasomal degradation is NIK. Upon BV6 induced cIAP1/2 depletion NIK accumulates and activates the non-canonical NF-κB signaling pathway. This section focuses around the hypothesis that NIK is a main driver of the BV6 induced transcriptional regulation.
For that, an siRNA mediated *NIK* knock-down was performed. In both RH30 and RD cell lines, siRNA mediated knock-down was successful, as a relative mRNA quantification shows loss of *NIK* transcription and suppressed NIK accumulation depicted by western blot (fig. 5.35 & 5.36). Loss of NIK accumulation is followed by a decreased partial degradation of p100 to p52 (fig. 5.37 & 5.38). Further, this blocked down-stream signaling significantly reduces the mRNA up-regulation of *MMP9*, *CCL5* and *cIAP2*

(fig. 5.39, 5.40 & 5.47). These observations lead to acceptance of the hypothesis that NIK might be a main facilitator of the BV6 induced transcriptional regulation. A similar NIK dependent regulation induced upon BV6 treatment was previously reported in glioblastoma cells. The report shows evidence of a NIK dependent p100 processing to p52 and target gene transcription of e.g. *IL-8*, *MMP9*, *TNF*α and *MCP-1* [215].
In RD cells an in-house qRT-PCR analysis showed a NIK independent transcription of *cIAP1* and *IL-8* (fig. 5.40). This might demonstrate an additional transcriptional pathway, possibly a crosstalk of the non-canonical NF-κB signaling pathway could activate a NIK independent canonical NF-κB signaling pathway. This assumption could be affirmed by a reduced but present p65 phosphorylation in both RH30 and RD cells within the background of NIK knock-down (fig. 5.37 & 5.38).
Such crosstalk events were previously described in a HEK 293 system for NIK and Cot to induce p65 phosphorylation [216]. Further, a NIK induced IKKα mediated phosphorylation of IκBα was described in endothelial cells [89]. These investigations indicate an up-stream crosstalk event within the NF-κB pathways, which might be present in BV6 treated RMS cells.

The aim of this PhD thesis is to dissect the molecular mechanisms of the BV6 induced sensitization towards an NK cell mediated killing. As described earlier, this sensitization might be caspase-8 dependent and putatively involves a BV6 induced ripoptosome complex. A recent study in keratinocytes reported that cIAP1/2 depletion leads to a NIK accumulation, subsequent NIK facilitated ripoptosome formation and cell death induction [217]. Boutaffala et al. could demonstrate that the ripoptosome formation and cell death induction depend on NIK stabilization and accumulation upon non-canonical NF-κB pathways activation. Further, RIPK1 was identified as a possible substrate of NIK mediated phosphorylation [218].
In contrast to the previously mentioned report, the project in hand could not show enough evidence that the BV6 induced sensitization towards an NK cell mediated killing depends on NIK. An siRNA mediated *NIK* knock-down did not rescue RMS spheroids from NK cell mediated attack, nor from BV6 induced sensitization (fig. 5.41).
Thereby, the hypothesis of an NIK dependent BV6 induced sensitization of RMS cells towards NK cell mediated attack can be rejected.
Treatment of cancer cells by cytotoxic compounds revealed a transcriptional up-regulation of several genes in connection with enhanced immune cell attack. In lung cancer cells cannabinoid stimulation could increase ICAM-1 on target cells, leading to an enhanced killing by LAK cells [219]. *ICAM-1* transcription could also be induced upon treatment with a selective cyclooxygenase-2 inhibitor in lung cancer cells, leading to an increased

killing by LAK cells [220]. Further, treatment with a p53-reactivating compound increased the surface presentation of ULBP2 on lung cancer cell and enhanced NK cell mediated lysis [221]. Additional, the induction of cellular senescence and accompanied phenotypical and transcriptomical changes induced *ICAM-1* and *TNFα*, which results in an enhanced NK cell attack [222].
Treatment of multiple myeloma cells [139] or murine cancer cells [223] with bortezomib, led to an increased surface presentation of DR5 and loss of HLA-E, which sensitized target cells towards an NK cell killing. Fischer et al. could describe a transcriptional up-regulation of *DR4* and *DR5* in RMS cells by BV6 associated with an increased NK cell mediated killing [25]. These findings were validated by the study in hand and additionally shows an increased surface presentation of DR5 on RH30 cells and of DR4 and DR5 on RD cells.
However, this study lacks a direct link between transcriptional involvement and BV6 induced sensitization.

6.2.3 CCL5 within NK cell killing

The exploratory RNAseq analysis was broadly validated by Fluidigm®, in-house qRT-PCR and identified a variety of genes.
One of this differentially expressed gene is the C-C motif chemokine 5 *CCL5*. First evidence that CCL5 might be relevant in sarcoma cells is shown by a correlation of CCL5 expression and survival probability of the SARC study group data within the TCGA database (fig. 5.46). It seems, as if higher CCL5 expression levels (upper 20 %) correlate to significantly increased survival probability. The human protein atlas collected CCL5 expression data in a variety of tumor types, together 71 % showing a better prognosis at elevated CCL5 expression [224, 225].
However, the SARC study group of the TCGA database include a variety of rare solid tumor types, not restricted to rhabdomyosarcoma. In RD cells CCL5 expression was previously reported [226, 227]. Hikichi et al. demonstrated increased CCL5 levels in RD cells upon NF-κB activation by TNFSF14 (LIGHT) [227]. The ligand TNFSF14 is able to activate the non-canonical NF-κB pathway [89]. TWEAK as a similar activator of the non-canonical NF-κB pathway could induce CCL5 expression in podocytes [228]. In lung cancer cells active LTβR induces CCL5 expression in an NF-κB mediated mechanism [229]. By that *CCL5* was established to be a non-canonical NF-κB target gene and could explain the presented results of an increased *CCL5* transcription in a NIK mediated mechanism upon BV6 stimulation in RMS cells and in RH30 spheroids (fig. 5.47). Knock-down of *NIK* could reduce the BV6 induced mRNA up-regulation in RH30 and RD cells. Further, BV6 (2 μM, 9 h) could up-regulate *CCL5* in glioblastoma

cells [209]. Following the transcriptional up-regulation in RMS cells, *CCL5* is translated into its proteins increasingly stored intracellular and secreted into the cell culture supernatant (fig. 5.48 & 5.49). Liu et al. could observe an intracellular CCL5 storage in granula with a similar appearance as observed here in RMS cells [230]. The project in hand shows original evidence of a BV6 induced *CCL5* transcription and secretion in rhabdomyosarcoma cells.

In combination with NK cells CCL5 was mentioned as acting pro-migratory on IL-2 activated NK cells [231–233]. This pro-migratory effect was still present in a tumor derived CCL5 manner. It was shown, that secreted CCL5 by psoriatic keratinocytes could induce chemotaxis in NK cells, however the effect on NK cell cytotoxicity was not further evaluated in this study [234]. Further, in an *in vivo* melanoma model infection with the arenavirus lymphocytic choriomeningitis virus increased CCL5 expression, which correlated with an enhanced NK cell infiltration and CCL5 dependent tumor growth control [235]. Apart from NK cells, in an ovarian cancer model, CCL5 expression seems to have pro-migratory effect on $CD8^+$ T-cells and prolonged survival *in vivo* [236]. In BV6 treated RMS cells the elevated CCL5 concentration might lead to a pro-migratory environment for NK cells and might increase their cytotoxicity.
The study in hand demonstrated, that NK cells are able to infiltrate RH30 and RD spheroids (fig. 5.25). Despite that, BV6 pre-treatment of RMS spheroids, which putatively increases CCL5 secretion, did not affect the migratory behaviour of NK cells (fig. 5.26).
Although CCL5 does not influence the migratory behaviour of NK cells. The increased CCL5 concentrations might enhance NK cell cytotoxicity of already penetrated NK cells within RMS spheroids. To study this effect, a CRISPR/Cas9 mediated *CCL5* knock-out was carried out.
The used guide RNAs targeted exon 2 of *CCL5* and a knock-out effect was validated. First, amplification of exon 2 on the genomic DNA isolated from knock-out cells showed a faster migrating signal than parental or guide control cells (fig. 5.51(a)). Second, sequencing of this amplicon revealed a missing nucleotide sequence. Sequence analysis revealed that the Cas9 cleavage sites of the used guide RNAs #1 and #2 approximately match the beginning and end of the missing fragment (fig. 5.51(b)). As a third approach to validate the *CCL5* knock-out mRNA was isolated from RH30-GFP knock-out cells which depicts a missing signal for *CCL5*. These approaches suggest that in *CCL5* knock-out RH30-GFP cells a nucleotide fragment within exon 2 of *CCL5* was cleaved out, resulting in an absent mRNA transcription and possibly missing protein expression. Using these knock-out and guide Ctrl cells, RMS-GFP spheroids were generated. As

the data presents, no difference could be observed upon BV6 pre-treatment and NK cell co-cultivation. Despite the absent of CCL5, BV6 is still able to induce a sensitizing effect towards an NK cell mediated killing. This leads to the rejection of the hypothesis that CCL5 is responsible for the BV6 induced sensitizing effect in RMS cells.

6.2.4 SSTR2 as a novel therapeutic target

Second, the somatostatin receptor 2 as a top candidate induced by BV6 in RH30 cells was analyzed in more detail. The SSTR2 is predominantly associated with neuroendocrine tumors (NET) and known for its anti-secretory function in these [237, 238]. Although, SSTR2 is expressed on a variety of tumor types, rhabdomyosarcoma rarely expresses SSTR2 [239]. Several studies show alternating results, specially when patient material was analyzed. In one study, 3 out of 5 primary rhabdomyosarcoma samples were positive for somatostatin receptors, however the receptor subtype (SSTR1-5) was not further specified [240]. Further, it was described that not only rodent, but human *SSTR2* has two alternative splicing variants a long variant *SSTR2A* and a shorter variant *SSTR2B* [241]. In spite of a similar binding affinity of SSTR2A and SSTR2B the transcription variants differ in their functional outcome, as exclusively SSTR2B putatively suppresses forskolin-stimulated cAMP formation [242]. Harda et al. analyzed 15 primary samples of different tumor types, all tumor samples, among them 2 rhabdomyosarcoma samples, were identified as positive for at least one somatostatin receptor subtype (SSTR1-5). The two rhabdomyosarcoma samples predominantly expressed SSTR1, 2 and 4 [243]. Fruhwald et al. had a cohort of 29 primary tissue samples of patients ages 1 month to 17 years. Within this cohort one rhabdomyosarcoma sample identified as positive for SSTR2 expression by immunohistochemistry [244]. Another study, using primary tissue samples, focused on the expression of the splice variant SSTR2A and SSTR5 and compared a cohort of 40 olfactory neuroblastoma samples with 40 sinonasal carcinoma and further to 12 nonepithelial sinonasal tumors (among them 3 rhabdomyosarcoma samples). Only 30 out of the 40 olfactory neuroblastoma samples were positive for SSTR2A, none of the sinonasal carcinoma and none of the nonepithelial sinonasal tumors (among them 3 rhabdomyosarcoma) showed a positive signal for SSTR2A [245]. Taken together, rhabdomyosarcoma show a rather heterogeneous somatostatin receptor expression pattern.

Here, *SSTR2* was identified by RNAseq as a top up-regulated target gene by BV6 treatment in RH30 cells, the heatmap also shows a basal SSTR2 transcription in untreated RH30 cells (fig. 5.43). The detailed analysis was carried out in RH30 cells based on the fact that the RNAseq was performed in RH30 cells and a comparison of *SSTR2* mRNA induction in RMS spheroids identified exclusively RH30 spheroids to increase *SSTR2*,

but not RD spheroids. Following up on this regulation, several qRT-PCR primers were designed to distinguish between the *SSTR2A* and *SSTR2B* splicing variants (fig. 5.54). These analyses resulted in identifying exclusively *SSTR2A* as the transcribed variant in untreated RH30 cells and as the only variant as being up-regulated by BV6 treatment (fig. 5.55 - 5.57). Recently, increased SSTR2 expression was described for nasopharyngeal carcinoma infected with Epstein-Barr virus in a putative NF-κB mediated manner [246]. The involvement of NF-κB could be validated in the presented study, as knockdown of *NIK* in RH30 cells could suppress the BV6 induced *SSTR2A* transcription (fig. 5.58). This validated *SSTR2A* as a BV6 induced target gene in combination with the non-canonical NF-κB signaling pathway in RH30 cells. The identified transcriptional up-regulation of *SSTR2A* was followed by an increased surface presentation of SSTR2 on BV6 stimulation RH30 cells (fig. 5.59).

Treatment of breast cancer cells with a somatostatin analog octreotide in combination with docetaxel was described as an anti-proliferative and apoptosis inducing combination [247]. In primary human somatotroph tumors SSTR2 activation by octreotide at nanomolar concentrations could induce an increased caspase-3 activity [248]. Additionally, sub-nanomolar concentrations of octreotide could increase the number of apoptotic nuclei in HL-60 cells, where *SSTR2* expression was only analyzed on an mRNA level [249].
The presented study demonstrated that octreotide as a single treatment could not induce cell death in untreated RH30 cell (see fig. 5.60) even at concentrations as high as 100 μM. As illustrated above, SSTR2 is not highly expressed under basal conditions. However, BV6 stimulated an increased SSTR2 surface presentation. Here the assumption is, that a combination of BV6 with various octreotide concentrations synergize to enhance cell death induction in RH30 cells. Despite being not significant, a slight enhanced trend of increased cell death at an octreotide concentration of 100 μM co-treated with 5 μM BV6 might be perceivable in RH30 cells (fig. 5.60). Taken together, it seems as if the up-regulated SSTR2 on RH30 is not clearly able to synergize with BV6 to increase cell death in RH30 cells.
Additional studies described an *in vivo* expression and SSTR2 induced signaling as tumor growth promoting and pro-survival in small cell lung cancer cell [250]. Activation of SSTR2 might have different outcomes, depending on the molecular tumor background and putatively on the expressed splicing variant.
Nonetheless, one therapeutic aspect of targeting SSTR2 might be of interest. That it, the utilization as a tumor imaging strategy by using radiolabelled somatostatin analogs, e.g. ^{68}Ga-DOTATOC, ^{68}Ga-DOTATATE or ^{111}In-pentetreotide [237–239]. The combi-

nation of BV6 and its induced up-regulation of SSTR2 on RMS cells, as shown by the presented results, might build the foundation as an imaging strategy of tumor entities showing a low basal SSTR2 expression. As Gennaro et al. propose hybrid imaging strategies for RMS by combining positron emission tomography with conventional computed tomography or magnetic resonance imaging [251], an additional layer of a specific BV6 inducible SSTR2 targeted approach might give further insight of the molecular tumor background and might help in diagnostic staging.

A different hypothetical strategy using the BV6 induced up-regulation of SSTR2 on RMS cells, is the utilization of an anti-SSTR2 targeting chimeric antigen receptor (CAR) expressed by cytotoxic lymphocytes. A recent publication used a novel anti-SSTR CAR construct to generate CAR T-cells. They could show an *in vivo* neuroendocrine tumor growth reduction upon administration of their anti-SSTR CAR T-cell product [252]. The combination of this specific SSTR targeting strategy, by either generating CAR T-cells, or CAR NK cells, with a BV6 induced up-regulation of SSTR2 on normally SSTR2 low expressing cells, might lead to the development of a novel therapeutic targeting approach. That is, to exploit a BV6 induced expression of a novel tumor antigen as a novel target for a specialized cytotoxic lymphocyte attack.

7 Conclusion, limitations and outlook

Taking all the results together, this doctoral thesis demonstrates a detailed transcriptional regulation mediated by BV6 in alveolar (RH30) and embryonal (RD) rhabdomyosarcoma cells.

The first limitation of the study is the focus on BV6 as the only investigated Smac mimetic. Future studies should use several Smac mimetic compounds, to elucidate a pan-Smac mimetic mechanism.

Further, evidence is shown that BV6 induces the accumulation of NIK and subsequent activation of both, the canonical and non-canonical, NF-κB signaling pathways. This activation results in a global transcriptome change. Here, a bulk RNA sequencing, in cooperation with TRON gGmbH, was performed to analyze this transcriptomic change in RH30 cells upon BV6 treatment.

The second limitation is evident by the bulk RNAseq performed only in RH30 cells. This focus was chosen, because of the more aggressiveness of the alveolar RMS subtype. To describe a common RMS mechanism, several RMS cell types should have been analyzed by RNAseq.

Nevertheless, a variety of BV6 induced target gene regulations could be identified and validated using a high-throughput Fluidigm® qRT-PCR analysis (in cooperation with TRON gGmbH). Further validated in embryonal RD cells by in-house qRT-PCR analysis (performed by me).

CCL5 and *SSTR2* were validated in more detail as BV6 induced, NIK mediated target genes in RH30 cells.

The overall induced activation of NF-κB and subsequent gene transcription was not only analyzed in RMS 2D monolayer cell cultures, but additionally analyzed in multicellular RMS tumor spheroids. Both culture methods showed similar activation patterns.

Here, another limitation is evident. That is, a thorough global transcriptome and proteome comparison of 2D against 3D culture is absent. By that, differentially expressed genes and proteins could have been identified, which might be responsible for the different NK cell killing sensibilities of spheroids compared to monolayer cultures.

The observed transcriptional change depends mainly on NIK accumulation and signal transduction. NIK knock-down could suppress the up-regulation of several BV6 induced target genes. Accumulation of NIK and non-canonical NF-κB activation is the direct consequence of cIAP1/2 degradation by BV6. This NIK accumulation is an up-stream event within the signal transduction pathway. However, no direct NF-κB transcription factor, neither p65 or p50 for the canonical, nor RelB or p52 for the non-canonical NF-κB signaling pathways was functionally studied by knock-down experiments. As

a follow-up study, additional knock-down/out experiments of transcription factors for instance p65 or p52, could help to describe the signal transduction pathway in more detail.
Functionally it was shown that NIK does not mediate the BV6 induced sensitization towards an NK cell attack. As *NIK* knock-down could not suppress the NK cell induced killing.
The proposed NIK independency is restricted by the used siRNA mediated technique. Analysis by western blot validated a reduced NIK expression on the day of BV6 treatment. The *NIK* targeting siRNA possibly degrades within the target cells. Thereby, NIK might be re-expressed over the co-cultivation period of five days. Re-expressed NIK might be able to active the non-canonical NF-κB pathway. However, in cellular steady-state conditions NIK is constitutively proteasomal degraded. Further, BV6 is only used as a pre-treatment for 24 h during this time western blot confirmed the absence of NIK within RMS spheroids. As a follow up, a more stable CRISPR/Cas9 NIK knock-out might be helpful to elucidate a detailed functional role of NIK during long periods of co-culture experiments.
Again, evidence is shown to describe NIK and subsequent NF-κB activation as a central element of the BV6 induced transcription. The presented study focused around NF-κB and NIK as direct target of cIAP1/2. But, it lacks other, additional transcriptional pathways putatively activated by BV6, e.g. IRF1 [116] or AP-1 [115].

Further aspects investigated, regarding a molecular mechanism of the observed BV6 induced sensitization, was a putative involvement of death receptors and down-stream caspase activation. Here, it was shown that BV6 could induce the transcriptional up-regulation and surface presentation of DR5 on RMS cells. Following this, co-treatment of BV6 and TRAIL showed an additive cell death inducing effect. However, NK cell killing and BV6 induced sensitization was not mediated by TRAIL, as TRAIL neutralizing antibody did not show a rescue effect in co-cultivation models. Further, BV6 induced sensitization and NK cell killing was also shown to be mainly independent of TNFα, as a TNFα neutralizing antibody (Enbrel) did not show a significant rescue effect. NK cells not only rely on death receptor mediated target cell killing, but they secrete cytotoxic granula to induce a mainly granzyme B mediated killing. However, a granzyme B inhibitor did not show any rescue effect.
These experiments were performed with exogenous added antibodies and inhibitors. As an alternative and follow-up study, knock-down/out experiments of TRAIL, TNFα, granzyme B or other cytotoxic proteins within NK cells might be a relevant method to study NK cell killing mechanisms. The other way around, knock-down/out studies of

death receptors, e.g. DR4/5, TNFR1 or other cell death inducing proteins, might aid to elucidate the killing mechanism within the target cells, i.e. RMS cells.
Within target RD-GFP spheroids, caspase-8, not caspase-9, could be identified being involved within the NK cell killing mechanism, thereby the mitochondrial involvement within BV6 mediated sensitization can be disregarded.
However, the up-stream activation of caspase-8 was not experimentally investigated. Here, immunoprecipitation experiments of caspase-8 might be helpful to identify interaction partners. Thereby, fully assemble the BV6 induced sensitization mechanism of caspase-8 activation. Again, as proposed above, the ripoptosome, as a death receptor independent, caspase dependent cell death inducing signaling complex might be of interest as a follow-up project [253].

Novel aspects of this study are a detailed description of BV6 mediated NIK dependent transcriptional activation in 2D and also in 3D multicellular RMS tumor spheroids. Further, the application of RMS-GFP spheroids as an NK cell co-culture model in combination with BV6 as a sensitizing compound could be described/established for the first time. By that, validating several studies showing such a BV6 sensitization in 2D co-culture methods for CIK [121] or NK cells [25]. Using these spheroid models, different phenotypes of the alveolar (RH30) and embryonal (RD) spheroids became apparent. Thereby, advancing the field of RMS 3D culture methods and phenotypical differences of RMS spheroid subtypes. Additionally, the bulk RNAseq analysis of BV6 treated RH30 cells validated previous regulated genes of transcriptomic BV6 studies in breast cancer cells [115] and CLL cells [214]. This implies a putative BV6 induced transcriptional pan-cancer effect, which needs further validation.

Nonetheless, the combination of BV6 in its cell death sensitizing function together with *ex vivo* activated cytotoxic lymphocytes might be of therapeutic interest to develop a cellular immunotherapy. Within the background of a specialized CAR NK cell immunotherapy, further sensitization by a pro-cell death compound might be of clinical value to eradicate previous hard to target solid cancer entities.

8 Summary/Deutsche Zusammenfassung

Neben Leukämien, Hirntumoren und Lymphome sind auch Weichteilsarkome häufige Krebserkrankungen bei Kindern und Jugendlichen. Innerhalb der Gruppe der Weichteilsarkome ist das Rhabdomyosarkom (RMS) die am häufigsten anzutreffende Tumorentität. Diese bösartigen Wucherungen, vor allem in der Kopf-Hals-Region, Extremitäten oder im Urogenitalsystem, entstammen undifferenzierten Zellen mesenchymalen Ursprungs.
Rhabdomyosarkome werden laut der WHO in vier unterschiedliche Unterarten klassifiziert, wobei die embryonale und alveolare Unterarten die größten Anteile mit ungefähr 60 % und 20 % ausmachen. Embryonale Rhabdomyosarkome (eRMS) zeichnen sich unter anderem durch einen Verlust der Heterozygotie des Chromosoms 11p15.5 aus. Bei der embryonalen Unterart können auch weitere Mutationen auf anderen Chromosomen beteiligt sein, sodass insgesamt eine sehr heterogene Population entsteht. Allerdings hat die embryonale Unterart eine bessere Prognose als die aggressivere alveolare Form des RMS. Diese Unterart zeichnet sich vor allem durch Gentranslokationen (t(2;13)(q35;q14), t(1;13)(p36;q14)) aus. Durch diese Translokationen entstehen PAX3-FOXO1 oder PAX7-FOXO1 Transkriptionsfaktor-Fusionsproteine, die eine verstärkte Transkription ihrer Zielgene veranlassen und unweigerlich zur Entartung und Ausbildung des alveolären RMS führen.
Obwohl die Entwicklung kombinatorischer Therapieansätze zu einer Steigerung der Langzeitüberlebensraten geführt hat, sind Hochrisikogruppen und metastasierende Tumore davon ausgeschlossen, sodass der Bedarf an neuen Therapiestrategien zur Behandlung aggressiver, metastasierender RMS immer noch vorhanden ist.

In der vorliegende Studie wird ein kombinatorisches Vorgehen präsentiert, wie RMS Zellen durch ein zelltodstimulierendes Agens zu einem Angriff durch natürliche Killerzellen (NK-Zellen) sensibilisiert werden. Da es sich bei dem Rhabdomyosarkom um einen soliden Tumor handelt, wurden aus zwei verschiedenen RMS Zelllinien dreidimensionale kugelähnliche Gebilde (Sphäroide) generiert. Diese multizellulären RMS Sphäroide sollen eine *in vivo* ähnliche Tumormikroumgebung bilden, die es ermöglichen soll, translationalere Ergebnisse zu generieren als die klassische Kultivierung in einer Einzelzellebene. Bei den beiden RMS Zelllinien handelt es sich einmal um die RD Zellen, repräsentativ für die embryonale RMS Unterart. Zum anderen, werden RH30 Zellen verwendent, die repräsentativ für die alveoläre RMS Unterart sind.
Bei den NK-Zellen handelt es sich um eine Immunzellpopulation, charakterisiert durch eine Oberflächenexpression von CD59 bei gleichzeitig fehlender CD3 Präsentation, die

infizierte oder entartete Zielzellen erkennt und diese abtöten kann. Dabei gibt es mehrere Strategien, wie die NK-Zellen ihre Zielzellen töten. Eine Methode ist es, Todesliganden auf ihrer Oberfläche zu präsentieren, die Todesrezeptoren auf den Zielzellen binden und in diesen den klassischen extrinsisch vermittelten apoptotischen Zelltod einleiten. Beschrieben wird dieser durch eine Aktivierung von Caspase-8, die zur Aktivierung der Caspase-Kaskade und letztendlich zum Zelltod führt. Ein weiterer Mechanismus ist es, zytotoxische Vesikel in ihrem Inneren zu lagern und diese bei Kontakt mit der Zielzelle gerichtet auszuschütten. Innerhalb der zytotoxischen Vesikel befinden sich lytische Enzyme, beispielsweise Granzyme und Granulysine, die durch eine Perforin-gebildete Pore ins Innere der Zielzelle gelangen und dort wieder die Caspase-Kaskade aktivieren können, aber auch eigene Zielproteine schneiden, inaktivieren und degradieren können. Dies führt ebenfalls zum Zelltod der Zielzelle.
Bei dem zelltodstimulierenden Agens handelt es sich um ein sogenanntes Smac Mimetikum, das BV6. Dieses ahmt das zelleigene Protein Smac nach, welches während der mitochondrialen Beteiligung innerhalb des apoptotischen Zelltodmechanismus vom Mitochondrium freigegeben wird und zu einer Aktivierung von Caspasen führt. Im Ruhezustand der Zelle wird die Aktivität von Caspasen durch endogene Apoptoseinhibitoren (IAP) blockiert. Smac sowie BV6 führen zu einem Abbau dieser IAP Proteine, was wiederum zu einer Freisetzung der Caspasen und Aktivierung des apoptotischen Zelltodmechanismuses führt.
Das Ziel der vorliegenden Arbeit ist es, den molekularen Mechanismus der anfangs beschriebene Sensibilisierung von BV6 in Kombination mit NK-Zellen aufzuklären.

Neben der Blockierung von Caspasen spielen IAP Proteine auch eine Rolle in den Signalwegen der NF-κB abhängigen Transkription. Hier sind hauptsächlich zwei Signalwege zu nennen: der kanonische, welcher durch IAP Proteine eher aktiviert wird und der nicht-kanonische NF-κB Signalweg, welcher durch IAP Proteine eher inaktiviert wird. Durch die Behandlung mit BV6 werden die IAP Proteine blockiert und degradiert. Dies führt im Umkehrschluss zu einer Aktivierung des nicht-kanonischen NF-κB Signalweges, charakterisiert durch die Stabilisierung, Akkumulation und Aktivierung der NF-κB-induzierenden Kinase (NIK). Dies führt zu einer partiellen Degradation von p100 zu p52, gefolgt von einer Translokation von p52 in den Zellkern, wo die Transkription von Zielgenen aktiviert wird. Dieses Verhalten konnte in beiden RMS Sphäroiden beobachtet werden. Entgegen der angenommenen Inaktivierung des kanonischen NF-κB Signalweges induziert BV6 auch diesen Signalweg. Dies wurde ersichtlich durch eine gesteigerte Phosphorylierung des Inhibitorischen Proteins IκBα und weiteren Phosphorylierung des Transkriptionsfaktors p65. Phosphoryliertes p65 bildet ebenfalls Dimere

mit anderen Rel Proteinen und transloziert in den Zellkern zur Transkription von Zielgenen.
Diese Transkription wurde mit Hilfe einer globalen RNA Sequenzierung von BV6 behandelten RH30 Zellen weiter untersucht. Die Ergebnisse der RNAseq wurden anhand von 21 ausgewählten Genen unter Verwendung einer Fluidigm®-Plattform (hochdurchsatz quantitative Echtzeit-Polymerasekettenreaktion (qRT-PCR)) validiert. Die RNAseq Analyse ergab, dass 182 Gene nach der BV6 Behandlung unterschiedlich exprimiert wurden. Weitere Auswertungen haben ebenfalls die anfängliche Hypothese einer Mitwirkung der NF-κB Signalwege bestätigt. Unter den interessanten Genen sind *NFKBIA* (IκBα), *BIRC3* (cIAP2), *NFKB2* (p100), *CCL5* und *SSTR2*.
Der Somatostatinrezeptor 2 (SSTR2) wird selten mit dem Rhabdomyosarkom in Verbindung gebracht, sondern eher im Zusammenhang mit neuroendokrinen Tumoren beschrieben. SSTR2 wird häufig als Zielstruktur in der bildgebenden Diagnostik dieser Tumorentitäten verwendet. Die verstärkte Expression und Oberflächenpräsentation von SSTR2 auf den alveolären RH30 Zellen könnte für genau diese Anwendung verwendet werden. So könnte ein vorher nicht mit dem Rhabdomyosarkom assoziiertes Protein als Neoantigen für eine verbesserte Bildgebung verwendet werden. Weiterhin könnte die induzierte SSTR2 Präsentation als Zielstruktur für einen gezielten Angriff mit sogenannten chimären Antigenrezeptor (CAR) exprimierenden Immunzellen, entweder CAR T-Zellen oder CAR NK-Zellen, verwendet werden. Dieser CAR besitzt die Fähigkeit eine gewünschte Sequenz auf den gewünschten Zielzellen zu erkennen und zytotoxische Immunzellen zu diesen hinzuführen und anzugreifen. Im Verlauf der Studie wurde die induzierte Expression von SSTR2 auf BV6 behandelten RH30 Zellen bestätigt. Weiterhin kann gezeigt werden, dass es sich bei der Expression um *SSTR2A* handelt, eine der beiden alternativen Splicing Varianten.
Als zweites induziertes Gen wurde das Chemokin *CCL5* betrachtet. CCL5 konnte bereits mit NK-Zellen in Verbindung gebracht werden, im Sinne von einer CCL5 induziert gerichteten Migration und verstärkten zytotoxischen Aktivierung von NK-Zellen. Im Zusammenhang mit der von BV6 ausgehenden Sensibilisierung könnte CCL5 die fehlende Verbindung sein, wie BV6 die Sensibilisierung auslöst. Darauf aufbauend wurde die BV6 induzierte mRNA Transkription mittels qRT-PCR validiert sowie die Translation und Lagerung in intrazellulären Granula durch Immunfluoreszenz Methoden bestätigt. Weiterhin konnte eine erhöhte CCL5 Konzentration im Zellkulturüberstand, nach BV6 Behandlung, gemessen werden. Für eine funktionelle Überprüfung, ob CCL5 an der BV6 induzierten Sensibilisierung mitwirkt, wurden *CCL5* knock-out RH30 Zellen mittels der CRISPR/Cas9 Methode generiert. Durch Sequenzierung konnte bestätigt werden, dass in den RH30 Zellen ein Fragment innerhalb von Exon 2

herausgeschnitten wurde und keine mRNA von *CCL5* mehr entsteht. Mit Hilfe dieser Zellen konnten Sphäroide generiert werden, die entgegen der aufgestellten Hypothese, keine Minimierung des NK Zellangriffs bewirkten. So muss angenommen werden, dass CCL5 keinen Einfluss auf die BV6 induzierte Sensibilisierung und auf den generellen NK-Zellangriff hat.
Die Degradierung der cIAP Protein durch die Behandlung mit BV6 hat zur Folge, dass die NF-κB induzierende Kinase (NIK) in der Zellen akkumuliert und den nicht-kanonischen NF-κB Signalweg induziert. Es konnte gezeigt werden, dass BV6 eine globalen Veränderung des Transkriptoms auslöst. Darauf aufbauend lässt sich eine Hypothese formulieren, dass diese transkriptionellen Veränderungen NIK abhängig ablaufen und grundlegend zu der Sensibilisierung des NK-zellvermittelten Angriffs beitragen könnten. Die Expression von NIK konnte mittels RNA-Interferenz reduziert werden. Darauffolgend reduzierte sich die partielle Degradation von p100 zu p52 und die Phosphorylierung von p65. Ebenso konnte die Transkription einiger Zielgene, beispielsweise von *MMP9*, *BRIC3*, *CCL5* und *CXCL8*, erniedrigt werden. Zusammenfassend konnte NIK als vermutlich zentrales Element innerhalb der BV6 induzierten Transkription identifiziert werden.
Als weitere funktionelle Überprüfung, ob NIK auch in Kombination mit NK-Zellen einen Einfluss auf die beobachtete Sensibilisierung von RMS Sphäroiden hat, wurde auch hier die Expression von NIK durch RNA-Interferenz reduziert. Auch hier konnte weder ein positiver, noch ein negativer Einfluss auf das Angriffsverhalten der NK Zellen zu den RMS Sphäroiden beobachtete werden. Trotz der zentralen Rolle innerhalb der BV6 herbeigeführten transkriptionellen Regulation hat NIK keine Rolle im Zusammenhang mit dem NK-zellvermittelten Angriff und der Sensibilisierung zum Zelltod.

Wie oben bereits beschrieben, haben IAP Proteine neben ihrem Einfluss auf die NF-κB Signalwege, ebenfalls eine inhibierende Funktion auf Caspasen innerhalb der apoptotischen Zelltodmechanismen. Auch wurde bereits der Todesrezeptor vermittelte zelltodinduzierende Mechanismus der NK-Zellen vorgestellt. Daraus ergibt sich die nächste Hypothese: BV6 induzierte Sensibilisierung ist abhängig von Todesrezeptoren auf der Oberfläche der RMS Zellen, welche von NK-Zellen aktiviert werden. Die Überprüfung der Hypothese wurde mit neutralisierenden Antikörpern, die spezifisch die Todesliganden TNFα oder TRAIL blockieren, durchgeführt. In beiden Fällen konnte keine Erniedrigung eines NK-zellvermittelten Zelltodes beobachtet werden. Vermutlich sind die Todesrezeptoren nicht für die beschriebene BV6 Sensibilisierung verantwortlich. Da kein genereller Einfluss auf das Tötungsverhalten der NK-Zellen zu sehen ist, könnte der zweite Mechanismus, wie NK-Zellen ihre Ziele angreifen, die Neutralisierung der

Todesliganden kompensieren.
Innerhalb des apoptotischen Zelltodsignalweges befinden sich Caspasen an mehreren Stellen, entweder an apikal induzierender Stelle oder sowie an exekutiven Stellen, die direkt zur Apoptose führen. Mittels eines Breitband-Inhibitors für Caspasen (zVAD.fmk) konnte gezeigt werden, dass die BV6 Sensibilisierung und der NK-zellvermittelte Zelltod Caspasen abhängig ist. Weiterhin konnte in BV6 behandelten und mit NK-Zellen co-kultiviertem RMS Sphäroiden eine erhöhte Caspase-3 Aktivierung auf Proteinebene gezeigt werden. Caspase-3 ist eine der exekutiven Caspasen, welche benutzt wird, um die Aktivierung apoptotischer Zelltodsignalwege nachzuweisen.
Für weitere detailliertere Untersuchung, welche apikale Caspase dafür verantwortlich sein könnte, wurde die Methode der RNA-Interferenz genutzt, um die Expression von Caspase-9 und -8 zu erniedrigen. Caspase-9 wird innerhalb des intrinsischen Apoptosepfades aktiviert, wohingegen Caspase-8 innerhalb Todesrezeptorkomplexen gebunden ist und dort aktiviert wird. Eine Expressionserniedrigung dieser Caspasen sollte eine Reduktion des NK zellvermittelten Zelltodes zur Folge haben. RNA-Interferenz und Expressionserniedrigung von Caspase-9 konnte dieses Verhalten nicht zeigen, sodass angenommen werden muss, dass diese apikale Caspase nicht von Relevanz für die BV6 induzierte Sensibilisierung ist. Hingegegen konnte für die Expressionserniedrigung von Caspase-8 eine Reduktion des NK zellvermittelten Zelltods für RD Sphäroiden beobachten werden, sodass hier eine Caspase-8 Abhängigkeit durchaus vorhanden ist.

Die vorliegende Studie konnte eine BV6 induzierte Transkription in RD und RH30 Zellen sowie in Sphäroiden umfassend zeigen und diese auch für einige Zielgene über weitere Methoden validieren. Darüber hinaus konnte NIK als zentrales Element für diese BV6 induzierte NF-κB abhängige Transkription identifiziert werden. Allerdings haben die NIK vermittelten Signalwege keinen Einfluss auf die beobachtete Sensibilisierung zu einem vermittelten Zelltod durch die NK-Zellen.
Innerhalb der Apoptosemechanismen konnte eine Caspase-8 Abhängigkeit und generell der Einfluss von Caspasen als erforderlich für den NK-zellvermittelten Zelltod und die BV6 induzierte Sensibilisierung beschrieben werden. Neutralisierung von Todesrezeptoren, in deren Rezeptorkomplexen Caspase-8 aktiviert wird, konnte hingegen keine Reduktion des NK-zellvermittelten Zelltodes auslösen.
Zusammenfassend bewirkt BV6 einen NIK unabhängigen, vermutlich Todesrezeptor unabhängigen, jedoch caspasenabhängigen NK-zellvermittelten Zelltodmechanismus. Dieser sollte noch weiter untersucht werden, um die molekularen Ursachen zu verstehen und einen zukünftigen therapeutischen Ansatz in Kombination mit NK-Zellen zu entwickeln.

9 References

[1] C. O. Weber and R. Virchow. “Anatomische Untersuchung einer hypertrophischen Zunge nebst Bemerkungen über die Neubildung quergestreifter Muskelfasern.” In: *Archiv für pathologische Anatomie und Physiologie und für klinische Medicin* 7.1 (1854), pp. 115–125.

[2] A. P. Stout. “Rhabdomyosarcoma of the Skeletal Muscles.” eng. In: *Ann Surg* 123.3 (1946), pp. 447–472.

[3] C. Chen, H. Dorado Garcia, M. Scheer, and A. G. Henssen. “Current and Future Treatment Strategies for Rhabdomyosarcoma.” In: *Front Oncol* 9 (2019), p. 1458.

[4] J. Leiner and F. Le Loarer. “The current landscape of rhabdomyosarcomas: an update.” eng. In: *Virchows Arch* 476.1 (2020), pp. 97–108.

[5] C. J. Drummond and M. E. Hatley. “A Case of mistaken identity: Rhabdomyosarcoma development from endothelial progenitor cells.” eng. In: *Mol Cell Oncol* 5.4 (2018), e1448246.

[6] R. C. Horn and H. T. Enterline. “Rhabdomyosarcoma: a clinicopathological study and classification of 39 cases.” In: *Cancer* 11.1 (1958), pp. 181–199.

[7] E. R. Rudzinski, J. R. Anderson, D. S. Hawkins, S. X. Skapek, D. M. Parham, and L. A. Teot. “The World Health Organization Classification of Skeletal Muscle Tumors in Pediatric Rhabdomyosarcoma: A Report From the Children’s Oncology Group.” In: *Arch. Pathol. Lab. Med.* 139.10 (2015), pp. 1281–1287.

[8] I. Dziuba, P. Kurzawa, M. Dopierala, A. B. Larque, and D. Januszkiewicz-Lewandowska. “Rhabdomyosarcoma in children - current pathologic and molecular classification.” In: *Pol J Pathol* 69.1 (2018), pp. 20–32.

[9] P. H. B. Sorensen, J. C. Lynch, S. J. Qualman, R. Tirabosco, J. F. Lim, H. M. Maurer, J. A. Bridge, W. M. Crist, T. J. Triche, and F. G. Barr. “PAX3-FKHR and PAX7-FKHR gene fusions are prognostic indicators in alveolar rhabdomyosarcoma: a report from the children’s oncology group.” eng. In: *J Clin Oncol* 20.11 (2002), pp. 2672–2679.

[10] F. Ramadan, A. Fahs, S. E. Ghayad, and R. Saab. "Signaling pathways in Rhabdomyosarcoma invasion and metastasis." en. In: *Cancer Metastasis Rev* 39.1 (2020), pp. 287–301.

[11] R. Fan, D. M. Parham, and L. L. Wang. "An Integrative Morphologic and Molecular Approach for Diagnosis of Rhabdomyosarcoma and Subclassification of Rhabdomyosarcoma." In: *Arch Pathol Lab Med* (2022).

[12] J. F. Shern, J. Selfe, E. Izquierdo, R. Patidar, H. C. Chou, Y. K. Song, M. E. Yohe, S. Sindiri, J. Wei, X. Wen, E. R. Rudzinski, D. A. Barkauskas, T. Lo, D. Hall, C. M. Linardic, D. Hughes, S. Jamal, M. Jenney, J. Chisholm, R. Brown, K. Jones, B. Hicks, P. Angelini, S. George, L. Chesler, M. Hubank, A. Kelsey, S. A. Gatz, S. X. Skapek, D. S. Hawkins, J. M. Shipley, and J. Khan. "Genomic Classification and Clinical Outcome in Rhabdomyosarcoma: A Report From an International Consortium." In: *J Clin Oncol* 39.26 (2021), pp. 2859–2871.

[13] A. C. Taylor, L. Shu, M. K. Danks, C. A. Poquette, S. Shetty, M. J. Thayer, P. J. Houghton, and L. C. Harris. "p53 mutation and MDM2 amplification frequency in pediatric rhabdomyosarcoma tumors and cell lines." en. In: *Medical and Pediatric Oncology* 35.2 (2000), pp. 96–103.

[14] S. Malempati and D. S. Hawkins. "Rhabdomyosarcoma: review of the Children's Oncology Group (COG) Soft-Tissue Sarcoma Committee experience and rationale for current COG studies." eng. In: *Pediatr Blood Cancer* 59.1 (2012), pp. 5–10.

[15] S. X. Skapek, A. Ferrari, A. A. Gupta, P. J. Lupo, E. Butler, J. Shipley, F. G. Barr, and D. S. Hawkins. "Rhabdomyosarcoma." en. In: *Nat Rev Dis Primers* 5.1 (2019), pp. 1–19.

[16] S. Gallego, I. Zanetti, D. Orbach, D. Ranchère, J. Shipley, A. Zin, C. Bergeron, G. L. de Salvo, J. Chisholm, A. Ferrari, M. Jenney, H. C. Mandeville, T. Rogers, J. H. Merks, P. Mudry, H. Glosli, G. M. Milano, S. Ferman, G. Bisogno, and o. b. o. t. E. P. S. T. S. S. Group (EpSSG). "Fusion status in patients with lymph node-positive (N1) alveolar rhabdomyosarcoma is a powerful predictor of prognosis: Experience of the European Paediatric Soft Tissue Sarcoma Study Group (EpSSG)." en. In: *Cancer* 124.15 (2018), pp. 3201–3209.

[17] A. Ferrari, L. Bergamaschi, S. Chiaravalli, V. Livellara, G. Sironi, O. Nigro, N. Puma, G. Gattuso, C. Morosi, P. Gasparini, R. Caccavo, E. Pecori, O. Alessandro, S. Vennarini, L. Gandola, M. Massimino, and M. Casanova. "Metastatic rhabdomyosarcoma: Evidence of the impact of radiotherapy on survival. A retrospective single-center experience." en. In: *Pediatric Blood & Cancer* n/a.n/a (2022), e29853.

[18] K. A. Dyson, B. D. Stover, A. Grippin, H. R. Mendez-Gomez, J. Lagmay, D. A. Mitchell, and E. J. Sayour. "Emerging trends in immunotherapy for pediatric sarcomas." In: *J Hematol Oncol* 12.1 (2019), p. 78.

[19] A. Makimoto. "Optimizing Rhabdomyosarcoma Treatment in Adolescents and Young Adults." In: *Cancers (Basel)* 14.9 (2022).

[20] K. Mochizuki, S. Kawana, S. Yamada, M. Muramatsu, H. Sano, S. Kobayashi, Y. Ohara, N. Takahashi, M. Hakozaki, H. Yamada, Y. Hashimoto, and A. Kikuta. "Various checkpoint molecules, and tumor-infiltrating lymphocytes in common pediatric solid tumors: Possibilities for novel immunotherapy." In: *Pediatr Hematol Oncol* 36.1 (2019), pp. 17–27.

[21] L. D. H. Gossel, C. Heim, L. M. Pfeffermann, L. M. Moser, H. B. Bonig, T. E. Klingebiel, P. Bader, W. S. Wels, M. Merker, and E. Rettinger. "Retargeting of NK-92 Cells against High-Risk Rhabdomyosarcomas by Means of an ERBB2 (HER2/Neu)-Specific Chimeric Antigen Receptor." In: *Cancers (Basel)* 13.6 (2021).

[22] B. E. Gryder, M. E. Yohe, H. C. Chou, X. Zhang, J. Marques, M. Wachtel, B. Schaefer, N. Sen, Y. Song, A. Gualtieri, S. Pomella, R. Rota, A. Cleveland, X. Wen, S. Sindiri, J. S. Wei, F. G. Barr, S. Das, T. Andresson, R. Guha, M. Lal-Nag, M. Ferrer, J. F. Shern, K. Zhao, C. J. Thomas, and J. Khan. "PAX3-FOXO1 Establishes Myogenic Super Enhancers and Confers BET Bromodomain Vulnerability." In: *Cancer Discov* 7.8 (2017), pp. 884–899.

[23] A. R. Moghadam, S. C. da Silva Rosa, E. Samiei, J. Alizadeh, J. Field, P. Kawalec, J. Thliveris, M. Akbari, S. Ghavami, and J. W. Gordon. "Autophagy modulates temozolomide-induced cell death in alveolar Rhabdomyosarcoma cells." In: *Cell Death Discov* 4 (2018), p. 52.

[24] N. Dolgikh, M. Hugle, M. Vogler, and S. Fulda. "NRAS-mutated rhabdomyosarcoma cells are vulnerable to mitochondrial apoptosis induced by co-inhibition of MEK and PI3K." In: *Cancer Research* (2018), canres.1737.2017–canres.1737.2017.

[25] K. Fischer, S. Tognarelli, S. Roesler, C. Boedicker, R. Schubert, A. Steinle, T. Klingebiel, P. Bader, S. Fulda, and E. Ullrich. "The Smac Mimetic BV6 Improves NK Cell-Mediated Killing of Rhabdomyosarcoma Cells by Simultaneously Targeting Tumor and Effector Cells." In: *Frontiers in Immunology* 8 (2017).

[26] V. Särchen, S. Shanmugalingam, S. Kehr, L. M. Reindl, V. Greze, S. Wiedemann, C. Boedicker, M. Jacob, K. Bankov, N. Becker, S. Wehner, T. M. Theilen, S. Gretser, E. Gradhand, C. Kummerow, E. Ullrich, and M. Vogler. "Pediatric multicellular tumor spheroid models illustrate a therapeutic potential by combining BH3 mimetics with Natural Killer (NK) cell-based immunotherapy." In: *Cell Death Discov* 8.1 (2022), p. 11.

[27] L. Chen, T. Oke, N. Siegel, G. Cojocaru, A. J. Tam, R. L. Blosser, J. Swailes, J. A. Ligon, A. Lebid, C. Morris, A. Levin, D. S. Rhee, F. M. Johnston, J. B. Greer, C. F. Meyer, B. H. Ladle, E. D. Thompson, E. A. Montgomery, W. Choi, D. J. McConkey, R. A. Anders, D. M. Pardoll, and N. J. Llosa. "The Immunosuppressive Niche of Soft-Tissue Sarcomas is Sustained by Tumor-Associated Macrophages and Characterized by Intratumoral Tertiary Lymphoid Structures." In: *Clin Cancer Res* 26.15 (2020), pp. 4018–4030.

[28] J. N. Kather, C. Horner, C. A. Weis, T. Aung, C. Vokuhl, C. Weiss, M. Scheer, A. Marx, and K. Simon-Keller. "CD163+ immune cell infiltrates and presence of CD54+ microvessels are prognostic markers for patients with embryonal rhabdomyosarcoma." In: *Sci Rep* 9.1 (2019), p. 9211.

[29] D. Hanahan and R. A. Weinberg. "The Hallmarks of Cancer." English. In: *Cell* 100.1 (2000), pp. 57–70.

[30] D. Hanahan and R. A. Weinberg. "Hallmarks of Cancer: The Next Generation." English. In: *Cell* 144.5 (2011), pp. 646–674.

[31] B. Eluard, C. Thieblemont, and V. Baud. "NF-kappaB in the New Era of Cancer Therapy." In: *Trends Cancer* 6.8 (2020), pp. 677–687.

[32] D. Hanahan. “Hallmarks of Cancer: New Dimensions.” In: *Cancer Discov* 12.1 (2022), pp. 31–46.

[33] L. Galluzzi et al. “Molecular mechanisms of cell death: recommendations of the Nomenclature Committee on Cell Death 2018.” en. In: *Cell Death Differ* 25.3 (2018), pp. 486–541.

[34] J. F. R. Kerr, A. H. Wyllie, and A. R. Currie. “Apoptosis: A Basic Biological Phenomenon with Wide-ranging Implications in Tissue Kinetics.” In: *Br J Cancer* 26 (1972), pp. 239–257.

[35] S. Elmore. “Apoptosis: A Review of Prgrammed Cell Death.” In: *Toxicol Pathol* 35.4 (2007), pp. 495–516.

[36] D. R. Green. “A Matter of Life and Death.” en. In: *Cold Spring Harb Perspect Biol* 14.1 (2022), a041004.

[37] G. C. Cavalcante, A. P. Schaan, G. F. Cabral, M. N. Santana-da-Silva, P. Pinto, A. F. Vidal, and A. Ribeiro-dos-Santos. “A Cell’s Fate: An Overview of the Molecular Biology and Genetics of Apoptosis.” In: *International Journal of Molecular Sciences* 20 (2019).

[38] D. R. Green. “The Mitochondrial Pathway of Apoptosis Part I: MOMP and Beyond.” en. In: *Cold Spring Harb Perspect Biol* 14.5 (2022), a041038.

[39] D. R. Green. “The Mitochondrial Pathway of Apoptosis Part II: The BCL-2 Protein Family.” en. In: *Cold Spring Harb Perspect Biol* 14.6 (2022), a041046.

[40] F. J. Bock and S. W. G. Tait. “Mitochondria as multifaceted regulators of cell death.” en. In: *Nat Rev Mol Cell Biol* 21.2 (2020), pp. 85–100.

[41] H. Kalkavan and D. R. Green. “MOMP, cell suicide as a BCL-2 family business.” In: *Cell death and differentiation* 25.1 (2018), pp. 46–46.

[42] L. Dorstyn, C. W. Akey, and S. Kumar. “New insights into apoptosome structure and function.” In: *Cell Death Differ* 25.7 (2018), pp. 1194–1208.

[43] M. L. Würstle, M. A. Laussmann, and M. Rehm. “The central role of initiator caspase-9 in apoptosis signal transduction and the regulation of its activation

and activity on the apoptosome." eng. In: *Exp Cell Res* 318.11 (2012), pp. 1213–1220.

[44] O. Julien and J. A. Wells. "Caspases and their substrates." en. In: *Cell Death Differ* 24.8 (2017), pp. 1380–1389.

[45] L. E. Araya, I. V. Soni, J. A. Hardy, and O. Julien. "Deorphanizing Caspase-3 and Caspase-9 Substrates In and Out of Apoptosis with Deep Substrate Profiling." en. In: *ACS Chem. Biol.* 16.11 (2021), pp. 2280–2296.

[46] D. Goldschneider and P. Mehlen. "Dependence receptors: a new paradigm in cell signaling and cancer therapy." eng. In: *Oncogene* 29.13 (2010), pp. 1865–1882.

[47] A.-M. Negulescu and P. Mehlen. "Dependence receptors – the dark side awakens." en. In: *The FEBS Journal* 285.21 (2018), pp. 3909–3924.

[48] A. Ashkenazi and R. S. Herbst. "To killa tumor cell: the potential of proapoptotic receptor agonists." In: *The Journal of Clinical Investigation* 118.6 (2008), pp. 1979–1990.

[49] B. B. Aggarwal, S. C. Gupta, and J. H. Kim. "Historical perspectives on tumor necrosis factor and its superfamily: 25 years later, a golden journey." In: *Blood* 119.3 (2012), pp. 651–665.

[50] D. Brenner, H. Blaser, and T. W. Mak. "Regulation of tumour necrosis factor signalling: live or let die." In: *Nature Reviews Immunology* 15.6 (2015), pp. 362–374.

[51] I. Lavrik, A. Golks, and P. H. Krammer. "Death receptor signaling." eng. In: *J Cell Sci* 118.Pt 2 (2005), pp. 265–267.

[52] M. R. Sprick, E. Rieser, H. Stahl, A. Grosse-Wilde, M. A. Weigand, and H. Walczak. "Caspase-10 is recruited to and activated at the native TRAIL and CD95 death-inducing signalling complexes in a FADD-dependent manner but can not functionally substitute caspase-8." In: *EMBO J* 21.17 (2002), pp. 4520–30.

[53] K. Schleich, U. Warnken, N. Fricker, S. Öztürk, P. Richter, K. Kammerer, M. Schnölzer, P. H. Krammer, and I. N. Lavrik. "Stoichiometry of the CD95 Death-Inducing Signaling Complex: Experimental and Modeling Evidence for a

Death Effector Domain Chain Model." English. In: *Molecular Cell* 47.2 (2012), pp. 306–319.

[54] H. A. Elrod and S.-Y. Sun. "Modulation of death receptors by cancer therapeutic agents." In: *Cancer Biology %& Therapy* 7.2 (2008), pp. 163–173.

[55] F. H. Igney and P. H. Krammer. "Death and Anti-death: Tumor Resistance to Apoptosis." In: *Nature Reviews Cancer* 2 (2002), pp. 277–288.

[56] M. E. Peter and P. H. Krammer. "The CD95(APO-1/Fas) DISC and beyond." en. In: *Cell Death Differ* 10.1 (2003), pp. 26–35.

[57] U. Fischer, C. Stroh, and K. Schulze-Osthoff. "Unique and overlapping substrate specificities of caspase-8 and caspase-10." In: *Oncogene* 25.1 (2006), pp. 152–9.

[58] H. Li, H. Zhu, C.-j. Xu, and J. Yuan. "Cleavage of BID by Caspase 8 Mediates the Mitochondrial Damage in the Fas Pathway of Apoptosis." English. In: *Cell* 94.4 (1998), pp. 491–501.

[59] V. Tchikov, U. Bertsch, J. Fritsch, B. Edelmann, and S. Schütze. "Subcellular compartmentalization of TNF receptor-1 and CD95 signaling pathways." In: *Eur. J. Cell Biol.* 90.6-7 (2011), pp. 467–475.

[60] M. Heinrich, J. Neumeyer, M. Jakob, C. Hallas, V. Tchikov, S. Winoto-Morbach, M. Wickel, W. Schneider-Brachert, A. Trauzold, A. Hethke, and S. Schütze. "Cathepsin D links TNF-induced acid sphingomyelinase to Bid-mediated caspase-9 and-3 activation." In: *Cell Death Differ.* 11.5 (2004), pp. 550–563.

[61] B. Edelmann, U. Bertsch, V. Tchikov, S. Winoto-Morbach, C. Perrotta, M. Jakob, S. Adam-Klages, D. Kabelitz, and S. Schütze. "Caspase-8 and caspase-7 sequentially mediate proteolytic activation of acid sphingomyelinase in TNF-R1 receptosomes." In: *EMBO J.* 30 (2011), pp. 379–394.

[62] J. Fritsch, R. Fickers, J. Klawitter, V. Särchen, P. Zingler, D. Adam, O. Janssen, E. Krause, and S. Schütze. "TNF induced cleavage of HSP90 by cathepsin D potentiates apoptotic cell death." In: *Oncotarget* 7.46 (2016), pp. 75774–75789.

[63] M. S. Hayden and S. Ghosh. "Shared principles in NF-kappaB signaling." In: *Cell* 132.3 (2008), pp. 344–62.

[64] Q. Zhang, M. J. Lenardo, and D. Baltimore. "30 Years of NF-kappaB: A Blossoming of Relevance to Human Pathobiology." In: *Cell* 168.1-2 (2017), pp. 37–57.

[65] S. Mitchell, J. Vargas, and A. Hoffmann. "Signaling via the NFB system." eng. In: *Wiley Interdiscip Rev Syst Biol Med* 8.3 (2016), pp. 227–241.

[66] M. Karin and Y. Ben-Neriah. "Phosphorylation meets ubiquitination: the control of NF-[kappa]B activity." eng. In: *Annu Rev Immunol* 18 (2000), pp. 621–663.

[67] B. Hoesel and J. A. Schmid. "The complexity of NF-kappaB signaling in inflammation and cancer." In: *Mol Cancer* 12 (2013), p. 86.

[68] K. M. Pflug and R. Sitcheran. "Targeting NF-kappaB-Inducing Kinase (NIK) in Immunity, Inflammation, and Cancer." In: *Int J Mol Sci* 21.22 (2020).

[69] J. Li, Q. Yin, and H. Wu. "Structural basis of signal transduction in the TNF receptor superfamily." In: *Advances in immunology* 119 (2013), p. 135.

[70] H. Li, M. Kobayashi, M. Blonska, Y. You, and X. Lin. "Ubiquitination of RIP Is Required for Tumor Necrosis Factor -induced NF-B Activation*." en. In: *Journal of Biological Chemistry* 281.19 (2006), pp. 13636–13643.

[71] N. Peltzer, M. Darding, and H. Walczak. "Holding RIPK1 on the Ubiquitin Leash in TNFR1 Signaling." en. In: *Trends in Cell Biology* 26.6 (2016), pp. 445–461.

[72] Y.-R. Xu and C.-Q. Lei. "TAK1-TABs Complex: A Central Signalosome in Inflammatory Responses." In: *Frontiers in Immunology* 11 (2021).

[73] L. Cabal-Hierro and P. S. Lazo. "Signal transduction by tumor necrosis factor receptors." In: *Cell. Signalling* 24.6 (2012), pp. 1297–1305.

[74] C. Wang, L. Deng, M. Hong, G. R. Akkaraju, J. Inoue, and Z. J. Chen. "TAK1 is a ubiquitin-dependent kinase of MKK and IKK." eng. In: *Nature* 412.6844 (2001), pp. 346–351.

[75] S. Sato, H. Sanjo, K. Takeda, J. Ninomiya-Tsuji, M. Yamamoto, T. Kawai, K. Matsumoto, O. Takeuchi, and S. Akira. "Essential function for the kinase TAK1

in innate and adaptive immune responses." en. In: *Nat Immunol* 6.11 (2005), pp. 1087–1095.

[76] A. Adhikari, M. Xu, and Z. J. Chen. "Ubiquitin-mediated activation of TAK1 and IKK." eng. In: *Oncogene* 26.22 (2007), pp. 3214–3226.

[77] Z. J. Chen, V. Bhoj, and R. B. Seth. "Ubiquitin, TAK1 and IKK: is there a connection?" en. In: *Cell Death & Differentiation* 13.5 (2006), pp. 687–692.

[78] I. Alkalay, A. Yaron, A. Hatzubai, A. Orian, A. Ciechanover, and Y. Ben-Neriah. "Stimulation-dependent I kappa B alpha phosphorylation marks the NF-kappa B inhibitor for degradation via the ubiquitin-proteasome pathway." en. In: *Proc. Natl. Acad. Sci. U.S.A.* 92.23 (1995), pp. 10599–10603.

[79] E. Zandi, Y. Chen, and M. Karin. "Direct phosphorylation of IkappaB by IKKalpha and IKKbeta: discrimination between free and NF-kappaB-bound substrate." eng. In: *Science* 281.5381 (1998), pp. 1360–1363.

[80] A. Hoffmann, A. Levchenko, M. L. Scott, and D. Baltimore. "The IkappaB-NF-kappaB signaling module: temporal control and selective gene activation." eng. In: *Science* 298.5596 (2002), pp. 1241–1245.

[81] A. A. Beg, S. M. Ruben, R. I. Scheinman, S. Haskill, C. A. Rosen, and A. S. Baldwin. "I kappa B interacts with the nuclear localization sequences of the subunits of NF-kappa B: a mechanism for cytoplasmic retention." en. In: *Genes Dev.* 6.10 (1992), pp. 1899–1913.

[82] F. Yang, E. Tang, K. Guan, and C. Y. Wang. "IKK beta plays an essential role in the phosphorylation of RelA/p65 on serine 536 induced by lipopolysaccharide." In: *J Immunol* 170.11 (2003), pp. 5630–5.

[83] H. Sakurai, H. Chiba, H. Miyoshi, T. Sugita, and W. Toriumi. "IkappaB kinases phosphorylate NF-kappaB p65 subunit on serine 536 in the transactivation domain." In: *J Biol Chem* 274.43 (1999), pp. 30353–6.

[84] F. Christian, E. L. Smith, and R. J. Carmody. "The Regulation of NF-kappaB Subunits by Phosphorylation." In: *Cells* 5.1 (2016).

[85] S. T. Smale. "Dimer-specific regulatory mechanisms within the NF-B family of transcription factors." en. In: *Immunological Reviews* 246.1 (2012), pp. 193–204.

[86] B. J. Zarnegar, Y. Wang, D. J. Mahoney, P. W. Dempsey, H. H. Cheung, J. He, T. Shiba, X. Yang, W. C. Yeh, T. W. Mak, R. G. Korneluk, and G. Cheng. "Noncanonical NF-kappaB activation requires coordinated assembly of a regulatory complex of the adaptors cIAP1, cIAP2, TRAF2 and TRAF3 and the kinase NIK." In: *Nat Immunol* 9.12 (2008), pp. 1371–8.

[87] S. Lee, M. Challa-Malladi, S. B. Bratton, and C. W. Wright. "Nuclear Factor-B-inducing Kinase (NIK) Contains an Amino-terminal Inhibitor of Apoptosis (IAP)-binding Motif (IBM) That Potentiates NIK Degradation by Cellular IAP1 (c-IAP1) *." English. In: *Journal of Biological Chemistry* 289.44 (2014), pp. 30680–30689.

[88] G. Qing, Z. Qu, and G. Xiao. "Stabilization of Basally Translated NF-B-inducing Kinase (NIK) Protein Functions as a Molecular Switch of Processing of NF-B2 p100 *." English. In: *Journal of Biological Chemistry* 280.49 (2005), pp. 40578–40582.

[89] P. Kucharzewska, C. X. Maracle, K. C. M. Jeucken, J. P. van Hamburg, E. Israelsson, M. Furber, S. W. Tas, and H. K. Olsson. "NIK-IKK complex interaction controls NF-kappaB-dependent inflammatory activation of endothelium in response to LTbetaR ligation." In: *J Cell Sci* 132.7 (2019).

[90] L. Ling, Z. Cao, and D. V. Goeddel. "NF-B-inducing kinase activates IKK- by phosphorylation of Ser-176." In: *Proceedings of the National Academy of Sciences* 95.7 (1998), pp. 3792–3797.

[91] U. Senftleben, Y. Cao, G. Xiao, F. R. Greten, G. Krahn, G. Bonizzi, Y. Chen, Y. Hu, A. Fong, S. C. Sun, and M. Karin. "Activation by IKKalpha of a second, evolutionary conserved, NF-kappa B signaling pathway." In: *Science* 293.5534 (2001), pp. 1495–9.

[92] G. Xiao, A. Fong, and S.-C. Sun. "Induction of p100 Processing by NF-B-inducing Kinase Involves Docking IB Kinase (IKK) to p100 and IKK-mediated Phosphorylation *." English. In: *Journal of Biological Chemistry* 279.29 (2004), pp. 30099–30105.

[93] C. Du, M. Fang, Y. Li, L. Li, and X. Wang. "Smac, a mitochondrial protein that promotes cytochrome c-dependent caspase activation by eliminating IAP inhibition." In: *Cell* 102.1 (2000), pp. 33–42.

[94] F. L. Scott, J.-B. Denault, S. J. Riedl, H. Shin, M. Renatus, and G. S. Salvesen. "XIAP inhibits caspase-3 and -7 using two binding sites: evolutionarily conserved mechanism of IAPs." In: *The EMBO Journal* 24.3 (2005), pp. 645–655.

[95] P. Cetraro, J. Plaza-Diaz, A. MacKenzie, and F. Abadía-Molina. "A Review of the Current Impact of Inhibitors of Apoptosis Proteins and Their Repression in Cancer." en. In: *Cancers* 14.7 (2022), p. 1671.

[96] M. Birnbaum, R. J. Clem, and L. Miller. "An apoptosis-inhibiting gene from a nuclear polyhedrosis virus encoding a polypeptide with Cys/His sequence motifs." In: *Journal of virology* (1994).

[97] S. M. Srinivasula and J. D. Ashwell. "IAPs: What's in a Name?" English. In: *Molecular Cell* 30.2 (2008), pp. 123–135.

[98] F. Cossu, M. Milani, E. Mastrangelo, and D. Lecis. "Targeting the BIR Domains of Inhibitor of Apoptosis (IAP) Proteins in Cancer Treatment." In: *Comput Struct Biotechnol J* 17 (2019), pp. 142–150.

[99] S. M. Srinivasula, R. Hegde, A. Saleh, P. Datta, E. Shiozaki, J. Chai, R. A. Lee, P. D. Robbins, T. Fernandes-Alnemri, Y. Shi, and E. S. Alnemri. "A conserved XIAP-interaction motif in caspase-9 and Smac/DIABLO regulates caspase activity and apoptosis." In: *Nature* 410.6824 (2001), pp. 112–116.

[100] T. Samuel, K. Welsh, T. Lober, S. H. Togo, J. M. Zapata, and J. C. Reed. "Distinct BIR Domains of cIAP1 Mediate Binding to and Ubiquitination of Tumor Necrosis Factor Receptor-associated Factor 2 and Second Mitochondrial Activator of Caspases *." English. In: *Journal of Biological Chemistry* 281.2 (2006), pp. 1080–1090.

[101] Y. E. Choi, M. Butterworth, S. Malladi, C. S. Duckett, G. M. Cohen, and S. B. Bratton. "The E3 Ubiquitin Ligase cIAP1 Binds and Ubiquitinates Caspase-3 and -7 via Unique Mechanisms at Distinct Steps in Their Processing *." English. In: *Journal of Biological Chemistry* 284.19 (2009), pp. 12772–12782.

[102] G. Wu, J. Chai, T. L. Suber, J.-W. Wu, C. Du, X. Wang, and Y. Shi. "Structural basis of IAP recognition by Smac/DIABLO." en. In: *Nature* 408.6815 (2000), pp. 1008–1012.

[103] E. Varfolomeev, J. W. Blankenship, S. M. Wayson, A. V. Fedorova, N. Kayagaki, P. Garg, K. Zobel, J. N. Dynek, L. O. Elliott, H. J. Wallweber, J. A. Flygare, W. J. Fairbrother, K. Deshayes, V. M. Dixit, and D. Vucic. "IAP antagonists induce autoubiquitination of c-IAPs, NF-kappaB activation, and TNFalpha-dependent apoptosis." In: *Cell* 131.4 (2007), pp. 669–81.

[104] J. Chai, C. Du, J. W. Wu, S. Kyin, X. Wang, and Y. Shi. "Structural and biochemical basis of apoptotic activation by Smac/DIABLO." In: *Nature* 406.6798 (2000), pp. 855–862.

[105] R. Ali, S. Singh, and W. Haq. "IAP Proteins Antagonist: An Introduction and Chemistry of Smac Mimetics under Clinical Development." In: *Curr Med Chem* 25.31 (2018), pp. 3768–3795.

[106] H. Sun, Z. Nikolovska-Coleska, C.-Y. Yang, L. Xu, M. Liu, Y. Tomita, H. Pan, Y. Yoshioka, K. Krajewski, P. P. Roller, and S. Wang. "Structure-Based Design of Potent, Conformationally Constrained Smac Mimetics." In: *J. Am. Chem. Soc.* 126.51 (2004), pp. 16686–16687.

[107] H. Sun, Z. Nikolovska-Coleska, J. Lu, J. L. Meagher, C.-Y. Yang, S. Qiu, Y. Tomita, Y. Ueda, S. Jiang, K. Krajewski, P. P. Roller, J. A. Stuckey, and S. Wang. "Design, Synthesis, and Characterization of a Potent, Nonpeptide, Cell-Permeable, Bivalent Smac Mimetic That Concurrently Targets Both the BIR2 and BIR3 Domains in XIAP." In: *J. Am. Chem. Soc.* 129.49 (2007), pp. 15279–15294.

[108] M. Schirmer, L. Trentin, M. Queudeville, F. Seyfried, S. Demir, E. Tausch, S. Stilgenbauer, S. M. Eckhoff, L. H. Meyer, and K.-M. Debatin. "Intrinsic and chemo-sensitizing activity of SMAC-mimetics on high-risk childhood acute lymphoblastic leukemia." eng. In: *Cell Death Dis* 7 (2016), e2052.

[109] K. Belz, H. Schoeneberger, S. Wehner, A. Weigert, H. Bönig, T. Klingebiel, I. Fichtner, and S. Fulda. "Smac mimetic and glucocorticoids synergize to induce apoptosis in childhood ALL by promoting ripoptosome assembly." In: *Blood* 124.2 (2014), pp. 240–250.

[110] I. Eckhardt, S. Roesler, and S. Fulda. "Identification of DR5 as a critical, NF-kappaB-regulated mediator of Smac-induced apoptosis." In: *Cell Death Dis* 4 (2013), e936.

[111] S. Cristofanon, B. A. Abhari, M. Krueger, A. Tchoghandjian, S. Momma, C. Calaminus, D. Vucic, B. J. Pichler, and S. Fulda. "Identification of RIP1 as a critical mediator of Smac mimetic-mediated sensitization of glioblastoma cells for Drozitumab-induced apoptosis." en. In: *Cell Death Dis* 6.4 (2015), e1724–e1724.

[112] M. El-Mesery, M. E. Shaker, and A. Elgaml. "The SMAC mimetic BV6 induces cell death and sensitizes different cell lines to TNF- and TRAIL-induced apoptosis." en. In: *Exp Biol Med (Maywood)* 241.18 (2016), pp. 2015–2022.

[113] A. Koch, B. Jeiler, J. Roedig, S. J. L. van Wijk, N. Dolgikh, and S. Fulda. "Smac mimetics and TRAIL cooperate to induce MLKL-dependent necroptosis in Burkitt's lymphoma cell lines." en. In: *Neoplasia* 23.5 (2021), pp. 539–550.

[114] R. C. Brands, M. J. J. Scheurer, S. Hartmann, A. Seher, C. Freudlsperger, J. Moratin, C. Linz, A. C. Kübler, and U. D. A. Müller-Richter. "Sensitization of head and neck squamous cell carcinoma to apoptosis by combinational SMAC mimetic and Fas ligand-Fc treatment in vitro." en. In: *Journal of Cranio-Maxillofacial Surgery* 48.7 (2020), pp. 685–693.

[115] N. Schmidt, T. Haydn, I. Schneider, H. Busch, M. Boerries, and S. Fulda. "Smac mimetic induces an early wave of gene expression via NF-kB and AP-1 and a second wave via TNFR1 signaling." In: *Cancer Letters* 421 (2018), pp. 170–185.

[116] I. Eckhardt, A. Weigert, and S. Fulda. "Identification of IRF1 as critical dual regulator of Smac mimetic-induced apoptosis and inflammatory cytokine response." In: *Cell Death Dis* 5 (2014), e1562.

[117] R. Li, D. Ruttinger, W. Urba, B. A. Fox, and H. M. Hu. "Targeting and amplification of immune killing of tumor cells by pro-Smac." In: *Int J Cancer* 109.1 (2004), pp. 85–94.

[118] K. Brinkmann, A. Hombach, J. M. Seeger, D. Wagner-Stippich, D. Klubertz, M. Krönke, H. Abken, and H. Kashkar. "Second mitochondria-derived activator of caspase (SMAC) mimetic potentiates tumor susceptibility toward natural killer cell-mediated killing." In: *Leukemia & Lymphoma* 55.3 (2014), pp. 645–651.

[119] Z. Chen, J. Chen, H. Liu, W. Dong, X. Huang, D. Yang, J. Hou, and X. Zhang. "The SMAC Mimetic APG-1387 Sensitizes Immune-Mediated Cell Apoptosis in Hepatocellular Carcinoma." In: *Front Pharmacol* 9 (2018), p. 1298.

[120] J. Michie, P. A. Beavis, A. J. Freeman, S. J. Vervoort, K. M. Ramsbottom, V. Narasimhan, E. J. Lelliott, N. Lalaoui, R. G. Ramsay, R. W. Johnstone, J. Silke, P. K. Darcy, I. Voskoboinik, C. J. Kearney, and J. Oliaro. "Antagonism of IAPs Enhances CAR T-cell Efficacy." In: *Cancer Immunology Research* 7.2 (2019), pp. 183–192.

[121] E. Rettinger, A. Glatthaar, B. A. Abhari, S. Oelsner, V. Pfirrmann, S. Huenecke, S. Kuci, H. Kreyenberg, A. M. Willasch, T. Klingebiel, S. Fulda, and P. Bader. "SMAC mimetic BV6 enables sensitization of resistant tumor cells but also affects cytokine-induced killer (CIK) cells: a potential challenge for combination therapy." In: *frontiers in Pediatrics* 2.75 (2014).

[122] M. A. Caligiuri. "Human natural killer cells." In: *Blood* 112.3 (2008), pp. 461–9.

[123] M. E. Ivanova, N. Lukoyanova, S. Malhotra, M. Topf, J. A. Trapani, I. Voskoboinik, and H. R. Saibil. "The pore conformation of lymphocyte perforin." In: *Science Advances* 8.6 (2022), eabk3147.

[124] I. Prager, C. Liesche, H. van Ooijen, D. Urlaub, Q. Verron, N. Sandstrom, F. Fasbender, M. Claus, R. Eils, J. Beaudouin, B. Onfelt, and C. Watzl. "NK cells switch from granzyme B to death receptor-mediated cytotoxicity during serial killing." In: *J Exp Med* 216.9 (2019), pp. 2113–2127.

[125] L. A. Gwalani and J. S. Orange. "Single Degranulations in NK Cells Can Mediate Target Cell Killing." eng. In: *J Immunol* 200.9 (2018), pp. 3231–3243.

[126] M. F. Sanchez, F. Murad, G. S. Gulculer Balta, A. Martin-Villalba, A. J. Garcia-Saez, and D. C. Carrer. "Early activation of CD95 is limited and localized to the cytotoxic synapse." In: *FEBS J* 285.15 (2018), pp. 2813–2827.

[127] M. Lettau, D. Kabelitz, and O. Janssen. "Lysosome-Related Effector Vesicles in T Lymphocytes and NK Cells." en. In: *Scandinavian Journal of Immunology* 82.3 (2015), pp. 235–243.

[128] C. S. Backes, K. S. Friedmann, S. Mang, A. Knorck, M. Hoth, and C. Kummerow. "Natural killer cells induce distinct modes of cancer cell death: Discrimination, quantification, and modulation of apoptosis, necrosis, and mixed forms." In: *J Biol Chem* 293.42 (2018), pp. 16348–16363.

[129] A. López-Soto, S. Gonzalez, M. J. Smyth, and L. Galluzzi. "Control of Metastasis by NK Cells." en. In: *Cancer Cell* 32.2 (2017), pp. 135–154.

[130] J. S. Orange. "Formation and function of the lytic NK-cell immunological synapse." In: *Nat Rev Immunol* 8.9 (2008), pp. 713–25.

[131] S. Kumar. "Natural killer cell cytotoxicity and its regulation by inhibitory receptors." en. In: *Immunology* 154.3 (2018), pp. 383–393.

[132] E. Vivier, E. Tomasello, M. Baratin, T. Walzer, and S. Ugolini. "Functions of natural killer cells." In: *Nat Immunol* 9.5 (2008), pp. 503–10.

[133] S. Duan, W. Guo, Z. Xu, Y. He, C. Liang, Y. Mo, Y. Wang, F. Xiong, C. Guo, Y. Li, X. Li, G. Li, Z. Zeng, W. Xiong, and F. Wang. "Natural killer group 2D receptor and its ligands in cancer immune escape." en. In: *Mol Cancer* 18.1 (2019), pp. 1–14.

[134] Z.-L. Ou, Z. Luo, W. Wei, S. Liang, T.-L. Gao, and Y.-B. Lu. "Hypoxia-induced shedding of MICA and HIF1A-mediated immune escape of pancreatic cancer cells from NK cells: role of circ_0000977/miR-153 axis." In: *RNA Biology* 16.11 (2019), pp. 1592–1603.

[135] A. M. Paczulla, K. Rothfelder, S. Raffel, M. Konantz, J. Steinbacher, H. Wang, C. Tandler, M. Mbarga, T. Schaefer, M. Falcone, E. Nievergall, D. Dorfel, P. Hanns, J. R. Passweg, C. Lutz, J. Schwaller, R. Zeiser, B. R. Blazar, M. A. Caligiuri, S. Dirnhofer, P. Lundberg, L. Kanz, L. Quintanilla-Martinez, A. Steinle, A. Trumpp, H. R. Salih, and C. Lengerke. "Absence of NKG2D ligands defines leukaemia stem cells and mediates their immune evasion." In: *Nature* 572.7768 (2019), pp. 254–259.

[136] J. P. Medema, J. de Jong, L. T. Peltenburg, E. M. Verdegaal, A. Gorter, S. A. Bres, K. L. Franken, M. Hahne, J. P. Albar, C. J. Melief, and R. Offringa. "Blockade of the granzyme B/perforin pathway through overexpression of the serine protease inhibitor PI-9/SPI-6 constitutes a mechanism for immune escape by tumors." In: *Proc Natl Acad Sci U S A* 98.20 (2001), pp. 11515–20.

[137] C. Sordo-Bahamonde, S. Lorenzo-Herrero, A. R. Payer, S. Gonzalez, and A. Lopez-Soto. "Mechanisms of Apoptosis Resistance to NK Cell-Mediated Cytotoxicity in Cancer." In: *Int J Mol Sci* 21.10 (2020).

[138] L. Ferrari de Andrade, S. Kumar, A. M. Luoma, Y. Ito, P. H. Alves da Silva, D. Pan, J. W. Pyrdol, C. H. Yoon, and K. W. Wucherpfennig. "Inhibition of MICA and MICB Shedding Elicits NK-Cell-Mediated Immunity against Tumors Resistant to Cytotoxic T Cells." In: *Cancer Immunol Res* 8.6 (2020), pp. 769–780.

[139] M. Carlsten, A. Namazi, R. Reger, E. Levy, M. Berg, C. St Hilaire, and R. W. Childs. "Bortezomib sensitizes multiple myeloma to NK cells via ER-stress-induced suppression of HLA-E and upregulation of DR5." In: *Oncoimmunology* 8.2 (2019), e1534664.

[140] N. Sawasdee, M. Wattanapanitch, N. Thongsin, N. Phanthaphol, C. Chiawpanit, C. Thuwajit, P. T. Yenchitsomanus, and A. Panya. "Doxorubicin sensitizes breast cancer cells to natural killer cells in connection with increased Fas receptors." In: *Int J Mol Med* 49.3 (2022).

[141] Y. Li, Y. Zhang, G. Cao, X. Zheng, C. Sun, H. Wei, Z. Tian, W. Xiao, R. Sun, and H. Sun. "Blockade of checkpoint receptor PVRIG unleashes anti-tumor immunity of NK cells in murine and human solid tumors." en. In: *J Hematol Oncol* 14.1 (2021), pp. 1–17.

[142] M. H. Hofmann, R. Mani, H. Engelhardt, M. A. Impagnatiello, S. Carotta, M. Kerenyi, S. Lorenzo-Herrero, J. Bottcher, D. Scharn, H. Arnhof, A. Zoephel, R. Schnitzer, T. Gerstberger, M. P. Sanderson, G. Rajgolikar, S. Goswami, S. Vasu, P. Ettmayer, S. Gonzalez, M. Pearson, D. B. McConnell, N. Kraut, N. Muthusamy, and J. Moll. "Selective and Potent CDK8/19 Inhibitors Enhance NK-Cell Activity and Promote Tumor Surveillance." In: *Mol Cancer Ther* 19.4 (2020), pp. 1018–1030.

[143] M. Vogler, H. Walczak, D. Stadel, T. L. Haas, F. Genze, M. Jovanovic, U. Bhanot, C. Hasel, P. Möller, J. E. Gschwend, T. Simmet, K.-M. Debatin, and S. Fulda. "Small Molecule XIAP Inhibitors Enhance TRAIL-Induced Apoptosis and Antitumor Activity in Preclinical Models of Pancreatic Carcinoma." In: *Cancer Research* 69.6 (2009), pp. 2425–2434.

[144] V. Vetma, C. Guttà, N. Peters, C. Praetorius, M. Hutt, O. Seifert, F. Meier, R. Kontermann, D. Kulms, and M. Rehm. "Convergence of pathway analysis and pattern recognition predicts sensitization to latest generation TRAIL ther-

apeutics by IAP antagonism." en. In: *Cell Death Differ* 27.8 (2020), pp. 2417–2432.

[145] S. C. Sun. "The non-canonical NF-kappaB pathway in immunity and inflammation." In: *Nat Rev Immunol* 17.9 (2017), pp. 545–558.

[146] J. Wagner, V. Pfannenstiel, A. Waldmann, J. W. J. Bergs, B. Brill, S. Huenecke, T. Klingebiel, F. Rodel, C. J. Buchholz, W. S. Wels, P. Bader, and E. Ullrich. "A Two-Phase Expansion Protocol Combining Interleukin (IL)-15 and IL-21 Improves Natural Killer Cell Proliferation and Cytotoxicity against Rhabdomyosarcoma." In: *Front Immunol* 8 (2017), p. 676.

[147] J. G. Doench, N. Fusi, M. Sullender, M. Hegde, E. W. Vaimberg, K. F. Donovan, I. Smith, Z. Tothova, C. Wilen, R. Orchard, H. W. Virgin, J. Listgarten, and D. E. Root. "Optimized sgRNA design to maximize activity and minimize off-target effects of CRISPR-Cas9." eng. In: *Nat Biotechnol* 34.2 (2016), pp. 184–191.

[148] J. Schindelin, I. Arganda-Carreras, E. Frise, V. Kaynig, M. Longair, T. Pietzsch, S. Preibisch, C. Rueden, S. Saalfeld, B. Schmid, J. Y. Tinevez, D. J. White, V. Hartenstein, K. Eliceiri, P. Tomancak, and A. Cardona. "Fiji: an open-source platform for biological-image analysis." In: *Nat Methods* 9.7 (2012), pp. 676–82.

[149] Y. Zhou, B. Zhou, L. Pache, M. Chang, A. H. Khodabakhshi, O. Tanaseichuk, C. Benner, and S. K. Chanda. "Metascape provides a biologist-oriented resource for the analysis of systems-level datasets." In: *Nat Commun* 10.1 (2019), p. 1523.

[150] M. Marcusson-Stahl and K. Cederbrant. "A flow-cytometric NK-cytotoxicity assay adapted for use in rat repeated dose toxicity studies." In: *Toxicology* 193.3 (2003), pp. 269–79.

[151] A. D. Sennepin, S. Charpentier, T. Normand, C. Sarré, A. Legrand, and L. M. Mollet. "Multiple reprobing of Western blots after inactivation of peroxidase activity by its substrate, hydrogen peroxide." In: *Analytical biochemistry* 393.1 (2009), pp. 129–131.

[152] K. J. Livak and T. D. Schmittgen. "Analysis of relative gene expression data using real-time quantitative PCR and the 2(-Delta Delta C(T)) Method." In: *Methods* 25.4 (2001), pp. 402–8.

[153] G. Riedel, U. Rudrich, N. Fekete-Drimusz, M. P. Manns, F. W. Vondran, and M. Bock. "An extended DeltaCT-method facilitating normalisation with multiple reference genes suited for quantitative RT-PCR analyses of human hepatocyte-like cells." In: *PLoS One* 9.3 (2014), e93031.

[154] T. D. Schmittgen and K. J. Livak. "Analyzing real-time PCR data by the comparative C(T) method." eng. In: *Nat Protoc* 3.6 (2008), pp. 1101–1108.

[155] H. Han, J.-W. Cho, S. Lee, A. Yun, H. Kim, D. Bae, S. Yang, C. Y. Kim, M. Lee, E. Kim, S. Lee, B. Kang, D. Jeong, Y. Kim, H.-N. Jeon, H. Jung, S. Nam, M. Chung, J.-H. Kim, and I. Lee. "TRRUST v2: an expanded reference database of human and mouse transcriptional regulatory interactions." eng. In: *Nucleic Acids Res* 46.D1 (2018), pp. D380–D386.

[156] J. Anaya. "OncoLnc: linking TCGA survival data to mRNAs, miRNAs, and lncRNAs." en. In: *PeerJ Comput. Sci.* 2 (2016), e67.

[157] B. Schenk and S. Fulda. "Reactive oxygen species regulate Smac mimetic/TNF-induced necroptotic signaling and cell death." en. In: *Oncogene* 34.47 (2015), pp. 5796–5806.

[158] S. Roesler, I. Eckhardt, S. Wolf, and S. Fulda. "Cooperative TRAIL production mediates IFNa/Smac mimetic-induced cell death in TNFa-resistant solid cancer cells." In: *Oncotarget* 7.4 (2016), pp. 3709–3725.

[159] F. Basit, R. Humphreys, and S. Fulda. "RIP1 protein-dependent assembly of a cytosolic cell death complex is required for inhibitor of apoptosis (IAP) inhibitor-mediated sensitization to lexatumumab-induced apoptosis." In: *J Biol Chem* 287.46 (2012), pp. 38767–77.

[160] M. T. Tomicic, C. Steigerwald, B. Rasenberger, A. Brozovic, and M. Christmann. "Functional mismatch repair and inactive p53 drive sensitization of colorectal cancer cells to irinotecan via the IAP antagonist BV6." en. In: *Arch Toxicol* 93.8 (2019), pp. 2265–2277.

[161] I. Ahmad, A. Dera, S. Irfan, P. Rajagopalan, M. Ali Beg, M. Alshahrani, M. Mir, M. Abohashrh, M. Alam, S. Wahab, A. Verma, and S. Srivastava. "BV6 enhances apoptosis in Lung cancer cells by ameliorating caspase expressions

through attenuation of XIAP, cIAP-1, and cIAP-2 proteins." en. In: *J Can Res Ther* 0.0 (2021).

[162] M. Fichtner, E. Bozkurt, M. Salvucci, C. McCann, K. A. McAllister, L. Halang, H. Düssmann, S. Kinsella, N. Crawford, T. Sessler, D. B. Longley, and J. H. M. Prehn. "Molecular subtype-specific responses of colon cancer cells to the SMAC mimetic Birinapant." en. In: *Cell Death Dis* 11.11 (2020), pp. 1–16.

[163] C. Krepler, S. K. Chunduru, M. B. Halloran, X. He, M. Xiao, A. Vultur, J. Villanueva, Y. Mitsuuchi, E. M. Neiman, C. Benetatos, K. L. Nathanson, R. K. Amaravadi, H. Pehamberger, M. McKinlay, and M. Herlyn. "The Novel SMAC Mimetic Birinapant Exhibits Potent Activity against Human Melanoma Cells." In: *Clinical Cancer Research* 19.7 (2013), pp. 1784–1794.

[164] J. Gallardo-Pérez, M. Espinosa, G. Ceballos-Cancino, A. Daniel, S. Rodríguez-Enríquez, A. Aviles, R. Moreno-Sánchez, J. Melendez-Zajgla, and V. Maldonado. "NF-kappa B is required for the development of tumor spheroids." en. In: *Journal of Cellular Biochemistry* 108.1 (2009), pp. 169–180.

[165] N. Müller-Sienerth, L. Dietz, P. Holtz, M. Kapp, G. U. Grigoleit, C. Schmuck, H. Wajant, and D. Siegmund. "SMAC Mimetic BV6 Induces Cell Death in Monocytes and Maturation of Monocyte-Derived Dendritic Cells." en. In: *PLOS ONE* 6.6 (2011), e21556.

[166] Y. Jiao, J. E. Davis, J. Rautela, E. M. Carrington, M. J. Ludford-Menting, W. Goh, R. B. Delconte, F. Souza-Fonseca-Guimaraes, R. Koldej, D. Gray, D. Huang, B. T. Kile, A. M. Lew, D. S. Ritchie, and N. D. Huntington. "Recipient BCL2 inhibition and NK cell ablation form part of a reduced intensity conditioning regime that improves allo-bone marrow transplantation outcomes." en. In: *Cell Death Differ* 26.8 (2019), pp. 1516–1530.

[167] B. Becknell and M. A. Caligiuri. "Interleukin-2, interleukin-15, and their roles in human natural killer cells." In: *Adv Immunol* 86 (2005), pp. 209–39.

[168] S. T. Beug, V. A. Tang, E. C. LaCasse, H. H. Cheung, C. E. Beauregard, J. Brun, J. P. Nuyens, N. Earl, M. St-Jean, J. Holbrook, H. Dastidar, D. J. Mahoney, C. Ilkow, F. Le Boeuf, J. C. Bell, and R. G. Korneluk. "Smac mimetics and innate immune stimuli synergize to promote tumor death." en. In: *Nat Biotechnol* 32.2 (2014), pp. 182–190.

[169] C. C. Dobson, T. Naing, S. T. Beug, M. D. Faye, J. Chabot, M. St-Jean, D. E. Walker, E. C. LaCasse, D. F. Stojdl, R. G. Korneluk, and M. Holcik. "Oncolytic virus synergizes with Smac mimetic compounds to induce rhabdomyosarcoma cell death in a syngeneic murine model." In: *Oncotarget* 8.2 (2017), pp. 3495–3508.

[170] M. Merker, V. Pfirrmann, S. Oelsner, S. Fulda, T. Klingebiel, W. S. Wels, P. Bader, and E. Rettinger. "Generation and characterization of ErbB2-CAR-engineered cytokine-induced killer cells for the treatment of high-risk soft tissue sarcoma in children." In: *Oncotarget* 8.38 (2017), pp. 66137–66153.

[171] A. S. Nunes, A. S. Barros, E. C. Costa, A. F. Moreira, and I. J. Correia. "3D tumor spheroids as in vitro models to mimic in vivo human solid tumors resistance to therapeutic drugs." en. In: *Biotechnology and Bioengineering* 116.1 (2019), pp. 206–226.

[172] M. T. Meister, M. J. A. G. Koerkamp, T. d. Souza, W. B. Breunis, E. Frazer-Mendelewska, M. Brok, J. DeMartino, F. Manders, C. Calandrini, H. H. D. Kerstens, A. Janse, M. E. M. Dolman, S. Eising, K. P. S. Langenberg, M. v. Tuil, R. R. G. Knops, S. T. v. Scheltinga, L. S. Hiemcke-Jiwa, U. Flucke, J. H. M. Merks, M. M. v. Noesel, B. B. J. Tops, J. Y. Hehir-Kwa, P. Kemmeren, J. J. Molenaar, M. v. d. Wetering, R. v. Boxtel, J. Drost, and F. C. P. Holstege. "Mesenchymal tumor organoid models recapitulate rhabdomyosarcoma subtypes." en. In: *EMBO Mol Med* e16001 (2022), pp. 1–23.

[173] A. Giannattasio, S. Weil, S. Kloess, N. Ansari, E. H. Stelzer, A. Cerwenka, A. Steinle, U. Koehl, and J. Koch. "Cytotoxicity and infiltration of human NK cells in in vivo-like tumor spheroids." In: *BMC Cancer* 15 (2015), p. 351.

[174] P. M. Lanuza, A. Vigueras, S. Olivan, A. C. Prats, S. Costas, G. Llamazares, D. Sanchez-Martinez, J. M. Ayuso, L. Fernandez, I. Ochoa, and J. Pardo. "Activated human primary NK cells efficiently kill colorectal cancer cells in 3D spheroid cultures irrespectively of the level of PD-L1 expression." In: *Oncoimmunology* 7.4 (2018), e1395123.

[175] T. Courau, J. Bonnereau, J. Chicoteau, H. Bottois, R. Remark, L. Assante Miranda, A. Toubert, M. Blery, T. Aparicio, M. Allez, and L. Le Bourhis. "Cocultures of human colorectal tumor spheroids with immune cells reveal the

therapeutic potential of MICA/B and NKG2A targeting for cancer treatment." In: *J Immunother Cancer* 7.1 (2019), p. 74.

[176] A. K. Ray, S. S. Somanchi, N. Dastgheyb, A. Aquino-Lopez, Z. E. Cobanoglu, B. Geier, and D. A. Lee. "Expression of carcinoma, apoptosis, and cell-death-related genes are determinants for sensitivity of pediatric cancer cell lines to lysis by natural killer cells." In: *Pediatr Blood Cancer* 66.10 (2019), e27783.

[177] T. T. Chang and M. Hughes-Fulford. "Monolayer and Spheroid Culture of Human Liver Hepatocellular Carcinoma Cell Line Cells Demonstrate Distinct Global Gene Expression Patterns and Functional Phenotypes." en. In: *Tissue Engineering Part A* 15.3 (2009), pp. 559–567.

[178] M. Schmidt, C. J. Scholz, C. Polednik, and J. Roller. "Spheroid-based 3-dimensional culture models: Gene expression and functionality in head and neck cancer." In: *Oncol Rep* 35.4 (2016), pp. 2431–40.

[179] T. S. Griffith, T. A. Kucaba, M. A. O'Donnell, J. Burns, C. Benetatos, M. A. McKinlay, S. Condon, and S. Chunduru. "Sensitization of human bladder tumor cells to TNF-related apoptosis-inducing ligand (TRAIL)-induced apoptosis with a small molecule IAP antagonist." en. In: *Apoptosis* 16.1 (2011), pp. 13–26.

[180] D. Finlay, M. Vamos, M. González-López, R. J. Ardecky, S. R. Ganji, H. Yuan, Y. Su, T. R. Cooley, C. T. Hauser, K. Welsh, J. C. Reed, N. D. Cosford, and K. Vuori. "Small-Molecule IAP Antagonists Sensitize Cancer Cells to TRAIL-Induced Apoptosis: Roles of XIAP and cIAPs." In: *Molecular Cancer Therapeutics* 13.1 (2014), pp. 5–15.

[181] I. Petak, L. Douglas, D. M. Tillman, R. Vernes, and J. A. Houghton. "Pediatric rhabdomyosarcoma cell lines are resistant to Fas-induced apoptosis and highly sensitive to TRAIL-induced apoptosis." In: *Clin Cancer Res* 6.10 (2000), pp. 4119–27.

[182] K. Izeradjene, L. Douglas, A. Delaney, and J. A. Houghton. "Influence of casein kinase II in tumor necrosis factor-related apoptosis-inducing ligand-induced apoptosis in human rhabdomyosarcoma cells." In: *Clin Cancer Res* 10.19 (2004), pp. 6650–60.

[183] R. Komdeur, C. Meijer, M. Van Zweeden, S. De Jong, J. Wesseling, H. J. Hoekstra, and W. T. van der Graaf. "Doxorubicin potentiates TRAIL cytotoxicity and apoptosis and can overcome TRAIL-resistance in rhabdomyosarcoma cells." In: *Int J Oncol* 25.3 (2004), pp. 677–84.

[184] M. Lettau, H. Schmidt, D. Kabelitz, and O. Janssen. "Secretory lysosomes and their cargo in T and NK cells." In: *Immunol. Lett.* 108 (2007), pp. 10–19.

[185] H. Schmidt, C. Gelhaus, M. Nebendahl, M. Lettau, C. Watzl, D. Kabelitz, M. Leippe, and O. Janssen. "2-D DIGE analyses of enriched secretory lysosomes reveal heterogeneous profiles of functionally relevant proteins in leukemic and activated human NK cells." en. In: *PROTEOMICS* 8.14 (2008), pp. 2911–2925.

[186] T. Yamamoto, K. Yoneda, E. Ueta, S. Doi, and T. Osaki. "Enhanced apoptosis of squamous cell carcinoma cells by interleukin-2-activated cytotoxic lymphocytes combined with radiation and anticancer drugs." en. In: *European Journal of Cancer* 36.15 (2000), pp. 2007–2017.

[187] P. Gorak-Stolinska, J.-P. Truman, D. M. Kemeny, and A. Noble. "Activation-induced cell death of human T-cell subsets is mediated by Fas and granzyme B but is independent of TNF-." en. In: *Journal of Leukocyte Biology* 70.5 (2001), pp. 756–766.

[188] T. Saito, D. Abe, and Y. Nogata. "Polymethoxylated flavones potentiate the cytolytic activity of NK leukemia cell line KHYG-1 via enhanced expression of granzyme B." en. In: *Biochemical and Biophysical Research Communications* 456.3 (2015), pp. 799–803.

[189] E. Varfolomeev, J. W. Blankenship, S. M. Wayson, A. V. Fedorova, N. Kayagaki, P. Garg, K. Zobel, J. N. Dynek, L. O. Elliott, H. J. Wallweber, J. A. Flygare, W. J. Fairbrother, K. Deshayes, V. M. Dixit, and D. Vucic. "IAP Antagonists Induce Autoubiquitination of c-IAPs, NF-B Activation, and TNF-Dependent Apoptosis." en. In: *Cell* 131.4 (2007), pp. 669–681.

[190] S. J. Riedl, M. Renatus, R. Schwarzenbacher, Q. Zhou, C. Sun, S. W. Fesik, R. C. Liddington, and G. S. Salvesen. "Structural Basis for the Inhibition of Caspase-3 by XIAP." en. In: *Cell* 104.5 (2001), pp. 791–800.

[191] D. Twiddy, D. G. Brown, C. Adrain, R. Jukes, S. J. Martin, G. M. Cohen, M. MacFarlane, and K. Cain. "Pro-apoptotic Proteins Released from the Mitochondria Regulate the Protein Composition and Caspase-processing Activity of the Native Apaf-1/Caspase-9 Apoptosome Complex *." English. In: *Journal of Biological Chemistry* 279.19 (2004), pp. 19665–19682.

[192] R. Pan, J. Ryan, D. Pan, K. W. Wucherpfennig, and A. Letai. "Augmenting NK cell-based immunotherapy by targeting mitochondrial apoptosis." In: *Cell* 185.9 (2022), 1521–1538 e18.

[193] L. S. Dickens, R. S. Boyd, R. Jukes-Jones, M. A. Hughes, G. L. Robinson, L. Fairall, J. W. Schwabe, K. Cain, and M. Macfarlane. "A death effector domain chain DISC model reveals a crucial role for caspase-8 chain assembly in mediating apoptotic cell death." In: *Mol Cell* 47.2 (2012), pp. 291–305.

[194] M. A. Hughes, N. Harper, M. Butterworth, K. Cain, G. M. Cohen, and M. MacFarlane. "Reconstitution of the Death-Inducing Signaling Complex Reveals a Substrate Switch that Determines CD95-Mediated Death or Survival." English. In: *Molecular Cell* 35.3 (2009), pp. 265–279.

[195] A. Oberst, C. Pop, A. G. Tremblay, V. Blais, J.-B. Denault, G. S. Salvesen, and D. R. Green. "Inducible Dimerization and Inducible Cleavage Reveal a Requirement for Both Processes in Caspase-8 Activation *." English. In: *Journal of Biological Chemistry* 285.22 (2010), pp. 16632–16642.

[196] K. Harada, S. Toyooka, N. Shivapurkar, A. Maitra, J. L. Reddy, H. Matta, K. Miyajima, C. F. Timmons, G. E. Tomlinson, D. Mastrangelo, R. J. Hay, P. M. Chaudhary, and A. F. Gazdar. "Deregulation of caspase 8 and 10 expression in pediatric tumors and cell lines." In: *Cancer Res* 62.20 (2002), pp. 5897–901.

[197] I. Petak, R. Vernes, K. S. Szucs, M. Anozie, K. Izeradjene, L. Douglas, D. M. Tillman, D. C. Phillips, and J. A. Houghton. "A caspase-8-independent component in TRAIL/Apo-2L-induced cell death in human rhabdomyosarcoma cells." In: *Cell Death & Differentiation* 10 (2003), pp. 729–739.

[198] F. C. Kischkel, D. A. Lawrence, A. Tinel, H. LeBlanc, A. Virmani, P. Schow, A. Gazdar, J. Blenis, D. Arnott, and A. Ashkenazi. "Death receptor recruitment of endogenous caspase-10 and apoptosis initiation in the absence of caspase-8." In: *J Biol Chem* 276.49 (2001), pp. 46639–46.

[199] J. Wang, H. J. Chun, W. Wong, D. M. Spencer, and M. J. Lenardo. “Caspase-10 is an initiator caspase in death receptor signaling.” In: *Proc Natl Acad Sci U S A* 98.24 (2001), pp. 13884–8.

[200] S. Horn, M. A. Hughes, R. Schilling, C. Sticht, T. Tenev, M. Ploesser, P. Meier, M. R. Sprick, M. MacFarlane, and M. Leverkus. “Caspase-10 Negatively Regulates Caspase-8-Mediated Cell Death, Switching the Response to CD95L in Favor of NF-kappaB Activation and Cell Survival.” In: *Cell Rep* 19.4 (2017), pp. 785–797.

[201] W. Shi, X. Li, X. Hou, H. Peng, Q. Jiang, M. Shi, Y. Ji, X. Liu, and J. Liu. “Differential apoptosis gene expressions of rhabdomyosarcoma cells in response to enterovirus 71 infection.” en. In: *BMC Infect Dis* 12.1 (2012), pp. 1–12.

[202] T. Tenev, K. Bianchi, M. Darding, M. Broemer, C. Langlais, F. Wallberg, A. Zachariou, J. Lopez, M. MacFarlane, K. Cain, and P. Meier. “The Ripoptosome, a signaling platform that assembles in response to genotoxic stress and loss of IAPs.” In: *Mol Cell* 43.3 (2011), pp. 432–48.

[203] M. Feoktistova, P. Geserick, B. Kellert, D. P. Dimitrova, C. Langlais, M. Hupe, K. Cain, M. MacFarlane, G. HÃ¤cker, and M. Leverkus. “cIAPs Block Ripoptosome Formation, a RIP1/Caspase-8 Containing Intracellular Cell Death Complex Differentially Regulated by cFLIP Isoforms.” In: *Molecular Cell* 43.3 (2011), pp. 449–463.

[204] Z. Li, H. Wang, J. Zhu, N. Nan, Y. Lin, X. Zhuang, L. Li, Y. Zhang, and P. Huang. “Inhibition of TWEAK/Tnfrsf12a axis protects against acute liver failure by suppressing RIPK1-dependent apoptosis.” en. In: *Cell Death Discov.* 8.1 (2022), pp. 1–11.

[205] M. Gyrd-Hansen and P. Meier. “IAPs: from caspase inhibitors to modulators of NF-kappaB, inflammation and cancer.” In: *Nat Rev Cancer* 10.8 (2010), pp. 561–74.

[206] H.-S. Jin, D.-H. Lee, D.-H. Kim, J.-H. Chung, S.-J. Lee, and T. H. Lee. “cIAP1, cIAP2, and XIAP Act Cooperatively via Nonredundant Pathways to Regulate Genotoxic Stress–Induced Nuclear Factor-B Activation.” en. In: *Cancer Research* 69.5 (2009), pp. 1782–1791.

[207] C. M. Gray, K. A. McCorkell, S. K. Chunduru, M. A. McKinlay, and M. J. May. "Negative feedback regulation of NF-kappaB-inducing kinase is proteasome-dependent but does not require cellular inhibitors of apoptosis." In: *Biochem Biophys Res Commun* 450.1 (2014), pp. 341–6.

[208] T. T. Huang, S. M. Wuerzberger-Davis, Z.-H. Wu, and S. Miyamoto. "Sequential Modification of NEMO/IKK by SUMO-1 and Ubiquitin Mediates NF-B Activation by Genotoxic Stress." en. In: *Cell* 115.5 (2003), pp. 565–576.

[209] C. Lindemann, V. Marschall, A. Weigert, T. Klingebiel, and S. Fulda. "Smac Mimetic-Induced Upregulation of CCL2/MCP-1 Triggers Migration and Invasion of Glioblastoma Cells and Influences the Tumor Microenvironment in a Paracrine Manner." en. In: *Neoplasia* 17.6 (2015), pp. 481–489.

[210] S. Miyamoto, M. Maki, M. J. Schmitt, M. Hatanaka, and I. M. Verma. "Tumor necrosis factor alpha-induced phosphorylation of I kappa B alpha is a signal for its degradation but not dissociation from NF-kappa B." In: *Proceedings of the National Academy of Sciences* 91.26 (1994), pp. 12740–12744.

[211] D. E. Nelson, A. E. C. Ihekwaba, M. Elliott, J. R. Johnson, C. A. Gibney, B. E. Foreman, G. Nelson, V. See, C. A. Horton, D. G. Spiller, S. W. Edwards, H. P. McDowell, J. F. Unitt, E. Sullivan, R. Grimley, N. Benson, D. Broomhead, D. B. Kell, and M. R. H. White. "Oscillations in NF-kappaB signaling control the dynamics of gene expression." eng. In: *Science* 306.5696 (2004), pp. 704–708.

[212] T. Saitoh, M. Nakayama, H. Nakano, H. Yagita, N. Yamamoto, and S. Yamaoka. "TWEAK induces NF-kappaB2 p100 processing and long lasting NF-kappaB activation." eng. In: *J Biol Chem* 278.38 (2003), pp. 36005–36012.

[213] E. M. Cherry, D. W. Lee, J. U. Jung, and R. Sitcheran. "Tumor necrosis factor-like weak inducer of apoptosis (TWEAK) promotes glioma cell invasion through induction of NF-kappaB-inducing kinase (NIK) and noncanonical NF-kappaB signaling." In: *Mol Cancer* 14 (2015), p. 9.

[214] D. Opel, A. Schnaiter, D. Dodier, M. Jovanovic, A. Gerhardinger, I. Idler, D. Mertens, L. Bullinger, S. Stilgenbauer, and S. Fulda. "Targeting inhibitor of apoptosis proteins by Smac mimetic elicits cell death in poor prognostic subgroups of chronic lymphocytic leukemia." en. In: *International Journal of Cancer* 137.12 (2015), pp. 2959–2970.

[215] A. Tchoghandjian, C. Jennewein, I. Eckhardt, K. Rajalingam, and S. Fulda. "Identification of non-canonical NF-B signaling as a critical mediator of Smac mimetic-stimulated migration and invasion of glioblastoma cells." en. In: *Cell Death Dis* 4.3 (2013), e564–e564.

[216] T. Wittwer and M. L. Schmitz. "NIK and Cot cooperate to trigger NF-kappaB p65 phosphorylation." In: *Biochem Biophys Res Commun* 371.2 (2008), pp. 294–7.

[217] M. Feoktistova, R. Makarov, S. Brenji, A. T. Schneider, G. J. Hooiveld, T. Luedde, M. Leverkus, A. S. Yazdi, and D. Panayotova-Dimitrova. "A20 Promotes Ripoptosome Formation and TNF-Induced Apoptosis via cIAPs Regulation and NIK Stabilization in Keratinocytes." In: *Cells* 9.2 (2020).

[218] L. Boutaffala, M. J. Bertrand, C. Remouchamps, G. Seleznik, F. Reisinger, M. Janas, C. Benezech, M. T. Fernandes, S. Marchetti, F. Mair, C. Ganeff, A. Hupalowska, J. E. Ricci, B. Becher, J. Piette, P. Knolle, J. Caamano, P. Vandenabeele, M. Heikenwalder, and E. Dejardin. "NIK promotes tissue destruction independently of the alternative NF-kappaB pathway through TNFR1/RIP1-induced apoptosis." In: *Cell Death Differ* 22.12 (2015), pp. 2020–33.

[219] M. Haustein, R. Ramer, M. Linnebacher, K. Manda, and B. Hinz. "Cannabinoids increase lung cancer cell lysis by lymphokine-activated killer cells via upregulation of ICAM-1." en. In: *Biochemical Pharmacology* 92.2 (2014), pp. 312–325.

[220] M. Schellhorn, M. Haustein, M. Frank, M. Linnebacher, and B. Hinz. "Celecoxib increases lung cancer cell lysis by lymphokine-activated killer cells via upregulation of ICAM-1." In: *Oncotarget* 6.36 (2015), pp. 39342–39356.

[221] S. Textor, N. Fiegler, A. Arnold, A. Porgador, T. G. Hofmann, and A. Cerwenka. "Human NK Cells Are Alerted to Induction of p53 in Cancer Cells by Upregulation of the NKG2D Ligands ULBP1 and ULBP2." In: *Cancer Research* 71.18 (2011), pp. 5998–6009.

[222] M. Ruscetti, J. Leibold, M. J. Bott, M. Fennell, A. Kulick, N. R. Salgado, C. C. Chen, Y. J. Ho, F. J. Sanchez-Rivera, J. Feucht, T. Baslan, S. Tian, H. A. Chen, P. B. Romesser, J. T. Poirier, C. M. Rudin, E. de Stanchina, E. Manchado, C. J. Sherr, and S. W. Lowe. "NK cell-mediated cytotoxicity contributes to

tumor control by a cytostatic drug combination." In: *Science* 362.6421 (2018), pp. 1416–1422.

[223] W. H. Hallett, E. Ames, M. Motarjemi, I. Barao, A. Shanker, D. L. Tamang, T. J. Sayers, D. Hudig, and W. J. Murphy. "Sensitization of tumor cells to NK cell-mediated killing by proteasome inhibition." In: *J Immunol* 180.1 (2008), pp. 163–70.

[224] M. Uhlen, P. Oksvold, L. Fagerberg, E. Lundberg, K. Jonasson, M. Forsberg, M. Zwahlen, C. Kampf, K. Wester, S. Hober, H. Wernerus, L. Björling, and F. Ponten. "Towards a knowledge-based Human Protein Atlas." en. In: *Nat Biotechnol* 28.12 (2010), pp. 1248–1250.

[225] J. Korbecki, S. Grochans, I. Gutowska, K. Barczak, and I. Baranowska-Bosiacka. "CC Chemokines in a Tumor: A Review of Pro-Cancer and Anti-Cancer Properties of Receptors CCR5, CCR6, CCR7, CCR8, CCR9, and CCR10 Ligands." In: *Int J Mol Sci* 21.20 (2020).

[226] T. J. Schall. "Biology of the RANTES/SIS cytokine family." In: *Cytokine* 3.3 (1991), pp. 165–83.

[227] Y. Hikichi, H. Matsui, I. Tsuji, K. Nishi, T. Yamada, Y. Shintani, and H. Onda. "LIGHT, a member of the TNF superfamily, induces morphological changes and delays proliferation in the human rhabdomyosarcoma cell line RD." In: *Biochem Biophys Res Commun* 289.3 (2001), pp. 670–7.

[228] L. Valino-Rivas, L. Gonzalez-Lafuente, A. B. Sanz, M. Ruiz-Ortega, A. Ortiz, and M. D. Sanchez-Nino. "Non-canonical NFkappaB activation promotes chemokine expression in podocytes." In: *Sci Rep* 6 (2016), p. 28857.

[229] D. Y. Yeh, C. C. Wu, Y. P. Chin, C. J. Lu, Y. H. Wang, and M. C. Chen. "Mechanisms of human lymphotoxin beta receptor activation on upregulation of CCL5/RANTES production." In: *Int Immunopharmacol* 28.1 (2015), pp. 220–9.

[230] F. Liu, Y. Zhang, Z. Q. Wu, and T. Zhao. "Analysis of CCL5 expression in classical Hodgkin's lymphoma L428 cell line." In: *Mol Med Rep* 4.5 (2011), pp. 837–41.

[231] A. A. Maghazachi, A. al-Aoukaty, and T. J. Schall. "C-C chemokines induce the chemotaxis of NK and IL-2-activated NK cells. Role for G proteins." In: *J Immunol* 153.11 (1994), pp. 4969–77.

[232] D. D. Taub, T. J. Sayers, C. R. Carter, and J. R. Ortaldo. "Alpha and beta chemokines induce NK cell migration and enhance NK-mediated cytolysis." In: *J Immunol* 155.8 (1995), pp. 3877–88.

[233] P. Loetscher, M. Seitz, I. Clark-Lewis, M. Baggiolini, and B. Moser. "Activation of NK cells by CC chemokines. Chemotaxis, Ca2+ mobilization, and enzyme release." In: *J Immunol* 156.1 (1996), pp. 322–7.

[234] C. Ottaviani, F. Nasorri, C. Bedini, O. de Pita, G. Girolomoni, and A. Cavani. "CD56brightCD16(-) NK cells accumulate in psoriatic skin in response to CXCL10 and CCL5 and exacerbate skin inflammation." In: *Eur J Immunol* 36.1 (2006), pp. 118–28.

[235] H. Bhat, G. Zaun, T. A. Hamdan, J. Lang, T. Adomati, R. Schmitz, S. K. Friedrich, M. Bergerhausen, L. B. Cham, F. Li, M. Ali, F. Zhou, V. Khairnar, V. Duhan, T. Brandenburg, Y. M. Machlah, M. Schiller, A. Berry, H. Xu, J. Vollmer, D. Haussinger, B. Thier, A. A. Pandyra, D. Schadendorf, A. Paschen, M. Schuler, P. A. Lang, and K. S. Lang. "Arenavirus Induced CCL5 Expression Causes NK Cell-Mediated Melanoma Regression." In: *Front Immunol* 11 (2020), p. 1849.

[236] D. Dangaj, M. Bruand, A. J. Grimm, C. Ronet, D. Barras, P. A. Duttagupta, E. Lanitis, J. Duraiswamy, J. L. Tanyi, F. Benencia, J. Conejo-Garcia, H. R. Ramay, K. T. Montone, D. J. Powell, P. A. Gimotty, A. Facciabene, D. G. Jackson, J. S. Weber, S. J. Rodig, S. F. Hodi, L. E. Kandalaft, M. Irving, L. Zhang, P. Foukas, S. Rusakiewicz, M. Delorenzi, and G. Coukos. "Cooperation between Constitutive and Inducible Chemokines Enables T Cell Engraftment and Immune Attack in Solid Tumors." In: *Cancer Cell* 35.6 (2019), 885–900 e10.

[237] M. Theodoropoulou and G. K. Stalla. "Somatostatin receptors: from signaling to clinical practice." In: *Front Neuroendocrinol* 34.3 (2013), pp. 228–52.

[238] G. Rindi, O. Mete, S. Uccella, O. Basturk, S. La Rosa, L. A. A. Brosens, S. Ezzat, W. W. de Herder, D. S. Klimstra, M. Papotti, and S. L. Asa. "Overview

of the 2022 WHO Classification of Neuroendocrine Neoplasms." eng. In: *Endocr Pathol* 33.1 (2022), pp. 115–154.

[239] H. Lee, M. Suh, H. Choi, S. Ha, J. C. Paeng, G. J. Cheon, K. W. Kang, and D. S. Lee. "A pan-cancer analysis of the clinical and genetic portraits of somatostatin receptor expressing tumor as a potential target of peptide receptor imaging and therapy." en. In: *EJNMMI Res* 10.1 (2020), pp. 1–9.

[240] J. C. Reubi, B. Waser, J. A. Laissue, and J. O. Gebbers. "Somatostatin and vasoactive intestinal peptide receptors in human mesenchymal tumors: in vitro identification." In: *Cancer Res* 56.8 (1996), pp. 1922–31.

[241] Y. C. Patel, M. Greenwood, G. Kent, R. Panetta, and C. B. Srikant. "Multiple Gene Transcripts of the Somatostatin Receptor SSTR2: Tissue-Selective Distribution and cAMP Regulation." en. In: *Biochemical and Biophysical Research Communications* 192.1 (1993), pp. 288–294.

[242] T. Reisine, H. Kong, K. Raynor, H. Yano, J. Takeda, K. Yasuda, and G. I. Bell. "Splice variant of the somatostatin receptor 2 subtype, somatostatin receptor 2B, couples to adenylyl cyclase." In: *Mol Pharmacol* 44.5 (1993), pp. 1016–20.

[243] K. Harda, Z. Szabo, E. Juhasz, B. Dezso, C. Kiss, A. V. Schally, and G. Halmos. "Expression of Somatostatin Receptor Subtypes (SSTR-1–SSTR-5) in Pediatric Hematological and Oncological Disorders." en. In: *Molecules* 25.23 (2020), p. 5775.

[244] M. C. Fruhwald, C. H. Rickert, M. S. O'Dorisio, M. Madsen, M. Warmuth-Metz, G. Khanna, W. Paulus, J. Kuhl, H. Jurgens, P. Schneider, and H. L. Muller. "Somatostatin receptor subtype 2 is expressed by supratentorial primitive neuroectodermal tumors of childhood and can be targeted for somatostatin receptor imaging." In: *Clin Cancer Res* 10.9 (2004), pp. 2997–3006.

[245] P. Czapiewski, M. Kunc, A. Gorczynski, J. Haybaeck, K. Okon, J. Reszec, A. Lewczuk, J. Dzierzanowski, J. Karczewska, W. Biernat, M. Turri-Zanoni, P. Castelnuovo, C. Taverna, A. Franchi, S. La Rosa, F. Sessa, and G. Kloppel. "Frequent expression of somatostatin receptor 2a in olfactory neuroblastomas: a new and distinctive feature." In: *Hum Pathol* 79 (2018), pp. 144–150.

[246] K. Viswanathan and P. M. Sadow. "Somatostatin receptor 2 is highly sensitive and specific for Epstein-Barr virus-associated nasopharyngeal carcinoma." eng. In: *Hum Pathol* 117 (2021), pp. 88–100.

[247] B. Karaca, M. Degirmenci, A. Ozveren, H. Atmaca, E. Bozkurt, B. Karabulut, U. A. Sanli, and R. Uslu. "Docetaxel in combination with octreotide shows synergistic apoptotic effect by increasing SSTR2 and SSTR5 expression levels in prostate and breast cancer cell lines." In: *Cancer Chemother Pharmacol* 75.6 (2015), pp. 1273–80.

[248] E. Ferrante, C. Pellegrini, S. Bondioni, E. Peverelli, M. Locatelli, P. Gelmini, P. Luciani, A. Peri, G. Mantovani, S. Bosari, P. Beck-Peccoz, A. Spada, and A. Lania. "Octreotide promotes apoptosis in human somatotroph tumor cells by activating somatostatin receptor type 2." In: *Endocr Relat Cancer* 13.3 (2006), pp. 955–62.

[249] R. Teijeiro, R. Rios, J. A. Costoya, R. Castro, J. L. Bello, J. Devesa, and V. M. Arce. "Activation of human somatostatin receptor 2 promotes apoptosis through a mechanism that is independent from induction of p53." In: *Cell Physiol Biochem* 12.1 (2002), pp. 31–8.

[250] J. M. Lehman, M. D. Hoeksema, J. Staub, J. Qian, B. Harris, J. C. Callison, J. Miao, C. Shi, R. Eisenberg, H. Chen, S. C. Chen, and P. P. Massion. "Somatostatin receptor 2 signaling promotes growth and tumor survival in small-cell lung cancer." In: *Int J Cancer* 144.5 (2019), pp. 1104–1114.

[251] N. Gennaro, A. Marrari, S. L. Renne, F. C. M. Cananzi, V. L. Quagliuolo, L. Di Brina, M. Scorsetti, G. Pepe, A. Chiti, A. Santoro, L. Balzarini, L. S. Politi, and A. F. Bertuzzi. "Multimodality imaging of adult rhabdomyosarcoma: the added value of hybrid imaging." In: *Br J Radiol* 93 (2020), p. 20200250.

[252] B. Mandriani, E. Pellè, F. Mannavola, A. Palazzo, R. M. Marsano, G. Ingravallo, G. Cazzato, M. C. Ramello, C. Porta, J. Strosberg, D. Abate-Daga, and M. Cives. "Development of anti-somatostatin receptors CAR T cells for treatment of neuroendocrine tumors." en. In: *J Immunother Cancer* 10.6 (2022), e004854.

[253] G. Imre, S. Larisch, and K. Rajalingam. "Ripoptosome: a novel IAP-regulated cell death-signalling platform." In: *Journal of Molecular Cell Biology* 3.6 (2011), pp. 324–326.

A Supplementary figures and data

A.1 Log_2 fold change data of RNAseq and Fluidigm® analysis

Tab. A.1: List of DEGs identified by RNAseq, after applying a threshold of p_{adj} value < 0.05 and $\log_2$ fold change $> |1|$

Gene name	$\log_2$ fold change	p_{adj} value
AC005180.2	1.47	4.69E-02
AC005358.2	1.25	1.91E-02
AC008906.1	1.19	2.28E-08
AC008957.3	4.58	3.51E-03
AC009549.1	1.60	8.00E-03
AC009879.3	1.02	5.19E-07
AC010980.2	-1.05	1.16E-02
AC013451.2	-1.38	9.61E-03
AC025580.2	2.04	2.79E-04
AC040977.2	1.20	1.53E-14
AC062015.1	-1.41	3.77E-02
AC068580.2	-1.24	4.50E-02
AC079781.5	1.02	1.82E-05
AC112236.2	-1.05	1.10E-02
AC116366.1	1.14	3.02E-03
AC132217.1	-1.64	1.54E-06
ACHE	1.88	4.44E-03
ADGRA1-AS1	-1.39	4.50E-02
ADGRG5	-1.75	4.55E-04
AFF3	1.73	7.89E-04
AL049569.1	-1.45	3.63E-03
AL049796.1	-1.33	1.84E-02

Tab. A.1: List of DEGs identified by RNAseq, after applying a threshold of p_{adj} value < 0.05 and $\log_2$ fold change $> |1|$ – continued.

Gene name	$\log_2$ fold change	p_{adj} value
AL355601.1	-2.63	1.30E-02
AL390719.1	1.10	1.58E-05
AL512625.2	-1.05	2.51E-02
AL590004.3	-1.12	1.59E-03
AL590560.1	1.98	4.92E-04
AL645608.8	1.20	1.84E-02
AL691420.1	-1.61	4.08E-02
ANKRD22	3.70	2.03E-07
AP000781.2	1.18	1.48E-08
AP005264.7	-1.35	2.31E-02
APOL1	1.14	9.27E-06
APOL3	2.05	2.53E-06
APOL6	1.43	8.98E-10
ASNS	1.07	1.82E-05
ATP13A2	-1.29	2.08E-03
BIRC2	1.43	1.26E-06
BIRC3	4.77	9.71E-30
C15orf48	1.90	2.96E-02
C17orf49	1.14	7.48E-11
C1orf105	-1.20	9.01E-03
C1QL3	1.34	3.37E-02
C1QTNF1	-1.21	2.37E-03
C3orf20	-1.18	3.77E-03
CAMK1G	2.30	1.90E-05
CAMK2A	2.01	4.18E-13
CAMK2B	-1.15	8.31E-03
CCL5	4.64	5.48E-22

Tab. A.1: List of DEGs identified by RNAseq, after applying a threshold of p_{adj} value < 0.05 and $\log_2$ fold change $> |1|$ – continued.

Gene name	$\log_2$ fold change	p_{adj} value
CD200	3.50	3.29E-05
CDH6	-1.06	2.05E-02
CTSS	1.53	3.29E-10
DCLK1	1.51	1.23E-09
DDX58	1.30	1.02E-06
DDX60	1.32	6.95E-03
DOK7	-1.54	2.86E-03
EGOT	4.03	3.08E-05
ENTPD2	-1.06	5.02E-03
ERAP1	1.15	1.53E-14
ESYT3	-1.83	3.65E-04
EXOC3L4	1.76	4.15E-03
FAM178B	-1.31	3.96E-03
FBXW4P1	-1.58	7.01E-03
FCRLA	1.22	2.98E-05
FCRLB	1.55	6.39E-05
FETUB	1.59	6.29E-04
GBP4	2.02	2.08E-03
GBP5	2.65	1.77E-04
GCNT3	2.44	3.55E-03
GDPD5	-1.00	1.21E-02
GFPT2	2.64	1.05E-08
GPA33	-1.64	1.94E-03
GPR132	1.35	9.24E-03
GREM1	1.25	4.14E-11
GSG1	-1.03	2.26E-02
HDAC9	1.94	1.92E-16

Tab. A.1: List of DEGs identified by RNAseq, after applying a threshold of p_{adj} value < 0.05 and $\log_2$ fold change $> |1|$ – continued.

Gene name	$\log_2$ fold change	p_{adj} value
HSD3BP5	1.49	2.22E-02
IFIH1	3.93	3.89E-18
IFIT1	1.29	3.12E-03
IFIT2	1.70	1.44E-06
IFIT3	2.80	2.07E-17
IGF2	-1.57	2.30E-08
IGLC1	-1.06	1.41E-03
IGLC2	-1.04	1.18E-04
IGLC3	-1.02	2.17E-04
IGLC5	-1.21	4.63E-05
IGLC6	-1.35	4.25E-05
IGLC7	-1.34	6.30E-03
IGLJ2	-1.10	2.84E-04
IGLJ3	-1.00	5.53E-04
IGLL5	-1.05	3.51E-03
IL2RG	1.07	3.90E-03
IL7R	1.30	1.07E-08
INS-IGF2	-1.59	1.55E-07
ITGAM	4.42	1.36E-54
ITGAX	1.68	3.64E-03
KLHDC7B	2.65	5.46E-05
KRT7	1.54	1.86E-05
KRT7-AS	1.07	2.54E-02
LACTB	1.09	2.68E-09
LAMC2	1.21	2.56E-09
LINC00460	1.61	4.92E-04
LINC00475	-1.32	6.13E-03

Tab. A.1: List of DEGs identified by RNAseq, after applying a threshold of p_{adj} value < 0.05 and $\log_2$ fold change $> |1|$ – continued.

Gene name	$\log_2$ fold change	p_{adj} value
LINC00511	-1.36	7.42E-15
LINC00622	1.45	3.53E-02
LINC00943	2.08	6.91E-05
LINC00944	1.53	4.16E-07
LINC01238	-1.21	2.85E-02
LINC01711	-1.21	8.60E-03
LINC02328	2.04	1.79E-09
LINC02393	2.99	7.48E-03
LRIG1	1.23	1.34E-13
LRRN4CL	-1.01	2.91E-02
LSP1	-1.31	5.25E-04
LTBP2	-1.36	5.61E-04
MCF2L	-1.40	1.24E-05
MEOX1	3.28	6.44E-13
MGAT4C	3.14	9.13E-03
MIR497HG	1.24	7.42E-15
MIR7847	-1.76	7.07E-04
MMP9	2.63	5.19E-07
MSTN	-1.35	2.88E-08
MXRA5Y	-1.10	9.04E-04
NAV3	1.30	1.42E-08
NDST4	-1.08	1.58E-02
NFKB2	1.58	2.21E-09
NFKBIA	2.07	7.83E-11
NLGN4Y	1.54	3.22E-07
NMNAT2	1.22	3.84E-02
NUPR1	2.46	3.68E-03

Tab. A.1: List of DEGs identified by RNAseq, after applying a threshold of p_{adj} value < 0.05 and $\log_2$ fold change $> |1|$ – continued.

Gene name	$\log_2$ fold change	p_{adj} value
OAS2	1.24	2.97E-02
OR10AC1	1.94	2.36E-02
P2RY6	-1.45	8.66E-03
PAMR1	1.29	3.17E-03
PKD1L1	1.25	1.87E-03
PLA2G4C	2.81	6.14E-33
PLA2G4C-AS1	2.97	4.58E-21
PLCH2	-1.57	7.69E-03
PLEKHD1	-1.07	2.39E-02
RARRES3	1.77	1.59E-03
RASGRP3	1.26	1.80E-13
RN7SL263P	-2.06	1.54E-02
RPL12P14	1.48	2.84E-04
RSAD2	3.49	3.04E-13
SAA1	1.65	1.58E-02
SBK3	-1.09	3.70E-02
SBSPON	1.39	2.20E-02
SCARA5	1.67	4.92E-04
SEMA4A	1.45	8.72E-04
SEMA5A	1.46	4.67E-02
SHROOM2	-1.05	7.24E-11
SIGLEC15	2.45	1.05E-06
SLAMF8	2.58	2.61E-04
SLC16A9	1.36	6.26E-04
SLC1A3	1.28	4.41E-07
SLC26A9	1.23	5.87E-03
SLC28A3	2.33	5.73E-04

Tab. A.1: List of DEGs identified by RNAseq, after applying a threshold of p_{adj} value < 0.05 and $\log_2$ fold change $> |1|$ – continued.

Gene name	$\log_2$ fold change	p_{adj} value
SLC38A3	1.89	1.64E-04
SLC43A3	1.22	2.23E-09
SLC4A4	2.42	1.52E-05
SLFN5	1.44	1.08E-11
SSTR2	3.49	4.10E-50
SSX4	-1.50	2.99E-03
SSX4B	-1.47	3.85E-03
STK31	-1.34	8.00E-03
TENM4	1.53	5.55E-03
TLR5	2.17	5.80E-04
TMCO4	-1.21	1.08E-06
TMEM119	1.34	1.57E-02
TMEM229B	1.14	2.76E-04
TNFRSF9	2.78	4.51E-16
TRAF1	3.50	9.62E-25
TRIB3	1.03	1.36E-02
TRIM29	3.80	1.34E-13
TRIM47	1.44	6.62E-04
UNC13A	4.10	9.21E-33
VEGFC	1.15	1.27E-12
VXN	1.03	4.59E-07
WFDC5	4.40	4.34E-04
ZNF668	-1.00	3.31E-03
ZNF697	1.01	6.05E-08
ZP4	2.22	2.32E-02

Tab. A.2: Correlation of GOIs identified by RNAseq with Fluidigm® analysis

Gene name	$\log_2$ fold change (Fluidigm)	$\log_2$ fold change (RNAseq)
BIRC2	1.40	1.43
CAMK1G	0.04	2.30
CCL5	7.76	4.64
CTSS	1.60	1.53
ESYT3	-1.84	-1.83
IFIT3	4.07	2.80
IL7R	1.27	1.30
ITGAM	4.82	4.42
MSTN	-1.32	-1.35
NFKB2	1.78	1.58
NFKBIA	1.86	2.07
NUPR1	3.35	2.46
PLA2G4C	2.90	2.81
PLCH2	-1.29	-1.57
SSTR2	3.54	3.49
TLR5	1.82	2.17
TNFRSF9	2.72	2.78
TRAF1	3.32	3.50
TRIB3	1.46	1.03
TRIM29	5.36	3.80
VEGFC	1.29	1.15

A.2 Sequencing data for *CCL5* knock-out validation

(a) Sequencing of *CCL5*-exon2 of knock-out RH30 clone 1, forward primer.

(b) Sequencing of *CCL5*-exon2 of knock-out RH30 clone 1, reverse primer.

Fig. A.1: Sequencing of exon 2 of *CCL5* knock-out RH30 cell clone 1.

(a) Sequencing of *CCL5*-exon2 of guide control RH30 clone 2, forward primer.

(b) Sequencing of *CCL5*-exon2 of guide control RH30 clone 2, reverse primer.

Fig. A.2: Sequencing of exon 2 of *CCL5* of guide control RH30 cell clone 2.

C Declaration on oath

Except where stated otherwise by reference or acknowledgment, the work presented was generated by me, Vinzenz Särchen, under the supervision of my advisors during my doctoral studies. All contributions from colleagues are explicitly referenced in the thesis. The material listed below was obtained in the context of collaborative research:

Method 4.2.1.5: Formation of multicellular tumor spheroids. Together with Dr. Sara Kehr (a former PhD student in the Institute for Experimental Cancer Research in Pediatrics) we established the formation of multicellular RMS tumor spheroids in the Institute for Experimental Cancer Research in Pediatrics. Here, the collaboration is in regard to the empirical determination of the used cell numbers for the spheroid formation and initial microscopical setup to acquire fluorescence images.
All spheroid experiments, including spheroid generation, cultivation, treatment, microscopic acquisition and analysis shown in this PhD thesis were performed by me.

Method 4.2.1.6: NK cell enrichment and maintenance. Together with a medical doctoral candidate Senthan Shanmugalingam and a laboratory technician Sara Wiedemann, whom I co-supervised and showed laboratory techniques, we rotated in NK cell culture enrichment and maintenance.

Method 4.2.6.4: RNA sequencing analysis: Together with Lisa Marie Reindl (PhD student at the University Hospital Frankfurt, Goethe-University, in the group of Prof. Dr. Evelyn Ullrich) we performed the sample preparation of RH30 cells treated with BV6. Additionally, we prepared NK cells co-cultured with RH30 cells for RNAseq analysis. The samples were transferred to TRON gGmbH, Mainz, Germany for bulk RNA sequencing and initial data acquisition and analysis was performed by Dr. Thomas Bukur of TRON gGmbH, Mainz, Germany.

Figure 5.42: The principle component analysis of RNAseq results for BV6 treated RH30 cells was performed by Dr. Thomas Bukur of TRON gGmbH, Mainz, Germany, he performed initial data analysis of the RNAseq raw data.

Figure 5.43(b): Heatmap of top 50 differentially expressed genes, Dr. Thomas Bukur of TRON gGmbH, Mainz, Germany performed initial data analysis of the RNAseq raw data and generated the heatmap. I performed additional pathway enrichment analysis of the already fold change calculated RNAseq data.

Table 5.1: RNA sequencing data of two chosen genes of interest for further validation experiments, Dr. Thomas Bukur, TRON gGmbH Mainz performed initial data analysis and calculated fold changes and adjusted p-values for differentially expressed genes, I performed additional pathway enrichment analysis of the already fold change calculated RNAseq data.

Table A.1: List of DEGs identified by RNAseq, Dr. Thomas Bukur, TRON gGmbH Mainz. He calculated fold changes and adjusted p-values for differentially expressed genes, I performed additional pathway enrichment analysis of the already fold change calculated RNAseq data.

Table A.2: Correlation of GOIs by RNAseq with Fluidim®, Martin Suchan, TRON gGmbH Mainz. He acquired data and performed initial raw data analysis. I performed further data analysis of fold change calculations, data adaptations and correlation analysis between Fluidigm® and RNAseq analysis data.

The following parts of the thesis have been previously open access published in Särchen et al. [26], under Creative Commons Attribution 4.0 International License.

Together with Dr. Sarah Kehr, I established the RMS spheroid methodology in our institute and co-supervised a medical doctoral candidate Senthan Shanmugalingam. All three of us participated equally as first authors and performed experiments, analyzed data, interpreted results and prepared the manuscript.
Figure 5.25: Migration of NK cells into RMS-GFP spheroids at different E:T ratios. I performed spheroid generation and NK cell staining, co-cultivation, image acquisition and analysis of the dataset.

I, Vinzenz Särchen, declare under oath, that I followed the guidelines of good scientific practice and the non-use of commercial doctoral consultants.